UNIVERSIDAD NACIONAL AUTÓNOMA DE MÉXICO

POSGRADO EN CIENCIA E INGENIERÍA DE MATERIALES

"Lithium Niobate powders: its Chemical Composition and a study of its Second Harmonic Generation response"

QUE PARA OPTAR POR EL GRADO DE:
DOCTOR EN CIENCIA E INGENIERÍA DE MATERIALES

PRESENTA:

OSWALDO SÁNCHEZ DENA

TUTOR PRINCIPAL
DR. JORGE ALEJANDRO REYES ESQUEDA
INSTITUTO DE FÍSICA

COMITÉ TUTOR
DRA. MARÍA ELENA VILLAFUERTE CASTREJÓN
INSTITUTO DE INVESTIGACIONES EN MATERIALES
DR. JOSÉ RURIK FARÍAS MANCILLA
IIT-UNIVERSIDAD AUTÓNOMA DE CIUDAD JUÁREZ

Ciudad Universitaria, Cd. Mx, diciembre 2019

HOJA DE DATOS 1

Sustentante

Oswaldo Sánchez Dena

Universidad Nacional Autónoma de México

Posgrado en Ciencia e Ingeniería de Materiales

Doctorado

ossdena@gmail.com

Comité tutoral

Tutor principal

Dr. Jorge Alejandro Reyes Esqueda

Investigador Titular B

Universidad Nacional Autónoma de México

Instituto de Física

reyes@fisica.unam.mx

1er miembro

Dr. José Rurik Farías Mancilla

Investigador Titular C

Universidad Autónoma de Ciudad Juárez

Departamento de Física y Matemáticas

rurik.farias@uacj.mx

2do miembro

Dra. María Elena Villafuerte Castrejón

Investigador Titular C

Universidad Nacional Autónoma de México

Instituto de Investigaciones en Materiales

mevc@unam.mx

HOJA DE DATOS 2

Sinodales

Dr. José Manuel Hernández Alcántara (Presidente)

Instituto de Física, Universidad Nacional Autónoma de México

josemh@fisica.unam.mx

Dr. Jorge Alejandro Reyes Esqueda (Primer vocal; **tutor principal**)

Instituto de Física, Universidad Nacional Autónoma de México

reyes@fisica.unam.mx

Dra. María Herlinda Montiel Sánchez (Segundo vocal)

Instituto de Ciencias Aplicadas y Tecnología

Universidad Nacional Autónoma de México

herlinda.montiel@icat.unam.mx

Dr. José Ocotlán Flores Flores (Tercer vocal)

Instituto de Ciencias Aplicadas y Tecnología

Universidad Nacional Autónoma de México

ocotlan.flores@icat.unam.mx

Dr. Juan Carlos Alonso Huitrón (Secretario)

Instituto de Investigaciones en Materiales, Universidad Nacional Autónoma de México

alonso@unam.mx

II

Datos del trabajo escrito

Lithium Niobate powders: their Chemical Composition and a
study of their Second Harmonic Generation response

175 pages, 49 figures: **2019**

DEDICATORIA

con amor a mi única hija, LM.

Deseo con todas las fuerzas de mi ser que puedas ser feliz.
Una persona siempre respetuosa y humilde.
Que siempre seas consciente de Dios.

III

AGRADECIMIENTOS

SUMMARY

This is an investigation of experimental character that can be conceived as constituted from the results obtained by two separate conducted researches. First, it addresses the problem of determining the chemical composition (CC) of lithium niobate powders (LiNbO$_3$; LN). Existent methods for determining the composition of LN *single crystals* are mainly based on their variations due to changes in their electronic structure, which accounts for the fact that most of these methods rely on experimental techniques using light as the probe. Nevertheless, these methods used for single crystals fail in accurately predicting the chemical composition of LN powders (LNPws) and despite of the increasing interest –because of the importance of their possible applications in actual and future nanooptoelectronic devices, as well as the facility to produce them in large quantities—, an accurate and trusting method to determine their CC did not exist, previously to this work. Therefore, here a first step was given in this direction by developing a facile method based mainly on imposing X-Ray Diffraction (XRD) as a seed characterization technique. Its validation is supported by the characterization of several samples synthesized by the standard and inexpensive method of mechanosynthesis, where the Li and Nb content is varied in a controlled way. Raman Spectroscopy (RS), UV-vis Diffuse Reflectance (DR) and Differential Thermal Analysis (DTA) enrich this work, representing various alternatives for the independent and accurate determination of the CC of LNPws. An empirical equation that describes this fundamental property in terms of a corresponding experimental parameter is given for each of these four characterization techniques. The results regarding this first conducted research can also be consulted in:

VI

On the other hand, this investigation also addresses the study of the Second Harmonic Generation (SHG) response from LNPws with an averaged stoichiometric composition, accordingly to the first research conducted. The study was conducted in terms of the depth of the prepared sample, that is, a Z-sectioning of the SHG response was performed as the beam focus of the fundamental wave is translated from +z to -z position, passing from the

air/powder interface (z=0). Also, in terms of the linear polarization state of light, at both the excitation and detection stages. The former itself, besides being able to estimate the sample thickness and roughness of granular media at the micrometric scale, gives information on the scattering properties of the sample by deconvolution of the measured SHG intensity profile and fitting to the Beer-Lambert law. In the present investigation, contrary to other similar approaches found on the literature, neither z-correction was needed to be applied the intensity profile nor it was necessary to consider a contrast between the phase-matched SHG arising from the properly oriented crystallites and the most probable non-phase-matched SHG that arises from a larger number of randomly oriented crystallites. The initial performed analysis to the Z-sectioning part (no polarization of light involved) led to the conclusion that under these experimental conditions (both optical and sample preparation) light tends to scatter more forwardly (Mie scattering regime). This implied that the "bulk" SHG could be differentiated at all instances, thus the surface properties of the prepared sample could readily be probed at the air/powder interface and at layers beneath it, down to the powder/susbtrate interface. The results regarding this second conducted research will soon be published:

VII

Sánchez-Dena, O.; […] Reyes-Esqueda, J.A.; Brevet, P-F. *To be published*

Other published work related at different levels to the current doctorate research project, which was developed in the period mid-2016 to mid-2019, are:

Sánchez-Dena, O.; García-Ramírez, E.V.; Fierro-Ruiz, C.D.; Vigueras-Santiago, E.; Farías, R.; Reyes-Esqueda, J.A. Effect of size and composition on the second harmonic generation from lithium niobate powders at different excitation wavelengths. *Mater. Res. Express* **2017**, 4, 035022; DOI:10.1088/2053-1591/aa62e5.

Fierro-Ruíz, C. D.; Sánchez-Dena, O.; Cabral-Larquier, E. M.; Elizalde-Galindo, J. T.; Farías, R. Structural and Magnetic Behavior of Oxidized and Reduced Fe Doped $LiNbO_3$ Powders. *Crystals*, **2018**, 8, 108. DOI:10.3390/cryst8030108.

Structurally this work of thesis is formed out of three main blocks or pieces, hereafter referred to as parts. Each part is considered as a unit of the whole but has been written in such a manner that it is not strictly necessary to read one to understand another. Said differently, each part is self-consistent, and it is also consistent with the rest of the thesis. Hence to whom disposes time and finds it pertinent, it is invited to read it completely. However, it is also acknowledged that today we all live in a society in which time runs out, so that if you already

dominate the concepts and theoretical basis of the subject –PART I—, and know about the method of synthesis and the characterization techniques –PART II—, then you might go without hesitation directly to PART III where: the performed experimental procedures are described in detail, the obtained results are simultaneously introduced and discussed, and the conclusions are given. Independently of the interests of any potential reader, to all it is strongly suggested to read the Introduction, located at the top of PART I. Lastly, here it is also important to mention that transcendental for this researching project to be developed are two scientific collaborations at the institutional level, one domestic and one international. The former held between the *Universidad Nacional Autónoma de México* (UNAM) and the *Universidad Autónoma de Ciudad Juárez* (UACJ), headed by Dr. Jorge Alejandro Reyes Esqueda (Instituto de Física, UNAM) and Dr. José Rurik Farías Mancilla (Departamento de Física de Matemáticas, UACJ). The latter held between UNAM and the *Institut Lumiere Matiere, Université Claude Bernard Lyon 1,* headed by the same (UNAM) and Prof. Pierre Francois Brevet.

CONTENTS

X

PART II

TECHNIQUES AND EXPERIMENTAL METHODS

(THEORETICAL INTRODUCTION)

EXPERIMENTAL

Chapter 3: Materials + Nonlinear optics

*: succinct introduction and presentation of relevant references

XI

PART III

RESULTS

(PRESENTATION AND DISCUSSION)

Chapter 5: Materials

Chapter 6: Nonlinear optics

Results on the depth profile of the polarization-resolved Second Harmonic Generation in a pressed and compacted sample of $LiNbO_3$ micropowders……………………………129

XII

PART I

GENERAL OUTLOOK

STRUCTURE OF THE THESIS

THEORETICAL FRAMEWORK

Introduction

Physics and Materials Science are full of amazement, powerful and captivating concepts, beautiful constructed theories, novel experimental findings and niche technological applications. Giving an example of such has been avoided on purpose so that none stands out among the others; anyone working in these fields would pick a favorite one. In my case I would choose, on top of the list, the concept of Second Harmonic Generation (SHG): I still remember the strong impression it caused to me when I heard of this second order nonlinear optical process for the first time in a talk given by an invited speaker of the Faculty of Sciences, where I was sophomore student of the Physics career… I was really amazed by the fact that there exists certain type of materials (and not all!) capable of doubling the frequency of the incoming monochromatic (laser) light. Particularly, to have visible laser light (λ=532nm) out of infrared laser light (λ=1064nm)! Yet this only (necessarily but not sufficiently) by use of a suitable material.

Another important concept that would occupy such a list is the perovskite structure: not much before graduating from the Physics career I tried to induce the Meissner effect at a high temperature (that of liquid nitrogen) by preparing a perovskite-based ceramic. The experiment failed but since then I was conscious of the relevance of perovskites to Materials Science and, significantly, to recently accomplished technology. It thus seems quite natural that today I am writing a doctorate thesis having these two abstractions as carotids.

This work of thesis deals with two main aspects, independently. Firstly, and more important, with the accurate determination of the chemical composition (CC) of lithium niobate (LiNbO$_3$; LN) powders; the results of this investigation can also be consulted in [1]. Historically, the room temperature structure of LN has been often related to those of ilmenite and corundum. Rigorously speaking LN adopts neither of these, it is nowadays broadly accepted that LN possess a distinct structure, one of its own thus forming a new family of crystalline structures. Recent authorities in the field mainly address to it as a 'pseudoilmenite', but in a more profound sense, of more physical importance, it might also be conceptually conceived as a variant of the family of distorted perovskites. Secondly, in this thesis it is also highlighted the importance of performing a combined analysis resulting from the depth profiling of the polarization-resolved (PR) powder SHG (PSHG), that is, the characterization of polar distortion by means of rotation of the incident linear polarization

(fundamental wave) and fixation of the outgoing polarization (harmonic wave) with an analyzer, as the beam focus of the fundamental wave is translated from +z to -z position, passing from the air/powder interface (z=0). These experiments were performed to a single sample of LN powder of (averaged) stoichiometric composition, which was properly characterized according to [1]; the results of this investigation will be soon published in [2].

The two main components of this dissertation are thus LN and SHG. A succinct introduction to these researching fields is given in the following lines, separately. The work of Luo et al might just be a good example of what could be understood as the state-of-the-art developments in research that merges these two subjects [3]. As it will be described, research in the powdered version of LN is uncommon to both disciplines, and thus the investigations developed in this work of thesis broaden the existent knowledge.

LITHIUM NIOBATE:

"LN is one of the most favorite multifunctional crystals", quoting Pang et al [4]. According to Weis and Gaylord, it is a completely synthetic material, that is, it cannot be found in nature [5]. In the words of Volk and Wöhlecke, authors of the most comprehensive monograph written up-to-date on LN (*Lithium Niobate. Defects, Photorefraction and Ferroelectric Switching*; Springer), LN crystals are "colorless, chemically stable and insoluble in water and organic solvents, and have high melting points" [6]. By colorless it is meant a high transparency window of the order < 0.1 cm^{-1} for radiation in between 400 and 5000 nm [7]. This combined to the fact that LN crystals are non-centrosymmetric and have a high nonlinear coefficient, make them suitable materials for SHG and Optical Parametric Generation in this range of the electromagnetic spectrum [7, 8]. High melting points along with a high Curie temperature (T_c~1210 °C) translates into the exhibition of the spontaneous polarization (ferroelectricity) in broad range of temperatures (from T_{room} to T_c). A classic text considered today an important consulting reference was written by Räuber (1978, *CHEMISTRY AND PHYSICS OF LITHIUM NIOBATE; North-Holland*) [9]: it is stated, on the other hand, that LN "is a fairly useless material from a chemical point of view, its only application being as a starting material for crystal growth".

The LiNbO$_3$ phase was first described by Zachariasen in 1928 [10]; he is considered one of the giants in crystal structure analysis, alongside Pauling and Belov [11]. The first ever synthesis of LN can be traced back to 1937 [12, 13]: apparently "small crystals having the

shape of small prims" were obtained, although this information could not be corroborated in the present investigation. Remeika is credited for having grown LN single crystals for the first time a little before 1949 and, in this year, the same and Matthias published the first report on the ferroelectric behavior of such crystals [14, 15]. In 1965 Ballman – and Fedulov *et al*, this is not often mentioned in recent literature—managed to grow larger crystals by using the Czochralski method [15-17]. Since then a parallel grow begun in scientific and engineering activities, remarkably at the Bell Laboratories, and ever since this pioneering work – published in 1966, five papers [7, 18-21]— details on the structure of this material are known with high precision, thus allowing the explanation and prediction of a myriad of well-known applications addressed to it (existent and potential), these are described elsewhere [3-6, 8-9, 12-14, 22-24]. Particularly, references in [7, 20-21] constitute a paramount contribution to the whole scientific community involved in the study of LN: they form the basis of all further discussions on the LN crystal structure.

Research at the fundamental and applied science levels has not stopped in the past five decades. Back in the late 1970's LN was important for the development of surface acoustic waves (SAW) devices, it took second place only to quartz in the market of single crystalline piezoelectrics [9]. Today, according to Bartayste et al, "about 70% of radio-frequency (RF) filters, based on surface acoustic waves, are fabricated on these single crystals" [25]. As for the future, a glimpse to the role of this material to achieve practical integrated on-chip applications might be grasped as LN is already considered to be for photonics what silicon has been being for electronics [26]. Such a statement is not a reckless one, neither it is arbitrary, since it rests upon the breathtaking results published by Zhang et al (December 2017, 72 cites by mid-2019) [27]. The implications entailed in [27], have been reinforced and updated by the same group recently [28].

Here I would like to emphasize the paramountcy LN has to the recent scientific research. Perhaps an effective way to quantify the success of a researching field is to analyze the number of peer-reviewed publications in scientific journals in a period. Volk and Wöhlecke have had used the WebOfScience database to track the number of publications between 1965 and 2007 (annually) devoted to LN and $BaTiO_3$ (see 'Fig. 1.1', p. 2 in [6]). By today both materials likely surpass the thousand publications. Here it is added that another indicative of the LN success nowadays is the fact that, for a least four consecutive years, specialized issues

on this material have been being prepared by the *Crystals* journal, MDPI editorial. The results of this investigation –those related to the chemical composition of LN powders, reference in [1]— have been published in the current special issue, entitled '*Recent Progress in Lithium Niobate',* having Robert A. Jackson and Zsuzsanna Szaller as guest editors [13]. Anecdotally, by refining the same analysis to the specific case of research in Mexico, one can notice – typing 'Lithium Niobate' and 'LiNbO3' by separate—that around a hundred articles have been produced up-to-day. Also, according to this database the first ever Mexican scientific article on LN was published in 1984 and authored by Villafuerte-Castrejón et al [29]. Proudly, Prof. Villafuerte-Castrejón has been part of the advisory committee of this doctoral research project.

Volk and Wöhlecke address to LN as an oxide ferroelectric which unique combination of physical properties has "promoted its career in science and devices" [6]. However, given the great variety of physical properties that can be ascribed to it, (ferroelectric) LN can be classified into several subclasses of materials. Apart from its structure, the definition or description of this material could be given in accordance with the specific property or application to be investigated. Effectively, LN can be labeled as any of the following: dielectric, uniaxial crystal, metallic oxide, ceramic, ferroelectric, pyroelectric, piezoelectric, photorefractive, photovoltaic, *non-centrosymmetric* nonlinear optical medium and *frequency converter*, among others. The exacerbation/detriment of a property associated with each of these terms is to be tuned by a proper control of point defects, either intrinsic or extrinsic [30-33]. Particularly important are the extrinsic defects, such as those present in ion doped LN crystals, for which the intrinsic capabilities of the crystal might not only be improved but new ones could also arise [33]. Historically, this has been a major subject of interest for the scientific community involved in the study of LN. This work of thesis has been limited, however, to the subject of intrinsic defects, that is, the study of the compositional change in the crystal, parametrized by the ratio R={Li}/{Nb} (the brackets denoting concentration in mol %). A comprehensive review on doped-LN single crystals might be consulted in [34].

Solid solutions (SSs) of LN have an intrinsic nature to deviate from the stoichiometric (ST) point R=1. This will further be discussed in detail in the corresponding theoretical framework. Meanwhile Figure I-1 showing the binary phase diagram that describes the Li_2O—Nb_2O_5 system, would suffice to visualize this argument. Another important point – or

perhaps the most important – is the congruent (CG) one R=0.969, for which the highest uniformity of properties is attained [6]. This point is so-called CG because, as it can be seen in Figure I-1, within the LN phase an inflection on the liquidus-solidus curve takes place at this point, implying a preservation of the chemical composition in the process of passing from the Li_2O:Nb_2O_5 melt to the growing crystal. Said differently, CG means that $R_{melt(liq)}=R_{crystal(sol)}=0.969$. For off-congruent melts "the composition of the melt and the crystal are slightly varying during the growth and the crystal becomes compositionally non-uniform, particularly along the growth axis" [6].

6
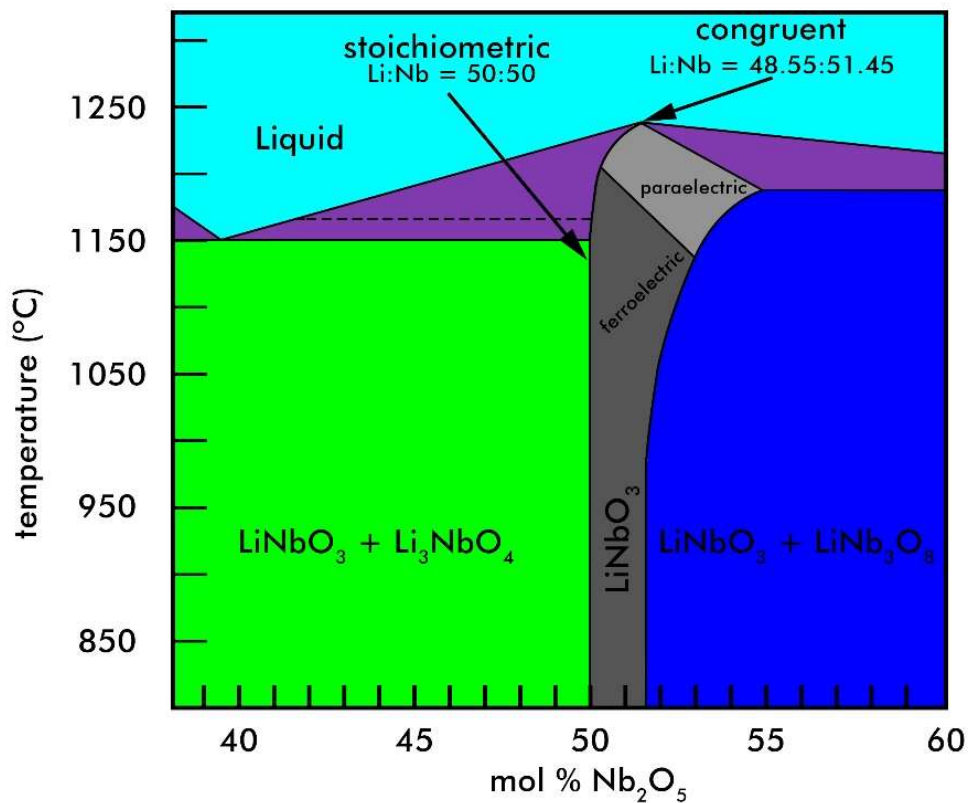
Figure I-1. Schematic phase diagram of the Li_2O-Nb_2O_5 pseudobinary system in the vicinity of $LiNbO_3$ – redrawn from the publications by Volk and Wöhlecke [6], and Hatano et al. [39].

In general, under regular circumstances of growth (Czochralski method), high quality ST LN crystals are not obtained even for a $R_{melt(liq)} \geq 1$. Basically not even near ST (nST) LN crystals were available until 1992, year in which three independent methods for this purpose were reported, entailing a modification to the Czochralski method (double crucible Czochralski method) [35], growth from melts containing K_2O [36], and diffusion of Li from

a powder richer in this element than the crystal, a process that takes several days and requires high temperature heating treatments ($\geq 1000°$ C) [37]. Today, the synthesis of ST LN single crystals still is a state-of-the-art matter: reason behind the fact that a Z-cut of ST wafer costs around 12 times more than one possessing a CG composition [38]. ST LN crystals are important because a more perfect lattice translates into a lower density of local field distortions and the lessening of anharmonic crystal interactions (phonon coupling), both being prerequisites for any kind of resonance with a small linewidth [6].

In what concerns this investigation, two more transcendental features are to be noticed from the phase diagram. One is the existence of two-component phases that delimit the LN single-phase. These are homogenous mixtures of LN and a SS secondary phase: methaniobates Li_3NbO_4 and $LiNb_3O_8$. Because of the preference of single or pure phase compounds over those with a mixture of phases, added to the fact that LN "sub-CG compositions present poor physical properties and do not have potential applications" [40], these phases are often referred to as 'parasitical'. Interestingly, in the presence of Li_3NbO_4 ($LiNb_3O_8$), the existent SS of single-phase LN is of fixed ST (most defective possible) composition: in these cases, the formation of the parasitical phases compensates the excess (deficiency) of Li_2O. In addition, above it has been stated that most of the physical properties attributed to LN single crystals strongly depend on the number of intrinsic defects, that is, the chemical composition (CC) or R={Li}/{Nb} or the Li (Nb) content c_{Li} (c_{Nb}). Table I-1 shows this by comparing the values of several optical and non-optical parameters for the nST and CG compositions. In the case of the Curie temperature T_c –the temperature at which the paraelectric-ferroelectric phase transition turns out in many perovskite-type materials—, its sensitivity to the CC can be readily seen in the phase diagram, not only for two fixed points but rather continuously on the whole LN single-phase. To determine the CC (or c_{Li}) within a LN crystal by means of an empirical linear equation having T_c as the independent variable is nowadays a well-known method [41]; rigorously, the trend is a quadratic one, but for practical purposes a linear fit might be used (see discussion in [41]).

Table I-1. Optical and non-optical coefficients for LN single crystals with congruent (CG) and near-stoichiometric (nST) compositions, as given by Volk and Wöhlecke [6].

Property	CGLN	nSTLN
OPTICAL		
Transparency region (nm)	320-5000	300-5000
Refractive index @ 633nm (n_o, n_e)	(2.286, 2.203)	(2.288, 2.190)
EO coefficient @ 633nm		
$r_{33}^T, r_{31}^T, r_{22}^T$ (pm V^{-1})	32, 10, 6.8	38, 10.4, ---
$r_{33}^S, r_{31}^S, r_{22}^S$ (pm V^{-1})	31, 8.6, 3.4	---, ---, 4.5
NLO coefficient @ 1060 nm		
d_{33}, d_{31}, d_{22}	34, 6, 3	42, 5, 2.5
NON-OPTICAL		
Crystal structure	Trigonal	
Space and point group (RT, hex)	R3c 3m	
Lattice constant a_H (pm)	515.0	514.7
Lattice constant c_H (pm)	1386.4	1385.6
Melting point (C)	1255	<1200
Curie temperature (C)	1140	1206
Density (g cm^{-1})	4.647	4.635
Thermal expansion @ 300 K		
α_a 10^{-6} (K^{-1})	14.1	14.1
α_c 10^{-6} (K^{-1})	4.1	6.0
Specific heat at RT (kJ kg^{-1} K^{-1})	0.628	0.651
Thermal conductivity at RT (Wm^{-1}K^{-1})	3.92	5.97
Spontaneous polarization (µC cm^{-2})	71	62
Dielectric constant $\varepsilon_{11}^T, \varepsilon_{33}^T, \varepsilon_{11}^S, \varepsilon_{33}^S$	84, 30, 44, 29	54, 42, 42, 41

Being a light element, the Li concentration within LN SSs can be directly estimated only by chemical methods: chromatography [42], atomic absorption analysis [43], and inductively coupled plasma atomic emission spectroscopy (ICP-AES) [44]. Apart from being destructive, these methods also consume large amount of material and offer a poor precision (no better than 0.2 mol%) [25, 45]. Likewise, the use of calorimetric methods for the determination of the T_c has the main drawback of reaching T values very close to the melting point of the material, as it can be seen in Figure I-1. In 1993 Schlarb et al [46] and Malovichko et al [47], independently revived the practical importance of other indirect methods (optical and non-

optical, see Table I-2) to describe the CC of LN single crystals. Among these, the measurement of the difference in the refractive indexes for a fixed wavelength (birefringence) and the Raman linewidths of certain vibrational modes Γ in Raman Spectroscopy (RS), are outlined. Noticing that these papers were published just one year after nST single crystals were available, their novel content can be outlined in three main aspects: 1) introducing a new chemistry, the ternary system $K_2O\text{-}Li_2O\text{-}Nb_2O_5$, "responsible for the unexpected growth" of STLN single crystals [47], 2) characterization covered over the whole compositional range, including the ST point, and 3) information of the crystal composition instead of the melt composition. From my point of view these works are nowadays seminal in the sense that they reviewed and informed to the community about the number of different existent indirect methods to describe the LNCC. Such information was back then "scattered throughout a number of publications" (the quote can be found in [48] under another context). The review was perhaps improved three years later by Wöhlecke et al [45].

Table I-2. Some indirect optical and non-optical methods for the determination of the chemical composition of LN single crystals, according to references in [45-47].

Method	Measured parameter	Equation; accuracy (mol%)	References
OPTICAL			
Fundamental UV optical absorption	fundamental absorption edge	nonlinear; 0.02	[49, 50]
Polarized Raman Spectroscopy	Linewidth of Raman modes	linear; 0.05	[45-47]
Sellmeier equation	refractive index (extraordinary)	nonlinear; ---	[51]
Dispersion of birefringence	refractive index (ordinary and extraordinary)	linear; <0.01	[45-47]
Phase matching temperature for SHG	phase matching temperature for SHG	linear; <0.01	[37, 52-55]
Spontaneous noncolinear frequency doubling	cone angle	nonlinear; ---	[56]
Holographic scattering (photorefractive effect)	reading and writing angles with respect to the normal of the crystal surface	---; ---	[57]

NON-OPTICAL			
Melt composition	Li$_2$O content of the melt $c_{Li, melt}$	nonlinear; 0.3	[44-45, 58]
Differential Thermal Analysis (DTA)	Curie temperature	nonlinear/linear; 0.1	[37]/[41]
X-ray and neutron diffraction + structure refinement	cell volume	linear; 0.3	[43, 59]
Density measurements	density	---; ---	[43, 60-62]
Nuclear Magnetic Resonance (NMR) and Electron Paramagnetic Resonance (EPR)	Linewidth of NMR and EPR signals	linear for Fe doping concentrations smaller than 0.01 mol%; ---	[47, 63-64]
Velocity of surface acoustic waves (SAW)	velocity of SAW	---; 0.01	[65, 66]

Focusing on the RS method, a set of two linear equations in terms of Γ (linewidth) are given in [45-47] to determine the LNCC, specifically in single crystals. These are independent equations, each to be used according to the measured linewidth of a given Raman mode (the bands located either at 153 cm^{-1} or at 876 cm^{-1}), and they involve different experimental/geometrical restrictions like the (crystallographic) axis of excitation (the crystal cut), the direction of detection, and the state of the linear polarization of the light at the excitation and detection stages. The specifics on these experimental configurations will be discussed in detail in the corresponding theoretical framework. Anywise, for the moment it is only important to realize that such geometrical restrictions imply a limited description to single crystals. No one, after consciously reading references in [45-47] would expect to describe the CC of LN powders (LNPws) by use of such equations. Unfortunately (or fortunately?) during my first approach to LNPws I was told to use them to determine their CC: non-polarized Raman experiments were done! Sometime later and after many samples synthesized, I necessarily end up distrusting this procedure.

More important was to find out that practically no accurate, trusting and facile method (i.e. indirect) had been reported for this purpose. Contrary to what could be expected, the approach of using the same empirical equation (formulated for single crystals) to describe powders, does not work even for T_C measurements. Since temperature is a scalar quantity

(light propagates and interacts with matter in vector-like form), it would be permissible to expect a single description of the LN CC in terms of T_C, regardless of the SS being a single crystal or a powder. Interestingly, this is not the case: the systematic measurement of lower T_C values (about 10°C) for LNPws compared to equivalent single crystals has already been addressed [45]. The reason behind this fact might remain yet unexplained.

In this investigation, a custom-made Raman system has been crafted in open air to obtain control on the polarization state of the light at the excitation and detection stages; of all the commercial Raman systems I had access to, none featured polarization of light as an experimental variable, neither did I could modify any of them. With this system, verification of the linear equation for the Raman active mode centered at 876 cm^{-1}, as given in [45-47], could be done on bought ST and CG LN single-crystal wafers [38]. While this served to calibrate the assembled system, it also allowed to confidently state that the abovementioned linear equation does not describe LNPws. Then, with a commercially available system it was observed that the linear relationship remains for the linewidth Γ of the same Raman mode (876 cm^{-1}) in the case of powders, however under simpler circumstances where the polarization state of light at the excitation and detection stages is disregarded. Thus, in accordance to references [45-47], the accurate determination of the CC of LNPws is proposed by means of a linear fit in terms of the calculated Γ, but on this instance from *non-polarized* Raman spectra (instead of polarized).

The main contribution of this work is the method itself to determine the CC of the synthesized powders on a first instance. No direct method was used. Instead an *a priori* probing of the formed phases from 11 different synthesized samples by analysis of X-ray diffraction (XRD) experimental data was done, relying on the existent information in the phase diagram that describes the pure LN phase along with its surrounding parasitical phases (Figure I-1). In this way the linear relationship obtained for the *averaged* Nb content in the crystallites $\langle c_{Nb} \rangle$, in terms of Γ, is affixed to two known or expected values, those of the two edges that delimit the pure ferroelectric phase: the boundary with phase $LiNb_3O_8$ on one side (Nb excess) and the boundary with phase Li_3NbO_4 on the other (Li excess).

The nanocrystalline LNPws were obtained by a mechanochemical-calcination route [67-69]. Gradual addition of Li or Nb has been systematically performed by increasing the mass percentage of a precursor containing the desired ion species. The quantification of secondary-

phase percentages was carried out with structure refinement by the standard Rietveld method. An alternative linear equation to determine the CC is also given in terms of the calculated cell volumes by means of the same structure refinement. Additionally, linear fitting of the measured band gap energy (E_g) by means of UV-vis Diffuse Reflectance (DR), is also used for this purpose. Differential Thermal Analysis (DTA) was utilized as a verification technique for specific samples and a fourth empirical equation that describes the CC in terms of the Curie temperature was obtained this way. The four distinct methods are based on standard characterization techniques, accessible nowadays to large scientific communities in developing countries. Scanning Electron Microscopy (SEM) was utilized to verify that the particle size distributions do not vary drastically from one sample to another.

Historically, LNPws have been overlooked for research in favor of LN single crystals and thin films. This explains why a doctorate thesis has been written in 2019 mainly to describe the CC of LNPws, being LN a material which has been extensively studied ever since 1966 or even before. Today, LNPws are important because of their role in the field of lead-free piezoelectric materials. This research field is nowadays vast and very active due to the environmental laws and regulations imposed by government in 2003, the so-called RoHS directive, which may be considered as "the most disruptive event in the history of electronic manufacturing" [70]. Being approved in 2006 to minimize health and safety risks, this directive basically dictated that new generation electrical and electronic devices was to be manufactured without any of the following compounds: "lead, mercury, cadmium, hexavalent chromium, polybrominated biphenyls or polybrominated diphenyl ethers" [70].

The true is that so far, neither the RoHS directive has been fully applied nor research on lead-based materials has been stopped. This because lead zirconate ($Pb(Zr_xTi_{1-x})O_3$; PZT) and lead titanate ($PbTiO_3$; PT) perovskites by far feature the best performances on these grounds (sensors, actuators and other electronic components) "at reasonably low production costs" [71]. Notwithstanding, researching interests on lead-free materials is far from dropping, and today most experts share the common belief that a possible way to replace lead-based materials are SSs of alkali metal niobates (AMN) [71-73]. LN belongs into this category of materials and despite it has not been tested by itself in this direction, yet LNPws have been mixed with alike powders in the sense of forming a novel green compact to be sintered into a high-performance ceramic. Complex ternary and four-component systems

involving LNPws have been studied: $NaNbO_3$—$LiNbO_3$—$PbTiO_3$ and $(1-x)(Na, Li)NbO_3$—$xPb(Ti, Zr)O_3$, respectively [54]. The latter has shown a considerable increase of the electrophysical parameters ($\frac{\varepsilon_{33}^T}{\varepsilon_0}$, K_p, d_{31}) [73]. Although AMN systems are still inferior than systems based on PZT, the four-component transition already features good figures of merit for applications in microwave devices (for a low content of x) and low-frequency electromechanical converters (for $0.70<x<0.85$) [73].

Other recent developments on LNPws are certainly attracting the attention of scientists and engineers who seek to exploit their potential use in a wide range of applications that span from the construction industry to nonlinear optics. Cementation materials based on LN have been proposed to improve the air quality of the environment by Artificial Photosynthesis [74]. This is considered important for the global warning reduction problem. Regarding LNPws, in here it is emphasized that not only would they be cheaper and easier than single crystals to be implemented into cemented materials, but also probably enhance the intrinsic surface effects which are the basis for an improvement of the lifetime of the carriers (photo-generated electrons and holes) involved in Artificial Photosynthesis [75]. In addition, Fe-doped LNPws also show, after a post-thermal treatment in a controlled reducing atmosphere, a rather strong ferromagnetic response at room temperature for a doping concentration of the order of 1% mol: this may be considered a first report of the manifestation of ferromagnetism in nanocrystalline LNPws within the regime of very low doping concentrations [76].

Yet in another application based on the powder-in-tube method, a novel fabrication process has been demonstrated for the realization of polarization-maintaining optical fibers [77]. This has been accomplished by use of material different than LN, but comprehension of the main mechanism behind this technology, and by considering the LN mechanical properties (see Table I-1), one can conclude that LNPws are, in principle, good candidates for the fabrication of this type of optical components. Also, possible tuning on the intensity of the Second Harmonic Generation (SHG) that arises from LN micropowders could be ascribed to a proper control of their chemical composition and grain size [24]. This could soon translate into major technical benefits given that neither a critical adjustment of the orientation or temperature in the material (phase matching condition) nor the accurate engineering of a microstructure (quasi-phase matching condition) are substantially needed when the SHG from disordered materials – such as LNPws—are exploited [24, 78]. Quoting

Skipetrov, personally it is exciting that "this could make the nonlinear optical technology accessible to a much wider range of potential users" [78].

SECOND HARMONIC GENERATION:

Optical SHG is a nonlinear optical process in which the light incident in a medium is altered due to its (special) interaction with matter, having as a result the existence of light (the response of the medium) that possesses the double in frequency with respect to the incident light. Hence due to this, SHG is also referred to as *frequency doubling*. It is an intrinsic and unique property of the medium and not of light itself, despite the term *nonlinear* stands for the consideration of magnitudes larger than unity of the electric field carried by the incident light. It might also be defined as "the process whereby two photons at a fundamental frequency ω are annihilated and a single photon at the harmonic frequency 2ω is created," quoting Brevet. Such definition is to be found often on recent publications authored by Brevet, preventing (I personally sustain) ambiguity between SHG and hyper-Rayleigh Scattering (HRS), the latter being a term linked to SHG, but which is not equivalent [79]. Prof. Brevet is head of the *Optique Non Linéaire et Interfaces* group, at the *Institut Lumiere Matiere, Université Claude Bernard Lyon 1*. His work on SHG can be traced back to 1995 (ResearchGate, https://www.researchgate.net/profile/Pierre-Francois_Brevet).

Now as formulating a good analogy between the abstract concept and another more familiar is often indicative of one understanding the concept, here I dare to give one. The game of jumping the rope, as played by children, might help to grasp the concept of SHG. The associated energy to the wavelength (E=hc/λ) being proportional to the number of children jumping the rope at a time, while the transversal character of the wave depicted by the arm and hand movement of the children holding the rope. Also noticing that to obtain SHG and THG, not only more energy needs to be deposited to the system (the frequency applied by the children holding the rope), but also the degree of dexterity or practice needed increases; at playing the game, one can readily verify that THG is much more difficult to attain compared to SHG, and this later is not as easily attained as the fundamental oscillation is. In this respect, SHG is always present for non-centrosymmetric materials with a high nonlinear coefficient, but to obtain reasonable SH intensities the process must be optimized, usually by experimental techniques denoted as phase-matching (anisotropic single crystals) and quasi-phase matching (isotropic engineered crystals) [78, 80-82].

Optimization is important, at least in what respects regular crystals, free from internal and surface defects. In this context, it is worth to have a pause and re-tell an anecdote once mentioned by Skipetrov [78]. The canons tell that the field of (experimental) Nonlinear Optics was born with the first report on the *generation of optical harmonics* (i.e. SHG) by Franken et al (1961) [83]. Just one year before Maiman have had demonstrated the operation of a laser system based on ruby [84]. The nonlinear process stimulated by Franken et al was not phase-matched thus they observed a weak converted signal [83]. According to Skipetrov, the harmonic signal was so weak that "it is said, that the editorial staff of Physical Review Letters mistook it for irrelevant noise and carefully removed the tiny spot it produced on the photographic plate" [78] (see Figure I-2).
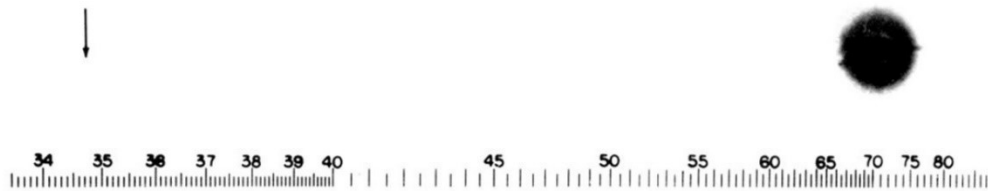
Figure I-2. Shown figure in the mentioned article by Franken *et al*; near the vertical arrow, a spot corresponding to the harmonic signal was originally put by the authors and it was removed by the editorial board of the journal. *Reprinted from reference in [83]; © Physical Review Letters, 1961.*

Besides it is largely exploited by the laser industry to span the spectrum of light-matter interaction, due to its non-invasive character and sensitivity to any point symmetry violation, SHG also stands as a convenient tool for biological-sample imaging [85], surface characterization [86, 87] and probing of complex ferroic domain patterns [88]. A few applications, the already stablished ones, have been mentioned. Others have had being envisioned/predicted [89]. In fundamental science, and within the context of the weak scattering of light by suspensions of metallic nanoparticles, the realization of PR experiments can disentangle between the electric dipolar and quadrupolar origin of SHG from centrosymmetric media (forbidden in principle), in terms of the shape and size of the nanoparticles [90, 91]. This type of analysis also sheds some light on the problem of light transport in random media [92]. In addition, PR-SHG has proved to be of great use in the case of *single*, small and arbitrarily oriented non-centrosymmetric structures, for example in

the determination of the Point Symmetry Group, which is manly achieved by diffraction-based methods but fail in the case of aperiodic materials, yet with a certain degree of organization [93]. By PR experiments in LN single nanocrystals, Knabe et al could also refute the general idea of the existence of a phase transition from non-centrosymmetric to centrosymmetric structure in perovskite-based structures at the nanoscale [94]. Indeed, nanosized LN single crystals (down to 5 nm) inherit the nonlinear properties from that of bulk single crystals: this means that both, the magnitude and the orientation nature of the nonlinear coefficient are preserved.

In the context of powdered materials (strong scattering), just recently experiments have been performed to study quantitively the SHG activity of pharmaceutical materials, as a means for quality control [95]. Loss of crystallinity within organic powders induced by mechanical grinding can also be monitored by this nonlinear second order process [96]. PSHG experiments are thus no longer secondary as they are conceived by the Kurtz-Perry (KP) method [97]: powders are considered as survey materials only, and a PSHG study is done solely to predict the nonlinear second order capabilities of unavailable single crystals. Yet, another feature that makes PSHG more attractive nowadays is the already mentioned possibility of tuning the SHG intensity that arises from LN micropowders, ascribed to a proper control of the CC and grain size [24].

As previously stated, this work of thesis also highlights the importance of performing a combined analysis resulting from the depth profiling of the PR-PSHG. Unexpectedly, after an exhaustive search on the literature, existent reports on PSHG do not involve PR experiments, excluding those attained within the context of Coherent Backscattering (CBS) or Weak Localization of light [98, 99]. Such scarceness might be justified by the fact that incident light with linear polarization in disordered media (fully random in terms of its refractive index) is strong depolarized or randomized due to the very large number of elastic scattering events. This is in fact the reason behind why the KP method –by far the most popular approach to PSHG— disregards the polarization state of the fundamental wave and still is reliable to predict the SHG character of the unavailable single nonlinear crystals (phase matchable or not) and in determining the averaged effective nonlinear coefficients in the powders. Moreover, in a revision of the KP method a refined model is given which accounts

for scattering effects, shows that the measured SHG should not be affected by the depolarization effects at the fundamental frequency [100].

Hence, apparently PR measurements on PSHG have been being omitted systematically for research, even though an enhanced nonlinear backscattering –readily identified by a sharp peak in the angular distribution of the SHG intensity, the CBS cone— has been predicted for a medium, which is both nonlinear and disordered (i.e. a nonlinear powder) [101]. In addition, it has been demonstrated that the linear polarization of the pump light tunes the width of the CBS cone at the fundamental frequency, this being attributed to a reorientation of the microcrystalline LN particles suspended in water [102]. In summary, maybe because of surface inhomogeneities and strong scattering, it can be said that powders have been relegated within the context of Nonlinear Optics, although they are tacitly considered easier and far less expensive to synthesize, compared to single crystals.

The current investigation addresses the study of the SHG response from LNPws with an averaged stoichiometric composition, accordingly to the first research conducted (already introduced). The study was conducted in terms of the depth of the prepared sample, that is, a Z-sectioning of the SHG response was performed as the beam focus of the fundamental wave is translated from +z to -z position, passing from the air/powder interface (z=0). Also, in terms of the linear polarization state of light at both the excitation and detection stages. Besides being able to estimate the sample thickness and roughness of granular media at the micrometric scale, the Z-sectioning gives information on the scattering properties of the sample by deconvolution of the measured SHG intensity profile and fitting to the Beer-Lambert law. Contrary to other similar approaches found in the literature, neither Z-correction was needed to be applied to the intensity profile nor it was necessary to consider a contrast between the phase-matched SHG arising from the properly oriented crystallites and the most probable non-phase-matched SHG that arises from a larger number of randomly oriented crystallites. The initial performed analysis to the Z-sectioning part (no polarization of light involved) led to the conclusion that under these experimental conditions (both optical and of sample preparation), light tends to scatter more forwardly (Mie scattering regime). This implied that the 'bulk' SHG could be differentiated at all instances from the surface SHG. In this way, the surface properties of the prepared sample could readily be probed at the air/powder interface and at layers beneath it, down to the powder/susbtrate interface.

Then by combining the depth profiling with PR experiments it was found that the overall polar distortion along a direction of a characteristic double-lobe plot, rotated in counter-clockwise sense for instances in which the focal point stood above the air/powder interface and rotated back (not fully) for layers beneath this interface. Analysis of the collected double-lobe plots happened to shed light on the size and orientation distributions of the crystallites constituting the powder. In accordance to previous reports, it was found that a small dispersion in the values for the SHG intensity minima stands for a fixed averaged crystallite size which is consistent layer by layer of the prepared sample, while variations in the maxima values stand for various distributions of possible orientations of the crystallites. It is believed that the crystallites closer to the edges are more easily randomly oriented than those that have been more compacted inside the powder. At the center of the sample it is more likely to exist a single-type of domain in which most of the crystallites are oriented along a common axis, this being induced doubly by the exerted pressure on both ends, although it was gentle. This puts in evidence the SHG potential application for non-invasive and remote sensing, which in turn may open interesting areas for the nonlinear optics of granular media such as the study of the dynamics pertaining to the prediction of certain natural phenomena such as avalanches, volcano eruptions and sand distribution on beaches. Moreover, a recent report demonstrates that *continuously sheared granular matter* "reproduces quantitatively the main statistical laws of seismicity" [103]. It means that the physics behind earthquakes is somehow connected to the physics that governs certain experiments at the laboratory scale in granular media. This way, new valuable information could be obtained on earthquakelike dynamics by use of new characterization techniques, such as depth profiling the PR-PSHG for example.

This introduction is to be concluded with a final comment on the linkage between SHG and LN. Back in 1966, when Abrahams et al did their paramount contribution (references in [7, 20-21]), the importance of LN regarding SHG was since then highlighted. Indeed, just by reading the introduction of one of their seminal papers, it can be noticed that apart from its intrinsic ferroelectricity, such detailed studies on the structure of LN were back then, also motivated because of the capability of this material in frequency doubling. Quoting, LN single domain crystals were "capable of producing two orders of magnitude more second harmonic than any other known phase-matchable material" [7]. Such attributes have had being highlighted accordingly to the previously written report by Boyd et al (1964) [104].

Structure of the thesis

So far only a general outlook has been given, which circumscribes and, in some sense, justifies the *raison d'être* of this thesis. The main obtained results also have been outlined. In the subsequent pages (chapters 1 and 2) most of the introduced concepts will be "polished", some other will be given, and the aspects that constitute the theoretical framework of this work of thesis will be discussed.

Chapter 1 is devoted to the material aspects of Lithium Niobate ($LiNbO_3$; LN). Its structure, defect models and ferroelectricity are introduced. These topics are treated in a rather succinct way, given the overwhelming information existent on them. Particular importance is given to proper references, which can be consulted for further details. Space and ink have been employed to discuss some historical aspects regarding how the structure of LN has been conceived and reformulated through the course of time. This is important since this type of information is barely mentioned in recent references. By the end of this chapter, the already existent descriptions of the chemical composition (CC) of LN single crystals, based on indirect methods are presented. Only the four characterization techniques used in this investigation are treated.

Chapter 2 treats the Nolinear Optics (NLO) part of this work of thesis. It begins by introducing the concept of NLO, intuitively. The main characteristics that distinguish NLO from linear optics are explained. Then, the concept of *nonlinear optical phenomena* is formally introduced from to different frameworks: classical Electrodynamics and Quantum Mechanics. The description of the Second Harmonic Generation (SHG) process follows, including the techniques usually utilized to optimize it in different types of media. This chapter ends with a discussion of the experimental aspects and the theoretical framework mostly used to describe the SHG response from powders, namely the Kurtz-Perry method.

In PART II, some theoretical aspects and all the experimental developments are given regarding the synthesis and characterization techniques employed in this work of thesis. Chapter 3 describes in detail the fundamental aspects behind the Mechanosynthesis method of synthesis and the mechanisms involved in the high-energy ball milling process. In a more succinct fashion, other methods of synthesis are discussed, as well as the subjects of Powder X-Ray Diffraction (XRD) and the Rietveld method. In the case of the other characterization techniques (Raman Spectroscopy, UV-vis Diffuse Reflectance, Scanning Electron

Microscopy and Differential Thermal Analysis), practically only a list of relevant references treating these subjects is given. For practical reasons the basics on the experimental configurations to do the combined analysis resulting from the depth profiling of the polarization-resolved powder SHG are omitted. Finally, all the experimental procedures done during this investigation are described in detail in Chapter 4.

In PART III, the obtained experimental results are simultaneously presented and discussed. Chapter 5 is devoted to the obtained results on the first and main investigation developed in this work of thesis, that is, the determination of the CC of LNPws. Likewise, Chapter 6 is devoted to the obtained results regarding the SHG response of the LN micropowders with (averaged) stoichiometric composition. Then, the conclusions and perspectives pertaining both investigations are given. After the listing of the corresponding references, the Appendix A follows, where an example is given regarding the calculation of the overall uncertainty in the method involving the determination of the CC of LNPws by XRD and Rietveld refinement.

Chapter 1: Materials Science

Lithium Niobate

The inexorable tendency of lithium niobate ($LiNbO_3$; LN) to crystallize in a congruent composition (R={Li}/{Nb}=0.969) has been introduced above from a phenomenological point of view (see Figure I-1). To understand the *why* and *how* on the formation of the type of intrinsic defects or lattice imperfections involved, a formal discussion of a proper defect model must be given. In this respect the description of the crystalline structure should precede. However, in practice, when these two concepts are nowadays addressed in a theoretical framework, little or nothing new can be said. These subjects have been extensively studied, formulated and re-formulated through the course of time. All angles and edges have been covered –at least under the context of the present investigation.

One thus has no other option than to re-tell the story as close as possible to an original and recent source because, after decades of work and a myriad of written reports by sharp minds, the story can hardly be better told. The crucial point then resides in doing an exhaustive research of the available references, select the best and pass their content on. This

being said, yet in the spirit of presenting a fluid reading while avoiding redundancy (reprinting from an original source), the present chapter saves ink and paper by being limited to describe such concepts in a very succinct way, at the same time it provides the minimum of references to acquire a comprehensive knowledge on these grounds. The phenomenon of ferroelectricity will be treated in the same way. LN is an important ferroelectric material and although this work of thesis contributes nothing new to this subject, by describing what really causes ferroelectricity –that is, which are the necessary and sufficient conditions for its manifestation— a deeper insight to both subjects, the LN crystal structure and defect models, will be achieved.

The three concepts already mentioned will be contained within the first section of this chapter. At its end, a subsection will be devoted in relating some historical aspects regarding the classification of the LN crystal structure. This is important because once there existed a debate on whether it could be conceived as belonging to the large family of distorted-perovskite structures rather than being related to the ilmenite or corundum structures, as it has often been quoted. This is barely mentioned in recent references, while thinking of the LN structure as related to that of perovskite aids in grasping it in a more natural fashion; not only the structural aspects but also the ferroelectric behavior it features.

A second and last section introduces the precedents on the determination of the chemical composition (CC) of LN single crystals. Only the four experimental techniques herein used will be discussed: X-Ray Diffraction (DRX) + Rietveld refinement, Raman Spectroscopy (RS), optical absorption (as equivalent to UV-vis Diffuse Reflectance used instead when powders are to be characterized), and Differential Thermal Analysis. This section is thus a review of the independent descriptions in terms of an experimental parameter corresponding to each characterization technique (cell volume, linewidth of Raman mode, optical absorption edge, and the Curie temperature), which have been previously reported and are "scattered throughout a number of publications" (quote from reference in [48]). Regarding other experimental techniques not used in this work of thesis, the same kind of information can be consulted in the corresponding references given in Table I-2.

Lastly, it is emphasized that except from the last section, it is assumed that the theoretical framework that follows describes LN single crystals irrespective of the scale: large single crystals or nanocrystals. Whereas the structure, the defect models and the ferroelectricity of

LN are concepts nominally developed in terms of large single crystals, all the experimental work on this thesis has been done on LN powders (LNPws). The latter are herein pictured as being constituted by a myriad of nanocrystals with random distributions on their size, shape, orientation and CC, that aggregate to form larger particles at the microscale. On one hand, it has been predicted that perovskites and related structures would undergo a structural change (and hence a modification of their properties would follow) if the dimensions of a single crystal are lowered down to a critical size of about six unit cells [105, 106]. However, on the other hand, the absence of such a phase transition has been experimentally demonstrated for the case of LN single nanocrystals down to a size of 5 nm [94]. Later it will be shown that the synthesized crystallites have an averaged size no less than 100 nm. In addition, because the length scales at the unit cell level are –and those related to the chemical bonding— of the order of angstroms, it is thus assumed that the derived implications in this chapter will also be valid for the LNPws. Not those in the last section, of course.

1.1 Structure, defect models and ferroelectricity in Lithium Niobate

In my opinion, the story of the LN structure has been better told in the classic text by Räuber (1978) because the concept, which is a complex one, is therein built up step by step, details on pertinent symmetry issues are given along with a series of intermediate visual aids (figures) that contribute to a better understanding of the actual structure [9]. Conversely, references in [5, 30] and other recent ones (all that were consulted), limit themselves to merely impose it by a text 1-2 pages long and a sole figure. References in [5, 30] also excel in this topic and, because they are more recent (especially that in [30]), they may provide more reliable experimental data (atomic positions, lattice dimensions, phase transition temperatures, and compositional variations) than that in [9]. Nevertheless, in this respect, it is important to remind the outstanding work by Abrahams et al (1966) [7, 20-21], considered the most extensive and detailed structure analysis of LN. According to Räuber, in [7, 20-21] "all position parameters of the ions have been determined with high precision and form the basis of all further discussions on the structure" [9].

Reference in [5] provides a detailed discussion on the symmetry elements of the point group pertaining the ferroelectric phase (trigonal, space group *R3c*, point group *3m*), sense of the *c*-axis and cleavage planes. It also describes separately the two most common choices

of axes or unit cell abstractions (ferroelectric phase): hexagonal and rhombohedral. These two choices are convenient for crystallographic purposes, the rhombohedral being the most used in describing the LN structure. They are both shown in Figure I-3. For most physical applications, the tensor properties are neither described in terms of the hexagonal system nor the rhombohedral but in terms of a cartesian one, denoted as 'orthohexagonal' in [9]. The conventional definition of the latter in terms of the hexagonal system is also described in [5].
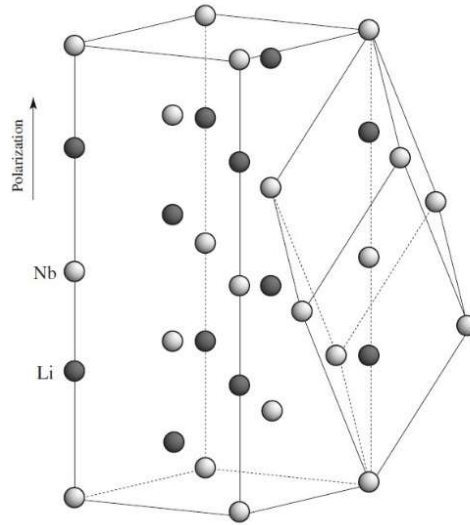
Figure I-3. Conventional rhombohedral and hexagonal unit cells in LiNbO$_3$, having two formula weights (10 atoms) and six formula weights (30 atoms), respectively. The oxygen atoms are omitted. *Reprinted from reference in [107]; © Physical Review B, 2010.*

Hence, while the structure description given by Räuber stands out from the others, perhaps the best approximation to it probably relies in properly combining and adapting the information found on these three references. Complementary information and/or a different way to introduce the concept may be consulted from references in [34, 107]. Räuber in addition takes into consideration the description by Megaw [108-110], namely considering the structure of LN resulting from a set of large distortions of the atomic arrangement within a reference structure of higher symmetry, the ideal cubic perovskite; in this case, a fourth unit cell abstraction takes place, the 'pseudocubic' setting [9]. This will be further discussed in the next subsection.

Figure I-4 shows a scheme of the LN crystal structure (stoichiometric composition) stable for $T < T_c \sim 1210$ °C (ferroelectric); as before mentioned, the Curie point moves accordingly to the chemical composition, roughly from 1100 to 1200 °C [9]. The basic net is formed by six equidistant plane layers of oxygen per unit distance, stacked in the direction

of the polar axis c [9]. The essential feature to be noticed from the low-T LN structure (non-centrosymmetric, space group $R3c$, point group $3m$) is the partial filling of the octahedral interstcials in a c-row: one-third filled by Li ions, one-third by Nb ions and one-third are empty. This can be schematically depicted as –Nb–Li–□–Nb–Li–, where □ denotes a vacant octahedral site. The Li octahedron is larger than the Nb one [30]. Such a distorted octahedral environment is addressed to a transition from the nonpolar or paraelectric phase (for for $T>$ T_c, centrosymmetric structure, space group $R\overline{3}c$, point group $\overline{3}m$) to the paraelectric phase as T decreases. Small displacements of the Li and Nb cations are involved, respect to the oxygen layers and along the c axis, measured to be of 45 and 25 pm, respectively [21, 30]. The displacements in oxygen are neglected in first order (~ 6 pm) and, thus the oxygen framework is assumed to be fixed [21]. In the paraelectric phase, the Li cations are localized *within* the oxygen planes, whereas the Nb cations are in the center of the oxygen octahedra, that is, *between* the planes.

24
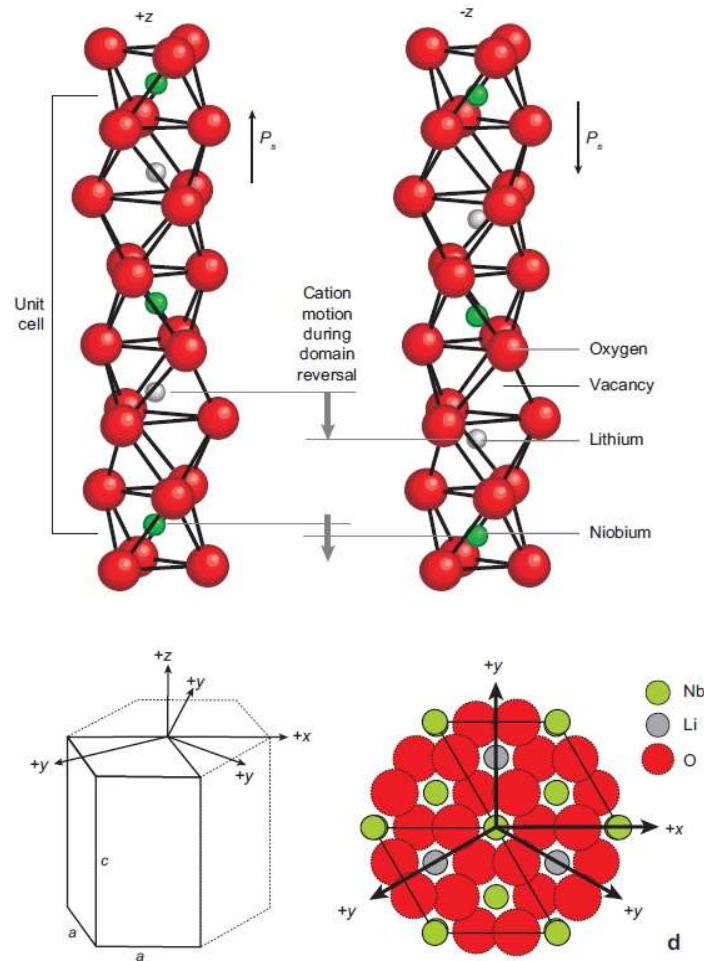
Figure I-4. Crystal structure of ferroelectric LiNbO$_3$ under two cation displacement possibilities with respect to each equidistant oxygen octahedra. **Upper left:** Z+ orientation of cation displacement. **Upper right:** Z- orientation of cation displacement **Bottom left:** conventional choice of axes for the 'orthohexagonal' setting (*XYZ*) with respect to the hexagonal setting (*a, c*). Notice that whereas in the hexagonal setting all axes have an equal length, in the cartesian one they all are different. **Bottom right:** projection of the atomic arrangement along the *c*-axis. *Reprinted/adapted from reference in [111]; © Annual Review of Materials Research, 2007.*

It is important to realize, however, that such a scheme of the LN structure is an idealized one. Remind that, on regular circumstances of growth, LN single crystals are non-stoichiometric (see Figure I-1 and the corresponding discussion in the introduction). Instead, the congruent (CG) composition prevails, characterized by excess of Nb. Non-stoichiometry in LN "must be made possible, or even favoured, by the structure of this compound", accordingly to Räuber [9]. Likewise, Kang et al have stated that the CG point of the "LN material might be a macro behavior of the fundamental intrinsic defects" [34]. This can be understood in terms of crystal chemistry: "during crystallization, the Li–O bond in the LN crystal is much weaker than the Nb–O bond, and thus Li vacancies form easily in the unit cell. Therefore, the non-stoichiometric crystal forms due to lack of Li in the lattice" [34].

It is thus natural to reason that a Li deficiency implies a Nb surplus, or better said, "a decreasing Li content is accompanied by an increasing content of the heavier Nb" [30]. But how do these tendencies simultaneously conciliate as to have a stable LN solid solution (SS)? The occurrence of a stacking fault, envisioned as the relatively excess Nb partially occupying Li vacancies, has been proposed and termed as 'Nb anti-site' (Nb$_{Li}$) [60, 112]. This is schematically shown in Figure I-5. A consensus does exist in this point. According to Volk and Wöhlecke, the existence of this type of anti-site defects has been repeatedly proven by detailed structure studies, which might be consulted from references in [43, 59, 61, 113]; they "formed the basis for defect models in LiNbO$_3$" [30]. However, the way in how the cations (both species) and their respective vacancies (V$_{Li}$ and V$_{Nb}$) accommodate within the structure for a charge compensation –that is, "the solution of the non-ST LN crystal structure with a stable charge equilibrium" [34]—, has left to the construction of several defect models where no consensus is to be found. The three most widely accepted models through the history of LN research are summarized in the next paragraphs. This information has been mostly adapted/reprinted from references in [30, 34].
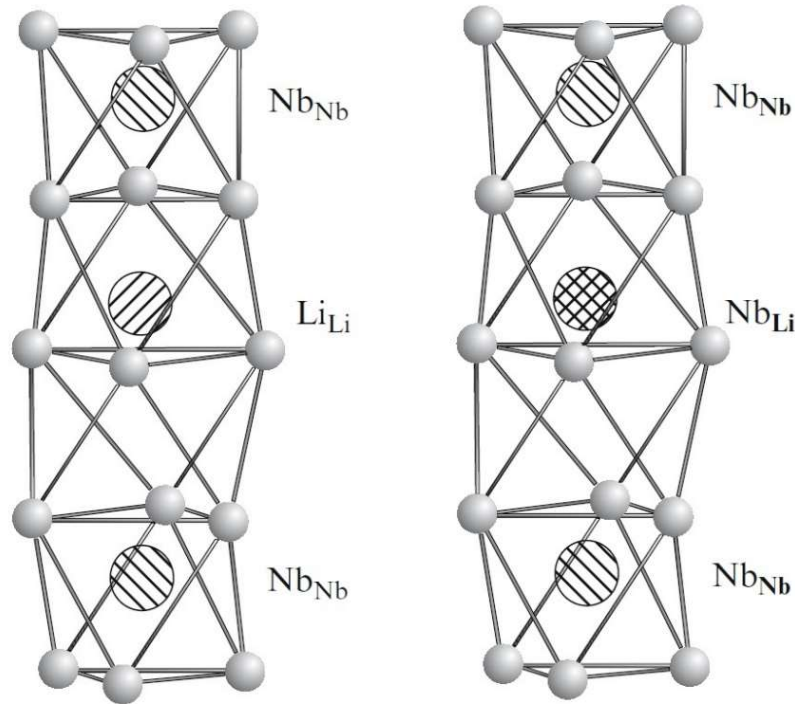
Figure I-5. Comparison between the ideal and nonideal LN structure. **Left:** free from point defects (ST composition). **Right:** under the most likely situation in which Nb anti-sites are present (CG composition). *Reprinted/adapted from reference in [30]; © Springer, 2009.*

Oxygen vacancy model: proposed by Fay et al (1968) [114], it can be illustrated by the following constitutional formula: $[Li_{1-2x}V_{2x}]Nb[O_{3-x}V_x]$. Its basic viewpoint relies in that Li vacancies form due to the lack of Li_2O (used as a raw material in the initial melt, Czochralski method) at the congruent point, while corresponding oxygen vacancies form for charge compensation. At the earliest stages of discussions of the CGLN defect structure, it was reasonable to assume oxygen vacancies as the most probable defect, which is characteristic for all oxides. However, nowadays it is well known that LN "is to some extent a unique oxide containing no oxygen vacancies" [30]. The model predicts the crystal density to decrease with greater Li_2O deficiency (i.e. increasing concentration of V_{Li}), which is inconsistent with the observations obtained in the experimental studies by Lerner et al (1968) [60]. The Nb anti-site defect copes with this situation but the inexistence of oxygen vacancies in LN crystals has been demonstrated by detailed structure measurements [59, 61, 113], supported by electronic-structure calculations [115].

Niobium vacancy model: proposed by Peterson and Carnevale (1972) [112], it can be illustrated by the following constitutional formula: $[Li_{1-5x}Nb_{5x}][Nb_{1-4x}V_{4x}]O_3$, where the Nb

in the first bracket denotes the Nb anti-site defect Nb_{Li}. It successfully describes the relationship between the density and the Li content of the crystal. Oxygen vacancies are neglected, and Li are filled with excess Nb ions. Meanwhile, some Nb vacancies are generated at the former Nb^{5+} sites for charge compensation. However, according to this model, in CGLN (R={Li}/{Nb}=0.969), there are 5.9 mol% Nb_{Li} and 4.7 mol% V_{Nb}. Such a highly charged Nb anti-site concentration is believed to be structurally unstable. In principle, the Nb_{Li} is in agreement with the Hume-Rothery rules for solid solutions given that the measured ionic radii for Li^+ and $Nb^{5+}$are 0.74 and 0.64 $\mathbf{\AA}$ (6-fold coordination), respectively [116]. In the analysis of the atomic size effects and their influence within a structure, reliable experimental data is usually taken from the 'effective' ionic radii as given in the important contribution by Shannon and Prewitt (1969) [117].

Lithium vacancy model: proposed by Lerner et al (1968) [60], it can be illustrated by the following constitutional formula: $[Li_{1-5x}V_{4x}Nb_x]NbO_3$, it also includes Nb_{Li} and neglects V_O. The concentration in of Nb_{Li} is four times higher compared to the Nb vacancy model. The Li vacancy model differs from the Nb one in that no Nb vacancies are formed. Instead, four V_{Li} stand for compensation of a single Nb_{Li}. The existence of a high concentration of Li vacancies in CGLN was confirmed by structure report found in [113], as well as by Nuclear Magnetic Resonance (NMR) studies [118]. Figure I-6 illustrates the filling of Nb anti-sites and vacancies, according to the two different postures pertaining to the Nb and Li vacancy models, respectively. Nowadays, the Li vacancy model is commonly accepted as valid and considerations of all defect reconstructions in LN are discussed in this framework. Reports supporting this model, based on computational simulations, can be consulted in [119, 120]. Nonetheless, recently a new model has been proposed based on the coexistence of all three cation stacking faults Nb_{Li}, V_{Nb}, and V_{Li} [121, 122]. According to this model, the Nb and Li vacancy models are simply the two opposite ultimate states of this model. In 1998, Wilkinson et al had already indicated this possibility [113].

○ Li ● Nb ∘ O ▫ V_{oct} ☐ V_{Li} ◇ V_{Nb}

$5Nb_{Li} + 4V_{Nb}$

Y

X

$Nb_{Li} + 4V_{Li}$
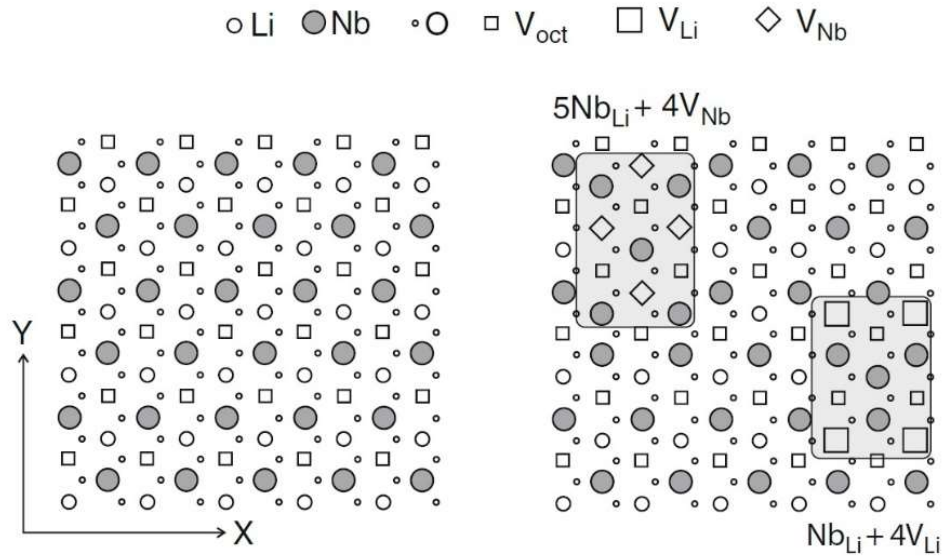
Figure I-6. Lithium niobate structure in a projection onto the (001) plane. **Left:** ideal or stoichiometric case. **Right:** congruent composition showing the Nb_{Li} intrinsic defect with two alternatives of its compensation by Nb vacancies (right) and Li vacancies (left). *Reprinted/adapted from reference in [30]; © Springer, 2009.*

On the other hand, "the defect scenario discussed [above] characterizes the LN structure at moderate temperatures and cannot be applied to high temperatures. For example, neutron diffraction studies led to the conclusion that at high temperatures the Li position is split, so at 600K about 9% Li atoms are missing on the regular site, being distributed between Li and vacant positions, i.e., the empty octahedron [123, 124]; this fraction increases with rising temperature. A synchrotron X-ray diffraction analysis of stoichiometric LN evidenced a small fraction of Li atoms on vacant sites even at room temperature [125]. It should be noted that the properties of the relative crystal $LiTaO_3$ [(LT)] is very often discussed in terms of identical structure defects Ta_{Li} and missing oxygen vacancies. Actually, the structure and optical properties of LN and LT are very similar. However, so far there is no direct proof of the existence of such stacking faults in LT, so considerations based on this defect model are speculative in contrast to LN. Summarizing [this discussion on defect models], the cornerstone of the LN defect structure model is the existence of Nb_{Li} defects and missing oxygen vacancies, established by structure investigations." (quote in [30]).

A final remark is given regarding the non-stoichiometry of LN crystals. Kuz'minov and Osiko have pointed out that the 'disturbance' of stoichiometry in LN crystals is primarily due to the lack of oxygen in niobium pentoxide (Nb_2O_5), which is used as a raw material in the

initial melt (Czochralski method) [126]. Accordingly, depending on the technology of its production, niobium pentoxide can adopt a wide range of compositions Nb_2O_{5-x}, and stoichiometric (ST) LN crystals were believed to only be obtained when ST Nb_2O_5 is used in the melt, that is, without deficit of oxygen. Although this last statement is less likely to be correct because STLN crystals are hardly obtained without entailing a modification to the Czochralski method or an assisting process, as described in the introduction (corresponding references in [35-37]), the lack of oxygen in Nb_2O_5 indeed can influence the CG point, which is disputed to be in the range 48.38 mol% to 48.60 mol% of the Li content [34].

Regarding ferroelectricity, its origin relies on the "non-centrosymmetric arrangement of the constituent ions and their corresponding electrons" (at low temperatures) [127, 128]. So far, this accounts only for the so-called 'spontaneous' polarization but not for its switching. The first concept stands for the existence of at least two discrete stable or metastable states of different nonzero electric polarization in zero applied electric field, whereas *switching* describes the possibility to switch between these states with an applied electric field $\vec{E}$, which "changes the relative energy of the states through the coupling of the field to the polarization $-\vec{E} \cdot \vec{P}$" [129]. Some non-centrosymmetric polar structures, the wurtzite structure as an example, do not exhibit ferroelectric behavior since its intrinsic polarization cannot be switched at known experimental conditions [127]. Ferroelectricity, as well as other related properties like piezoelectricity, pyroelectricity and Second Harmonic Generation (SHG), are sensitive to T, and most ferroelectrics exhibit a "phase transition from the ferroelectric state, with multiple symmetry-related variants, to a nonpolar paraelectric phase, with a single variant, with increasing T" [129]. The measured Curie temperatures range for a gamut of ferroelectric materials from 1 K to 1000 K; for very high Ts the probability of the material melting down before the transition occurs, increases. The discussion that follows in the next paragraph has been mostly adapted/reprinted from reference in [129].

The symmetry-breaking relation between the high-symmetry paraelectric structure and the ferroelectric one is consistent with a second-order transition, described by the Landau order-disorder theory, where a finite discontinuity in the heat capacity of the system having this transition has been addressed as a direct thermodynamic consequence (thus it can be probed by a thermometric procedure like DTA). Also, this analysis naturally leads to the prediction that the dielectric susceptibility diverges at the transition. From there, the link is

made, through the Lyddane-Sachs-Teller relation, to the vanishing frequency of a polar phonon, which is the central idea of 'soft-mode' theory of ferroelectrics [130]. Indeed, observation of the *T*-dependence of polar phonons was a key ingredient in the great progress made in understanding the physics of ferroelectricity in the 1960s and 1970s. Phonon spectroscopy continues to play a central role in the characterization of ferroelectric transitions, both via neutron scattering and optical spectroscopy [131, 132]. For a detailed description of the Landau theory, references in [133, 134] might be consulted. However, despite the success of this theoretical framework, there is still a controversy regarding the origin of ferroelectricity or of "ionic offcentering in known ferroelectrics" [127, 128].

Prototypical displacive transitions, characterized by a zone-centre vibrational mode *–the soft mode—* "with a vanishing frequency at the phase transition and an eigenvector similar to the displacements observed in the ferroelectric phases", were long considered to be behind this type of phase transitions [128, 135]. As already mentioned, at some point of history Megaw stated that most ferroelectric structures, specially perovskites, can be considered to be derivatives of a nonpolar, centrosymmetric prototype phase [108-110]. Thus, displacive type transitions might be pictured as the *physical* multitudinous "shifting of either the A or B cations (or both) offcenter relative to the oxygen anions" [127]; and as consequence of the dipole moment created by this shift, the emerging of a spontaneous polarization. Nevertheless, in this respect the so-called order-disorder type transitions have become popular lately. The difference between these types of transitions resides on whether a collective displacement of the cation sublattice is involved (displacive) or rather several local displacements of individual cations (order-disorder) [128]. In LN and LT, the latter are thought to be induced by the second-order John Teller (SOJT) effect of the NbO_6 and TaO_6 octahedral units, respectively [128].

These ideas can be traced back to 1992, when Cohen does a paramount contribution regarding perovskite oxides [135]: he realized that the "great sensitivity of ferroelectrics to chemistry, defects, electrical boundary conditions and pressure arises from a delicate balance between long-range Coulomb forces (which favor the ferroelectric state) and short-range repulsions (which favor the nonpolar [paraelectric] state)". Most importantly, he concluded that "for ferroelectric perovskites in general, hybridization between the B cation and O is essential to weaken the short-range repulsions and allow the ferroelectric transition. Most

ferroelectric oxide perovskites have B cations whose lowest unoccupied states are *d*-states (Ti^{4+}, Nb^{5+}, Zr^{4+}, and so on). This allows for *d*-hybridization with the O that softens the B–O repulsion and allows the ferroelectricity instability at low pressures" [135]. Hence, generally speaking (not only perovskites), the existence or absence of ferroelectric behavior is "determined by *balance* between these short-range repulsions, that favor the non-ferroelectric symmetric structure, and additional bonding considerations which act to stabilize the distortions necessary for the ferroelectric phase" [127]. The 'additional bonding considerations' have had already being pointed out by Megaw in 1952 [136]. The discussion that follows in the next paragraph has been mostly adapted/reprinted from reference in [127].

The changes in chemical bonding that stabilize distorted structures have been long recognized in the field of coordination chemistry, and are classified as SOJT effects [137-139], or sometimes *pseudo*-Jahn-Teller effects [140], in the chemistry literature. Their origin can be seen by writing down a perturbative of the energy of the electronic ground state *E(Q)*, as a function of the coordinate of the distortion *Q* [127, 141]:

$$E(Q) = E(0) + \langle 0| \left(\frac{\delta H}{\delta Q}\right)_0 |0\rangle Q + \frac{1}{2}\left(\langle 0| \left(\frac{\delta^2 H}{\delta Q^2}\right)_0 |0\rangle - 2 \sum_n{}' \frac{\left|\langle 0| \left(\frac{\delta H}{\delta Q}\right)_0 |n\rangle\right|^2}{E_n - E(0)} \right) Q^2$$

$$+ \cdots$$

<div align="right">Eq. I-1</div>

E(0) is the energy of the undistorted ground state, and the E_ns the excited-state energies. The term that is linear in *Q* is the first-order Jahn-Teller contribution, which is nonzero only for degenerate states. This term is responsible for the characteristic tetragonal distortions in d^1 and d^4 perovskites, for example. Of the second-order terms, the first is always positive, whereas the second, $2 \sum_n{}' \frac{\left|\langle 0| \left(\frac{\delta H}{\delta Q}\right)_0 |n\rangle\right|^2}{E_n - E(0)}$ is always negative, provided that it is nonzero. If the second term is larger than the first, then a distortion will cause a second-order reduction in energy. The first term describes the increase in energy on distortion, in the absence of redistribution of the electrons, and is dominated by the Coulomb repulsions between electron clouds. Therefore, it is smallest for closed-shell ions that lack spatially extended valence electrons. Two criteria must be satisfied for the second term to be large. First, the energy

denominator, $E_n - E(0)$, must be small, therefore there must be low-lying excited states available. Second, the matrix element $\langle 0 | \left(\frac{\delta H}{\delta Q} \right)_0 | n \rangle$ must be nonzero; this occurs if the product of the symmetry representations for the ground and excited state and the distortion is totally symmetric. Thus, for a non-centrosymmetric distortion, if the ground state is centrosymmetric, then the lowest excited state must be non-centrosymmetric. Note that this term represents the mixing of the ground state with the excited states as a result of the distorting perturbation, and as such is associated with the formation of new chemical bonds in the low-symmetry configuration [142]. A non-centrosymmetric distortion then results if the lowering in energy associated with the mixing of term two is larger than the repulsion opposing the ion shift, described by term one [143].

In conclusion, nowadays ferroelectricity is often associated with materials having d^0 transition metal ions (V^{5+}, Nb^{5+}, Ta^{5+}, Ti^{4+}, Zr^{4+}, and so on) and cations with a lone pair s^2 electrons (Pb^{2+} and Bi^{3+}) [128, 144]. In terms of crystal chemistry, these are SOJT active cations and, by breaking the centrosymmetric structure, have the potential of energy gain [128, 145]. The d^0 ions tend toward more covalent character in their bonding, which can lead to asymmetric coordination geometries that favor the development of a spontaneous polarization [144]. In the case of LN and LT, the Nb and Ta ions have 5+ formal charge with d^0 configuration, leading to cation displacement along the trigonal c axis [128].

1.1.1 Early thoughts on the structure of Lithium Niobate: its relation to basic structures of higher symmetry

In this subsection an additional comment is given regarding the LN crystal structure, mostly a historical recount. Volk and Wöhlecke –as previously said, authors of the most comprehensive monograph written on LN— refer to it as a 'pseudoilmenite, taking a side on the once important debate on whether it really could be formally considered as an ilmenite or if it would better be conceived as a highly distorted perovskite, as postulated by Megaw (1954) [108]. In 1928 Zachariasen described LN for the first time in history [10]. Reference in [10] could not be consulted but by reading the first report on the ferroelectric behavior of LN (and isostructural $LiTaO_3$; LT) by Matthias and Remeika (1949), it can be inferred that the LN structure was originally described by Zachariasen as being isostructural to that of ilmenite [$FeTiO_3$]. In putting the original mineral composition inside square brackets, it is

meant the whole family of ilmenite structures, according to the convention introduced by Muller and Roy [146]. Matthias and Remeika (1949) had pointed out that something did not fit entirely by assuming that LN crystals adopt [FeTiO₃], stating that whereas the latter is a centrosymmetric structure, at the same time "the existence of a spontaneous polarization […] indicates the absence of a center of symmetry" [14]. If LN manifested ferroelectric behavior, why would it adopt a centrosymmetric structure?

By 1952 the ilmenite-type picture persisted, year in which a second article was written by Schweinler [147], curiously under the same title to that of Matthias and Remeika: "*Ferroelectricity in the Ilmenite Structure*" (Schweinler cites the work of the other!). Anecdotally, although the title is invariant to both references, apart from the content they differ by a trifle: whereas the most recent one indeed labels LN as LiNbO₃, the older does it as 'LiCbO₃'… Historically, niobium (in Greek mythology the daughter of tantalum) was originally named columbium in honor of America, continent whence arose the mineral; in 1950, 149 years after its discovery, the International Union of Pure and Applied Chemistry (IUPAC) adopted "Niobium" as the official name [148]. In 1954 Megaw put perovskite into the scene, refuting kinship between LN and ilmenite. In her own words: "it is misleading to classify the LiNbO₃ structure as a member of the ilmenite family" [108]. Her explanation was based on the results presented in the doctoral thesis by Bailey [149], which is acknowledged to be the first extensive study on the LN crystal structure (a room *T*) [9]. Accordingly, Bailey was the first to show that the LN structure at room *T* is not identical to that of ilmenite due to a different stacking sequence of the cations [9].

Megaw referred to the structures of ferroelectrics (the LN structure per se) as *psedosymmetric structures of polar symmetry* that result as a competing effect between isotropic (ionic character) and directed (covalent character) binding. By assuming that the LN structure for the paraelectric phase at high *T* was the ideal cubic perovskite –back then the experimental information on the LN structure was only available temperatures far low from the curie temperature $T_c \sim 1210$ °C —, she proposed the continuous transition to the ferroelectric phase structure under the hypothesis of a monotonically increment of the covalent character as *T* decreases, as far as the overall binding characteristics are still mainly ionic [108]. Indeed, 12 years later Abrahams *et al* (1966) concluded (also supported on the results by Peterson [150]) that LN "is not primarily an ionic crystal, but one in which directed,

largely covalent, bonds play a determining role" [7]. Remarkably, Megaw's prediction (the covalency role in ferroelectrics) reverberates up-today because it is in full agreement to the current most widely accepted theoretical framework regarding the innermost causal of ferroelectricity, that is, the stabilization of structural distortion by means of SOJT effects (introduced above). Moreover, it is interesting to notice that apparently back in 1954 Megaw was not aware of the work by Buerger (1947), whom in the spirit of explaining the "genesis of twin crystals" and superstructures developed a formalism to describe some of the relations pertaining a crystal structure, called the *basic structure*, and those derived from it by (mathematical) generalization, called the *derivative structures* [151, 152]. The derivative structures would always present a lower symmetry respect to the basic structure. According to Bärnighausen whom refined and further extended the ideas of Buerger into the so-called *Bärnighausen trees* [153, 154], Megaw (1973) herself introduced the terms *aristotype* and *hettotype* as synonyms of basic and derivative structure, respectively [155]; these are nowadays widely accepted and used.

The conceptualization conceived by Megaw relied on a profound analysis of the crystallographic data obtained for LN (Bailey, 1952 [149]) and ilmenite (Barth and Posnjak, 1934 [156]): disregarding details, she concluded that whereas the transition paraelectric-ferroelectric in LN is continuous and reversible, implying however large atomic displacements of the order of $2.0 \, Å$ for Li and $0.7 \, Å$ for oxygen, the ilmenite structure cannot be attained by any distortion of a perovskite structure given that such a transition would involve a "serious rearrangement of the structure and is irreversible" [108]. Instead of considering a kinship between the LN and ilmenite structures, she rather proposed the former to be more closely related to the rhombohedral variant of $BaTiO_3$ which possibly "represents the early stages of a distortion which $LiNbO_3$ shows fully developed" [108]. Megaw herself found an "obvious difficulty" in her explanation due to the large magnitude of the displacements involved, which in 1957 changed to $1 \, Å$ for Li and $0.6 \, Å$ for O in a book she wrote, where she also acknowledges that such displacements might not be *physically* possible [109]. These values were in conflict to the results found by Abrahams et al in a series of three papers which are considered the most extensive and detailed structure analysis of LN [7, 20-21]. Reference in [21] is a study of the atomic arrangement in polycrystalline LN as a function of T, from room T (24 °C) to 1200 °C. In it, and accounting also for the results in single

crystal LN at room T by X-Ray and neutron diffraction (references [7] and [20], respectively), it is shown that in this range of temperatures the atomic arrangement is essentially unchanged: whereas a fixed oxygen framework exists given the non-significant displacement of magnitude 0.06 $\mathring{A}$ within the oxygen layers, the Nb and Li cations exhibit small displacements (along the same direction) of magnitude 0.25 $\mathring{A}$ and 0.45 $\mathring{A}$, respectively [21]. Besides this fact, Megaw's model was refuted given that "evidence for a change in crystal system between the ferroelectric and paraelectric phases" was not found: the comparison of the diffractograms obtained below and above T_c did not show appreciable changes in the positions of the lines, only did the intensities change in a non-reproducible way, "due to sintering and probably to preferred orientation of the resulting larger grains" [21].

The large discrepancy to the calculated displacements by Megaw relied on the original ambiguity in determining the Nb position relative to those of Li and O as originally done by Bailey [7]. Also, in the large error of about 1 $\mathring{A}$ present in the Bailey's determination of the atomic coordinate of Li [21]. Together, these two aspects constitute the main criticism from Abrahams *et al* to Megaw's work (1954). Accordingly, in view of the ambiguity and inaccuracy present in the work of Bailey (1952), Shiozaki and Mitsui (1963) did neutron diffraction on polycrystalline LN to improve the results [7, 9, 156], but these also conflict with those obtained by Abrahams et al [20]. Hence it can be said that Abrahams et al favored kinship of the LN structure to ilmenite instead of perovskite, and probably due to this they erroneously addressed the space group for the nonpolar paraelectric phase as $R\bar{3}$ instead of $R\bar{3}c$ [21]. According to Megaw (1968), however, they did point out $R\bar{3}c$ as a possible alternative [110]. On behalf of Landau´s theory of phase transitions, space group $R\bar{3}$ can be ruled out [9]. $R\bar{3}c$ being the proper space group for the paraelectric phase was shown by Niizeki et al (1968) [157]. In case of ferroelectric phase, the space group assigned by Bailey was confirmed, $R3c$, with lattice constants a = b = 5.148 $\mathring{A}$, c = 13.863 $\mathring{A}$ and atomic positions in the hexagonal reference [21]:

Nb: (0, 0, 0)

O: (0, 0, 0.2829) $\pm$ (0, 0, 23)

Li: (0.0492, 0.3446, 0.0647) $\pm$ (4, 5, 4)

where the error values, without decimal point, correspond to the least significant digit in the function value. In *R3c* the z-position of the origin can be arbitrarily chosen [9]. Clearly in the ferroelectric phase neither Nb nor Li is aligned to the oxygen lattice, hence Abrahams et al chose the Nb site as the origin since it is the principal X-ray and neutron scatterer –given it is bigger/heavier than Li [7]. Megaw did not give up and in 1968, based on all the results by Abrahams et al [7, 20, 21], she found a better justification for the LN structure relationship to that of perovskite by a reparameterization trick [110]. She proposed to redefine the origin in z-position (this can be done because the choice is arbitrary) such as it lies midway between two oxygen layers, in the vicinity of a Nb cation. In this way a high symmetry structural reference is obtained, an "idealized structure with hexagonally close-packed oxygen atoms" which upon successive approximations in terms of small quantities expressing displacement parameters –the actual Nb–O framework in LN as determined by Abrahams et al— can be obtained [110]. Other kind of successive approximations or displacement parameters would lead to the ideal perovskite framework. The reparameterization gives the following coordinates for the actual structure in terms of the ideal [110]:

$$\text{Nb: } (0, 0, w)$$

$$\text{O: } (u, \frac{1}{3} + v, \frac{1}{12})$$

$$\text{Li: } (0, 0, \frac{1}{3} + w')$$

with $u = 0.0492$, $v = 0.0113$, $w = 0.0186$, $w' = -0.01318$. The value of the axial ratio is $\frac{c}{a} = 2\sqrt{2}\left(1 + \frac{1}{2}\eta\right)$, with $\eta = -0.0936$. The idealized structure is then described when all the parameters are equal to zero. It can be regarded as the zero-order approximation to the actual Nb–O framework in LN and is a centrosymmetric structure with axis ratio $c/a = 2\sqrt{2}$. In the first-order approximation $u \neq 0$ while the rest of the parameters remain equal to zero, a higher symmetry structure is described where c/a tends to decrease from its ideal value. Particularly, the perovskite framework is described by this first-order approximation when $u = 1/6$. Insertion of Li into the octahedral interstices causes a symmetry reduction, thus allowing parameters *u, w, w'* to be different from zero, that is, the second-order approximation which describes the actual LN structure [110]. Moreover, regarding the effect of temperature, unexpectedly as *T* increases the actual structure (ferroelectric phase) would not tend towards the idealized structure, the zero-order model, but rather towards the first-order model with

increasing *u,* while *v* and *w* would tend to zero. Again, by stating this Megaw avoids saying that the ferroelectric LN structure can be derived from the ideal cubic perovskite, in her own words: "it is not suggested that a change of framework configuration from one extreme to the other can take place in any actual material" [110]. The fact that a ferroelectric phase follows from a small distortion of a high symmetry reference phase has demonstrated to be a powerful principle [129]. Yet according to Räuber, Megaw's ideas were widely accepted in the late 1970's [9]. The detailed discussion of the LN structure, as presented by Räuber, assumes the reparameterization trick originally proposed by Megaw.

Although this conceptualization might not be necessarily correct, however by understanding its *pros* and *cons*, the LN structure might be grasped in more natural fashion. For a deeper insight, perhaps prior knowledge on the corundum, ilmenite and perovskite structures would be of advantage for a proper comparison: these can be consulted from references in [159-161], [156, 159-160] and [129, 154, 160-163], respectively. In particular, the book by Lima-di-Faria provides useful descriptive charts in pages [11]: 99, 100, and 103, respectively. A review on the phase transitions between these polymorphs on titanates and related systems, reveals a trend of ilmenites transforming into perovskite [$CaTiO_3$] at high pressures which then quench to the LN structure on pressure release [160]. By applying pressure, the LN structure transforms reversibly to the perovskite one. Interestingly, at room *T* both phase transitions [$FeTiO_3$] (ilmenite) $\rightarrow$ [$CaTiO_3$] and [$LiNbO_3$] $\rightarrow$ [$CaTiO_3$], the same amount of pressure is needed, around 16 GPa [159-160, 164-165].

1.2 Precedents on the determination of the chemical composition of Lithium Niobate single crystals: various nondestructive methods

X-RAY DIFFRACTION (DRX) + STRUCTURE REFINEMENT

Based on all the references that have been consulted to write this thesis, and to the best of my knowledge, the first report showing an appreciable increase of the lattice constants of LN with decreasing Li content was done by Abrahams and Marsh (1986) [61]. By use of a Bond diffractometer [166], they were able to determine (at RT) the hexagonal *a-* and polar *c-* axes in cuts from CG and near ST (nST) single crystals. Only two experimental points were available, and little could have been said on the functional form that relates these parameters to the chemical composition. Even so, it was stated back then that if "a linear relationship

holds between the lattice constant and composition, the Bond measurement method would provide a convenient way to determine the composition at room temperature" [61].

In the early 90s two independent investigations further extended the available knowledge by preparing a larger number of samples and by applying structure refinement to both, neutron and X-ray diffraction (RT) [43, 59]. Accordingly, the tendency reported by Abraham and Marsh (1986) was corroborated, and furthermore the dependence of the lattice constant on the Li content was found to be linear [43, 59]. The linear character of the trend is more easily observed in terms of the cell volume ($V=\sqrt{3}a^2c/2$) though, according to Wöhlecke et al (1996) [45], whom on account of the data given in [43], formulated the following equation:

$$c_{Li} = -2.965V + 992.8$$

Eq. I-2

Noticing, however, that the studies in [43, 59] were done on powdered samples instead of single crystals. Yet it can be said that this methodology or equation is seldom used for the determination of the chemical composition (CC) of LN single crystals. It is possible that this is due to the very small influence of one parameter on the other. A final comment is given regarding the work of Abrahams and Marsh (1986). Crystals with a nST composition were prepared and studied by them. In the Introduction to this work of thesis it was stated that practically no ST or nST LN crystals were available until 1992, when the investigations in [35-37] were published. Hence, the method based on lithium vapor-phase equilibration to convert CG LN crystals into nST ones, developed by O'Bryan et al (1984; referenced in [61] as a non-published article), precedes that of Bordui et al (1992) [37].

POLARIZED RAMAN SPECTROSCOPY

In the framework of the group theory, vibrations pertaining the LN system (space group *R3c*, point group *3m;* RT) with vanishing wave **k** vector can be divided –in first approximation— into 5A_1, 5A_2, and 10 (twofold degenerate) *E* phonon branches. Of these, one A_1 and one *E* are the acoustic branches, the five A_2 fundamentals are Raman and infrared inactive, and the remaining 4A_1 and 9*E* optical branches are both Raman and infrared active. Accordingly, with two molecules per unit cell, the irreducible representation of the optical modes, according to group theory, can be expressed as: $\Gamma = 4\ A_1 + 5A_2 + 9E$. Because the A_2 are

nonpolar and inactive, therefore there are 13 directional dispersion branches of phonons. This paragraph has been adapted/reprinted indistinctly from references in [167, 168]. According to Sanna et al, the assignment of the phonon modes in LN has been a subject of debate for long time [168]; the above description is adopted by these references, which is also supported by earlier reports written by Hermet et al [169] and Margueron et al. [170]. All of these have a common root on the seminal paper by Schaufele and Weber (1966) [171]. Likewise, the next two paragraphs have been reprinted from different excerpts in [167].

As far as individual bands of interest in this discussion are concerned, bands located in the range of 550–700 cm^{-1} may be cumulative assigned to the Nb–O stretching modes involving essentially oxygen atom shifts. In particular, the band at 631 cm^{-1} involves only Nb–O stretching, namely, oxygen atom shifts corresponding to the antisymmetric stretching mode of NbO$_6$ octahedra. Among other bands available, only frequencies in the range of 250–400 cm^{-1} are influenced by Li cation displacements, while the O–Nb–O bending modes appear at and below 432 cm^{-1}, thus they are strongly coupled with the Li–O stretching and O–Li–O bending modes. The modes at 334 and 255 cm^{-1} exhibit deformation in the NbO$_6$ framework, mainly by oxygen atom shifts and small shifts of Li atoms. The mode at 276 cm^{-1} mainly encompasses the lithium-oxygen framework represented by Li–O stretching and O–Li–O bending modes. The lowest frequencies at 238 and 152 cm^{-1} may be mainly assigned to deformation of the Nb–O framework, while below 300 cm^{-1} Nb vibrational motions appear. The band observed at around 876 cm^{-1} represents pure stretching vibrations of Nb–O bonds. Non-polarized Raman spectra of synthesized LN, Li$_3$NbO$_4$ and LiNb$_3$O$_8$ powders are shown in Figure I-7, according to Bartasyte et al (2013) [40]. It can be noticed that LN and its corresponding 'parasitical phases' have completely different Raman spectra, as a consequence of having different symmetries. The frequencies of 15 (41) modes of Li$_3$NbO$_4$ (LiNb$_3$O$_8$) have been determined by the same group, as shown in Figure I-8.
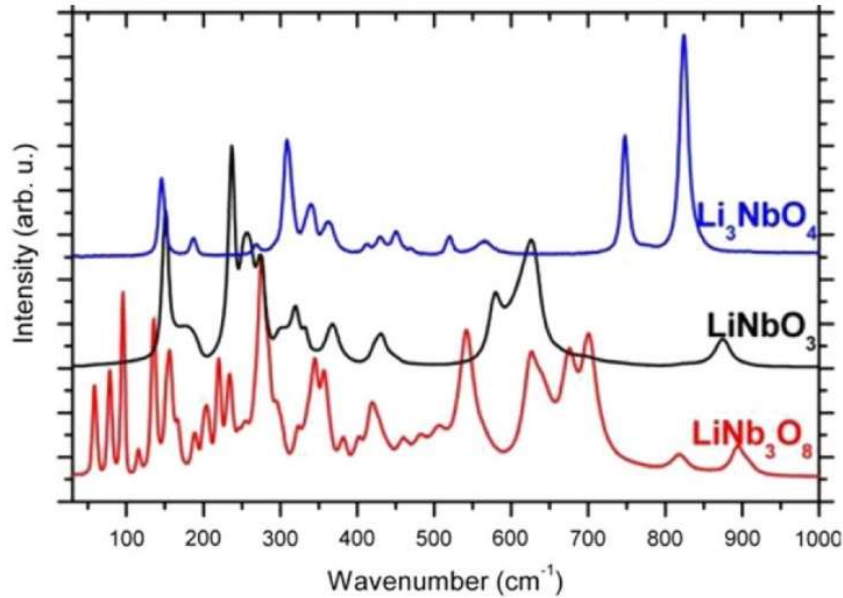
Figure I-7. Non-polarized Raman spectra of LN powders and their corresponding parasitical or secondary phases: Li_3NbO_4 (Li excess) and $LiNb_3O_8$ (Nb excess). *Reprinted/adapted from reference in [40]; © IOP Publishing Ltd, 2013.*
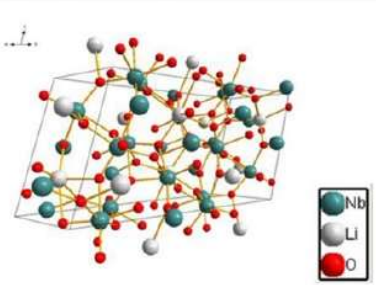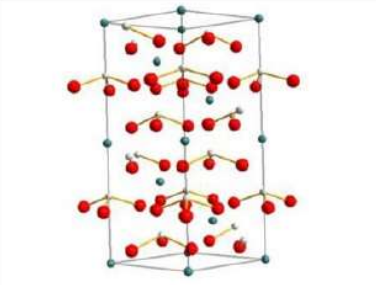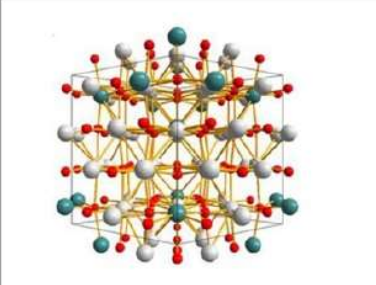
Phase: $LiNb_3O_8$	$LiNbO_3$	Li_3NbO_4
Space group: $P2_1/a$	R3c	I-43m
Raman active modes		
$36 A_g + 36 B_g$	$9 E + 4 A_1$	$13 T_2 + 8 E + 6 A_1$
Wavenumbers (cm^{-1})		
59 79 96 **116 136** 153 157 167 189 **201 206 220** 234 246 254 276 285 296 302 323 336 345 357 362 382 401 419 429 460 **482** **505 542** 565 625 641 675 **701 738 819** 893 898	155 199 240 241 253 265 276 277 298 334 334 343 364 370 421 425 433 457 580 632 659 667 870 879	146 187 269 310 335 341 363 412 430 451 **470** **520** 565 **748 824**

Figure I-8. Space group, structure, Raman active modes and their corresponding wavenumbers for LN, Li_3NbO_4 and $LiNb_3O_8$, as determined by Margueron et al (2012, first) [170] and Bartasyte et al (2013, last two) [40]. *Reprinted/adapted from reference in [40]; © IOP Publishing Ltd, 2013.*

On the other hand, regarding single crystalline materials with definite principal axes, knowledge of the state of the linear polarization of the scattered light turns to be of great importance. While the so-called *selection rules* for Raman-active phonons can be determined univocally by standard methods of group theory, the relative intensities of given Raman modes can be rationalized according to the polarization directions of the incoming and scattered (monochromatic) light. Accordingly, the experimental collection of polarized Raman spectra from known crystallographic planes might serve as a means for providing physical insight into the actual symmetry of properties of phonon branches or, vice versa, the knowledge of the selection rules for the investigated crystal can be applied to quantitative assessments of unknown crystallographic directions. This powerful idea lies deeply on the Raman tensor formalism, which is based on the simple concept that different phonon branches in a crystal will correspond to different symmetries of vibration and will, thus, be conditional on irreducible representations of the space group of the studied crystal lattice. Yet a direct proportionality relationship exists between the second-rank Raman tensor that describes the inherent properties of a phonon with respect to Raman scattering and the polarizability tensor described in the theory of quantum mechanics, and from therein, the term 'selection rules.' The matrices of the Raman tensor components representing the 13 directional dispersion branches of phonons in LN (the A_1 and E types of active phonon modes) are expressed as follows (within the orthogonal coordinate system) [167-168, 171]:

$$\mathcal{R}_{A_1} = \begin{pmatrix} a & 0 & 0 \\ 0 & a & 0 \\ 0 & 0 & b \end{pmatrix}; \ \mathcal{R}_{E(-X)} = \begin{pmatrix} 0 & -c & -d \\ -c & 0 & 0 \\ -d & 0 & 0 \end{pmatrix}; \ \mathcal{R}_{E(Y)} = \begin{pmatrix} c & 0 & 0 \\ 0 & -c & d \\ 0 & d & 0 \end{pmatrix}$$

Eq. I-3

where, depending on the scattering geometry A_1 or E modes as well as longitudinal (LO) or transversal (TO) modes can be observed [168]. The $\mathcal{R}_{A_1}$ tensor describes the scattering process in which the polarization states of the incoming and scattering photons are parallel [168]. The E mode is a composite one, consisting of two components $E(-X)$ and $E(Y)$ that might turn to be fully overlapping [167]; it describes the scattering process in which the polarization states of incoming and scattering photons are perpendicular [168]. The cumulative Raman intensity can be described according to [167]:

$$I_E = xI_{E(X)} + (1-x)I_{E(Y)}$$

where the weight parameter x can be assumed equal to 0.5, provided that band symmetry is observed. The scattering geometry in polarized Raman experiments is perhaps better described in terms of the notation introduced by Porto and Krishnan (1967) [172]; in general, *A(BC)D* stands for light propagating in the A direction with linear polarization B, before the sample, while selective detection is done on the D direction with linear polarization C ($\boldsymbol{D} = \overline{\boldsymbol{A}}$ represents a backscattering experimental configuration). The Raman selection rules and effective tensor elements for all the possible backscattering configurations are shown in Table I-3. The high sensitiveness of the functional form (and intensity) of the recorded Raman spectra in LN with the experimental configuration might be observed from the educational video 'Convenient Application of Polarized Raman Spectroscopy,' provided by the HORIBA Raman Academy [173].

Table I-3. Selection rules and Raman tensor elements for all experimental backscattering configurations. X, Y, Z refer to the orthogonal reference system for tensor properties. TO and LO stand for transversal and longitudinal optical modes, respectively. Taken from the publication by Sanna et al [168].

Configuration	Symmetry	Effective TO	Effective LO
$X(YY)\overline{X}$	A_1(TO), E(TO)	$a^2 + c^2$	
$X(YZ)\overline{X}$	E(TO)	d^2	
$X(ZY)\overline{X}$	E(TO)	d^2	
$X(ZZ)\overline{X}$	A_1(TO)	b^2	
$Y(XX)\overline{Y}$	A_1(TO), E(LO)	a^2	c^2
$Y(XZ)\overline{Y}$	E(TO)	d^2	
$Y(ZX)\overline{Y}$	E(TO)	d^2	
$Y(ZZ)\overline{Y}$	A_1(TO)	b^2	
$Z(XX)\overline{Z}$	A_1(LO), E(TO)	c^2	a^2
$Z(XY)\overline{Z}$	E(TO)	c^2	
$Z(YX)\overline{Z}$	E(TO)	c^2	
$Z(YY)\overline{Z}$	A_1(LO), E(TO)	c^2	a^2

In 1993 two independent works, by Schlarb et al [46] and Malovichko et al [47], reported a method to determine the CC of LN single crystals based on the relation of this parameter to the characteristic broadening or linewidth of certain Raman bands of the Raman spectra obtained under given polarization experimental conditions or selection rules. Accordingly, under conventional right-angle scattering geometries at RT, and for the E and A_1 modes located at 153 cm^{-1} and 876 cm^{-1}, respectively, the corresponding linewidths continuously increase as the Li content decreases (within the crystal and not in the melt). The trend is linear, as shown in Figure I-9. Thus, the CC of LN single crystal might be determined straightforwardly by use of any of the following equations (provided that the experimental conditions regarding the state of polarization of the incoming/scattered light are fulfilled) [45-47]:

$$c_{Li}[mol\%] = -0.4739\Gamma[cm^{-1}] + 53.03$$

band at 153 cm^{-1}; experimental: $Z(YZ)X$

Eq. I-5(a)

$$c_{Li}[mol\%] = -0.1837\Gamma[cm^{-1}] + 53.29$$

band at 876 cm^{-1}; experimental: $Z(YY)X$

Eq. I-5(b)
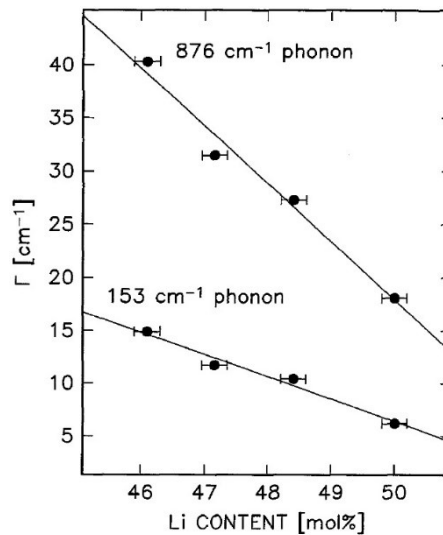
Figure I-9. Experimental data (dots) and least-squares fits (lines) on the halfwidths of the Raman lines at 153 cm-1 and 876 cm-1 in LN (vs Li content). *Reprinted/adapted from reference in [46]; © Springer-Verlag, 1993.*

In equations I-5, Γ represents the line broadening. However, it is not clearly stated, neither by Schlarb et al [46] nor by Malovichko et al [47], whether the complete linewidth (nominally being the Full Width at Half Maximum-FWHM) or just the halfwidth, is to be entered into these equations. An absolute accuracy of 0.2 mol% govern the concentrations data by use of this method [46]. Notwithstanding, again, no specifications regarding the resolution of the Raman bands or fitting techniques are given by Schlarb et al [46] or by Malovichko et al [47], although these procedures are critical for achieving great accuracy in the determination of the LN CC [46, 167, 174-175]. In this investigation, two distinct line shape fitting were explored (after normalization of the full spectra to maximum intensity): Gaussian and Lorentzian. It has been set Γ = FWHM and change of the intercept value from 53.29 to 54.8 (Eq. I-5(b)) was also tried, as suggested whenever no polished single crystals are available [46]. The choice of the E (153 cm^{-1}) and A_1 (876 cm^{-1}) modes is not arbitrary bur rather based upon certain criteria that simplify the adjustments and evaluations necessary to use Raman scattering as a standard characterization technique [46]:

➢ The recorded Raman intensity should be high enough
➢ The line should be well separated from the laser line and should not interfere with other Raman lines
➢ The directional dispersion should be zero, or at least small
➢ Optical damage should be minimized

Lastly, here it is important to acknowledge the contribution by Scott and Burns (1972) [176]. The idea of determining the CC of LN powders (LNPws) by means of a linear fit to data obtained from Raman spectra was first conceived in their pioneering work. Indeed, no equation is given in this work but it could easily be extracted from 'Figure 3' in [176], to describe LNPws instead of LN single crystals; again, it would not be easy to decide whether the complete linewidth Γ, or just the halfwidth, is to be entered in such a hypothetical equation, and if a Lorentzian or Gaussian distribution is to be used. Perhaps credit must also be given, within this context, to the work of Balanevskaya et al (1983) [177].

FUNDAMENTAL ABSORPTION EDGE

As it shown in Figure I-10 (left), the position of the fundamental absorption edge is very sensitive to the composition of LN single crystals. One of the earlier reports on this subject was written by Redfield and Burke (1974), whom also found that the spectral dependence of the absorption edge or band gap is linear at low temperatures (RT) while exponential at high ones (Figure I-10, right) [178]. According to Földvári et al (1984), a blue shift occurs from 320 to 311 nm upon moving from a near CG point to a near ST one [49]. Kovács et al (1997) have a given a corresponding linear equation for RT, with different sets of fitting parameters, depending on the character of the refractive index (ordinary and extraordinary), and the definition of the absorption edge (either corresponding to a value in the absorption coefficient of 20 cm^{-1} or 15 cm^{-1}) [50]:

$$c_{Li} = 50 - \left(\frac{E - E_0}{k}\right)^2$$

Eq. I-6
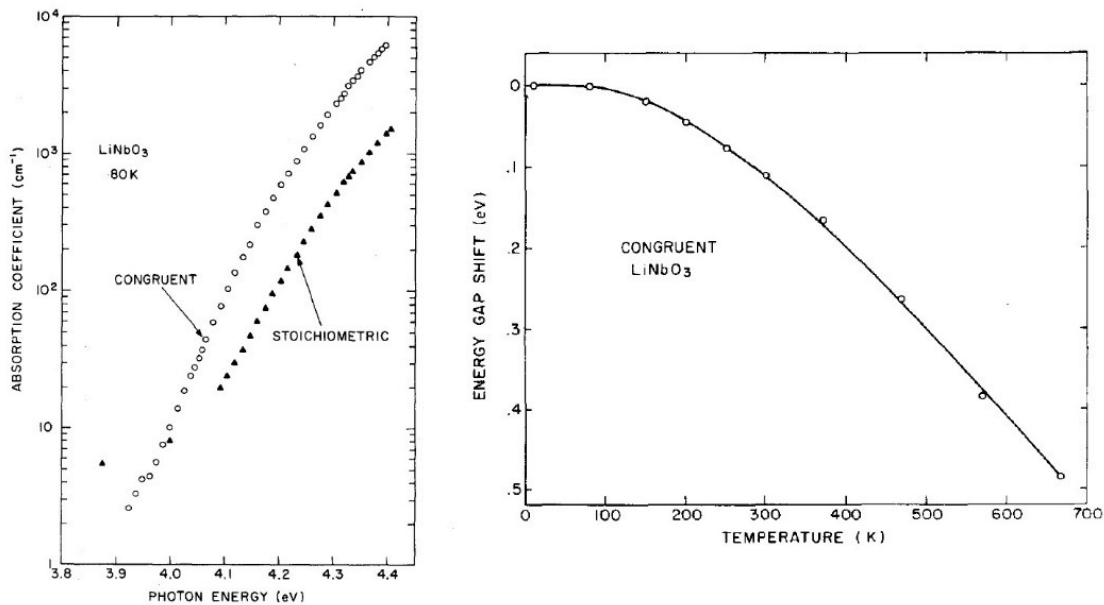
Figure I-10. Behavior of the fundamental absorption edge of undoped LN single crystals with respect to: **Left:** the chemical composition at 80 K. **Right:** Temperature for a fixed congruent composition. *As reported by Redfield and Burke in [178]; © American Institute of Physics, 1974.*

In Eq. I-6, E is the photon energy corresponding to the absorption edge at the chosen value of the absorption coefficient α, c_{Li} is Li_2O concentration in the sample in mol%, k and E_0 are the parameters of the fit (given in Table I-4). Correction of reflection losses is considered in the determination of α, according to [50]:

$$\alpha = -\frac{1}{x} ln\left(-b + \sqrt{b^2 + \frac{1}{R^2}}\right); b = \frac{(1-R)^2}{2TR^2}$$

Table I-4. Parameters for T = 22 °C in the calibration equation, Eq. I-6. The errors include all uncertainties of measurement and fitting. Taken from the publication by Kovács et al [50].

Refractive index	k [ev/$\sqrt{mol\%}$]	E_0 (eV) for $\alpha = 20$ cm^{-1}	E_0 (eV) for $\alpha = 15$ cm^{-1}
Ordinary	-0.189 ± 0.003	4.112 ± 0.002	4.092 ± 0.002
Extraordinary	-0.218 ± 0.003	4.136 ± 0.002	4.119 ± 0.002

where x is the thickness of the sample along the light propagation direction, $T=I/I_0$ and $R=(n-1)^2/(n+1)^2$ the transmittance and reflectance, respectively. The dispersion of the refractive index n is accounted for and calculated by use of the generalized Sellmeier equation for LN single crystals [51]. Although Eq. I-6 is a nonlinear relationship, the measurement of the UV absorption edge is a convenient method for characterizing the crystal composition. This method has an absolute accuracy of 0.1 mol% [50]. As shown in the inset of Figure I-11, a least squares linear fit can be applied in the dependence of E on the square root of the *deviation from the ST composition* $(50 - c_{Li})^{1/2}$. The method requires that the two sample surfaces crossed by the light beam to be polished to a moderate optical quality with a density of scratches less than 1% of the total area [45]. The orientation is not critical, better than five degrees are sufficient [45].
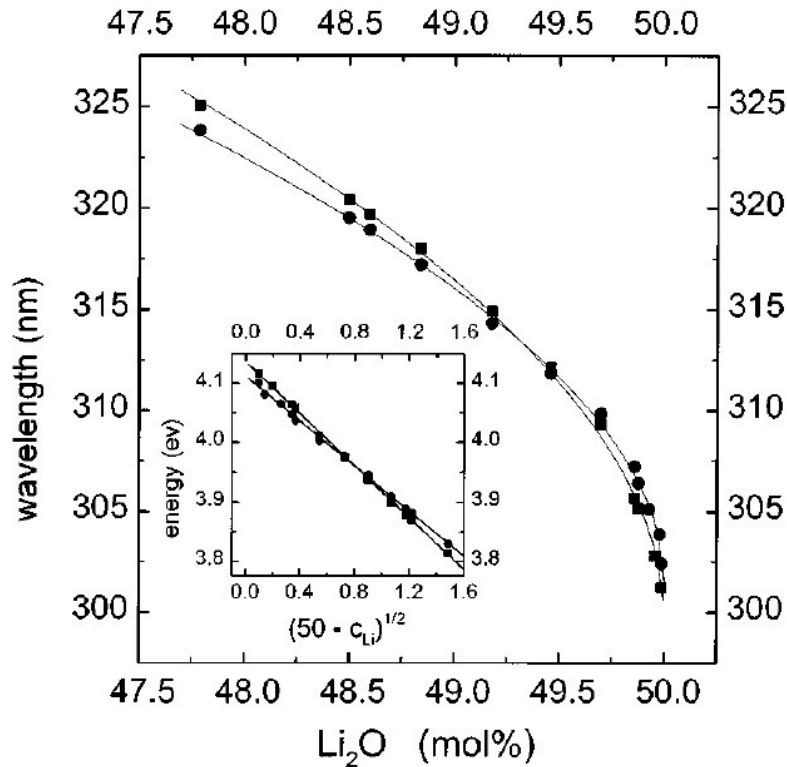
Figure I-11. The fundamental absorption edge of LN for T=22 °C at $\alpha = 20$ cm^{-1} as a function of the crystal composition. The squares and circles indicate measured values for the extraordinary and ordinary refractive index, respectively. The lines are calculated using Eq. I-6 with the parameter values given in Table I-4. The inset shows a least square linear fit for the dependence of the absorption edge energy on the square root of the deviation from the ST composition. *As reported by Kovács et al in [50]; © American Institute of Physics, 1997.*

Regarding LNPws, there is no point in using Eq. I-6 to describe their CC since the terms 'refractive index' and 'absorption coefficient' lack sense when related to powders (a powdered sample can be conceived as a material with infinite thickness from the optical point of view). Instead, UV-Diffuse Reflectance (DR) measurements are usually done in this respect under experimental circumstances that allow to describe the obtained functional form by means of the Kubelka-Munk theory. These concepts are introduced in PART II. Also, for practical purposes, a direct band gap is assumed for LN –noticing that it could also be assumed to be indirect [179]. Thus, under this assumption, the fundamental band gap is proportional to the square of the absorption coefficient α^2 (or in the case of powders, to the square of the Kubelka-Munk or *remission* function) [180].

DIFFERENTIAL THERMAL ANALYSIS

Measurement of the Curie temperature T_c –the temperature at which the paraelectric-ferroelectric phase transition takes place— is one of the earliest calibration methods for the determination of the CC of LN crystals [58]. The Curie temperature has been found to change linearly by roughly 150 °C in the solid solution (SS) range, which provides sufficient sensitivity for composition determinations [45]. An absolute accuracy of 0.1 mol% has been addressed to this method, yet it has the drawback that the crystal under investigation must be heated up to rather high temperatures (close to the melting point) [45, 46]. O'Bryan et al (1985) have determined T_c for a compositional range that covers SSs from 48.0 to 49.0 mol% Li$_2$O, by DTA. Both a linear and a nonlinear least squares fit have been reported [41]:

$$T_C = 36.70c_{Li} - 637.30$$

Eq. I-8(a)

$$T_C = 4.228c_{Li}^2 - 369.05c_{Li} + 9095.2$$

Eq. I-8(b)

where T_C and c_{Li} are inserted in °C and mol% units, respectively. The quadratic expression gives a better fit than the linear one, particularly for the compositional range close to the ST point [41]. However, in the literature it is often used the linear trend as reported in [37, 41]:

$$T_C = 39.064c_{Li} - 746.73$$

(Bordui et al [37]) Eq. I-8(c)

$$T_C = 39.26c_{Li} - 760.67$$

(Iyi et al [41]) Eq. I-8(d)

where the units are preserved respect to the previous equations. Considering the calculation of uncertainty values, the use of a linear least square fit might be preferred. As it will be shown in PART III of this thesis, where the obtained results are presented, the difference between the use of a linear and a quadratic expression in the calculation of T_C in

LNPws is of no more than 0.1%. Thus, in this investigation, a linear least square fit is proposed to be used instead of a quadratic one for the calculation of the CC of LNPws.

Chapter 2: Nonlinear Optics

Second Harmonic Generation

When an electromagnetic wave propagates within a nonlinear optical medium –that is, a medium in which its overall electric polarization depends nonlinearly on the applied electric field—, waves at frequencies different from that of propagating wave are generated. Second Harmonic Generation (SHG) is a well-known process of this type, where waves at frequency 2ω are generated from incident waves at frequency ω. In this chapter, SHG is conceptually treated, including the experimental conditions to its optimization. It starts by phenomenologically describing what it is understood by nonlinear optical phenomena.

2.1 Nonlinear optical phenomena

Generally speaking, in the field of optics it is assumed the existence of certain materials possessing certain *optical properties*, which manifest depending on *how* light propagates within the material, as well as near its surfaces. Any known optical property is attributed and/or derived depending on the manifestation of a basic optical phenomenon: reflection, propagation (refraction, absorption, luminescence, dispersion) and transmission [180]. For example, *birefringence* is a property of materials which are identified by presenting a refractive index dependency on the direction and polarization of the incident light, the wavelength being fixed. Another clear example is the *chromatic dispersion*: when white light impinges in a prism, the emergent light is decomposed into colors –characterized by a corresponding wavelength— due to the phenomenon of dispersion, having thus as result a refractive index which depends on λ.

Since its very origin and up-to-today, conventional optics is a physics derived discipline devoted greatly to study the phenomena and properties that manifest in materials due the presence of light. On the other hand, intuitively it can be said that Nonlinear Optics (NLO) studies the *changes* of such phenomena and properties as function of the intensity of the

incident light. Typically, only a LASER system can generate light sufficiently intense to modify the optical properties of a material. NLO then differs from optics in that the *optical parameters* –ascribed to materials to describe the phenomena and optical properties: reflectance, transmittance, refractive index (ordinary and extraordinary), absorption coefficient, among others— are no longer treated as constant respect to the intensity of light, instead they depend on this physical quantity [180]. In other words, in NLO the phenomena and optical properties are *nonlinear* in the sense that they occur when the material response to an applied optical field depends nonlinearly to the strength or magnitude of the electrical field carried out by light, that is, elevated to a power greater than 1.

2.1.1 Classical description

In the classical treatment of the light-matter interaction, the optical field or optical perturbation is described as a plane electromagnetic wave. The coupling between the electromagnetic wave and the medium is characterized by the electric polarization **P** of the medium, which is, to a first approximation, a collection of electric dipoles [181]. When the optical perturbation propagates through a dielectric, the oscillation of the electric field exerts a polarization force on the charged particles within the medium, changing its electronic configuration somehow. This change is interpreted as a charge redistribution that results into a collection of electric dipolar moments **p**, as shown in Figure I-12. It is expected that the charged particles oscillate in time coupled to the oscillation of the applied electric field and, thus, behave as microscopic antennas that transmit electromagnetic radiation. In the linear optical regime the frequency of the transmitted wave equals that of the applied wave [182].
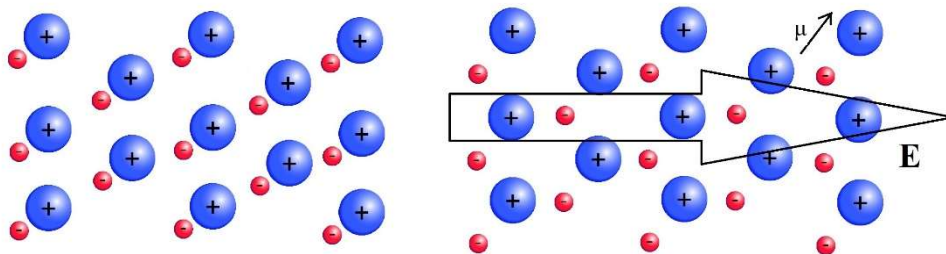
Figure I-12. Scheme representing the response of a dielectric medium to the application of an oscillating electric field. **Left:** in absence of the field. **Right:** in presence of the field.

The electric polarization is defined as the average of the net induced dipole moment per volume and given by the following equation:

$$\widetilde{P} = N\langle\widetilde{p}\rangle$$

<div align="right">Eq. I-9</div>

where N is the number of dipole moments per unit volume. By inserting time explicitly, the capacity of the electric field $\widetilde{E}(t)$ to move the charged particles can be expressed in terms of the linear polarization $\widetilde{P}_L(t)$ as [80]:

$$\widetilde{P} \approx \widetilde{P}_L(t) = \epsilon_0\chi^{(1)}\widetilde{E}(t)$$

<div align="right">Eq. I-10</div>

if nonlinear effects are considered this equation is merely a first order approximation. The nonlinear effects are associated to higher-order magnitudes of the electric field. The constant ϵ_0 is the vacuum electric permittivity and $\chi^{(1)}$ the linear electric susceptibility. The tilde (~) denotes physical quantities which vary rapidly in time; those that are constant or vary slowly in time are usually written without the tilde. The complete description of the phenomenon, that is, the equality in Eq. I-10, is obtained by means of its generalization by introducing a power series of the polarization respect to the electric field:

$$\widetilde{P}(t) = \widetilde{P}_L(t) + \widetilde{P}_{NL}(t) = \epsilon_0\left[\chi^{(1)}\widetilde{E}(t) + \chi^{(2)}\widetilde{E}^2(t) + \chi^{(3)}\widetilde{E}^3(t) + \cdots\right]$$

<div align="right">Eq. I-11</div>

where the quantities $\chi^{(2)}$ and $\chi^{(3)}$ are the second-order and third-order nonlinear electric susceptibilities, respectively. They acquire their tensor nature when the vector nature of the electric field is considered [80]. The physical processes that occur as a result of a presence of the second-order polarization, defined as $\widetilde{P}^{(2)} = \epsilon_0\chi^{(2)}\widetilde{E}^2(t)$, are different from those that occur as a result of a presence of the third-order polarization $\widetilde{P}^{(3)} = \epsilon_0\chi^{(3)}\widetilde{E}^3(t)$. The linear polarization $\chi^{(1)}$ is in principle much bigger in scale compared to nonlinear terms. This can be easily grasped by a simple estimation of the orders of magnitude for the common case in which the origin of the nonlinear optical processes steps out mainly from electron mobility

in an atom. When the magnitude of the applied electric field is of the same order of the electric field within an atom:

$$E_{at} = \frac{e}{4\pi\epsilon_0 a_0^2}$$

where e is electron charge and a_0^2 the Bohr radius for the Hydrogen atom. It is natural to think that the first nonlinear term, $\widetilde{P}^{(2)}$, is comparable to the linear one $\widetilde{P}_L$. Under non resonance conditions it can be estimated that $\chi^{(2)}$ is of the order of $\chi^{(1)}/E_{at}$, and $\chi^{(3)}$ of the order of $\chi^{(1)}/E_{at}^2$. For condensed matter $\chi^{(1)} \approx 1$, and also $E_{at} = 5.14\text{x}10^{11}$ V/m, then:

$$\left.\begin{array}{l} \chi^{(2)} = 1.94 \text{ x } 10^{-12} \dfrac{m}{V} \\[2mm] \chi^{(3)} = 3.78 \text{ x } 10^{-24} \dfrac{m^2}{V^2} \end{array}\right\}$$

Under normal circumstances it is known that the second-order nonlinear optical processes (NLOPs) only are present under the absence of spatial symmetry within a crystal, that is, in non-centrosymmetric crystals; the third-order NLOPs might occur in both, centrosymmetric and non-centrosymmetric media [183]. Now, in equations I-10 and I-11 it has been assumed that the polarization at time t only depends on the instantaneous magnitude of the electric field, which also implies the treatment of a lossless and dispersionless nolinear medium [80]. In the case where a dispersive material that might also present loss of energy, the intrinsic vector property of the electric field must be considered. In this way, both the electric field and total polarization depend on the position and frequency of the applied optical field. Then Eq. I-11 writes more generally as:

$$\widetilde{P}(r,t) = \sum_n P(\omega_n)e^{-i\omega_n t}$$

where a Fourier transform relates the time dependence to the frequency regime. The sum goes on both the positive and negative frequency components of the applied optical field. Likewise, the components of the second-order susceptibility tensor, $\chi_{ijk}^{(2)}(\omega_n + \omega_m, \omega_n, \omega_m)$, are defined as the proportional constants that relate the nonlinear polarization amplitude with the product of the amplitudes in the other components of the electric field, that is [80]:

$$P_i(\omega_n + \omega_m) = \sum_{jk} \sum_{(mn)} \chi_{ijk}^{(2)}(\omega_n + \omega_m, \omega_n, \omega_m)E_j(\omega_n)E_k(\omega_m)$$

<div align="right">Eq. I-14</div>

where the indexes *ijk* denote the spatial components of the fields. The notation *(nm)* indicates that in doing the summation over *n* and *m*, the value of $\omega_n + \omega_m$ is fixed, regardless of the interchange between ω_n and ω_m. The product $E(\omega_n)E(\omega_m)$ is associated to the time dependence $e^{-i(\omega_n + \omega_m)t}$, a contribution to the nonlinear polarization oscillating at a frequency $\omega_n + \omega_n$. In the same fashion are defined the components of the third-order susceptibility tensor $\chi_{ijkl}^{(3)}(\omega_o + \omega_n + \omega_m, \omega_o, \omega_n, \omega_m)$ [80]:

$$P_i(\omega_o + \omega_n + \omega_m)$$
$$= \sum_{jkl} \sum_{(mno)} \chi_{ijkl}^{(3)}(\omega_o + \omega_n + \omega_m, \omega_o, \omega_n, \omega_m)E_j(\omega_o)E_k(\omega_n)E_l(\omega_m)$$

<div align="right">Eq. I-15</div>

The reason behind the electric polarization plays a significant role in the classical description of the NLOPs is because a polarization that varies in time acts a source of new components of the electromagnetic field. This is noticed in the nonhomogeneous wave equation for nonlinear media [80]:

$$\nabla^2 \widetilde{E} - \frac{\epsilon^{(1)}}{c^2}\frac{\partial^2 \widetilde{E}}{\partial t^2} = \frac{1}{\epsilon_0 c^2}\frac{\partial^2 \widetilde{P}_{NL}}{\partial t^2}$$

<div align="right">Eq. I-16</div>

This equation expresses the fact that when the term on the right side is different from zero, there are accelerated charges and, thus, according to the Larmor theorem, these induce new components in the electric polarization, not present in incident radiation [184]. Noticing also that in the absence of sources the equation describes the case of a wave propagating at a velocity $c/$n in a medium with refractive index $\boldsymbol{n} = \sqrt{\epsilon^{(1)}}$.

2.1.2 Quantum Mechanics description

When light is thought as a photon flux its interaction with matter is described as a scattering of the photons due to the electrons present in the atoms or molecules in the material. Each photon carries a linear momentum *p=E/c*, which at the interaction instant is partially transferred to the molecules, the electrons remain bounded to the atoms. This process is considered an elastic scattering for the case of low intensity applied optical fields, that is, energy is conserved and thus the frequency of the scattered photons equals that of the incident ones [182]. In the interaction the photons are considered as *absorbed* and the molecules as reaching a *virtual excited state* with intermediate energy respect to the stationary states. Notwithstanding, the duration of such interaction or lifetime of the virtual state τ is sufficiently small so that it violates the following uncertainty relation:

$$\tau \Delta E \leq \frac{\hbar}{2}$$

Eq. I-17

where $\Delta \boldsymbol{E}$ stands for the energy difference between the virtual state of the molecule and its nearest excited state. Let us picture the molecules as a two-level system. Then the virtual state will be occupying an energy level close to state $|\boldsymbol{1}\rangle,$ as shown in Fig. I-13. Relaxation of the system, in other words the transition from the virtual state to ground state $|\boldsymbol{0}\rangle,$ is interpreted as the spontaneous emission of the scattered photons, associated to linear optical processes. For high-intensity applied fields the incident radiation increments the probability of multi-photonic interactions, that is, two or more photons are 'destroyed' and absorbed by a molecule in a unique process. Generally, in these cases the frequency of the scattered

photons is not the same as that of the absorbed photons. For example, two photons of frequency ω each, can be absorbed, 'creating' a third photon of frequency 2ω. This is the case of SHG, the main NOLP treated in this work of thesis.
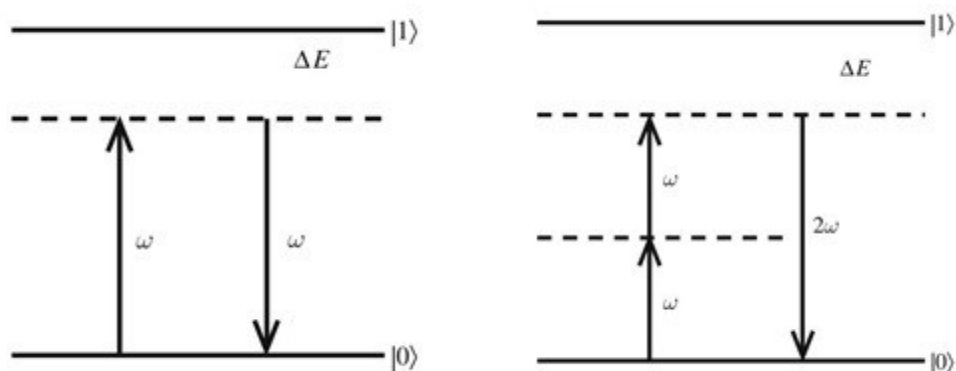
Figure I-13. Scheme of a two-level description of two distinct optical processes. **Left:** elastic scattering of incident photons with a frequency ω. **Right:** SHG in which two incident photons at frequency ω are involved and photon at frequency 2ω is generated. *Reprinted/adapted from reference in [182]; © Springer, 2006.*

Starting from these basic principles a great variety of multi-photonic interactions can be described, including the incidence of photons possessing different frequencies. However, it is important to have in mind that when $\Delta E \rightarrow 0$, the resultant optical processes cannot be considered as of an instantaneous scattering since the absorption in the excited state by the molecule must be considered. The theoretical treatment in the Quantum Mechanics description of NOLPs requires the solution to the time-dependent Schrödinger equation via the Density Matrix formalism and use of approximation methods (the quantum theory of perturbations), among other considerations. This approach can be further studied in references: [80] (chapter 3, p. 135-185), [86] (chapters 6.7 and 6.8, p. 49-58) and [182] (chapter 3, p. 10-27).

2.2 The process of Second Harmonic Generation

Let $\widetilde{P}^{(2)} = \epsilon_0 \chi^{(2)} \widetilde{E}^2(t)$ be the second-order polarization contribution to the overall electric polarization of the medium. Let us also assume the simplest case in which the incident light is a plane wave composed of a single frequency ω (monochromatic), so that the electric field is given by:

$$\widetilde{E}(t) = E\cos(\omega t)$$

where, inserting the polarization and using the trigonometric identity $cos^2(A) = \frac{1+\cos(2A)}{2}$, then:

$$\widetilde{P^2} = \frac{1}{2}\epsilon_0\chi^{(2)}[1 + cos(2\omega t)]$$

Thus, the second-order nonlinear polarization is composed of a zeroth-frequency contribution and one at frequency 2ω. Now according to the nonhomogeneous wave equation for nonlinear media (Eq. I-16), and given that the second derivative of the first term in Eq. I-19 vanishes, which implies that such a term does not induce a new frequency component in the electric polarization. However, it gives place to an optical process known as *optical rectification*, in which the established static electric field in the presence of a light pulse is exploited to generate ultrafast pulses in the THz regime with practical applications in the generation of femtosecond LASER pulses and in the study of water absorption in biological tissue [86]. The second term describes an optical response at frequency 2ω and is interpreted as the induced electric polarization at the harmonic frequency. On the other hand, SHG can also be thought as a particular case of other second-order NOLPs, namely *sum and difference frequency generation*. Let us assume, for example, an electric field carrying two frequencies, ω_1 and ω_2, being incident in a nonlinear medium with nonzero $\chi^{(2)}$. In this case [80]:

$$\widetilde{E}(t) = E_1 e^{-i\omega_1 t} + E_2 e^{-i\omega_2 t} + c.c$$

Again, letting $\widetilde{P}^{(2)} = \epsilon_0\chi^{(2)}\widetilde{E}^2(t)$, it gives:

$$\widetilde{P}^{(2)}(t) = \epsilon_0\chi^{(2)}\left[E_1^2e^{-i2\omega_1 t} + E_2^2e^{-i2\omega_2 t} + 2E_1E_2e^{-i(\omega_1+\omega_2)t} + 2E_1E_2^*e^{-i(\omega_1-\omega_2)t} + c.c\right] + 2\epsilon_0\chi^{(2)}\left[E_1E_1^* + E_2E_2^*\right]$$

<div align="right">Eq. I-21</div>

The first two terms represent SHG for each frequency ω_i. The third and fourth terms stand for the sum and difference frequency generation processes, respectively. The last one represents the optical rectification. By use of notation in Eqs. I-14 and I-15, it is possible to express with ease some of these processes in terms of the second-order susceptibility tensor:

$\chi_{ijk}^{(2)}(0, \omega, -\omega)$	Optical rectification
$\chi_{ijk}^{(2)}(2\omega, \omega, \omega)$	SHG
$\chi_{ijk}^{(2)}(\omega_1 + \omega_2, \omega_1, \omega_2)$	Sum frequency generation
$\chi_{ijk}^{(2)}(\omega_1 - \omega_2, \omega_1, \omega_2)$	Difference frequency generation

Even though there are four components with nonzero frequency and, in principle, all of these take place simultaneously, in practice no more than one will be present at an appreciable intensity since the nonlinear polarization only produces a significant response if an experimental condition known as *optical phase-matching* is satisfied, which can only be done for a single frequency at a time. Theoretically, and seen from the point of view of wave-like phenomena, what determines which of the processes is favored respect to others is the coherent summation of all the generated waves within the nonlinear medium [8]. When the pumping beam propagates along the material a multitude of secondary waves of different frequencies are generated and, due to the chromatic dispersion of the refractive index, each generated wave has its own propagation velocity which depends mainly on its frequency, among other considerations. For a given frequency, the relative phase between the generated waves will depend on their intrinsic propagation velocity as well as in the phase of the fundamental beam just at the location where the secondary waves are generated – thus, it also depends on the propagation velocity of the fundamental beam [8]. Optical phase-matching – hereafter referred simply as phase-matching— is the mostly used experimental technique to optimize the SHG process. Yet, it is not the only one. In the next subsection the main

techniques to optimize SHG in different type of materials are discussed. The importance of SHG optimization has already been highlighted in the introduction by retelling the anecdote with the original contribution by Franken et al (1961) [83], originally told by Skipetrov (2004) [78] (see Fig. I-2).

2.2.1 Phase-matching

Let us begin this subsection by performing a simple calculation, for which it is necessary the use of a result previously reported. Assume a plane wave of amplitude $\boldsymbol{E}^{(\omega)}$ and frequency $\boldsymbol{\omega}$, linearly polarized. Also, that the medium is infinite and that the plane wave propagates along the Z-axis. Then, the wave equation in Eq. I-16 can be restated as [185, 186]:

$$\frac{\partial \boldsymbol{E}^{(2\omega)}}{\partial \boldsymbol{z}} = -\frac{i\omega}{2n^{(2\omega)}c}\chi^{(2)}\left(\boldsymbol{E}^{(\omega)}\right)^2$$

Eq. I-22

where also the '*slowly varying envelope approximation*' has been utilized. Since it is a plane wave the amplitudes of the fields can be of the form:

$$\left. \begin{array}{l} E^{(2\omega)} = A_1 e^{-i(k_{2\omega}z-2\omega t)}, \\ E^{(\omega)} = A_2 e^{-i(k_\omega z-\omega t)} \end{array} \right\}$$

Eq. I-23

so that the differential partial equation in Eq. I-22 rewrites:

$$\frac{dA_1}{dz} + ik_{2\omega}A_1 = -\frac{i\omega}{2n^{(2\omega)}c}\chi^{(2)}(A_2)^2 e^{i\Delta kz}$$

Eq. I-24

where $\Delta \boldsymbol{k} = 2\boldsymbol{k_\omega} - \boldsymbol{k_{2\omega}}$. Neglecting the second term and integrating for nonlinear medium of length L:

$$A_1 = -\frac{i\omega}{2n^{(2\omega)}c}(A_2)^2 \int_0^L e^{i\Delta kz}\, dz = -\frac{i\omega}{2n^{(2\omega)}c}(A_2)^2 \left(\frac{e^{i\Delta kL}-1}{i\Delta k}\right)$$

<div align="right">Eq. I-25</div>

Using the general expression for the Poynting's vector [80]:

$$I_j = 2n_j\epsilon_0 c|A_j|^2$$

<div align="right">Eq. I-26</div>

Moreover, since:

$$\left|\frac{e^{i\Delta kL}-1}{\Delta k}\right|^2 = L^2\left(\frac{e^{i\Delta kL}-1}{\Delta kL}\right)\left(\frac{e^{-i\Delta kL}-1}{\Delta kL}\right) = 2L^2\frac{1-cos\Delta kL}{(\Delta kL)^2} = L^2\frac{sin^2\left(\frac{\Delta kL}{2}\right)}{\left(\frac{\Delta kL}{2}\right)^2}$$

59

<div align="right">Eq. I-27</div>

Then [186]:

$$I^{(2\omega)} = \frac{\omega^2 L^2}{8\epsilon_0 c^3 n^{(2\omega)}(n^{(\omega)})^2}|\chi^{(2)}|^2(I^{(\omega)})^2\left(\frac{sin\frac{\Delta kL}{2}}{\frac{\Delta kL}{2}}\right)^2$$

<div align="right">Eq. I-28</div>

where the exact form of the term $|\chi^{(2)}|^2$ depends explicitly in the election of the linear polarization state respect to the orientation of the nonlinear crystal. The las term denotes that the intensity of the harmonic wave is a function that oscillates according to the quantity Δk. A deviation from the maximum in intensity can be predicted whenever the condition $\Delta k = 0$ is not satisfied. This oscillatory behavior was first corroborated in 1962 by Maker et al (see Fig. I-14) [187]. The experiment is considered one of the fundamental experiments in SHG: it consisted in monitoring the intensity of the harmonic signal from a crystal quartz as a function of the rotation angle of the crystal, that is, as a function of the effective propagation length L (as a source a pulsed rubi LASER system was used) [187].
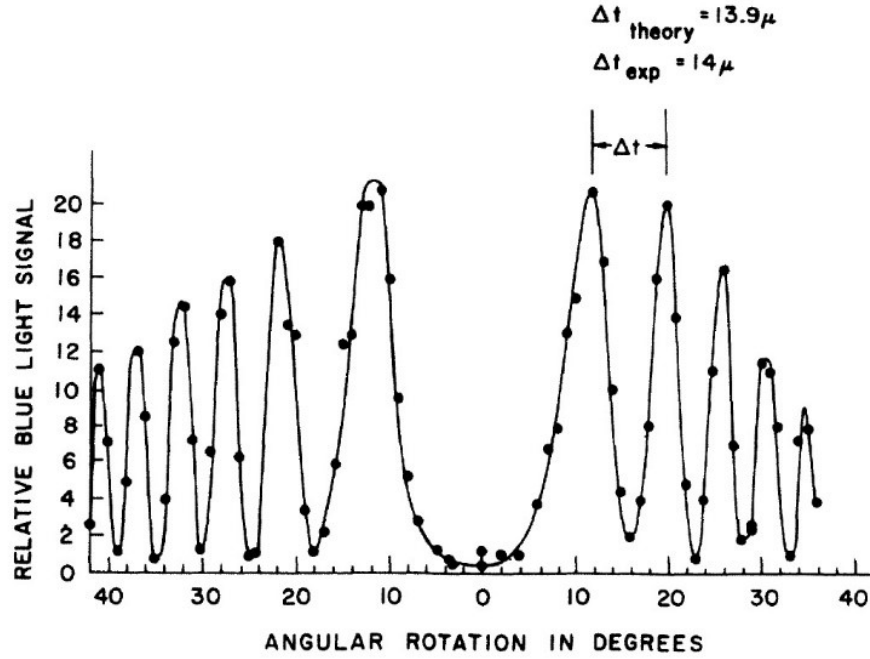
Figure I-14. Maker fringes: first experimental evidence of the necessity to match the involved waves (fundamental and harmonic) in the SHG process, respecting their phases. *As reported by Maker et al in [187]; © Physical Review Letters, 1962.*

The condition $\Delta \boldsymbol{k} = \boldsymbol{0}$ implies:

$$k_{2\omega} = 2k_{\omega}$$

<div align="right">Eq. I-29</div>

where $\boldsymbol{k_\omega}$ and $\boldsymbol{k_{2\omega}}$ are the wavevectors of the fundamental and harmonic waves, respectively. It is said that when this condition fulfills, the phase-matching (PM) condition has been achieved. Furthermore, if the beams are collinear, using the next dispersion relation:

$$|k| = \frac{\omega n(\omega)}{c}$$

<div align="right">Eq. I-30</div>

Eq. I-29 then reduces to:

$$n(2\omega) = n(\omega)$$

<div align="right">Eq. I-31</div>

In case this equality does not hold, the generated waves at different locations within the medium will not be in phase, so that constructive interference would not be present. Due to chromatic dispersion in the refractive index it is impossible that Eq. I-31 holds for isotropic

media [8]. On the other hand, PM can be achieved in anisotropic nonlinear media such as uniaxial crystals (i.e. LiNbO₃ single crystals), which are birefringent materials. Hence, by a proper choose of the propagation direction regarding both beams, it is possible to fix, for example, the ordinary refractive index to the beam at frequency $\boldsymbol{\omega}$, while the extraordinary refractive index to the beam at frequency $2\boldsymbol{\omega}$, achieving this way the PM condition.

On experimental grounds and regarding only uniaxial crystals, the PM condition is usually achieved by adjustment of the θ angle, defined by the optical axis of the crystal and the propagation direction of the fundamental beam. Control in the temperature of the crystal might also be used for this purpose. In the specific case of lithium niobate (LiNbO₃; LN), usually θ is kept fixed and the temperature is varied. This mainly due to two reasons: 1) the birefringence of LN single crystals is very sensitive to changes in T, and 2) for θ values different from 0 and 90°, and given certain technical limitations related to the Poynting's vector (**S**) and of propagation of the extraordinary ray (**k**), it results that the conversion efficiency significantly decreases due to a diminished spatial overlap between the involved beams [80]. Thus, as it is shown in Fig. I-15, PM is usually achieved in LN by fixing θ = 90°, whereas the temperature inside the crystal is varied [80, 188].
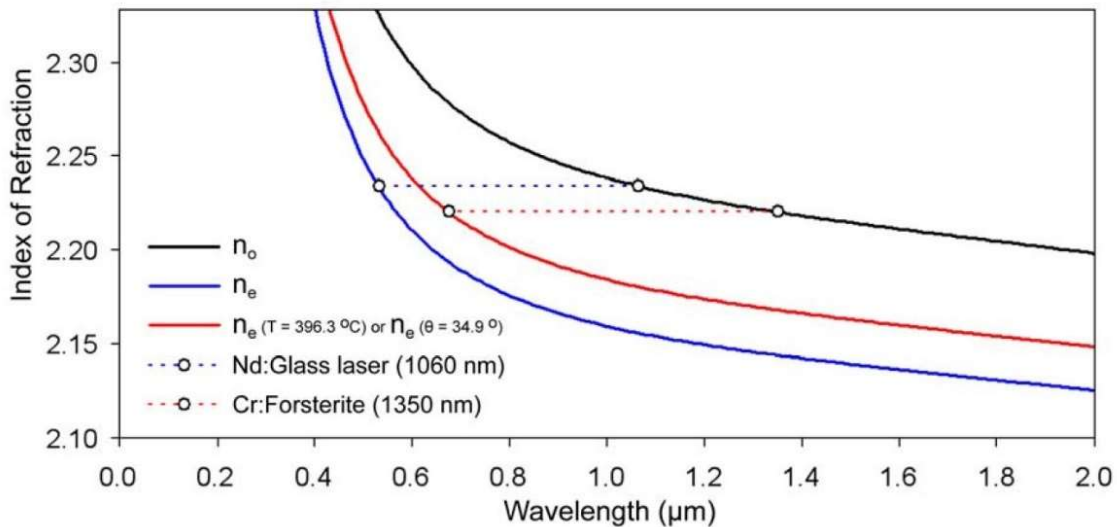
Figure I-15. A single crystal of LN at T=32 °C, to phase-match a fundamental beam with λ = 1064 nm and its corresponding harmonic wave. For λ = 1350 nm the phase-matching conditions is achieved either by adjusting θ=34.9 ° or T= 396.3 °C. *As reported by Wood in [188]; © Wood, B.D.; Master thesis: Simon Fraser University, 2009.*

In principle the PM condition would also be achieved by exploiting the phenomenon of anomalous dispersion for materials presenting a large optical absorption [80]. In other words, under circumstances of resonance there exists a narrow spectral zone in which the refractive index of the material decreases as the frequency of the incident beam increases [180]. Given that certain material might absorb light strongly at certain frequency, say 2ω, and being transparent for another –that would be ω—, the equality in the refractive indexes could be obtained since in one case the refractive index decreases with frequency, whereas in the other it increases. However, the use of anisotropic nonlinear media is the main strategy to optimize SHG, also in the case of the more complex processes of sum and difference of frequencies, either regarding type-I PM or type-II [81, 189].

Lastly, in Eq. I-28 it can be noticed that for values $\Delta k \neq 0$, the first intensity minimum in the harmonic wave is obtained when $\frac{\Delta k L}{2} = \pi$. Regarding conversion efficiency, it is thus convenient to define and optimum length for which the polarizations of both waves (fundamental and harmonic) are out of phase by π radians. This parameter is denoted as the *coherence length* and it is defined as:

$$l_c = \frac{2\pi}{\Delta k} = \frac{\lambda}{2|\Delta n|}$$

Eq. I-32

where λ is the pump or fundamental wavelength and $\Delta n = n(2\omega) - n(\omega)$. The coherence length describes the length within the material for which the intensity of the second harmonic signal falls dramatically to zero. What does this mean? If for example, one has a pumping beam with λ=1064 nm and a material in which $\Delta n \approx 0.01$, then $l_c \approx 53.2$ µm, that is, even though a piece as a large as desired of this material could be at hand, say 1mm, only the first 53.2 µm will be effective for SHG. This is the reason behind why materials with large coherence lengths are nominally sought for frequency doubling, although their intrinsic magnitude of the second-order nonlinear susceptibility must always be considered. Larger coherence lengths are obtained as $\Delta n \to 0$. Fig. I-16 aids the visualization of the SHG intensity sensitivity on the coherence length. This parameter is an intrinsic property of the material, usually of the order of tens of micrometers [185].
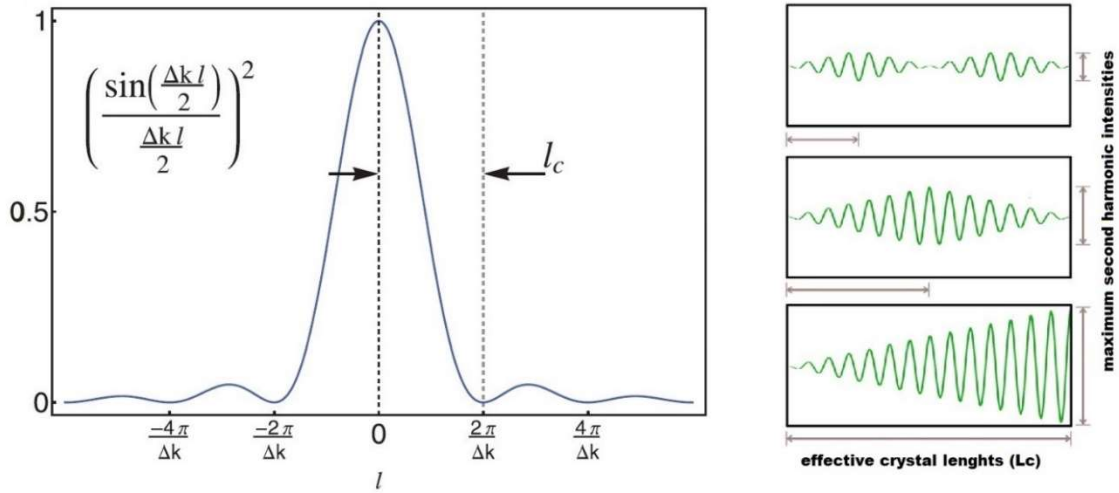
Figure I-16. The effect of the coherence length in the SHG intensity delivered by a material. **Left:** oscillatory term in Eq. I-28: deviations from $\Delta k = 0$ have an influence on the intensity of the converted signal, which becomes nonsignificant from a distance l_c within the material. **Right:** simulation on the propagation of the second harmonic wave within the material, showing distinct cases of the effective length of the crystal. *Reprinted/adapted from references in [188, 190]; © Wood, B.D.; Master thesis: Simon Fraser University, 2009 and The American Ceramic Society, 2011, respectively.*

2.2.2 Quasi-phase-matching

For a given anisotropic nonlinear material, the frequency regime in which PM can be achieved is generally small. Thus, to obtain more converted frequencies the use of other type of materials is necessary. Another technique to have large conversion efficiencies is known as *quasi-phase-matching* (QPM). It is based on the periodical alternation along the nonlinear medium on the phase of the generated waves [8, 22, 80, 191].

It is known that inside a material for which $\chi^{(2)} \neq \mathbf{0}$, the SHG processes being involved, the generated waves will constructively interfere whenever $\boldsymbol{L \leq l_c}$, with $\boldsymbol{l_c}$ the coherence length of the material, defined by Eq. I-32. Assume now that a fundamental wave enters a nonlinear medium for which the PM condition cannot be achieved. If somehow the phase of the generated waves could be inverted each $\boldsymbol{l_c}$ distance, then most of them would constructively interfere. This can be done if instead of a homogenous medium, it used one for which $\chi^{(2)}$ periodically changes its sign each $\boldsymbol{l_c}$ distance, as it is shown in Fig. I-17.
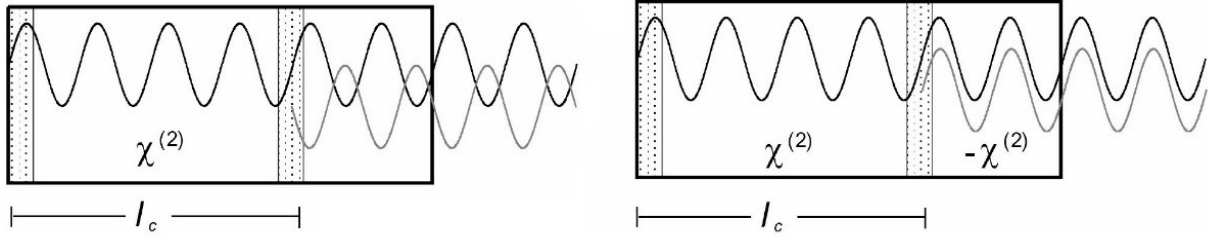
Figure I-17. Propagation of the second harmonic wave in two different media. **Left:** homogeneous medium for which the generated waves by two regions, separated by a distance l_c, are out of phase by π radians. **Right**: nonhomogeneous medium in which the sign of its optical nonlinearity is alternated each distance l_c: on this instance, the generated waves by the two regions separated by the same distance, will be in phase. *Reprinted/adapted from references in [8]; © Revista Mexicana de Física, 2002.*

64

Let Λ be the period on the alternation of the sign in $\chi^{(2)}$, in this case given by $\Lambda = 2l_c$. The QPM condition will be thus stated as follows [8]:

$$\frac{2\omega}{c}|\Delta n| = \frac{2\pi}{\Lambda}$$

Eq. I-33

Or, equivalently:

$$|n(\lambda) - n(\lambda/2)| = \frac{\lambda}{2\Lambda}$$

Eq. I-34

where λ is the fundamental wavelength. In short, what determines which frequencies or wavelengths are efficiently generated in QPM is the periodicity of the nonlinear medium Λ. QPM presents various advantages over PM, but the main one is that the medium can be altered so that a specific nonlinear process is exploited. It is even possible to generate multiple nonlinear processes simultaneously or in cascade, for example, to generate two tunable waves and then to have SHG from one of them within the same nonlinear crystal by simple inserting two different periodicities in a structure of ferroelectric domains. This cannot be done by regular PM [8]. Experimentally, to change the sign of the second-order optical nonlinearity is relatively simple if ferroelectrics are used. As previously described (last part of section 1.1), ferroelectrics can be described as anisotropic media having a spontaneous

polarization pointing towards a preferred direction, which can be inverted π radians by the application of a proper electric field. This is schematized in Fig. I-18. It turns out that in ferroelectrics with $\chi^{(2)} \neq \mathbf{0}$, both the magnitude and sign of the optical nonlinearity depends on the magnitude and sense of the spontaneous polarization. Hence, by the application of an electric field in selected regions of the material, the spontaneous polarization can be inverted locally and, consequently, and spatial alternation in the sign of the optical nonlinearity will be obtained [8].
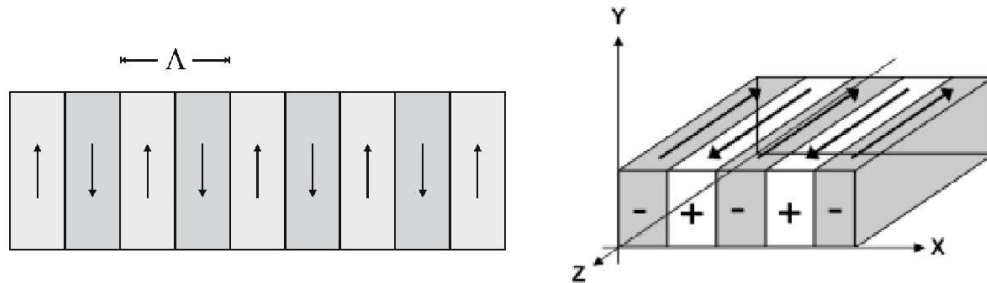
Figure I-18. Scheme of a periodic structure of ferroelectric domains. Left: 2-D. Right: 3-D. *Reprinted/adapted from reference in [22, 192]; © Springer-Verlag and Wiley, respectively.*

The original idea of QPM dates back to 1962, when Armstrong et al suggest the fine slicing of a nonlinear dielectric into various segments to be alternated periodically by a 180° rotation [193]. Several methods have been proposed in the literature to fabricate structures to achieve QPM [8, 194-196]; to mention just a few and, of which, references in [8, 195, 196] concern a material based on LN. The basic principles behind *'Ferroelectric Switching'* –that is, polarization reversal in ferroelectric domains— has been, and continues to be, an important research subject. The number of scientific works devoted to it is just overwhelming. It is out of context in what concerns this work of thesis. A phenomenological description, the approach of various models to describe the problem, and the most important results regarding the specific case of LN, can be consulted in [192] and the literature therein referenced.

2.3 *"Disorder is the new order"*

In the previous discussions, either concerning PM or QPM, the generated waves within a crystal interfere constructively because of the experimental conditions already described, however, it also happens due to the fundamental fact that there is sufficiency in what respects the dimensions of the material. Said differently, the phases are matched because: they have

enough space to do so! By contrast, it is said that in nanocrystals or harmonic nanoparticles (HNPs) the SHG cannot be phase-matched, given that the characteristic size of the nonlinear medium is much smaller compared to its intrinsic coherence length [185, 197]. This also implies that both, the orientation of the nanocrystals respect to fundamental beam propagation and their temperature, play a minor role in the SHG intensity.

In 2004 the term *disordered material* is coined to refer to a polycrystalline material consisting of several crystalline domains highly random regarding their size, shape and orientation, capable of frequency doubling. Back then, the possibility of having efficient processes for optical conversion in isotropic media is stated for the first time: SHG by Skipetrov [78] and difference frequency generation by Baudrier-Raybaut et al [198]. Given the context within this work of thesis, the work written by Skipetrov –entitled "Disorder is the new order"— is more relevant because it specifically treats SHG, apart from the fact that it gives a detailed discussion on the report written by Baudrier-Raybaut et al. Next, the main aspects of the work authored by Skipetrov are summarized [78]:

➢ Regarding only single crystals, the most viable ways to optimize SHG is by means of the experimental techniques of PM and QPM. However, there important limitations. On one hand, PM can only be achieved in anisotropic nonlinear materials, thus restricting the use of materials for SHG. QPM lessens this issue, but "the technology required to fabricate such a material is unfortunately rather involved, expensive and not widely accessible".

➢ PM can be achieved indirectly in a disordered material and, for this reason, the term employed is '*random-quasi-phase-matching*' (introduced by Baudrier et al [198]) or '*stochastic quasi-phase-matching*' (introduced by Morozov and Chirkin [199]).

➢ "The frequency-converted waves generated by different domains achieve random phases and interfere neither constructively nor destructively. The total intensity of the generated wave is then the sum of the intensities arising from individual domains and it grows linearly with the number of domains or the length of the sample".

➢ "Clearly the random phase-matching is less efficient than the 'truly' phase-matched process, because the latter benefits from the constructive interference of waves generated by different parts of the nonlinear medium. But it outperforms the phase-mismatched process for which the interference of partial waves is destructive".

Fig. I-19 shows the theoretically expected conversion efficiencies for different circumstances of the PM condition. From 2004 up to date, the researching field of SHG in disordered materials has growth and evolved considerably. Around 2006 various researching groups worldwide put efforts into the study of this field, aiming to exploit random-quasi-phase-matching for a practical application, namely as a an efficient optical-constrast mechanism to acquire images in cells and/or biological tissue [89]. Nowadays, 'bio-imaging', 'cell-imaging' and 'multi-photon microscopy' are well-stablished disciplines that offer a prominent alternative within the field of biomedicine in attempting to replace fluorescent biological markers [85, 200-202].
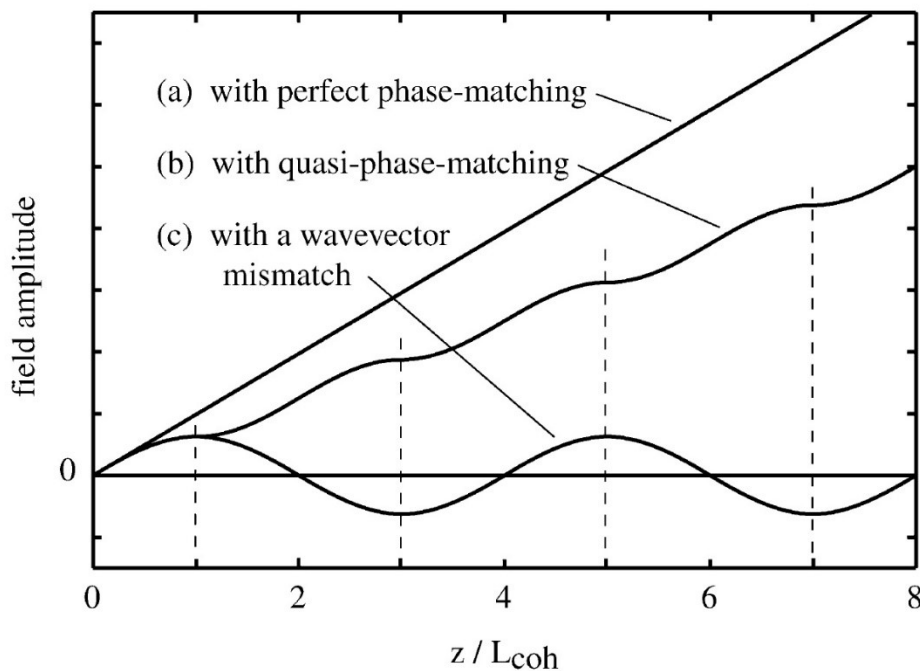
Figure I-19. Comparison in the conversion efficiency for various types of phase-matching conditions; $L_{coh} = 2/\Delta k$. (a): phase-matching, $\Delta k = 0$. (b): quasi-phase-matching, $\Delta k \neq 0$. (c): neither phase-matching nor periodic modulation on the sign of the optical nonlinearity. Presumably, the conversion efficiency describing a disordered material is higher than that corresponding to curve in (c). *Reprinted/adapted from reference in [80]; © Elsevier, 2008.*

2.4 The Kurtz-Perry method

The synthesized powders and studied for their SHG response are polycrystalline materials. They are conceived as formed by micrometer size particles made up of several single nanocrystals. However, although still a disordered or random material in the sense of optics, powders do not necessarily fit the description of disordered materials as conceived by Skipetrov and Baudrier-Raybaut, as discussed in the previous section –thin films and xerogels better fir such a description. In 1968 Kurtz and Perry developed a semiquantitative theoretical framework to describe the SHG arising from powders [97]. Even though within the context of this work of thesis this framework contributes little to the analysis of the obtained results (given in PART III, Chapter 6), it is considered important to be succinctly discussed at least, given its popularity and practical importance. To begin with, the SHG capabilities of yet unavailable single crystals can be predicted, the latter classified into five main categories of materials for SHG, among which those that are predicted to be phase-matchable and not phase-matchable. Also, with the concept of the *averaged coherence length* of the material, introduced by Kurtz and Perry, a reasonable explication could be grasped to the results previously obtained to this investigation (published in [24]).

In principle, the following approximations should hold within the Kurtz-Perry method:

➢ The powder particles are immersed in an index matching liquid
➢ The particles are single crystals with a narrow size distribution, random orientation and form a compact material
➢ In the analysis, the consideration of a plane wave and without pump depletion is valid if the an averaged is performed over the particles

The first approximation is stated to avoid tracking of the scattered light by each particle. It does not represent a necessary experimental condition as far as the total SHG signal is collected. Aramburu et al have done a detailed revision of the Kurtz-Perry method [100]. In it, it is "argued that many of the experimental works based on [this] method oversimply the technique and contain important errors": the use of an index matching liquid is seldom used in the experimental procedures, according to the revised literature, and most important, also the collection of the total SHG intensity is usually neglected, situation that naturally led to

nonreliable results. Besides, an extension to the consideration of scattering effects has also been done by Aramburu et al [100]. On the other hand, the second approximation is hardly satisfied by the synthesized materials in this investigation.

The averaged coherence length of a not phase-matchable material is defined as [181]:

$$\langle L_c \rangle = \langle \frac{\lambda_\omega}{4(n_{2\omega} - n_\omega)} \rangle$$

Eq. I-35

where $n_{2\omega}$ and n_ω are the refractive indexes of the material for the second harmonic and fundamental waves, respectively. The brackets represent an average over the particles with averaged size $\langle r \rangle$. Thus, if the SHG takes place in efficient way only over a distance $\langle L_c \rangle$ of the material, $\langle r \rangle \gg \langle L_c \rangle$ would then imply that there exists no correlation between the second harmonic waves arising from different particles [181]. Kurtz and Perry considered the net effect of each single particle (summation on the SHG intensities coming from every particle) and that of the random orientation (average of the nonlinear coefficient d over the spherical angles (φ, θ)), relating in this way the total SHG intensity in terms of a set of intrinsic parameters of the (not phase matchable) material itself [97, 181]:

$$I_{(2\omega)} \, \alpha \colon \langle d^2 \rangle L \langle L_c \rangle \frac{\langle L_c \rangle}{\langle r \rangle} \qquad (\langle r \rangle \gg \langle L_c \rangle)$$

$$I_{(2\omega)} \, \alpha \colon \langle d^2 \rangle \frac{L}{\langle L_c \rangle} \frac{r}{\langle L_c \rangle} \qquad (\langle r \rangle \ll \langle L_c \rangle)$$

Eq. I-36

where L is the sample thickness. The description for phase-matchable materials follows a similar analysis. Both behaviors or tendencies are shown in Fig. I-20. Phase-matchable materials tend to saturate regarding its SHG intensity for a given ratio $\langle r \rangle / \langle L_c \rangle$. On the other hand, not phase-matchable materials are characterized for presenting a maximum on the SHG intensity for a ratio close to 1.
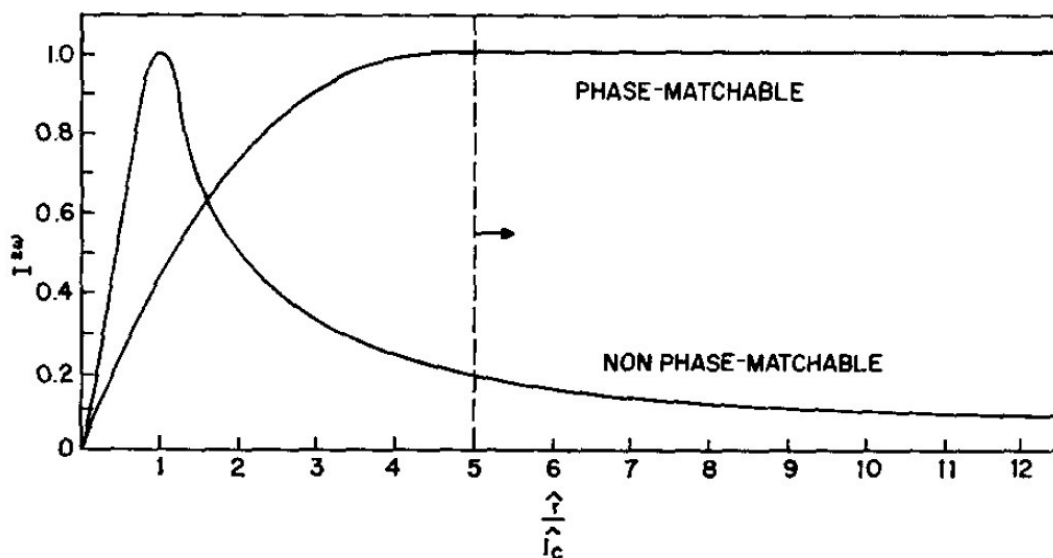
Figure I-20. Normalized SHG intensity showing the characteristic trends of two main categories of nonlinear powders in terms of the averaged particle size $\langle r \rangle$ and the averaged coherence length $\langle L_c \rangle$. *As reported by Kurtz and Perry in [97]; © AIP Publishing, 1968.*

References

Introduction

[1] Sánchez-Dena, O.; Villagómez, C.J.; Fierro-Ruíz, C.D.; Padilla-Robles, A.S.; Farías, R.; Vigueras-Santiago, E.; Hernández-López, S.; Reyes-Esqueda, J.A. Determination of the Chemical Composition of Lithium Niobate Powders. *Crystals* **2019**, 9, 340; DOI:10.3390/cryst9070340.

[2] Sánchez-Dena, O.; […] Reyes-Esqueda, J.A.; Brevet, P.F. *To be published* (2020).

[3] Luo, R.; Jiang H.; Rogers, S.; Liang, H.; He, Y.; Lin, Q. On-chip second-harmonic generation and broadband parametric down-conversion in a lithium niobate microresonator. *Opt. Exp.* **2017**, 25, 24531-24539; DOI:10.1364/OE.25.024531

[4] Pang, C.; Li, R.; Li, Z.; Dong, N.; Cheng, C.; Nie, W.; Böttger, R.; Zhou, S.; Wang, J.; Chen, F. Lithium Niobate Crystal with Embedded Au Nanoparticles: A New Saturable Absorber for Efficient Mode-Locking of Ultrafast Laser Pulses at 1μm. *Adv. Opt. Mater.* **2018**, 6, 180035; DOI:10.1002/adom.201800357.

[5] Weis, R.S.; Gayklord, T.K. Lithium Niobate: Summary of Physical Properties and Crystal Structure. *Appl. Phys. A* **1985**, *37*, 191-203; DOI:10.1007/BF00614817.

[6] Volk, T.; Wöhlecke, M. Introduction. In *Springer Series in Materials Science 115. Lithium Niobate. Defects, Photorefraction and Ferroelectric Switching,* 1rst ed.; Hull R., Osgood Jr. R. M., Parisi J., Warlimont H., Eds.; Springer: Berlin/Heidelberg, Germany, 2009; Volume 115, pp. 9-50, ISBN 978-3-540-70765-3.

[7] Abrahams, S.C.; Reddy, J.M.; Bernstein, J.L. Ferroelectric Lithium Niobate. 3. Single crystal X-ray diffraction study at 24 °C. *J. Chem. Phys. Solids* **1966**, 27, 971–1012; DOI:10.1016/0022-3697(66)90072-2.

[8] Cudney, R.S.; Ríos, L.A.; Orozco-Arellanes, M.J.; Alonso, F.; Fonseca, J. Fabricación de niobato de litio periódicamente polarizado para óptica no lineal. *Revista Mexicana de Física* **2002**, 48, 548-555.

[9] Räuber, A. CHEMISTRY AND PHYSICS OF LITHIUM NIOBATE. In *Current Topics in Materials Science,* 1st ed.; Kaldis E., Ed.; North-Holland: Amsterdam, Netherlands, 1978; Volume 1, p. 481-601, ISBN North-Holland 0 7204 0708 7.

[10] Zachariasen, F.W.H. Skr. Nor. Vidensk.-Akad. *[Kl.] 1: Mat. Naturv-idensk. Kl* **1928**, 4, 1.

[11] Lima-de-Faria, J. *Structural Mineralogy. An Introduction*, 1st. ed.; Springer Science+Business Media: Dordrecht, UK, 1994, DOI:10.1007/978-94-015-8392-3.

[12] Sumets, M.P.; Dybob, V.A.; Ievlev, V.M. LiNbO3 Films: Potential Application, Synthesis Techniques, Structure, Properties. *Inorg. Mater.* **2017**, 53, 1361-1377; DOI:10.1134/S0020168517130015.

[13] crystals: Special Issue "Recent Progress in Lithium Niobate," Special Issue Information (Guest Editors: Robert A. Jackson and Zsuzsanna Szaller). Available online: https://www.mdpi.com/journal/crystals/special_issues/Lithium_Niobate (accessed on 02 July 2019).

[14] Matthias, B.T.; Remeika, J.P. Ferroelectricity in the Ilmenite Structure. *Phys. Rev.* **1949**, 76, 1886-1887; DOI:10.1103/PhysRev.76.1886.2.

[15] Nassau, K. Early History of Lithium Niobate: Personal Reminiscences. In *Proc. SPIE 0460*, Proceedings of the Processing of Guided Wave Optoelectronic Materials I, Los Angeles Technical Symposium, United States, 26 September 1984, Holman R.L., Smyth D.M., Eds.; SPIE Digital Library; 2-5; DOI:10.1117/12.939449.

[16] Ballman, A. A. Growth of Piezoelectric and Ferroelectric Materials by the Czochralski Technique. *J. Am. Ceram. Soc.* **1965**, 48, 112-113. DOI:10.1111/j.1151-2916.1965.tb11814.x.

[17] Fedulov, S.A.; Shapiro, Z.I.; Ladyzhenskii, P. B. *Kristallografiya* **1965**, 10, 268.

[18] Nassau, K.; Levinstein, H.J.; Loiacono, G.M. Ferroelectric Lithium Niobate. 1. Growth, domain structure, dislocations and etching. *J. Chem. Phys. Solids* **1966**, 27, 839–888; DOI:10.1016/0022-3697(66)90070-9.

[19] Nassau, K.; Levinstein, H.J.; Loiacono, G.M. Ferroelectric Lithium Niobate. 2. Preparation of single domain crystals. *J. Chem. Phys. Solids* **1966**, 27, 989–996; DOI:10.1016/0022-3697(66)90071-0.

[20] Abrahams, S.C.; Hamilton, W.C.; Reddy, J.M. Ferroelectric Lithium Niobate. 4. Single crystal neutron diffraction study at 24 °C. *J. Chem. Phys. Solids* **1966**, 27, 1013–1018; DOI:10.1016/0022-3697(66)90073-4.

[21] Abrahams, S.C.; Levinstein, H.J.; Reddy, J.M. Ferroelectric Lithium Niobate. 5. Polycrystal X-ray diffraction study between 24 °C and 1200 °C. *J. Chem. Phys. Solids* **1966**, 27, 1019–1026; DOI:10.1016/0022-3697(66)90074-6.

[22] Arizmendi, L. Photonic applications of lithium niobate crystals. *Phys. Status Solidi (a)* **2004**, 201, 253–283; DOI:10.1002/pssa.200303911.

[23] Peach, R.C.; Craig, D.; Lewis, M.F.; West, C.L.; Morgan, D.F.; Fedorov, V.A.; Korkishko, Y.N.; Ciplys, D.; Remeika, R.; Hinkov, V. Acoustic wave propagation and properties. In *EMIS Datareviews Series. Properties of Lithium Niobate*, 1st ed.; Wong, K.K., Northstar Photonics Inc. USA, Eds.; The Institution of Electrical Engineers (INSPEC): London, UK, 2002; Volume 28, pp. 213–270, ISBN 0-85296-799-3.

[24] Sánchez-Dena, O.; García-Ramírez, E.V.; Fierro-Ruiz, C.D.; Vigueras-Santiago, E.; Farías, R.; Reyes-Esqueda, J.A. Effect of size and composition on the second harmonic generation from lithium niobate powders at different excitation wavelengths. *Mater. Res. Express* **2017**, 4, 035022; DOI:10.1088/2053-1591/aa62e5.

[25] Bartasyte, A.; Margueron, S.; Baron, T.; Oliveri, S.; Boulet, P. Toward Hight-Quality Epitaxial LiNbO₃ and LiTaO₃ Thin Films for Acoustic and Optical Applications. *Adv. Mater. Interfaces* **2017**, 4, 1600998; DOI:10.1002/admi.201600998.

[26] Harvard John A. Paulson School of Engineering and Applied Sciences, "Now entering, lithium niobate valley: Researcher demonstrate high-quality optical microstructures using lithium niobate" by Leah Burrows. Available online: https://www.seas.harvard.edu/news/2017/12/now-entering-lithium-niobate-valley (accessed on 02 July 2019).

[27] Zhang, M.; Wang, C.; Cheng, R.; Shams-Ansari, A.; Loncar, M. Monolithic ultra-high-Q lithium niobate microring resonator. *Optica* **2017**, 4, 1536-1537; DOI:10.1364/OPTICA.4.001536.

[28] Desiatov, B.; Shams-Ansari, A.; Zhang, M; Loncar, M. Ultra-low-loss integrated visible photonics using thin-film lithium niobate. *Optica* **2019**, 6, 380-384; DOI:10.1364/OPTICA.6.000380.

[29] Villafuerte-Castrejón, M.E.; García, J.A.; Cisneros, E.; Valenzuela, R.; West, A.R. PHASE-EQUILIBRIA IN THE SYSTEMS Li₂TiO₃-LiNbO₃, Li₂TiO₃-LiTaO₃ AND Li₂TiO₃-LiNbO₃-LiTaO₃. *Trans. J. Brit. Ceram. Soc.* **1984**, 83, 143-145.

[30] Volk, T.; Wöhlecke, M. Point defects in LiNbO3. In *Springer Series in Materials Science 115. Lithium Niobate. Defects, Photorefraction and Ferroelectric Switching*, 1st ed.; Hull, R., Osgood, R.M., Jr., Parisi, J.,Warlimont, H., Eds.; Springer: Berlin/Heidelberg, Germany, 2009; Volume 115, pp. 9–50, ISBN 978-3-540-70765-3.

[31] Schirmer, O.F.; Thiemann, O.; Wöhlecke, M. Defects in LiNbO₃—I. Experimental aspects. *J. Phys. Chem. Solids* **1991**, 52, 185–200; DOI:10.1016/022-3697(91)90064-7.

[32] Malovichko, G.; Grachev, V.; Schirmer, O. Interrelation of intrinsic and extrinsic defects—Congruent, stoichiometric and regularly ordered lithium niobate. *Appl. Phys. B* **1999**, 68, 785–793; DOI:10.1007/s003400050705.

[33] Kovács, L.; Kocksor, L.; Szaller, Z.; Hajdara, I.; Dravecz, G.; Lengyel, K.; Corradi, G. Lattice site of rare-earth ions in stoichiometric lithium niobate probed by OH$^-$ vibrational spectroscopy. *Crystals* **2017**, 7, 230; DOI:10.3390/cryst7080230.

[34] Kang, X,; Liang, L.; Song, W.; Wang, F.; Sang, Y.; Liu, H. Formation mechanism and elimination methods for anti-site defects in $LiNbO_3$/$LiTaO_3$ crystals. *CrystEngComm* **2016**, 18, 8136-8146; DOI:10.1039/C6CE01306F.

[35] Kitamura, K.; Yamamoto, J.K.; Iyi, N.; Kirnura, S.; Hayashi, T. Stoichiometric $LiNbO_3$ single crystal growth by double crucible Czochralski method using automatic powder supply system. *J. Cryst. Growth* **1992**, 116, 327-332; DOI:10.1016/0022-0248(92)90640-5.

[36] Malovichko, G.I.; Grachev, V.G.; Yurchenko, L.P.; Proshko, V.Ya.; Kokanyan, E.P.; Gabrielyan, V.T. Improvement of $LiNbO_3$ Microstructure by Crystal Growth with Potassium. *Phys. Stat. Solidi (a)* **1992**, 133, K29; DOI:10.1002/pssa.2211330124.

[37] Bordui, P.F.; Norwood, R.G.; Jundt, D.H.; Fejer, M.M. Preparation and characterization of off-congruent lithium niobate crystals. *J. Appl. Phys.* **1992**, 71, 875-879; DOI:10.1063/1.351308.

[38] MTI Corporation, LiNbO3 & Doped. Available online: http://www.mtixtl.com/linbo3.aspx (accessed on 02 July 2019).

[39] Hatano, H.; Liu, Y.; Kitamura, K. Growth and Photorefractive Properties of Stoichiometric $LiNbO_3$ and $LiTaO_3$. In *Photorefractive Materials and Their Applications 2,* 1rst ed.; Günter, P., Huignard, J. P., Eds.; Springer Series in Optical Series: New York, USA, 2007, pp. 127-164.

[40] Bartasyte, A.; Plausinaitiene, V.; Abrutis, A.; Stanionyte, S.; Margueron, S.; Boulet, P.; Kobata, T.; Uesu, Y.; Gleize, J. Identification of $LiNbO_3$, $LiNb_3O_8$ and Li_3NbO_4 phases in thin films synthesized with different deposition techniques by means of XRD and Raman Spectroscopy. *J. Phys.: Condens. Matter* **2013**, 25, 205901; DOI:10.1088/0953-8984/25/20/205901.

[41] O'Bryan, H.M.; Gallagher, P. K.; Brandle, C. D. Congruent Composition and Li-Rich Phase Boundary of $LiNbO_3$. *J. Am. Ceram. Soc.* **1985**, 68, 493-496. DOI:10.1111/j.1151-2916.1985.tb15816.x.

[42] Grabmaier, B.C.; Otto, F. Growth and investigation of MgO-doped $LiNbO_3$. *J. Cryst. Growth* **1986**, 79, 682-688; DOI:10.1016/0022-0248(86)90537-3.

[43] Iyi, N.; Kitamura, K.; Izumi, F.; Yamamoto, J.K.; Hayashi, T.; Asano, H.; Kimura, S. Comparative of defect structures in lithium niobate with different compositions. *J. Soild State Chem.* **1992**, 101, 340-352; DOI:10.1016/0022-4596(92)90189-3.

[44] Furukawa, Y.; Sato, M.; Kitamura, K.; Yajima, Y.; Minakata, M. Optical damage resistance and cristal quality of LiNbO3 single crystals with various [Li]/[Nb] ratios. *J. Appl. Phys.* **1992**, 72, 3250-3254; DOI:10.1063/1.351444.

[45] Wöhlecke, M.; Corradi, G.; Betzler, K. Optical methods to characterise the composition and homogeneity of lithium niobate single crystals. *Appl. Phys. B* **1996**, 63, 323-330. DOI:10.1007/BF01828734.

[46] Schlarb, U.; Klauer, S.; Wesselmann, M.; Betzler, K.; Wöhlecke M. Determination of the Li/Nb ratio in Lithium Niobate by Means of Birefringence and Raman Measurements. *Appl. Phys. A* **1993**, 56, 311-315. DOI:10.1007/BF00324348.

[47] Malovichko, G. I.; Grachev, V. G.; Kokanyan, E. P.; Schirmer, O. F.; Betzler, K.; Gather, B.; Jermann, F.; Klauer, S.; Schlarb, U.; Wöhlecke, M. Characterization of stoichiometric $LiNbO_3$ grown from melts containing K_2O. *Appl. Phys. A: Mater. Sci. Process.* **1993**, 56, 103-108. DOI:10.1007/BF00517674.

[48] Pardo, L.; Ricote, J. Preface. In *Springer Series in Materials Science 140. Multifunctional Polycrystalline Ferroelectric Materials: Processing and Properties,* 1rst ed.; Hull R., Osgood Jr. R. M., Parisi J., Warlimont H., Pardo L., Ricote J., Eds.; Springer: Berlin/Heidelberg, Germany, 2011; Volume 140, pp. v-vii, ISBN 978-90-481-2874-7.

[49] Földvári, I.; Polgár, K.; Voszka, R.; Balasanyan, R.N. A simple method to determine the real composition of $LiNbO_3$ crystals. *Cryst. Res. Techn.* **1984**, 19, 1659-1661; DOI:10.1002/crat.2170191231.

[50] Kovács, L. Ruschhaupt, G.; Polgár, K.; Corradi, G.; Wöhlecke, M. Composition dependence of the ultraviolet absorption edge in lithium niobate. *Appl. Phys. Lett.* **1997**, 70, 2801-2803; DOI:10.1063/1.119056.

[51] Schlarb, U.; Betzler, K. Refractive indices of lithium niobate as a function of temperature, wavelength, and composition: A generalized fit. *Phys. Rev. B* **1993**, 48, 15613-15620; DOI:10.1103/PhysRevB.48.15613.

[52] Byer, R.L.; Young, J.F.; Feigelson, R.S. Growth of High-Quality $LiNbO_3$ Crystals from the Congruent Melt. *J. Appl. Phys.* **1970**, 41, 2320-2325; DOI:10.1063/1.1659225.

[53] Luh, Y.S.; Fejer, M.M.; Byer, R.L.; Feigelson, R.S. Stoichiometric LiNbO₃ single-crystal fibers for nonlinear optical applications. *J.Cryst. Growth* **1987**, 85, 264-269; DOI:10.1016/0022-0248(87)90233-8.

[54] Jundt, D.H.; Fejer, M.M.; Byer, R.L. Optical properties of lithium-rich lithium niobate fabricated by vapor transport equilibration. *IEEE J. Quant. Electron.* **1990**, 26, 135-138; DOI:10.1109/3.44926.

[55] Schmidt, N.; Betzler, K.; Grabmaier, B.C. Composition dependence of the second-harmonic phase-matching temperature in LiNbO₃. *Appl. Phys. Lett.* **1991**, 58, 34-35; DOI:10.1063/1.105216.

[56] Reichert, A.; Betzler, K. Characterization of electrooptic crystals by non-collinear frequency doubling. *Ferroelectrics* **1992**, 126, 9-14; DOI:10.1080/00150199208227027.

[57] Arizmendi, L. Simple holographic method for determination of Li/Nb ratio and homogeneity of LiNbO₃ crystals. *J. Appl. Phys.* **1988**, 64, 4654-4656; DOI:10.1063/1.341246.

[58] Carruthers, J.R.; Peterson, G.E.; Grasso, M.; Bridenbaugh, P.M. Nonstoichiometry and Crystal Growth of Lithium Niobate. *J. Appl. Phys.* **1971**, 42, 1846-1851; DOI:10.1063/1.1660455.

[59] Zotov, N.; Boysen, H.; Frey, F.; Metzger, T.; Born, E. CATION SUBSTITUTION MODELS OF CONGRUENT LiNbO₃ INVESTIGATED BY X-RAY AND NEUTRON POWDER DIFFRACTION. *J. Phys. Chem. Solids* **1994**, 55, 145-152; DOI:10.1016/0022-3697(94)90071-X.

[60] Lerner, P.; Legras, C.; Dumas, J.P. STOECHIOMÉTIE DES MONOCRISTAUX DE MÉTANIOBATE DE LITHIUM. *J. Cryst. Growth* **1968**, 3, 231-235; DOI:10.1016/0022-0248(68)90139-5.

[61] Abrahams, S.C.; Marsh, P. Defect Structure Dependence on Composition in Lithium Niobate. *Acta Cryst.* **1986**, B42, 61-68; DOI:10.1107/S0108768186098567.

[62] Kovács, L.; Polgár, K. Density Measurements on LiNbO₃ Crystals Confirming Nb Substitution for Li. *Cryst. Res. Techn.* **1986**, 21, K101-K104; DOI:10.1002/crat.2170210629.

[63] Peterson, G.E.; Carruthers, J.R. ⁹³Nb NMR as a sensitive and accurate probe of stoichiometry in LiNbO₃ crystals. *J. Solid State Chem.* **1969**, 1, 98-99; DOI:10.1016/0022-4596(69)90013-9.

[64] Malovichko, G.I.; Grachev, V.G.; Schirmer, O.F. The effect of iron ions on the defect structure of lithium niobate crystals grown from K₂O containing melts. *Solid State Commun.* **1994**, 89, 195-198; DOI:10.1016/0038-1098(94)90681-5.

[65] Yamada, K.; Takemura, H.; Inoue, Y.; Omi, T.; Matsumura, S. Effect of Li/Nb Ratio on the SAW Velocity of 128°Y-X LiNbO₃ Wafers. *Jpn. J. Appl. Phys.* **1987**, 26, 219-222; DOI:10.7567/JJAPS.26S2.219.

[66] Kushibiki, J.; Takahashi, H.; Kobayashi, T.; Chubachi, N. Characterization of LiNbO₃ crystals by line-focus-beam acoustic microscopy. *Appl. Phys. Lett.* **1991**, 58, 2622-2624; DOI:10.1063/1.104813.

[67] Kocsor, L.; Péter, L.; Corradi, G.; Kis, Z.; Gubicza, J.; Kovács, L. Mechanochemical reactions of Lithium Niobate Induced by High-Energy Ball-Milling. *Crystals* **2019**, 9, 334; DOI:10.3390/cryst9070334.

[68] Kong, L. B.; Chang, T. S.; Ma, J.; Boey, F. Progress in synthesis of ferroelectric ceramic materials via high-energy mechanochemical technique. *Prog. Mater. Sci.* **2008**, 53, 207-322. DOI:10.1016/j.pmatsci.2007.05.001.

[69] Suryanarayana, C. Mechanical alloying and milling. *Prog. Mater. Sci.* **2001**, 46, 1-184. DOI:10.1016/S0079-6425(99)00010-9.

[70] Bretos, I.; Lourdes-Calzada, M. Chapter 5. Approaches Towards the Minimisation of Toxicity in Chemical Solution Deposition Processes of Lead-Based Ferroelectric Thin Films. In *Springer Series in Materials Science 140. Multifunctional Polycrystalline Ferroelectric Materials: Processing and Properties,* 1st ed.; Hull R., Osgood Jr. R. M., Parisi J., Warlimont H., Pardo L., Ricote J., Eds.; Springer: Berlin/Heidelberg, Germany, 2011; Volume 140, pp. 145-216, ISBN 978-90-481-2874-7.

[71] Galassi, C. Chapter 1. Advances in Processing of Bulk Ferroelectric Materials. In *Springer Series in Materials Science 140. Multifunctional Polycrystalline Ferroelectric Materials: Processing and Properties,* 1rst ed.; Hull R., Osgood Jr. R. M., Parisi J., Warlimont H., Pardo L., Ricote J., Eds.; Springer: Berlin/Heidelberg, Germany, 2011; Volume 140, pp. 1-37, ISBN 978-90-481-2874-7.

[72] Shrout, T.R.; Zhang, S.J. Lead-free piezoelectric ceramics: Alternatives for PZT? *J. Electroceram.* **2007**, 19, 111-124; DOI:10.1007/s10832-007-9047-0.

[73] Reznichenko, L.A.; Verbenko, I.A.; Shilkina, L.A.; Pavlenko, A.V.; Dudkina, S.I.; Andryushina, I.N.; Andryushin, K.P.; Abubakarov, A.G.; Krasnyakova, T.V. Chapter 1. Binary, Ternary and Four-Component Systems Based on Sodium Niobate: Phase Diagrams of States, the Role of the Number of Components and Defectiveness in the Formation of the Properties. In *Springer Proceedings in Physics 207. Advanced Materials: Proceedings of the International Conference on "Physics and Mechanics of New Materials and Their Applications", PHENMA 2017,* 1rst ed.; Parinov I.A., Chang, S.H., Gupta, V.K., Eds.; Springer International Publishing AG, part of Springer Nature: Switzerland, 2018; Volume 207, pp. 3-23, ISBN 978-3-319-78918-7.

[74] Nath, R. K.; Zain, M. F. M.; Kadhum, A. A. H. Artificial Photosynthesis using LiNbO$_3$ as Photocatalyst for Sustainable and Environmental Friendly Construction and Reduction of Global Warming: A Review. *Catal. Rev.: Sci. Eng.* **2013**, 56, 175-186. DOI:10.1080/01614940.2013.872013.

[75] Yang, W. C.; Rodriguez, B. J.; Gruverman, A.; Nemanich, R. J. Polarization-dependent electron affinity of LiNbO$_3$ surfaces. *Appl. Phys. Lett.* **2004**, 85, 2316-2318. DOI:10.1063/1.1790604.

[76] Fierro-Ruíz, C.D.; Sánchez-Dena, O.; Cabral-Larquier, E.M.; Elizalde-Galindo, J.T.; Farías, R. Structural and Magnetic Behavior of Oxidized and Reduced Fe Doped LiNbO$_3$ Powders. *Crystals*, **2018**, 8, 108. DOI:10.3390/cryst8030108.

[77] Kudinova, M.; Humbert, G.; Auguste, J. L.; Delaizir, G. Multimaterial polarization maintaining optical fibers fabricated with powder-in-tube technology. *Opt. Mater. Express* **2017**, 10, 3780-3790. DOI:10.1364/OME.7.003780.

[78] Skipetrov, S.E. Disorder is the new order. *Nature* **2004**, 432, 285-286; DOI:10.1038/432285a.

[79] Hollis, D.B. Review of hyper-Rayleigh and second-harmonic scattering in minerals and other inorganic solids. *Am. Mineral.* **1988**, 73, 701-706.

[80] Boyd, R. W. *Nonlinear Optics*, 3rd. ed.; Academic Press: San Francisco, USA, 2008, ISBN 978-0-12-369470-6.

[81] Midwinter, J.E.; Warner, J. The effects of phase matching method and of uniaxial crystal symmetry on the polar distribution of second-order non-linear optical polarization. *Br. J. Appl. Phys.* **1965**, 16, 1135-1142; DOI:10.1088/0508-3443/16/8/312.

[82] Fejer, M.M.; Magel, G.A.; Jundt, D.H.; Byer, R.L. Quasi-phase-matched second harmonic generation: tuning and tolerances. *IEEE J. Quantum Electron.* **1992**, 28, 2631-2654; DOI:10.1109/3.161322.

[83] Franken P.A.; Hill, A.E.; Peters, C.W.; Weinreich, G. Generation of Optical Harmonics. *Phys. Rev. Lett.* **1961**, 7, 118-119; DOI:10.1103/PhysRevLett.7.118.

[84] Maiman, T.H. Stimulated Optical Radiation in Ruby. *Nature* **1960**, 493-494; DOI:10.1038/187493a0.

[85] Dempsey, W.P.; Fraser, S.E.; Pantazis, P. SHG nanoprobes: Advancing harmonic imaging in biology. *BioEssays* **2012**, 34, 351-360; DOI: 10.1002/bies.201100106.

[86] Brevet, P.F. *Surface Second Harmonic Generation*, Presses polytechniques et universitaires romandes: France, 1997, ISBN 2-88074-345-1.

[87] Verbiest, T.; Clays, K.; Rodriguez, V. *Second-Order Nonlinear Optical Characterization Techniques: An Introduction*, CRC Press Taylor & Francis Group: Boca Raton, Florida, USA, 2009, ISBN 978-1-4200-7071-2

[88] Nordlander, J.; De Luca, G.; Strkalj, N.; Fiebig, M.; Trassin, M. Probing Ferroic States in Oxide Thin Films Using Optical Second Harmonic Generation. *Appl. Sci.* **2018**, 8, 570; DOI:10.3390/app8040570.

[89] Rogov, A.; Mugnier, Y. Bonacina, L. Harmonic nanoparticles: noncentrosymmetric metallic oxides for nonlinear optics. *J. Opt.* **2015**, 17, 033001; DOI:10.1088/2040-8978/17/3/033001.

[90] Nappa, J.; Revillod, G.; Russier-Antoine, I.; Benichou, E.; Jonin, C.; Brevet, P.F. Electric dipole origin of the second harmonic generation of small metallic particles. *Phys. Rev. B* **2005**, 71, 165407; DOI:10.1103/PhysRevB.71.165407.

[91] Russier-Antoine, I.; Lee, H.J.; Wark, A.W.; Butet, J.; Benichou, E.; Joinin, C.; Martin, O.J.F.; Brevet, P.F. Second Harmonic Scattering from Silver Nanocubes. *J. Phys. Chem. C* **2018**, 122, 17447-17455; DOI:10.1021/acs.jpcc.8b04299.

[92] Khebbache, N.; Maurice, A.; Djabi, S.; Russiere-Antoine, I.; Jonin, C.; Skipetrov, S.E.; Brevet, P.F. Second-Harmonic Scattering from Metallic Nanoparticles in a Random Medium. *ACS Photonics* **2017**, 4, 262-267; DOI:10.1021/acsphotonics.6b00520.

[93] van der Veen, M.A.; Vermoortele, F.; De Vos, D.E.; Verbiest, T. Point Group Symmetry Determination via Observables Revealed by Polarized Second-Harmonic Generation Microscopy: (1) Theory. *Anal. Chem.* **2012**, 84, 6378-6385; DOI:10.1021/ac300936q.

[94] Knabe, B.; Buse, K.; Assenmacher, W.; Mader, W. Spontaneous polarization in ultrasmall lithium niobate nanocrystals revealed by second harmonic generation. *Phys. Rev. B* **2012**, 86, 195428; DOI:10.1103/PhysRevB.86.195428.

[95] Chowdhury, A.U.; Zhang, S.; Simpson, J. Powders Analysis by Second Harmonic Generation Microscopy. *Anal. Chem.* **2016**, 88, 3853-3863; DOI:10.1021/acs.analchem.5b04942.

[96] Wanapun, D.; Kestur, U.S.; Taylor, L.S. Simpson, G.J. Single Particle Nonlinear Optical Imaging of Trace Crystallinity in an Organic Powder. *Anal. Chem.* **2011**, 83, 4745-4751; DOI:10.1021/ac1031397.

[97] Kurtz, S.K.; Perry, T.T. A Powder Technique for the Evaluation of Nonlinear Optical Materials. *J. Appl. Phys.* **1968**, 39, 3798-3813; DOI:10.1063/1.1656857.

[98] vand der Mark, M.B.; van Albada, M.P.; Lagendijk, A. Light scattering in strongly scattering media: Multiple scattering and weak localization. *Phys. Rev. B* **1988**, 3575-3592; DOI:10.1103/PhysRevB.37.3575.

[99] Aegerter, C.M.; Maret, G. Chapter 1. Coherent Backscattering and Anderson Localization. In *Progress in Optics,* 1st ed.; Wolf, E., Ed.; Elsevier B.V.: 2009, Volume 52, pp. 1-62, ISSN 0079-6638, DOI:10.1016/S0079-6638(08)00003-6.

[100] Aramburu, J.; Ortega, J.; Folcia, C.L.; Etxebarria, J. Second harmonic generation by micropowders: a revision of the Kurtz-Perry method and its practical application. *Appl. Phys. B* **2014**, 116, 211-233; DOI:10.1007/s00340-013-5678-9.

[101] Kratsov, V.E.; Agranovich, V.M.; Grigorishin, K.I. Theory of second-harmonic generation in strongly scattering media. *Phys. Rev. B* **1991**, 44, 4931-4942; DOI:10.1103/PhysRevB.44.4931.

[102] Zhang, X.; Li, J.; Shi, F.; Xu, Y.; Wang, Z.; Rupp, R.A.; Xu, J. Light-controllable coherent backscattering from water suspension of lithium niobate microcrystalline particles. *Opt. Lett.* **2010**, 35, 1746-1748; DOI:10.1364/OL.35.001746.

[103] Lherminier, S.; Planet, R.; Levi dit Vehel, V.; Simon, G.; Vanel, L.; Måløy, K.J.; Ramos, O. Continuously Sheared Granular Matter Reproduces in Detail Seismicity Laws. *Phys. Rev. Lett* **2019**, 122, 218501; DOI:10.1103/PhysRevLett.122.218501.

[104] Boyd, G.D.; Miller, R. C.; Nassau, K.; Bond, W.L.; Savage, A. LiNbO₃: AN EFFICIENT PHASE MATACHABLE NONLINEAR OPTICAL MATERIAL. *Appl. Phys. Lett.* **1964**, 5, 234-236; DOI:10.1063/1.1723604.

Chapter 1

[105] Junquera, J.; Ghosez, P. Critical thickness for ferroelectricity in perovskite ultrathin films. *Nature* **2003**, 422, 506-509; DOI:10.1038/nature01501.

[106] Binder, K. Finite size effects on phase transitions. *Ferroelectrics* **1987**, 73, 43-67; DOI:10.1080/00150198708227908.

[107] Sanna S.; Schmidt, W. G. Lithium niobate X-cut, Y-cut, and Z-cut surfaces from *ab initio* theory. *Phys. Rev. B* **2010**, 81, 214116; DOI:10.1103/PhysRevB.81.214116.

[108] Megaw, H.D. Ferroelectricity and Crystal Structure. II. *Acta Cryst.* **1954**, 7, 187-194; DOI:10.1107/S0365110X54000527.

[109] Megaw, H.D. *Ferroelectricity in Crystals,* 1st ed.; Methuen: London, 1957.

[110] Megaw, H.D. A Note on the Structure of Lithium Niobate, LiNbO₃. *Acta. Cryst.* **1968**, A24, 583-588; DOI:10.1107/S0567739468001282.

[111] Gopalan, V.; Dierolf, V.; Scrymgeour, D.A. Defect-Domain Wall Interactions in Trigonal Ferroelectrics. *Annu. Rev. Mater. Res.* **2007**, 37, 449-489; DOI:10.1146/annurev.matsci.37.052506.084247.

[112] Peterson, G.E.; Carnevale, A. 93Nb NMR Linewidths in Nonstoichiometric Lithium Niobate. *J. Chem. Phys.* **1972**, 56, 4848-4851; DOI:10.1063/1.1676960.

[113] Wilkinson, A.P.; Cheetham, A.K.; Jarman, R.H. The defect structure of congruently melting lithium niobate. *J. Appl. Phys.* **1998**, 74, 3080-3083; DOI:10.1063/1.354572.

[114] Fay, H.; Alford, W.J.; Dess, H.M. DEPENDENCE OF SECOND-HARMONIC PHASE-MATCHING TEMPERATURE IN LiNbO₃ CRYSTALS ON MELT COMPOSITION. *Appl. Phys. Lett.* **1968**, 12, 89-92, DOI:10.1063/1.1651911.

[115] DeLeo, G.G.; Dobson, J.L.; Masters, M.F.; Bonjack, L.H. Electronic structure of an oxygen vacancy in lithium niobate. *Phys. Rev. B* **1988**, 37, 8394-8400; DOI:10.1103/PhysRevB.37.8394.

[116] Ye, N.; Wang, J.-Y.; Boughton, R.I.; Hong, M.-C. Chapter 20. Functional Crystals. In *Modern Inorganic Synthethic Chemistry*, 2nd ed.; Xu R., Xu Y., Eds.; Elsevier B. V.: Amsterdam, Netherlands, 2017; p. 575-611, ISBN 978-0-444-63591-4.

[117] Shannon, R.D.; Prewitt, C.T. Effective Ionic Radii in Oxides and Flourides. *Acta Cryst.* **1969**, B25, 925-946; DOI:10.1107/S0567740869003220.

[118] Blumel, J.; Born, E.; Metzger, Th. Solid State NMR study supporting the lithium vacancy defect model in congruent lithium niobate. *J. Phys. Chem. Solids* **1994**, 55, 589-593; DOI:10.1016/0022-3697(94)90057-4.

[119] Donnerberg, H.; Tomlinson, S.M.; Catlow, C.R.A; Schirmer, O.F. Computer-simulation studies of intrinsic defects in LiNbO₃ crystals. *Phys. Rev. Lett.* **1989**, 40, 11909-11916; DOI:10.1103/PhysRevB.40.11909.

[120] Safaryan, F.P.; Feigelson, R.S.; Petrosyan, A.M. An approach to the defect structure analysis of lithium niobate single crystals. *J. Appl. Phys.* **1999**, 85, 8079-8082; DOI:10.1063/1.370645.

[121] Abdi, F.; Fontana, M.D.; Aillerie, M.; Bourson, P. Coexistence of Li and Nb vacancies in the defect structure of pure $LiNbO_3$ and its relationship to optical properties. *Appl. Phys. A* **2006**, 83, 427-434; DOI:10.1007/s00339-006-3565-5.

[122] Li, Y.; Sanna, S.; Schmidt, W.G. Modeling intrinsic defects in $LiNbO_3$ within the Slater-Janak transition state model. *J. Chem. Phys.* **2014**, 140, 234113; DOI:10.1063/1.4883737.

[123] Boysen, H.; Altorfer, F. A Neutron Powder Investigation of the High-Temperature Structure and Phase Transition in $LiNbO_3$. *Acta Cryst.* **1994**, B50, 405-414; DOI:10.1107/S0108768193012820.

[124] Lehnert, H.; Boysen, H.; Frey, F.; Hewat, A.; Radaelli, P. A neutron powder investigation of the high-temperature structure and phase transition in stoichiometric $LiNbO_3$. *Zeitschrift für Kristallographie-Crystalline Materials* **1997**, 212, 712-719.

[125] Etschmann, B.; Ishizawa, N.; Streltsov, V.; Oishi, S. A synchrotron X-ray diffraction analysis of near-stoichiometric $LiNbO_3$. *Zeitschrift für Kristallographie-Crystalline Materials* **2001**, 216, 455-461.

[126] Kuz'minov, Yu.S.; Osiko, V.V. Nonstoichiometric composition of lithium niobate crystal. *Ferroelectrics* **1993**, 142, 105-113; DOI:10.1080/00150199308237888.

[127] Spaldin, N.A. Analogies and Differences between Ferroelectrics and Ferromagnets. In *Physics of Ferroelectrics: A Modern Perspective,* 1st ed.; Rabe K.M., Ahn C.H., Triscone J-M., Eds.; Springer-Verlag: Berlin Heidelberg, Germany, 2007, pp. 175-217, ISBN 978-3-540-34590-9.

[128] Toyoura, K.; Ohta, M.; Nakamura, A.; Matsunaga, K. First-principles study on phase transition and ferroelectricity in lithium niobate and tantalite. *J. Appl. Phys.* **2015**, 118, 064103; DOI:10.1063/1.4928461.

[129] Rabe, K.M.; Dawber, M.; Lichtensteiger, C.; Ahn, C.H.; Triscone, J-M. Modern Physics of Ferroelectrics: Essential Background. In *Physics of Ferroelectrics: A Modern Perspective,* 1st ed.; Rabe K.M., Ahn C.H., Triscone J-M., Eds.; Springer-Verlag: Berlin Heidelberg, Germany, 2007, pp. 1-30, ISBN 978-3-540-34590-9.

[130] Cochran, W. Crystal stability and the theory of ferroelectricity. *Adv. Phys.* **1960**, 9, 387-423; DOI:10.1080/00018736000101229.

[131] Sirenko, A.A.; Bernhard, C.; Golnik, A.; Clark, A.M.; Hao, J.; Si, W.; Xi, X.X. Soft-mode hardening in $SrTiO_3$ thin films. *Nature* **2000**, 404, 373-376; DOI:10.1038/35006023.

[132] Gehring, P.M.; Wakimoto, S.; Ye, Z.-G.; Shirane, G. Soft Mode Dynamics above and below the Burns Temperature in the Relaxor $Pb(Mg_{1/3}Nb_{2/3})O_3$. *Phys. Rev. Lett.* **2001**, 87, 277601; DOI:10.1103/PhysRevLett.87.277601.

[133] Jona, F.; Shirane, G. *Ferroelectric Crystals,* Dover: New York, 1993, ISBN 978-0486673868.

[134] Chandra, P.; Littlewood, P.B. A Landau Primer for Ferroelectrics. In *Physics of Ferroelectrics: A Modern Perspective,* 1st ed.; Rabe K.M., Ahn C.H., Triscone J-M., Eds.; Springer-Verlag: Berlin Heidelberg, Germany, 2007, pp. 69-115, ISBN 978-3-540-34590-9.

[135] Cohen, R.E. Origin of ferroelectricity in perovskite oxides. *Nature* **1992**, 358, 136-138; DOI:10.1038/358136a0.

[136] Megaw, H.D. Origin of ferroelectricity in barium titanate and other perovskite-type crystals. *Acta Cryst.* **1952**, 5, 739-749; DOI:10.1107/S0365110X52002069.

[137] Öpik, U. Studies of the Jahn-Teller effect. I. A survey of the static problem. *Proc. Roy. Soc. A* **1957**, 238, 425-447; DOI:10.1098/rspa.1957.0010.

[138] Halasyamani, P.S.; Poeppelmeier, K.R. Noncentrosymmetric Oxides. *Chem. Mater.* **1998**, 10, 2753-2769; DOI:10.1021/cm980140w.

[139] Bersuker, I.B. *THE JAHN-TELLER EFFECT*, Cambridge University Press: Cambridge, 2006, ISBN-13 978-0-521-82212-1.

[140] Bersuker, I.B. Modern Aspects of the Jahn-Teller Effect Theory and Applications To Molecular Problems. *Chem. Rev.* **2001**, 101, 1067-1114; DOI:10.1021/cr0004411.

[141] Burdett, J.K. Use of the Jahn-Teller theorem in inorganic chemistry. *Inrog. Chem.* **1981**, 20, 1959-1962; DOI:10.1021/ic50221a003.

[142] Bersuker, I.B. *The Jahn-Teller Effect and Vibronic Interactions in Modern Chemistry,* Springer: New York, 1984, DOI:10.1007/978-1-4613-2653-3.

[143] Atanasov, M.; Reinen, D. Density Functional Studies on the Lone Pair Effect of the Trivalent Group (V) Elements: I. Electronic Structure, Vibronic Coupling, and Chemical Criteria for the Ocurrence of Lone Pair Distortions in AX_3 Molecules (A=N to Bi; X=H, and F to I). *J. Phys. Chem. A* **2001**, 105, 5450-5467; DOI:10.1021/jp004511j.

[144] Troiler-McKinstry, S. Chapter 3. Crystal Chemistry of Piezoelectric Materials. In *Piezoelectric and Acoustic Materials for Transducer Applications,* 1st, ed.; Safari A., Koray Akdogan E., Eds.; Springer Science+Business Media, LLC: USA, 2008; p. 39-56, DOI:10.1007/978-0-387-76540-2.

[145] Woodward, P.M.; Mizoguchi, H.; Kim, Y.-I.; Stoltzfus, M.W. Chapter 6. The Electronic Structure of Metal Oxides. In *Metal Oxides: Chemistry and Applications*, 1st. ed.; Fierro J.L.G., Ed.; CRC Press Taylor & Francis Group: Boca Raton, Florida, USA, 2006, p. 133-193, ISBN 0-8247-2371-6.

[146] Muller, O.; Roy, R. *The Major Ternary Structural Families,* Springer-Verlag: Berlin Heidelberg New York, 1974.

[147] Schweiler, H.C. Ferroelectricity in the Ilmenite Structure. *Phys. Rev.* **1952**, 87, 5-11; DOI:10.1103/Phys.Rev.87.5.

[148] Range Alves, A.; dos Reis Coutinho, A. The Evolution of the Niobium Production in Brazil. *Mater. Res.* **2015**, 18, 106-112; DOI:10.1590/1516-1439.276414.

[149] Bailey, P. Thesis. Bristol: 1952 (cited in [88]).

[150] Peterson, G.E. private communication: 1965 (cited in [7]).

[151] Buerger, M.J. Derivative Crystal Structures. *J. Chem. Phys.* **1947**, 15, 1-16; DOI:10.1063/1.1746278.

[152] Buerger, M.J. The genesis of twin crystals. *Am. Mineral.* **1945**, 30, 469-482.

[153] Bärnighausen, H. GROUP-SUBGROUP RELATIONS BETWEEN SPACE GROUPS: A USEFUL TOOL IN CRYSTAL CHEMISTRY. *MATCH, Commun. Math. Chem.* **1980**, 9, 139-175.

[154] Benz, K-W.; Neumann, W. *Introduction to Crystal Growth and Characterization*, 1st. ed.; Wiley-VCH Verlag GmbH & Co.: Weinheim, Germany, 2014, ISBN 978-3-527-68436-6.

[155] Megaw, H.D. *Crystal Structures: A Working Approach*, Saunders Company: Philadelphia, USA, 1973.

[156] Barth, T.F.W; Posnjak, E. The Crystal Structure of Ilmenite. *Zeitschrift für Kristallographie-Crystalline Materials* **1934**, 88, 265-270; DOI:10.1524/zkri.1934.88.1.265.

[157] Shiozaki, Y.; Mitsui, T. Powder neutron diffraction study of LiNbO$_3$. *J. Phys. Chem. Solids* **1963**, 24, 1057-1061; DOI:10.1016/0022-3697(63)90012-X.

[158] Niizeki, N.; Yamada, T.; Toyoda, H. Growth ridges, etched hillocks, and cristal structure of lithium niobate. *Jap. J. Appl. Phys.* **1967**, 6, 318-327; DOI:10.1143/JJAP.6.318.

[159] Wilson, N.C.; Muscat, J.; Mkhonto, D.; Ngoepe, P.E.; Harrison, N.M. Structure and properties of ilmenite from first principles. *Phys. Rev. B* **2005**, 71, 075202; DOI:10.1103/PhysRevB.71.075202.

[160] Navrotsky, A. Energetics and Crystal Chemical Systematics among Ilmenite, Lithium Niobate, and Perovskite Structures. *Chem. Mater.* **1998**, 10, 2787-2793; DOI:10.1021/cm9801901.

[161] Heinrich, V. E.; Cox, P.A. *The Surface Science of Metal Oxides*, 1st ed.; Cambridge University Press: Great Britain, 1994, ISBN 0 521 56687 8.

[162] Bhalla, A.S.; Guo, R.; Roy, R. The perovskite structure—a review of its role in ceramic science and technology. *Mat. Res. Innovat.* **2000**, 4, 3-26; DOI:10.1007/s100190000062.

[163] Johnsson, M.; Lemmens, P. Crystallography and Chemistry of Perovskites. In *Handbook of Magnetism and Advanced Magnetic Materials*, Kronmüller H., Parkin S., Eds.; John Wiley & Sons: 2007; Volume 4: Novel Materials, p. 1-9, ISNB 978-0-470-02217-7.

[164] Leinenweber, K.; Utsumi, W.; Tsuchida, Y.; Yagi, T.; Kurita, K. Unquenchable high-pressure perovskite polymorphs of MnSnO$_3$ and FeTiO$_3$. *Phys. Chem. Miner.* **1991**, 18, 244-250; DOI:10.1007/BF00202576.

[165] Mehta, A.; Leinenweber, K.; Navrotsky, A.; Akaogi, M. Calorimetric study of high pressure polymorphism in FeTiO$_3$: Stability of the perovskite phase. *Phys. Chem. Miner.* **1994**, 21, 207-212; DOI:10.1007/BF00202133.

[166] Bond, W.L. Precision Lattice Constant Determination. *Acta Cryst.* **1960**, 13, 814-818; DOI:10.1107/S0365110X60001941.

[167] Pezzotti, G. Raman spectroscopy of piezoelectrics. *J. Appl. Phys.* **2013**, 113, 211301; DOI:10.1063/1.4803740.

[168] Sanna, S.; Neufeld, S.; Rüsing, M.; Berth, G.; Zrenner, A.; Schmidt, W.G. Raman Scattering efficiency in LiTaO$_3$ and LiNbO$_3$ crystals. *Phys. Rev. B* **2015**, 91, 224302; DOI:10.1103/PhysRevB.91.224302.

[169] Hermet, P.; Veithen, M.; Ghosez, Ph. First-principles calculations of the nonlinear optical susceptibilities and Raman scattering spectra of lithium niobate. *J. Phys.: Condens. Matter* **2007**, 19, 456202; DOI:10.1088/0953-8984/19/45/456202.

[170] Margueron, S.; Bartasyte, A.; Glazer, A.M.; Simon, E.; Hlinka, J.; Gregora, I.; Gleize, J. Resolved E-symmetry zone-centre phonons in LiTaO3 and LiNbO3. *J. Appl. Phys.* **2012**, 111, 104105; DOI:10.1063/1.4716001.

[171] Schaufele, R.F.; Weber, M.J. Raman Scattering by Lithium Niobate. *Phys. Rev.* **1966**, 152, 705-708; DOI:10.1103/PhysRev.152.705.

[172] Porto, S.P.S.; Krishnan, R.S. Raman Effect of Corundum. *J. Chem. Phys.* **1967**, 47, 1009-1011; DOI:10.1063/1.1711980.

[173] Horiba Scientific: Webinar: Applied Polarized Raman Spectroscopy Webinar (by David Tuschel). Available online: http://www.horiba.com/us/en/scientific/products/raman-spectroscopy/raman-academy/webinars/applied-polarized-raman-spectroscopy-webinar/ (accessed on 23 September 2019).

[174] Repelin, Y.; Husson, E.; Bennani, F.; Proust, C. Raman spectroscopy of lithium niobate and lithium tantalite. Force field calculations. *J. Phys. Chem. Solids* **1999**, 60, 819-825: DOI:10.1016/S0022-3697(98)00333-3.

[175] Thermo Fisher Scientific, Application Note: Curve Fitting in Raman and IR Spectroscopy. Available online:https://www.thermofisher.com/search/results?query=Curve%20Fitting%20in%20Raman&focusarea=Search%20All (accessed on 25 September 2019).

[176] Scott, B.A.; Burns, G. Determination of Stoichiometry Variations in LiNbO3 and LiTaO3 by Raman Powder Spectroscopy. *J. Am. Ceram. Soc.* **1972**, 55, 225-230; DOI:10.1111/j.1151-2916.1972.tb11266.x

[177] Balanevskaya, A.É.; Pyatigorskaya, L.I.; Shapiro, Z.I.; Margolin, L.N.; Bovina, E.A. DETERMINATION OF THE COMPOSITION OF LiNbO$_3$ SPECIMENS BY RAMAN SPECTROSCOPY. *J. Appl. Spectrosc.* **1983**, 38, 491-493; DOI:10.1007/BF00662367.

[178] Redfield, D.; Burke, W.J.; Optical absorption edge of LiNbO$_3$. *J. Appl. Phys.* **1974**, 45, 4566-4571; DOI:10.1063/1.1663089.

[179] Thierfelder, C.; Sanna, S.; Schindlmayr, A.; Schmidt, W.G. Do we know the band gap of lithium niobate? *Phys. Status Solidi C* **2010**, 7, 362-365; DOI:10.1002/pssc.200982473.

[180] Fox, M. *Optical Properties of Solids*, 1st ed.; Oxford University Press: New York, USA, 2001, ISBN 0-19-850612.

Chapter 2

[181] Sutherland, R.L. *Handbook of Nonlinear Optics,* 2th ed.; Marcel Dekker: New York, USA, 2003, ISBN 0-8247-9426-5.

[182] Norman P.; Ruud, K. Microscopic Theory of Nonlinear Optics. In *Non-Linear Optical Properties of Matter: From Molecules to Condensed Phases,* 1st ed.; Papadopoulos, M.G., Sadlej, A.J., Lezsczynski, J., Eds.; Springer: 2006

[183] Powers, P.E.; Haus, J.W. *Fundamentals of Nonlinear Optics,* 2nd ed.; CRC Press: Boca Raton, FL, USA, 2017, ISBN-13 978-1-4987-3683-1.

[184] Jackson, J.D. *Classical Electrodynamics,* 2nd ed.; John Wiley & Sons: New York, USA, 1975, ISBN 0-471-43132-X.

[185] Brevet, P.F. Second Harmonic Generation in Nanostructures. In *Handbook of Nanoscale Optics and Electronics,* 1st ed.; Wiederrecht G., Ed.; Elsevier B.V.: Amsterdam, Netherlands, 2010, pp. 75-105, ISBN 978-0-12-375178-2.

[186] Svelto, O. *Principles of Lasers,* 5th ed.; Springer: New York, USA, 2010, DOI:10.1007/978-1-4419-1302-9.

[187] Maker, P.D.; Terhune, R.W.; Nisenoff, M.; Savage, C.M. Effects of Dispersion and Focusing on the Production of Optical Harmonics. *Phys. Rev. Lett.* **1962**, 8, 21-23; DOI:10.1103/PhysRevLett.8.21

[188] Wood, B.D. *A NONHYDROLYTIC SOLUTION-PHASE SYNTHESIS OF LITHIUM NIOBATE NANOSTRUCTURES,* Master thesis: Simon Fraser University, Canada, 2009.

[189] Zernike, F.; Midwinter, J.E. *Applied Nonlinear Optics,* 1st ed.; Dover: New York, USA, 1973, ISBN 0-486-45360-X.

[190] Denev, S.A.; Lummen, T.T.A.; Barnes, E.; Kumar, A.; Gopalan, V. Probing Ferroelectrics Using Optical Second Harmonic Generation. *J. Am. Ceram. Soc.* **2011**, 94, 2699-2727; DOI:10.1111/j.1551-2916.2011.04740.x.

[191] Byer, R.L. Quasi-Phasematched Nonlinear Interactions and Devices. *J. Nonlinear Opt. Phys. Mater.* **1997**, 6, 549-592; DOI:10.1142/S021886359700040X.

[192] Volk, T.; Wöhlecke, M. Polarization Reversal and Ferroelectric Domains in LiNbO$_3$ Crystals. In *Springer Series in Materials Science 115. Lithium Niobate. Defects, Photorefraction and Ferroelectric Switching,* 1rst

ed.; Hull R., Osgood Jr. R. M., Parisi J., Warlimont H., Eds.; Springer: Berlin/Heidelberg, Germany, 2009; Volume 115, pp. 153-212, ISBN 978-3-540-70765-3.

[193] Armstrong, J.A.; Bloembergen, N.; Ducuing, J.; Pershan, P.S. Interaction between Light Waves in a Nonlinear Dielectric. *Phys. Rev.* **1962**, 127, 1918-1939; DOI:10.1103/PhysRev.127.1918.

[194] Nakamura, K.; Ando, H.; Shimizu, H. Ferroelectric domain inversion caused in $LiNbO_3$ plates by heat treatment. *Appl. Phys. Lett.* **1987**, 50, 1413-1414; DOI:10.1063/1.97838.

[195] Yamada, M.; Nada, N.; Saitoh, M.; Watanabe, K. First-order quasi-phase matched LiNbO3 waveguide periodically poled by applying an external field for efficient blue second-harmonic generation. *Appl. Phys. Lett.* **1993**, 62, 435-436; DOI:10.1063/1.108925.

[196] Khanarian, G.; Norwood, R.A.; Haas, D.; Feuer, B.; Karim, D. Phase-matched second-harmonic generation in a polymer waveguide. *Appl. Phys. Lett.* **1990**, 57, 977-979; DOI:10.1063/1.103531.

[197] Lisinski, S.; Ratke, L.; Schaniel, D.; Jungk, T.; Soergel, E.; Boysen, H.; Woike, T. Second-harmonic generation in nano-structured $LiTaO_3$ – and $LiNbO_3$ -xerogels with randomly oriented ferroelectric grains. *Opt. Mater.* **2010**, 32, 504-509; DOI:10.1016/j.optmat.2009.11.003.

[198] Baudrier-Raybaut, M.; Haïdar, R.; Kupecek, Ph.; Lemasson, Ph.; Rosencher, E. Random quasi-phase-matching in bulk polycrystalline isotropic nonlinear materials. *Nature* **2004**, 432, 374-376; DOI:10.1038/nature03027.

[199] Morozov, E.Y.; Chirkin, A.S. Stochastic quasi-phase matching in nonlinear-optical crystals with an irregular domain structure. *Quantum Electronics* **2004**, 34, 227-232; DOI:10.1070/QE2004v034n03ABEH002617.

[200] Hsieh, C.-L.; Grange, R.; Pu, Y.; Psaltis, D. Bioconjugation of barium titanate nanocrystals with immunoglobulin G antibody for second harmonic radiation imaging probes. *Biomaterials* **2010**, 31, 2272-2277; DOI:10.1016/j.biomaterials.2009.11.096.

[201] Bonacina, L. Nonlinear Nanomedecine: Harmonic Nanoparticles toward Targeted Diagnosis and Therapy. *Mol. Pharmaceutics* **2012**, 10, 783-792; DOI:10.1021/mp300523e.

[202] Wang, Y.; Zhou, X.Y.; Chen, Z.; Cai, B. ; Ye, Z.Z.; Gao, C.Y.; Huang, J.Y. Synthesis of cubic $LiNbO_3$ nanoparticles and their application in vitro imaging. *Appl. Phys. A* **2014**, 117, 2121-2126; DOI:10.1007/s00339-014-8630-x.

PART II

EXPERIMENTAL METHODS AND TECHNIQUES

(THEORETICAL INTRODUCTION)

EXPERIMENTAL

(DESCRIPTIVE)

Chapter 3: Materials Science + Nonlinear Optics

Basics on the synthesis and characterization

Concerning the work done so far in the current investigations, the synthesis of the studied materials practically summarizes into the successive combination of the following processes: *grinding* (high-energy ball milling) and *thermal annealing* or calcination. In short, the precursors in the form of powders, lithium carbonate (Li_2CO_3) and niobium pentoxide (Nb_2O_5), are mixed in solid phase (RT) and grinded, and then subjected to a thermal annealing process (calcination). The precursors are bought (Alpha Aesar), and the technique used in the grinding process is closely related to that of *mechanochemical synthesis*.

Strictly speaking, mechanochemical synthesis (MS) denotes a grinding process in which chemical reactions are necessary involved: the simultaneous grinding of more than one precursor (chemically distinct), so that with the breaking of certain chemical bonds, the formation of new ones is favored. In the cases when no chemical reactions are involved, as in the case of the present investigation, where (in principle) the precursors are only grinded, it is convenient to denote them simply as *grinding*. However, given the similarity between concepts and involved variables in each of these processes, the former will be described in this conceptual framework pertaining the synthesis of the studied lithium niobate ($LiNbO_3$; LN) powders. On the other hand, to state that no chemical reactions take place in the grinding process might be not accurate to some extent. Apart from contamination issues depending on the chemical and physical characteristics of the used vial and grinding medium [1-3], in the preparation of LN powders (LNPws) by high-energy ball milling the product usually shows a greyish coloration (before calcination), also observed for LN single crystals after chemical reduction (near the surface) [4].

Kocksor et al have suggested that the sample darkening is a direct consequence of the "mechanochemical reduction of Nb (V) via polaron and bipolaron formation, oxygen release and Li_2O segregation, while subsequent oxidizing heat-treatments recovered the white color with evaporation of Li_2O and crystallization of a $LiNb_3O_8$ phase instead" [1]. These authors report a loss of Li at the calcination stage –causing the formation of a more stable $LiNb_3O_8$, a secondary phase highly deficient in Li—, whereas in the present investigation it is sustained the hypothesis of no loss of Li neither at the grinding stage nor at the calcination one. The

hypothesis is demonstrated by the self-consistent obtained results, noticing however, that none of the synthesis processes were exactly reproduced regarding this investigation in respect to the work by Kocksor et al [1, 5]: not only the temperature conditions and time intervals in the thermal treatments slightly differ but also the used mill: a Spex 8000 Mixer Mill was used in [1], in contrast, in here a less energy MSK-SFM-3 mill (by MTI Corporation) was used. The former type of mill is one of the most commonly used ball mills for this purpose (the latter one might be considered a generic mill). Interestingly, according to the experience accumulated within our researching group, the darkening of the samples is much more obvious when the Spex 8000 miller is used compared to the generic one.

Another common finding, which (again) was not observed in the present investigation, is the remaining of non-reacted and amorphous materials in the milled powder [6, 7]. This was noticed ever since the work of De Figueiredo et al, whom might be considered pioneers in the synthesis of LNPws via mechanical alloying [6]. Of course, these results and those described in the preceding paragraph, which contrast with the results herein reported, are subject of scrutiny and further investigation. The preparation of pure LNPws by a mechanochemical method assisted by a subsequent calcination at relatively high temperatures has been previously achieved and reported in [8-10].

The basics on the experimental configurations to do the combined analysis resulting from the depth profiling of the polarization-resolved powder Second Harmonic Generation, are omitted. Some relevant technical aspects will be treated explicitly in the corresponding presentation and discussion of the results pertaining this secondary investigation (PART III).

3.1 Mechanosynthesis/Milling

Two main categories exist regarding the grinding mechanisms to produce fine powders. The first is denoted as 'volume grinding', in which the solid particles are pulverized through the existent collisions between the particles and the grinding medium. Unimodal distributions regarding the particle size are typically obtained with this type of grinding, as shown in Figure II-1(top). The second one is known as 'surface grinding', where ultrafine particles are produced from the surfaces of the particles constituting the raw material, resulting from the existent frictional forces at the surfaces of the solid particles [11]. At this instance, bimodal particle size distributions are obtained under regular circumstances, that is, an agglomerate

of particles that share a common size (averaged) and another one with particles being considerably smaller, schematized in Figure II-1(bottom). Thus, surface grinding is a more efficient mechanism to produce fine and ultrafine powders, and it is nominally achieved via the principle of operation of different grinding machines or mills, used in the following techniques [11]: roller milling, friction milling, ball milling and agitation ball milling. Soon it will be shown that the grinding mechanism pertaining to MS is that of surface grinding because, regardless of the utilized mill, this will always be one –or a variant— of the just above mentioned.
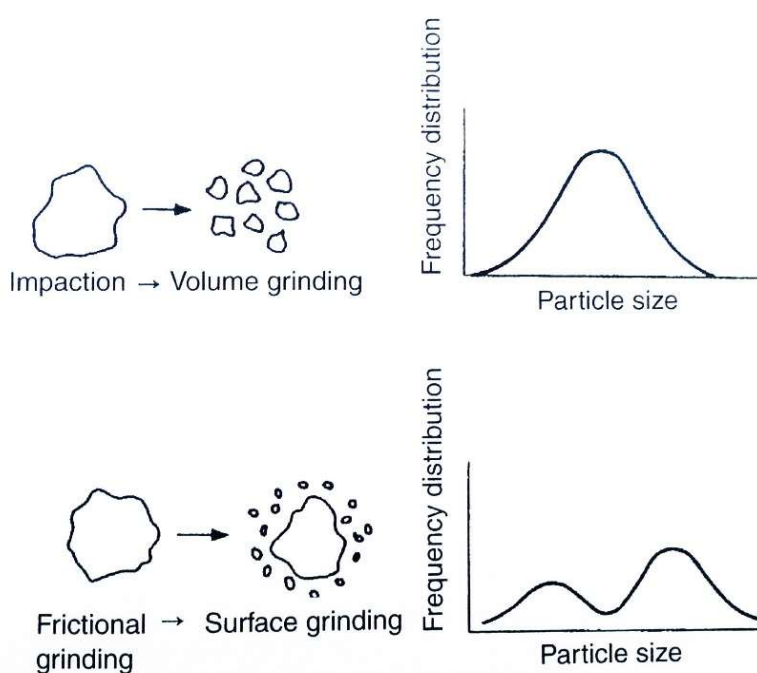
Figure II-1. Particle size distributions obtained via a grinding process. *Reprinted/adapted from reference in [12]; © Elsevier Inc., 2003.*

The process of MS starts at the stage of the *preparation of the precursors* with the correct proportions, followed by their mixing and placement into a *vial* in conjunction with the *grinding medium*. Once the vial has been sealed, it is fixed to the mill and *agitated* for a determined time interval, typically the necessary time to reach a stationary state for which (ideally) the chemical composition of each particle of the milled powder equals the initial proportion of the precursors [13]. Notwithstanding, this is only a suggestion and not a necessary condition, given that the *milling time* is a study variable. This is, without further ado, the MS process. It can be accompanied with the consolidation of the milled powder into

a uniform and compact solid, followed by a proper thermal annealing, aiming a designed microstructure and, thus, certain sought macroscopic properties. Hence, the main components involved in the MS process are: the raw materials in the form of powders (the precursors), the mill and the process variables. These will be further described by separate in the following lines.

3.1.1 Precursors

In general, the powders utilized in MS as precursors are accessible since they are normally produced at the industrial level and are commercially available. Of low cost and with high purity. Typically, the particle sizes fall in the range 1-200 μm [12, 14]. This is not a critical parameter, except for the fact that, in principle, it must be smaller than the dimensions of the grinding medium –usually reinforcing steel or zirconia (ZrO_2) balls. The characteristic size of the particles within the powder decreases as the milling time increases, obeying an exponential law; the value of a just a few micrometers is reached just after a few minutes of being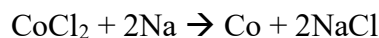 initialized the process [13]. To avoid chemical reactions inside the vial, the used precursor might then be: noble metals, master alloys, prealloyed powders and refractory compounds. In the case which chemical reactions are sought, it is necessary to consider proper combination of these with compounds belonging to the family of oxides such as carbides and nitrates, among others [13]. As an example, a common type of reaction that takes place in MS is:

$$MO + R \rightarrow M + R$$
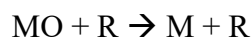
in which, a metallic oxide (MO) is reduced by the presence of a reactive metal (R: reducing agent), converting into a noble metal (M). Compounds such as chlorides and metallic sulfides have been reduced by MS [13]. Several reactions of this sort have been reported in the literature, for example, see Table 21 (p.126-127) in [13]. Some of these are:

$$3Ag_2O + 2Al \rightarrow 6Ag + Al_2O_3$$

$$CoCl_2 + 2Na \rightarrow Co + 2NaCl$$

$$3Fe_3O_4 + 8Al \rightarrow 9Fe + 4\ Al_2O_3$$

$$2ZnO + Ti \rightarrow 2Zn + TiO_2$$
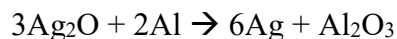
There are no limitations regarding the mechanical properties of the precursors. The possible combinations are: ductile-ductile, ductile-brittle and brittle-brittle [13]. Moreover, it is sometimes convenient to stablish the grinding in a liquid medium, denoted as wet grinding [15-17]. Compared to dry grinding, the wet grinding is considered a better method to produce fine powders; it is believed that in this process the produced particles absorb the particles of the solvent at a surface level, thus decreasing the surface energy of the produced particles at a higher rate [14]. It has also been reported that the amorphization of the powder is achieved faster under a wet environment compared to a dry one [18].

3.1.2 Mills

Different types of high-energy mills are commercially available. They differ, one from another, in the load capacity, mill efficiency and the coupling of additional devices for temperature control. The mostly used mills are classified as *vibrational shake*, planetary ball and attritor mills [13, 14]. Since in the present investigation the milling process was carried out with a mill of the first type, next it is only described the operational principle of this type of mills.

The SPEX is the vibrational shake mill most used by the community advocated to do research related to MS; designed and assembled by SPEX CertPrep (Metuchen, NJ) [19]. Figure II-2 shows a photograph of this mill and various of its internal components. A common variant of this mill is that it has a vial that contains within itself both the sample and the balls (grinding medium). The vial is tightened with a clamp and agitated at a rate of several thousands of times per minute [14]. The agitation movement –a sway— is combined with lateral movements at both ends of the vial, such that it would describe an '8' figure or infinity symbols in its movement. With the oscillatory movement of the vial, the balls impact the sample and the ends of the vial, thus simultaneously carrying out two process: grinding and mixing of the sample. The induced force or transferred energy by each impact is very high, since given the oscillation amplitude of the vial (~ 5 cm) and the frequency in the movement of the clamp (~ 1200 rpm), the speed of the balls is high (~ 5 ms^{-1}) [13]. The vial can be fabricated with different materials. Among these the following are highlighted: reinforced steel, aluminum oxide, tungsten carbide, zirconia, stainless steel, silicon nitride, agate, plastic and methacrylate [13].
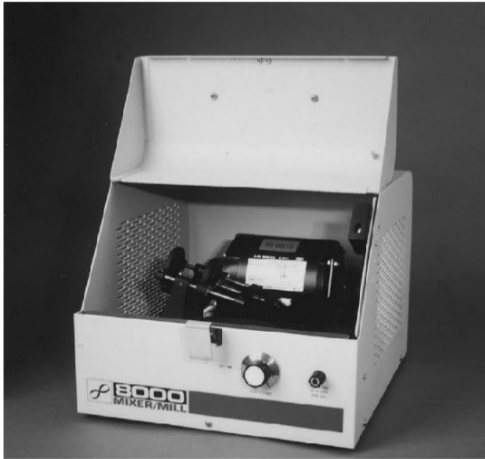
Figure II-2. Photographs. **Left:** typical SPEX 8000 mill in the assembled condition. **Right:** tungsten carbide vial set consisting of the vial, lid, gasket, and balls. *Reprinted/adapted from reference in [13]; © Elsevier Science Ltd., 2001: Courtesy of SPEX CertiPrep, Metuchen, NJ.*

On the other hand, the only apparent limitation of the SPEX mill, as compared to others, is its load capacity (~ 10-20 g). The planetary and attritor mills lead it in this point, they are capable to grind around 100 g and 0.5-40 kg at a time, respectively [13]. However, their main disadvantage, compared to the SPEX, is a much lower impact frequency of the balls, particularly the attritor mills, for which the speed of the balls hardly surpasses the limit of 0.5 ms^{-1}. For this reason, the planetary and attritor mills are not considered high-energy mills. The characteristic energy of a mill is relevant, given that as this parameter lessens, the necessary time to produce the same effect will considerably be extended. Industrial mills with load capacities around 1250 kg have also been constructed. It is nonetheless important to bear in mind the milling time. Quoting Suryanarana: "as a rule of thumb, it can be estimated that a process that takes only a few minutes in the SPEX mill may take hours in an attritor and a few days in a commercial mill even though the details can be different depending on the efficiency of the different mills" [13]. Figure II-3 shows the three different types of low-energy mills just mentioned.
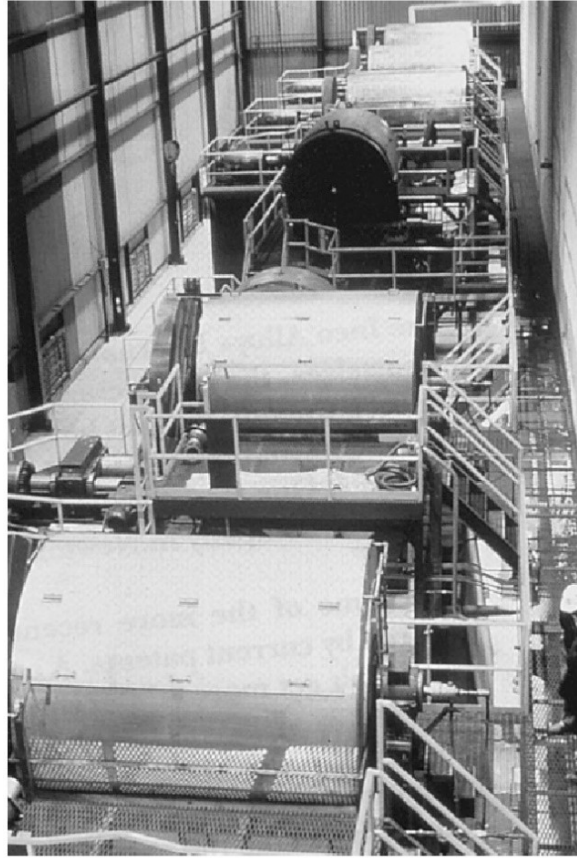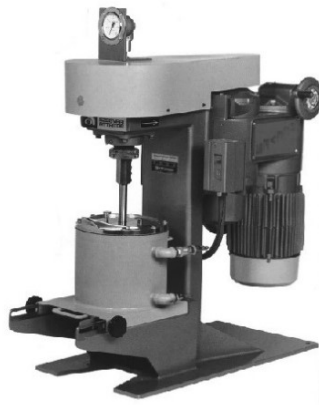
Figure II-3. Photographs of low-energy mills. **Upper left:** planetary (courtesy of Gilson Company, Inc., Worthington, OH). **Bottom left:** attritor (courtesy of Union Process, Akron, OH). **Right:** industrial (courtesy of Inco Alloys International). *Reprinted/adapted from reference in [13]; © Elsevier Science Ltd., 2001.*

3.1.3 Variables of the process

In MS the optimization of certain variables is involved so that a sought phase and/or microstructure is ultimately obtained. Some of the parameters that have a net effect in the characteristics and properties of the milled powder are: type of mill, vial, time and speed of the milling, grinding medium (composition, size and size distribution), ball-to-powder weight ratio (BPR), extent of filling the vial, temperature and atmosphere conditions, process control agent (surfactant), among others. The variation of two or more is not completely independent: it is well known that the milling time depends on the type of mill, the size of the grinding medium, the temperature and the BPR [13].

In the subsequent lines, the possible variations –and corresponding consequences— of some of these parameters are succinctly described; these have been chosen according to their

relevance to the present work of thesis. When a given variable is being treated, it is assumed that the rest do not have influence on it. Meanwhile it is worth mentioning that in the case of a SPEX mill, typically 5 g of sample are milled with a cylindrical vial (stainless steel) of 40 mm in diameter and 40 mm in length. Balls made of the same material as that of the vial usually stand for the grinding medium, with diameters of approximately 12.7 mm [14].

➢ **Milling time:** it is the most important of all the parameters. In general, it is chosen so that an equilibrium is reached between the fracture and cold-welding processes experienced by the powder particles [13]. The required milling time for a determined effect depends mostly in the used mill, the milling intensity, the BPR and the temperature inside the vial. Once these parameters have been fixed, the required times are estimated according to the sample that is to be milled. Even though it is possible to perform the process continuously along large time intervals, it is not recommended to extend this parameter further than the time just necessary, since the probability of contamination increases with the milling time [20]. The determination of the required time to obtain the desired result is, in most of the cases, only empirically done, that is, based on trial and failure. Yet in the cases in which it is necessary to employ large milling time intervals (t ≥ 60 min, SPEX mill), it is suggested that the process is performed discontinuously, that is, programming the mill so that it operates between shorter time intervals, alternated as follows: milling-pause-milling-pause-milling… This because the use of the mill in a continuous mode for large time intervals might cause a nonnegligible increment on the temperature at the surroundings of the engine and other components of the mill, probably causing a detriment in the efficiency and/or a breakdown of the mill.

➢ **Grinding medium:** the grinding medium must exert a high impact force on the surfaces of the powder, thus its density should be sufficiently high. According to the consulted literature, no other representation of the grinding medium has been found than a set of balls, made of dense material and of different diameter sizes. The balls are usually made of steel: hardened chromium, templated, stainless, as well as of tungsten-cobalt carbides [13]. Specific cases exist, where the balls are made of: copper, titanium, niobium, zirconia, agate, ytria-stabilized-

zirconia (YST), sapphire, and silicon nitride (Si_3N_4) [13]. The milling efficiency also depends strongly in the size of the balls: the energy transfer improves as the size of the balls increases [21-23]. Takacs and Pardavi-Horvarth have reported that a higher collision energy can be achieved by means of a proper combination of the diameters of the balls used in the process [24].

- **Vial:** to avoid possible contamination of the powder with more than one chemical species, the material of the vial must be the same as that of the balls. Regarding its shape, it has been reported that the process of metal alloying (without chemical reactions) becomes more effective when flat ended vials are used instead of concave ended ones [25].

- **Ball-to-powder weight ratio (BPR):** the BPR has a strong influence on the milling time. One is inversely proportional on the other. For example, in the milling of a mixture of a Ti-33 at. % Al powder mix with a SPEX mill, the amorphous phase was obtained in three different pair of variables [26]: BPR (milling time): 10:1 (7 hours), 50:1 (2 hours) and 100:1 (1 hour). The effect of the BPR has been studied for values going from 1:1 up to 220:1 [27, 28]. A BPR 10:1 is usually used, considering only the use of a SPEX mill.

- **Extent of filling the vial:** both production and efficiency will be low if the total mass (balls and powder) inside the vial is too small. On the other hand, when the vial is too full, less space is left for the movement of the balls and thus the collision energy is significantly reduced, translating into large milling times. Extent filling of the vial around 50 % (or less) of the capacity of the vial is recommended, considering both the mass of the processed powder and the total mass of the grinding media [13].

- **Atmosphere:** the main effect of this parameter has in the process is its influence in the contamination of the powder. Thus, to empty out the air, or rather that an inert gas (Ar or He) is applied into the sealed vials, is a common practice. It has been found that Nitrogen reacts with metallic powders, so that it is avoided, unless the goal is the production of nitrides. Argon is the most utilized element in the milling process, which prevents oxidation and contamination of the

sample. It has also been reported that the presence of regular air within the vial favors the production of oxides and nitrides [13].

3.2 Mechanisms in the high-energy ball milling process

In this process the particles that constitute the milled powder are exposed to an iterative combination of the following mechanisms: flattening, cold welding, fracture and recombination. Because there is a high mobility regarding the balls, there exist mainly three types of collisions: ball-ball, ball-powder and ball-walls (the internal walls of the vial). However, ball-powder-ball type collisions also exist; at some instances a given fraction of the powder is being pressed by two or more balls. It has been estimated that approximately a thousand particles with a total (aggregated) mass of 0.2 mg are confined in this type of collision [13]. This instance is schematized in Figure II-4. At the initial stage the impact force deforms the particles inelastically. As a result, work hardening and fracture take place at the surface level. New surfaces are formed, allowing the particles to weld. Thus, an effective increment of the averaged size of the particles follows. The size distribution widens with cases in which the new particles can be as three times larger than the original ones [13]. Then, deformation keeps its pace and the particles harden due to mechanical fatigue and/or fragmentation of their layers or fragile sheets. The formation of this type of fragments might continue as far as no significant agglomeration forces exist. This translates into the reverse effect: an effective decrease of the averaged size of the particles. At this stage, the tendency of the particles to fragment dominates their tendency to weld [13]. Yet because the ball impacts continue, the structure of the particles keeps being refined and refined, no matter the size of the particles remains constant (it repeatedly increases and decreases due to the mechanism competition above described). Consequently, the inter-layer spacing decreases, whereas the number of layers per particle increases.
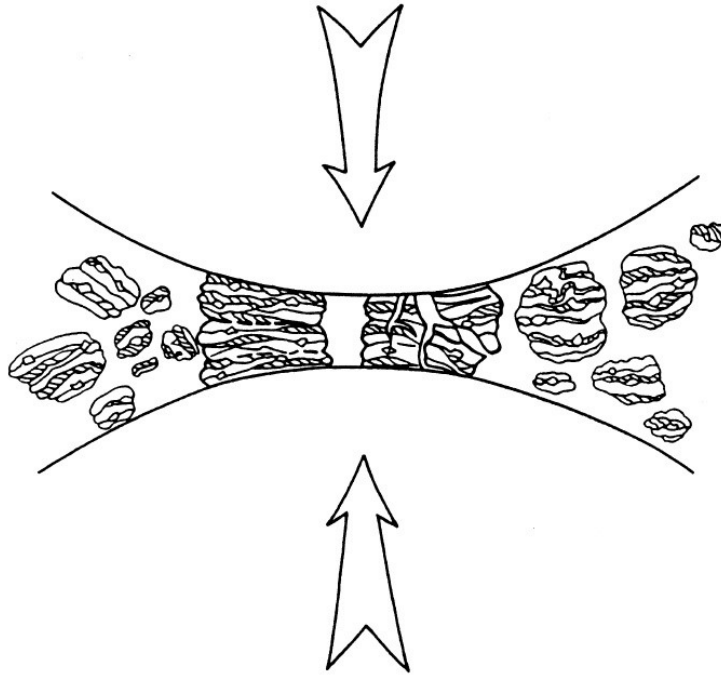
Figure II-4. Scheme of the ball-powder-ball type of collision that exist during the high-energy ball milling process. *Reprinted/adapted from reference in [13]; © Elsevier Science Ltd., 2001.*

Now, so far only the refinement mechanism of the particles has been discussed. The chemical reactions between the precursor have not been considered. Assuming the precursors are oxides, then the particle refinement (and fragmentation) results in defect formation and in an effective reduction of the diffusion distances. The interaction between the precursors thus enhances. Moreover, given the formation of new surfaces and interfaces, a substantial increment in the reactivity of the precursors is achieved [14]. This is what is understood by the 'chemical activation' of the precursors. If the process keeps going on, the chemical activation will also continue and, at some instance, the necessary chemical reactions for the formation of a new phase start to appear. If the process still goes on further, it is possible that other processes also take place, such as nucleation, particle growth and crystalline phase formation. The formation of an amorphous phase can even occur, which is not other than the extreme case of defect formation [14]. The localized heat transfer right at the impact zones (ball-powder-ball collisions) might contribute in this process. This hypothesis is justified by the fact that even when the temperature inside the vial hardly reaches 100 °C, the *in situ* temperature at each impact event can be large enough to activate the solid state reactions ($\sim$ > 800 °C) [29, 30].

3.3 Other methods of synthesis

Conventionally, LN powders are prepared by solid state-reactions between corresponding oxides (or oxide and carbonate) at temperature above 1000 °C. Although this method is simple, it may lead to the composition deviation from stoichiometry because of lithium evaporation at higher temperatures [31-33]. The topic of other non-conventional methods to produce LN powders of high quality has been extensively discussed by a Chinese group at:

State Key Laboratory of fine Chemicals, Department of Materials Science and Chemical Engineering, School of Chemical Engineering, Dalian University of Technology, PR China.

This group has mainly focused in soft-chemistry synthesis methods such as sol-gel and hydrothermal processes [34], combustion method with urea as fuel [32] and wet chemical synthesis [33]. Within references in [32-34], Liu et al have provided information on other methods of synthesis for this purpose. Also, a proper discussion on the advantages and disadvantages of some of these is also presented, as well as other reports on the ones already mentioned. These are: sol-gel [35-37], Pechini method [38], metal alkoxides [39], hydrothermal process [40], and the peroxide route [36]. The synthesis of other ferroelectric powders by similar methods can also be consulted in the literature: chemical coprecipitation [41-43], sol-gel process [44-46], hydrothermal process [47-50], combustion [51], and molten salt [52, 53]. Lastly, in PART III —where the results obtained in this investigation are simultaneously given and discussed— it will be shown that references in [32-34] are central to the conceived explanation of the results herein presented.

To show the superiority of the mechanochemical-calcination route employed in this work of thesis, compared to above described, in the lines that follow it will be succinctly described the method employed by Liu et al in [33]. It is based on the adoption of a kind of α-carboxylic acid (citric acid) to coordinate with niobium. Quoting [33]:

"The commonest and cheapest starting material used in niobium chemistry is niobium oxide. If niobium oxide is employed as a raw material to synthesize LN powders, the production cost would be dramatically decreased, which is of benefit for use in large scale production. However, niobium oxide shows an extremely high chemical stability, which reduces its application to a few systems. In contrast, hydrated niobium oxides ($Nb_2O_5 \cdot nH_2O$,

often called as niobic acid), are usually obtained as white precipitates with indeterminate water content [54], which are more reactive than niobium oxides, e.g., they can dissolve in aqueous solutions of NaOH, oxalic acid, tartaric acid, citrate acids and others [54]". Hence, in this method "niobium oxide is first activated into niobium acid, then citric acid is employed to coordinate with niobium acid to form Nb–citric acid complex. LN precursor is synthesized through evaporating the water soluble Nb–citric acid complex and lithium hydroxide. Finally, pure LN powders are obtained by calcinating the precursors at 600 °C" [33].

As described in section 3.2, in the present investigation the reactivity of the niobium oxide (Nb_2O_5) is carried out by means of the high-energy ball milling process (dry environment). Although the method by Liu et al effectively achieves the use of lower temperatures at the calcination stage (because a better reactivity of the niobium oxide is obtained), by employing MS the use of any kind of acids (inorganic or organic) is avoided. This is advantageous since the use of acids usually implies regulations to the exposure of hazardous or toxic fumes and vapors (ventilation issues), and thus the following of certain security protocols. On the other hand, the work by Liu et al is important because the obtention of a crystalline phase at the lowest possible temperature in the thermal treatment is a subject of intense research. The main characteristics on thermal or heat treatment can be consulted in [55, 56].

3.4 Characterization

Quoting Czichos: "whenever a material is being created, developed, or produced the properties of phenomena the material exhibits are of central concern. Experience shows that the properties and performance associated with a material are intimately related to its composition and structure at all levels, including which atoms are present and how the atoms are arranged in the material, and that this structure is the result of synthesis, processing and manufacture" [57]. Thus, these main elements, composition and structure, properties and performance, as well as their correlation, define the main categories of methods to characterize the materials.

Nowadays a great variety of methods and techniques are at hand to study practically any aspect of a material. The employment of a method or technique depends, as a starting point, in the nature of the material, as well as in the goal of the study. Some are more suitable than

others, can be destructive or not, difficult or not to implement, and some other could be inaccessible to most due to the complexity of the measurement devices and lack of infrastructure. As previously mentioned, in this investigation four nondestructive techniques/methods have been employed to describe the chemical composition (CC) of the synthesized LN powders: X-ray Diffraction (XRD) + structure refinement, Raman Spectroscopy (RS), UV-vis Diffuse Reflectance (DR), and Differential Thermal Analysis (DTA). Scanning Electron Microscopy (SEM) was also utilized to verify that the particle size distributions do not vary drastically from one sample to another. All these are considered standard characterization techniques and are nowadays accessible to most potential users, including the scientific communities in developing countries.

To attempt to discuss in detail all the experimental techniques used in this work of thesis not only would seem redundant but also is out context. Thus, in the subsections that follow only the appropriate references where the theoretical and experimental aspects regarding these five characterization techniques, will be given. In the case of DRX, a succinct discussion regarding powder DRX –as its theoretical and experimental aspects differ from single crystals— will be presented. Meanwhile, it is worth introducing the *Springer Handbook of Materials Measurement Methods*, which is a comprehensive monograph on the principles and bases of (almost) any characterization technique [58]. For example, regarding only the methods and techniques to characterize the CC and structure of a material, the chapters 4 (p. 105-152) and 5 (153-227) are useful, respectively. Furthermore, it only suffices a glance to tables 5.1, 5.2 and 5.3 in [58] to notice that they can be a good starting point whenever a decision must be taken, without previous experience, on which method or technique is to be used to characterize the structure of a given material. In such reference, the description of four characterization techniques herein utilized can be consulted in pages (not DR): (standard) DRX (159-163), powder DRX (181-182), Raman scattering:RS (176-177:111-112), DTA (586-588), and Microscopy and Topography i.e. SEM/TEM (163-171).

3.4.1 Powder X-ray Diffraction and Rietveld refinement

XRD is a well stablished characterization technique ever since the early 20th century. The available references (books, reviews and technical papers) discussing its principles and experimental aspects is just abundant. The book by Cullity et al is a canonic reference

regarding the fundamental aspects of standard XRD [59]. The book by Compton and Allison is also recognized as an authoritative reference in this field [60]. A more recent book on *Crystals and Crystal Structures* also provides more actualized information [61]. On the other hand, regarding powder XRD the references in [62-65] are recommended. Also, a book has been written regarding solely the abstract mathematical basis for powder DRX [66].

Powder DRX differs from that in single crystals (standard DRX) in that the reciprocal lattice in the powder is fully random regarding its orientation respect to incidence of X-rays beam. Consequently, the rays diffracted by equivalent crystallographic planes occurs in all possible directions, forming a cone of common diffraction angle 2θ, θ being the incidence angle with respect to the surface normal (Bragg angle) [67]. The diffraction pattern thus consists of rings of different diameters (Debye rings), which are correlated to interplanar distances *d*, according to the Bragg condition [62, 67]:

$$2dsen\theta = n\lambda$$

Eq. II-1

where n is an integer, λ the wavelength ($\sim 10^{-10}$ m), and d the atomic interplanar distance. Thus, the peaks in the diffraction pattern, well defined and narrow in the case of single crystals, tend to widen or to broaden for powders. This behavior is known as *line broadening*, it is schematized in Figure II-5. Nevertheless, the line broadening is not only due to the small dimensions and random orientation of the crystallites within the powder. There is also a contribution from *instrumental errors*, as well as from the *strain* distribution [13, 67]. The instrumental contribution originates from the spatial, angular and wavelength distribution of the incident X-ray beam, and it can be empirically evaluated by using a standard sample, usually a large and perfect single crystal such as Si [67]. The line broadening due to lattice strain is in most cases due to lattice defects such as dislocations [67].
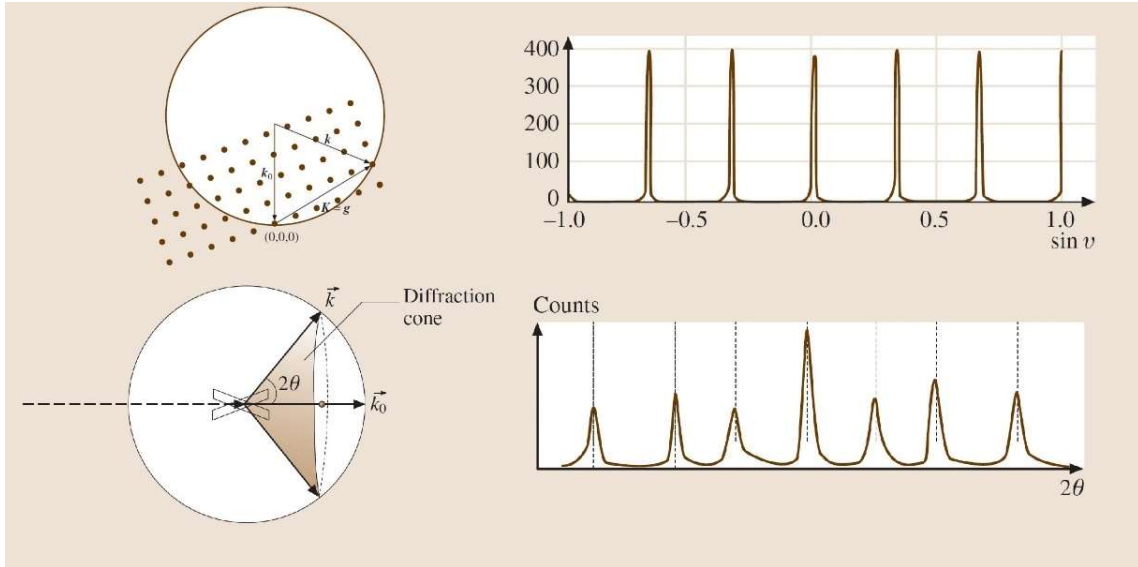
Figure II-5. Graphical reconstruction of the diffraction of waves by an Ewald sphere in the reciprocal space, and its corresponding graphical representation of a diffraction pattern. **Above:** single crystal. **Bottom:** for a powder constituted by several crystalline domains with a random orientation. *Reprinted/adapted from reference in [56]; © Springer-Verlag., 2006.*

The line broadening is a parameter directly related to the averaged crystallite size. Scherrer first showed that the average size of the crystallites that constitute a powder, *D,* relates to line broadening, β, by means of the following equation [62-65]:

$$D = \frac{K\lambda}{\beta cos\theta}$$

Eq. II-2

with *K* a constant with a value close to 1, related to the crystallite shape, as well as the form in which β and *D* are defined. The angle θ is the Bragg angle (half the angle in a typical diffractogram) and λ the wavelength of the incident X-ray beam. Care must be taken with the interpretation of β, since this parameter differs to the experimental breadth, usually denoted as *B* [62]. β is the line broadening due only to the material. Thus, if β_{inst} is the instrumental contribution to the line broadening, β is then defined as [67]:

$$\beta = B - \beta_{inst}$$

Eq. II-3

β is usually associated, statistically, as being equal to the angular part of the Full Width at Half Maximum (FWHM) of the intensity of given diffraction peak (usually the main diffraction peak), after β_{inst} has been subtracted from the experimental breadth [13, 62]. Other authors associate it with the integral breadth, which is defined as the width of a rectangle having the same area and height as the line profile of interest [67]. Eq. II-3 is known as the Scherrer equation, it estimates the average size of the crystallites within the powder. Short after its deduction in 1918, it was validated based on the independent works by von Laue, Bragg and Seljakow, among others [62, 68-70]. Its functional form is not altered according to the interpretation taken regarding the line broadening β, but it does have an influence on the value of K (a typical value is 0.9) [13, 14].

In the quantitative analysis by DRX (line broadening of the main diffraction peak) it is important to remind that the averaged crystallite size is determined. Two key words:

- ➢ **Crystallite:** in general, a powder particle is made of several individual particles. Likewise, each individual particle contains several crystallites, which are elsewhere defined as 'coherently diffraction domains' [13]. The determination of the average size of the particles can be done be standard optical microscopy techniques, or of grains in the case of high-resolution techniques. The use of diffraction-based techniques, such as DRX, allows the estimation of the averaged crystallite size.
- ➢ **Average:** the main shortcoming of the characterization of the averaged crystallite size by the determination of the line broadening in powder DRX pattern, is that is only correct within the range of crystallite sizes of 10-100 nm [13, 62, 67]. This is reason behind the fact the estimated values do not always agree with those measured on individual crystallites by Transmission Electron Microscopy (TEM), capable of characterizing univocally any crystallite, regardless of its size.

In the determination of the averaged crystallite size by means of the Scherrer equation (Eq. II-2), reliable results can only be obtained if the proper corrections are made to the line broadening contributions due to instrumentation and lattice strain. This can imply certain

technical problems or limitations. Nevertheless, in case these cannot be resolved, for example not having a standard sample to calibrate the instrumental contribution, the equation still might be used to do a study of trends; for example, whether the crystallite size tends to decrease or increase based on the change of certain parameters of synthesis.

Lastly, instead of calculating the FWHM of a single diffraction peak (the most intense one), the estimation of the averaged crystallite size can be further improved if all the diffracted peaks are considered, involving the calculation of weighted averaged line broadening (the full use of the information content of a powder diffractogram). This is normally done by means of a structure refinement method among which the Rietveld refinement method is highly used. Originally developed and implemented for neutron diffraction experiments in the late 60´s, today it has become a standard method in powder DRX for structure determination and quantitative phase analysis [71-73]. In the following paragraph the method is succinctly described. This information has been adapted/reprinted from different parts in [65].

In short, the Rietveld method is a complex minimization procedure: a least squares refinement procedure where the experimental step-scanned values are adapted to calculated ones. It uses step intensity data $y(i)$, whereby each data point is treated as an observation. The profiles are considered to be known, and a model for a crystal structure available. Hence, it can only slightly modify a preconceived model built on external previous knowledge. The starting parameters for such a model must be reasonably close to the final values. Moreover, the sequence into which the different parameters are being refined needs to be carefully studied. Nowadays the use of program packages specifically designed for this purpose, both commercial and public, is a common practice. Some of these are (CA: commercially available; FS (FS: free software): TOPAS (by Bruker; CA) [74], AUTOQUAN (BGMN; CA) [75], HighScore Plus (Malvern Panalytical; CA) [76], FullProf (FS) [77] and GSAS-2 (FS) [78], among others. With years and the steadily improving of the programs the number of parameters to be refined has been increased dramatically. In this investigation, the package X'Pert HighScore Plus from PANalytical, version 2.2b (2.2.2), released in 2006, has been used [79]. For a deeper introduction to the Rietveld method, references in [64, 65, 80-82] might be consulted; the book authored by Young is particularly recommended [80].

3.4.2 Raman Spectroscopy, UV-vis Diffuse Reflectance, Differential Thermal Analysis and Scanning Electron Microscopy

For the theoretical and technical aspects regarding Raman scattering and Raman Spectroscopy (RS), a comprehensive review has been written by Pezzotti [83]. This reference might well suffice for a quick introduction, as well as for a more profound study to these subjects; practical examples on the explicit morphology of the Raman selection rules pertaining different crystal structures are worked out and validated. The *Handbook of Raman Spectroscopy* (Lewis and Edwards, Eds.; 2001) might also be consulted [84]. Besides the general approach to Raman scattering based on Quantum Mechanics, a Classical theoretical treatment might bring a deeper insight of the process, this can be consulted in 'Chapter 3' of the book written by Long et al [85].

Knowledge on the UV-vis Diffusion Reflectance (DR) technique can be acquired by consulting the work authored by Torrent and Barrón [86]. The seminal papers by Kubelka should also be studied [87, 88]. For Differential Thermal Analysis (and Thermogravimetry in general), references in [89, 90] are useful. Lastly, regarding Scanning Electron Microscopy (SEM), references in [91, 92] may be consulted.

Chapter 4: Materials Science + Nonlinear Optics Experimental

All the experimental procedures done in this investigation are described in detail.

4.1 Synthesis

High purity lithium carbonate (Li_2CO_3) and niobium pentoxide (Nb_2O_5), from Alpha Aesar, were used as starting reagents in a 1:1 molar ratio. The respective masses of the precursors were determined such that 1 g of lithium niobate ($LiNbO_3$; LN) was produced from the following balanced chemical equation:

$$Li_2CO_3 + Nb_2O_5 \rightarrow 2LiNbO_3 + CO_2$$
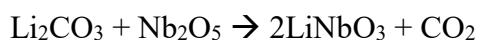
Eq. II-4

The resultant product was labeled—and hereafter referred to—as LN-STm (ST: stoichiometric, m: mixture) because, in principle, a ST mixture was obtained after milling with a 1:1 molar ratio in terms of Li and Nb. Variations in the chemical composition (CC) of the final resultant powders were sought by adding, at the milling stage, 1–5% of the mass in one of the precursors (with steps of 1% with resolution of 10^{-4} g) while keeping the mass of the other precursor constant, in both cases with respect to the masses measured for sample LN-STm, as shown in Table II-1. In this way, 10 more samples were synthesized and labeled as LN+1%LiP, LN+1%NbP, LN+2%LiP, and so on up to LN+5%NbP (P stands for precursor). It must be clarified that the percentages that appear on these labels are not in terms of the ion species solely, but in terms of the whole mass of the precursors that contain them.

Table II-1. Measured values for the masses of the precursors used in each of the 11 synthesis procedures.

Sample	Nb$_2$O$_5$ mass (g)	Li$_2$CO$_3$ mass (g)	Sample	Nb$_2$O$_5$ mass (g)	Li$_2$CO$_3$ mass (g)
LN+5%LiP	0.8989	0.2622	LN+1%NbP	0.9079	0.2498
LN+4%LiP	0.8988	0.2598	LN+2%NbP	0.9167	0.2496
LN+3%LiP	0.8991	0.2574	LN+3%NbP	0.9259	0.2497
LN+2%LiP	0.8990	0.2547	LN+4%NbP	0.9348	0.2498
LN+1%LiP	0.8989	0.2523	LN+5%NbP	0.9438	0.2498
LN-STm	0.8990	0.2498			

The high-energy milling was carried out in an MSK-SFM-3 mill (MTI Corporation) using nylon vials with YSZ balls; a powder:ball ratio of 0.1 was used for each sample preparation. The milling was performed in 30 min cycles, with 30 min pauses to avoid excessive heat inside the milling chamber, until 200 min of effective milling time was reached. Calcination of the resultant materials (amorphous) was done with a Thermo Scientific F21135 furnace in an air atmosphere. All samples were simultaneously calcined with the following programmed routine: 10 °C/min → 600 °C for 30 min → 2 °C/min → 850 °C for 120 min → cooling down slowly to room temperature.

4.2 Powder X-ray Diffraction and Rietveld refinement

These patterns were measured in air at room temperature using a Bruker D-8 Advance diffactometer with the Bragg-Brentano θ-θ geometry, a source of CuKα radiation ($\lambda = 1.5406$ Å), a Ni 0.5% CuKβ filter in the secondary beam, and a 1-dimensional position sensitive

silicon strip detector (Bruker, Linxeye, Karlsruhe, Germany). The diffraction intensity, as a function of the 2θ angle, was measured between 5.00° and 110.00°, with a step of 0.02° every 38.4 s. Sample LN-STm displays a pure ferroelectric LN phase, with Bragg peaks resembling those of the COD-2101175 card previously deposited with the Crystallographic Open Database; supplementary crystallographic data can be obtained free of charge from the Web page of the database [93].

Rietveld refinement was performed using computational package X'Pert HighScore Plus from PANalytical, version 2.2b (2.2.2), released in 2006 [79]. Instructions in the section named *Automatic Rietveld Refinement* from the HighScore Online Plus Help document were first followed and then adapted for phase quantification of the samples. In short, an archive with information about the atomic coordinates of LN ("2101175.cif") was downloaded from the Crystallopgraphic Open Database [93]. For the secondary phases $LiNb_3O_8$ and Li_3NbO_4, ICSD-2921 and ICSD-75264 from The Inorganic Crystal Structure Database were used, respectively [94]. The archives were then inserted, along with the experimental data, and Rietveld analysis in "Automatic Mode" was executed, followed by iterative executions in "Semi-automatic Mode," in which different "Profile Parameters" were allowed to vary until satisfactory indexes of agreement were obtained. The averaged crystallite size was also calculated by Rietveld refinement, following instructions from the *Size/Strain Analysis* section; a single lanthanum hexaboride (LaB_6) crystal was used in this case as the standard sample, analyzed with the ICSD-194636 card.

4.3 Raman Spectroscopy

Two Raman systems were employed in this investigation: one custom-made and one of standard use and commercially available. The former allowed for the set-up of different experimental conditions in terms of the polarization state of light at the incident-on-sample and detection stages, including non-polarized, parallel polarized (p), and cross polarized (s) situations. Adopting the Porto's formalism, these experimental conditions were: $Z(--)\bar{Z}$, $Z(YY)\bar{Z}$, $Z(YX)\bar{Z}$.

The commercially available system only featured the non-polarized configuration. It was a Witec alpha300R Confocal-Raman microscope with a 532 nm source of excitation wavelength and 4–5 cm^{-1} of spectral resolution. With this equipment, the Raman spectra were

collected in the range 100–1200 cm^{-1} at room temperature and light incident on the normal component of the sample with a power of 3.4 mW; a Nikon 10 objective was used to focus the incoming light on a 1:5 mm spot. An intensity of approximately 11Wcm^{-2} was delivered to the sample. The customized open-air Raman system consisted of an excitation beam output of a continuous wave diode laser at 638 nm wavelength with a power of 37 mW (Innovative photonic solution). The beam was linearly polarized from variable angle mounting and transmitted through a beam splitter to focus the excitation beam into the sample by an aspherized achromatic lens (NA = 0.5, Edmund optics). The excitation spot diameter measured at the focus point had a ~10 µm radius. The collected Raman scattered light from the sample through the aspheric lens and the beam splitter was focused by two silver coated mirrors and one bi-convex lens into a fiber Raman Stokes probe (InPhotonics) that was connected to a QE65 Raman Pro spectrometer (Ocean optics) for a Raman shift range detection between 250–3000 cm^{-1}. In its use for the characterization of the powders, the light at λ = 638 nm was incident at razing angle with P = 10 mW. The Raman spectra were collected in the range 200–1200 cm^{-1} at RT with a spectral resolution of 8 cm^{-1}. In this case, a laser intensity of approximately 3 kWcm^{-2} was delivered to the sample. Due to technical issues, most of the utilized experimental conditions were different from one Raman system to another—it is shown how this did not alter the obtained results—, except for the detection mode which in both cases was fixed at the backscattering-detection mode (see Figure II-6).

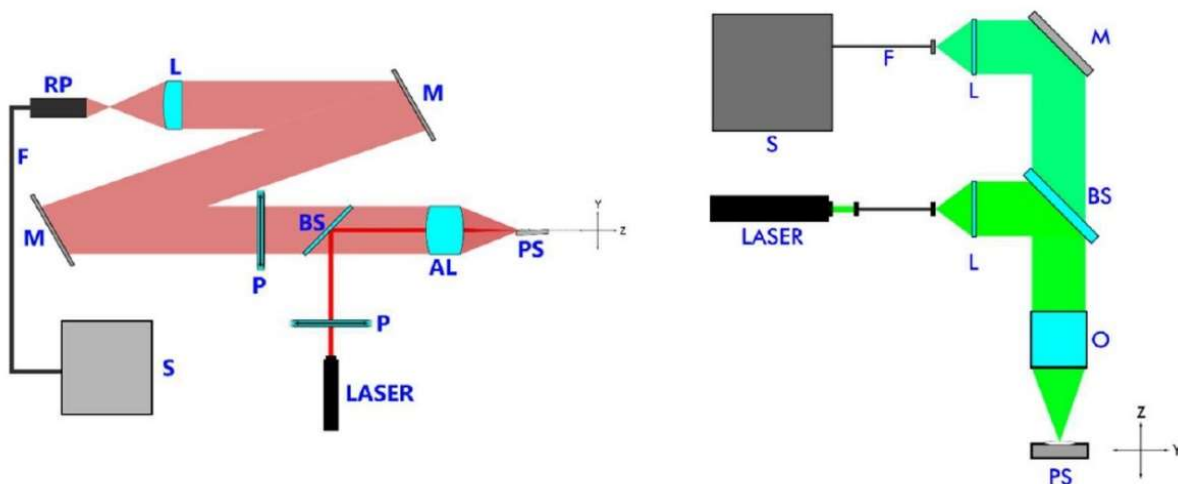**Figure II-6.** Scheme of the experimental configurations used for the acquisition of Raman spectra. **Left:** custom-made featuring both configurations, polarized and non-polarized. **Right:** commercially available featuring only non-polarized measurements. From left to right: RP—Raman probe, F—filter, M—mirror, L—lens, P—polarizer, BS—beam splitter, AL—aspheric lens, PS—powdered sample, S—spectrometer, O—objective.

4.4 UV-vis Diffuse Reflectance and Scanning Electron Microscopy

An Ocean Optics USB2000+ UV-VIS Spectrometer and an R400-Angle-Vis Reflection probe were used to collect the diffuse reflectance (DR) spectra of the samples and an Ocean Optics DH-2000-BAL Deuterium-Halogen light source was utilized. Commercially available aluminum oxide (Al_2O_3) was chosen as the standard reference. Precautions were taken so that the approximations necessary to apply the Kubelka-Munk Theory were accomplished [86-88]. These approximations are, mainly speaking, a preparation of the sample being thick enough so that the measured reflectance does not change with further increasing of this parameter (avoidance of Fresnel reflection) and an averaged size of the particles being smaller than such thickness, but larger relative to the wavelength (scattering independent of the wavelength).

The first of these experimental conditions was fulfilled by using a self-supporting pressed powder rectangular mount ($3 \times 3 \times 3$ mm); in all the experiments, an amount of approximately 1 g of powder was deposited. The second requirement was fulfilled by determination of the average size particle in the powders, using a field emission Scanning Electron Microscopy (SEM), with a JEOL JSM 5600-LV microscope (V = 20 kV, at 1500×, Mitaka, Tokyo, Japan). The micrographs were analyzed with ImageJ software: the edge length histograms were obtained from statistical analysis of at least 200 particles. Lastly, we followed the recommendation of grinding the powders in an agate mortar for a few minutes to avoid sample heterogeneity and regular reflection [86]: all samples were grinded for 10 min before measurements.

4.5 Differential Thermal Analysis

The Curie temperatures for the samples LN-STm, LN+1%NbP, LN+2%NbP, and LN+3%NbP were measured using differential scanning calorimetry (DSC) equipment coupled to thermogravimetry (TGA), SDT Q600 of TA instruments. The calorimeter was calibrated with respect to the copper melting point (1084 °C). The samples were analyzed in a wide temperature range between room temperature and 1200 °C, at a heating rate of 20 °C/min under a nitrogen atmosphere and using alumina containers. The ferroelectric-paraelectric state transition was observed around 1050–1080 °C. Subsequently, the samples were analyzed in four cooling cycles from 500 °C to 1200 °C at the same heating rate, 20

°C/min, and the process was seen to be reproducible, indicating that there was no permanent change in the volume of the pseudo-ilmenites.

4.6 Depth profile of the polarization-resolved Second Harmonic Generation in a pressed and compacted sample of LiNbO₃ micropowders

In this second and independent investigation, only the powder sample with a stoichiometric (ST) composition was studied –sample LN-STm. Regarding the sample preparation, instead of thick sample (hundreds of microns), a rather thin sample of pressed and compacted powder, about 8 µm thick, has been prepared by gently pressing the micropowder –with an average particle size of 2.6 µm and averaged crystallite size 100-300 nm— and then remove surplus by gently knocking and edge of the coverslip on which is supported the adhered powder. We hereafter refer to this prepared sample the "powder-print," in analogy to a fingerprint.

For Z-sectioning the second harmomnic response of a LN powder-print, a microscopy-like experimental arrangement (similar to that in [95]) has been constructed on a vertical plane, as shown in Figure II-7. At the entrance, light at the fundamental frequency (λ=800nm) moves downwards and passes through a dichroic mirror positioned about 45 degrees respect to the direction of propagation (z axis). Then it is focused into the sample by 10x objective (OLYMPUS Plan N, NA=0.25) which is mounted on a motorized translation stage (Thorlabs KMTS50E) with minimum incremental step of 0.05 µm. The backscattered light at both frequencies is collected and collimated by the same objective and, re-directed to the dichroic mirror which changes its direction by 90 degrees approximately. Then it is spectrally cleaned with a high-pass filter to remove any fundamental light, and properly re-aligned with a set of blue mirrors (i. e. with high reflectance at λ=400nm). At the exit, light propagates again on a horizontal plane and is focused (positive lens, f=5mm) for detection with a SPEX 500M spectrometer coupled to a photo-multiplier tube working in the photon counting regime. This is the experimental setup for the depth-profiling of the samples which always precedes polarization-resolved (PR) experiments. For a PR analysis at different z positions –chosen according to de depth profile—, the linear polarization at the entrance is rotated from 0 to 360 degrees with half-wave plate (HWP) put in a motorized computer-controlled holder, while at the detection stage the p-polarized and s-polarized modes with respect the zero at the entrance, are resolved by using an

analyzer (fixed in position) and HWP (fast axis positions 0 and 45 degrees), placed before spectrometer in the following order: HWP-A-S.
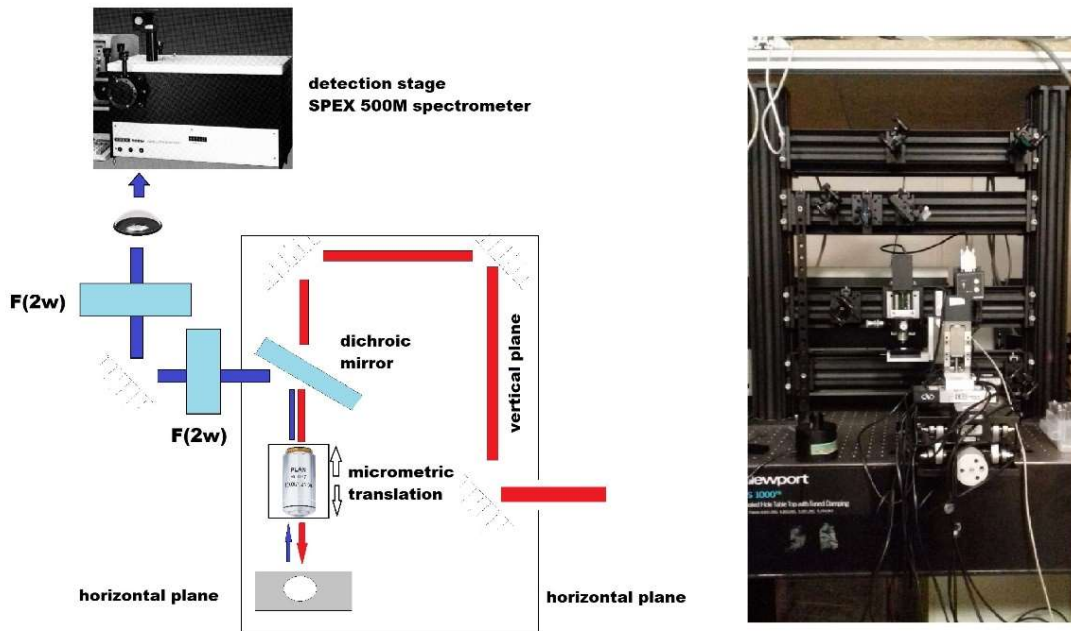

Figure II-7. Microscope-like experimental setup used for the SHG measurements. **Left:** schematized. **Right:** actual picture showing the installation at the laboratory of the *Optique Non Linéaire et Interfaces* group, at the *Institut Lumiere Matiere, Université Claude Bernard Lyon 1*.

As a light source, it has been used a Chameleon Discovery laser system by COHERENT, featuring 140 fs pulses operating at a repetition rate of 80 MHz, with an average power of about 700 mW at the laser exit for a fundamental wavelength of 800 nm. In here, details on the sample preparation of the powder-print are given. By gently pressed, it is meant the pressure applied to very small quantity of powder (about 0.1 mg) by means of putting three commercial microscope slides (1 mm thick according to provider) on top of the powder, without exerting any additional pressure. The powder is supported in a microscope coverslip (130 µm thick according to provider) and prior to pressing it is homogenously sliced with an edge of another coverslip. The (8 ± 2) µm thickness of the powder-print has been determined by comparing several depth profiles performed by roster scanning a 10x10 µm square (2 µm step) with a XY piezo-translation stage. It is being assumed that the maximum SHG intensity in the profile corresponds to a physical situation in which the beam focus is at the air/powder interface (z=0). Thus, by depth profiling the SHG intensity of an HWP (which is made of two different layers of crystal quartz), an estimate of the powder-print thickness can be

obtained by subtracting the z_{max} position of its profile to that of a profile done on the HWP placed on top of another coverslip (see Figure II-8). The thickness of the HWP is of 0.5 mm, and because these optical components have high flatness quality control, this value is precise and thus no uncertainty is associated to it in the calculations. Adding the HWP-on-bottom configuration, the thickness of the microscope slide and coverslip are measured to be (1.102 ± 0.002) mm and (127 ± 1) μm, respectively; these were obtained by roster scanning an area of 50 x 50 μm with a step of 10μm.
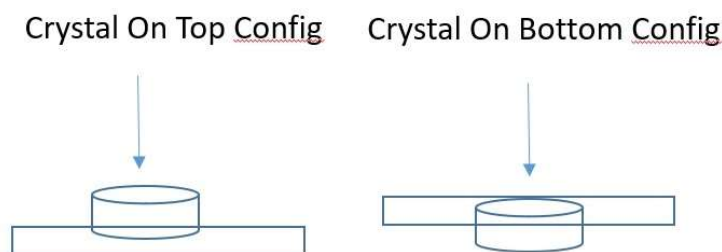
Figure II-8. Schematization of the experimental configurations used in combination with crystal quartz to determine the thickness of the analyzed powder-print sample preparation.

References

Chapter 3

[1] Kocsor, L.; Péter, L.; Corradi, G.; Kis, Z.; Gubicza, J.; Kovács, L. Mechanochemical Reactions of Lithium Niobate Induced by High-Energy Ball-Milling. *Crystals* **2019**, 9, 334; DOI:10.3390/cryst9070334.

[2] Chadwick, A.V.; Pooley, M.J.; Savin, S.L.P. Lithium ion transport and microstructure in nanocrystalline lithium niobate. *Phys. Status Solidi C* **2005**, 2, 302-305; DOI:10.1002/pssc.200460170.

[3] Heitjans, P.; Masoud, M.; Feldhoff, A.; Wilkening, M. NMR and impedance studies of nanocrystalline and amorphous ion conductors: lithium niobate as a model system. *Faraday Discuss.* **2007**, 134, 67-82; DOI:10.1039/B602887J.

[4] Sugak, D.Yu.; Syvorotka, I.I.; Buryy, O.A.; Yakhnevych, U.V.; Solskii, I.M.; Martynyuk, N.V.; Suhak, Yu.; Suchocki, A.; Zhydachevskii, Ya.; Jakiela, R.; Ubizskii, S.B.; Singh, G.; Janyani, V. Spatial distribution of optical coloration in single crystalline $LiNbO_3$ after high-temperature H_2/air treatments. *Opt. Mater.* **2017**, 70, 106-115; DOI:10.1016/j.optmat.2017.05.022.

[5] Sánchez-Dena, O.; Villagómez, C.J.; Fierro-Ruíz, C.D.; Padilla-Robles, A.S.; Farías, R.; Vigueras-Santiago, E.; Hernández-López, S.; Reyes-Esqueda, J.A. Determination of the Chemical Composition of Lithium Niobate Powders. *Crystals* **2019**, 9, 340; DOI:10.3390/cryst9070340.

[6] De Figueiredo, R.S.; Messaia, A.; Hernandes, A.C.; Sombra, A.S.B. Piezoelectric lithium niobate obtained by mechanical alloying. *J. Mater. Sci. Lett.* **1998**, 17, 449-451; DOI:10.1023/A:1006563924005.

[7] Pooley, M.J.; Chadwick, A.V. The Synthesis and Characterisation of Nanocrystalline Lithium Niobate. *Radiat. Eff. Defects Solids* **2003**, 158, 197-201; DOI:10.1080/1042015021000053213.

[8] Luo, J.H. Preparation of Lithium Niobate Powders by Mechanochemical Process. *Appl. Mech. Mater.* **2011**, 121-126, 3401-3405; DOI:10.4028/www.scientific.net/AMM.121-126.3401.

[9] Diaz-Moreno, C.A.; Farias-Mancilla, R.; Elizalde-Galindo, J.T.; González-Hernández, J.; Hurtado-Macias, A.; Bahena, D.; José-Yacamán, M.; Ramos, M. Structural Aspects LiNbO$_3$ Nanoparticles and Their Ferromagnetic Properties. *Materials* **2014**, 7, 7217-7225; DOI:10.3390/ma7117217.

[10] Fierro-Ruíz, C.D.; Sánchez-Dena, O.; Cabral-Larquier, E.M.; Elizalde-Galindo, J.T.; Farías, R. Structural and Magnetic Behavior of Oxidized and Reduced Fe Doped LiNbO$_3$ Powders. *Crystals*, **2018**, 8, 108. DOI:10.3390/cryst8030108.

[11] Yokoyama, T.; Urayama, K.; Naito, M.; Kato, M.; Yokoyama, T. The Angmill Mechanofusion System and its Applications. *KONA Powder and Particle J.* **1987**, 5, 59-69; DOI:10.14356/kona.1987011.

[12] Naito, M.; Shinohara, N.; Uematsu, K. Raw Materials. In *Handbook of Advandced Ceramics,* Somiya, S., Aldinger, F., Claussen, N., Spriggs, R.M., Uchino, K., Koumoto, K., Kaneno, M., Eds.; Elsevier: 2003; Volume I: Materials Science, p. 81-129, ISBN 0-12-654640-1.

[13] Suryanarayana, C. Mechanical alloying and milling. *Prog. Mater. Sci.* **2001**, 46, 1-184. DOI:10.1016/S0079-6425(99)00010-9.

[14] Kong, L. B.; Chang, T. S.; Ma, J.; Boey, F. Progress in synthesis of ferroelectric ceramic materials via high-energy mechanochemical technique. *Prog. Mater. Sci.* **2008**, 53, 207-322. DOI:10.1016/j.pmatsci.2007.05.001.

[15] Beke, B. *The Process of Fine Grinding,* 1st. ed.; Springer: Netherlands, 1981, ISBN 978-90-247-2462-8.

[16] Liao, Y.S; Luo, S.Y.; Yang, T.H. A thermal model of the wet grinding process. *J. Mater. Process. Technol.* **2000**, 101, 137-145; DOI:10.1016/S0924-0136(00)00440-4.

[17] Yekeler, M.; Ozkan, A.; Austin, L.G. Kinetics of fine wet grinding in a laboratory ball mill. *Powder Tech.* 114, 224-228; DOI:10.1016/S0032-5910(00)00326-0.

[18] Dolgin, B.P.; Vanek, M.A.; McGory, T.; Ham, D.J. Mechanical alloying of Ni, CO, and Fe with Ti. Formation of an amorphous phase. *J. Non-Cryst. Solids* **1986**, 87, 281-289; DOI:10.1016/S0022-3093(86)80002-3.

[19] SPEX Sample Prep, Laboratory Equipment for Sample Preparation & Handling. Available online: https://www.spexsampleprep.com/ (accessed on 07 October 2019).

[20] Suryanarayana, C. Does a disordered γ-TiAl phase exist in mechanically alloyed Ti—Al powders? *Intermetallics* **1995**, 3, 153-160; DOI:10.1016/0966-9795(95)92680-X.

[21] Lü, L.; Lai, M.O. *Mechanical Alloying,* 1st. ed.; Kluwer Academic Publishers: Boston, MA, 1998, ISBN 978-0-7923-8066-5.

[22] Padella, F.; Paradiso, E.; Burgio, N.; Magini, M.; Martelli, S.; Guo, W.; Iasonna, A. Mechanical alloying of the Pd-Si system in controlled conditions of energy transfer. *J. Less-Common Metals* **1991**, 175, 79-90; DOI:10.1016/0022-5088(91)90351-4.

[23] Park, Y.H.; Hashimoto, H.; Watababe, R. MORPHOLOGICAL EVOLUTION AND AMORPHIZATION OF Ti/Cu AND Ti/Al POWDERS DURING VIBRATORY BALL MILLING. *Mater. Sci. Forum* **1992**, 88-90, 59-66; DOI:10.4028/www.scientific.net/MSF.88-90.59.

[24] Takacs, L.; Pardavi-Horvarth, M. Nanocomposite formation in the Fe3O4-Zn system by reaction milling. *J. Appl. Phys.* **1994**, 75, 5864-5866; DOI:10.1063/1.355543.

[25] Harringa, J.L.; Cook, B.A.; Beaudry, B.J. Effects of vial shape on the rate of mechanical alloying in Si$_{80}$Ge$_{20}$. *J. Mater. Sci.* **1992**, 27, 801-804; DOI:10.1007/BF00554056.

[26] Suryanarana, C.; Chen, G.-H.; Froes, F.H. MILLING MAPS FOR PHASE IDENTIFICATION DURING MECHANICAL ALLOYING. *Scripta Metall. Mater.* **1992**, 26, 1727-1732; DOI:10.1016/0956-716X(92)90542-M.

[27] Chin, Z.-H.; Perng, T.P. Amorphization of Ni-S-C Ternary Alloy Powder by Mechanical Alloying. *Mater. Sci. Forum* **1997**, 235-238, 121-126; DOI:10.4028/www.scientific.net/MSF.235-238.121.

[28] Kis-Varga, M.; Beke, D.L. Phase Transitions in Cu-Sb Systems Induced by Ball Milling. *Mater. Sci. Forum* **1996**, 225-227, 465-470; DOI:10.4028/www.scientific.net/MSF.225-227.465.

[29] Takacs, L. Multiple combustion induced by ball milling. *Appl. Phys. Lett.* **1996**, 69, 436-438; DOI:10.1063/1.118086.

[30] Xue, J.; Wan, D.; Lee, S.-E.; Wang, J. Mechanochemical Synthesis of Lead Zirconate Titanate from Mixed Oxides. *J. Am. Ceram. Soc.* **1999**, 82, 1687-1692; DOI:10.1111/j.1151-2916.1999.tb01987.x.

[31] Kalinnikov, V.T.; Gromov, O.G.; Kunshina, G.B.; Ku'zmin, A.P.; Lokshin, E.P.; Ivanenko, V.I. Preparation of LiTaO$_3$, LiNbO$_3$, and NaNbO$_3$ from Peroxide Solutions. *Inorg. Mater.* **2004**, 40, 411-414; DOI:10.1023/B:INMA.0000023967.76203.61.

[32] Liu, M.; Xue, D. An efficient approach for the direct synthesis of lithium niobate powders. *Solid State Ionics* **2006**, 177, 275-280; DOI:10.1016/j.ssi.2005.11.007.

[33] Liu, M.; Xue, D.; Luo, C. Wet chemical synthesis of pure LiNbO$_3$ powders from simple niobium oxide Nb$_2$O$_5$. *J. Alloys Compd.* **2006**, 426, 118-122; DOI:10.1016/j.jallcom.2006.02.019.

[34] Liu, M.; Xue, D.; Li, K. Soft-chemistry synthesis of LiNbO$_3$ crystallites. *J. Alloys Compd.* **2008**, 449, 28-31; DOI:10.1016/j.jallcom.2006.03.104.

[35] Pitcher, M.W; He, Y.; Bianconi, P.A. Facile in situ synthesis of oriented LiNbO$_3$ single crystals in a polymer matrix. *Mater. Chem. Phys.* **2005**, 90, 57-61; DOI:10.1016/j.matchemphys.2004.09.030.

[36] Zhenxiang, C.; Kiyoshi, O.; Akimitsu, M.; Hideo, K. Formation of Niobates from Aqueous Peroxide Solution. *Chem. Lett.* **2004**, 33, 1620-1621; DOI:10.1246/cl.2004.1620.

[37] Zeng, H.C.; Tung, S.K. Synthesis of Lithium Niobate Gels Using a Metal Alkoxide-Metal Nitrate Precursor. *Chem. Mater.* **1996**, 8, 2667-2672; DOI:10.1021/cm960197n.

[38] Camargo, E.R.; Kakihana, M. Low temperature synthesis of lithium niobate powders based on water-soluble niobium malato complexes. *Soild State Ionics* **2002**, 151, 413-418; DOI:10.1016/S0167-2738(02)00547-7.

[39] Niederberger, M.; Pinna, N.; Polleux, J.; Antonietti, M. A General Soft-Chemistry Route to Perovskites and Related Materials: Synthesis of BaTiO$_3$, BaZrO$_3$, and LiNbO$_3$ Nanoparticles. *Angew. Chem. Int. Ed.* **2004**, 43, 2270-2273; DOI:10.1002/anie.200353300.

[40] An, C.; Tang, K.; Wang, C.; Shen, G.; Jin, Y.; Qian, Y. Characterization of LiNbO3 nanocrystals prepared via a convenient hydrothermal route. *Mater. Res. Bull.* **2002**, 37, 1791-1796; DOI:10.1016/S0025-5408(02)00869-3.

[41] Yoshikawa, Y.; Tsuzuki, K. Fabrication of Transparent Lead Lanthanum Zirconate Titanate Ceramics from Fine Powders by Two-Stage Sintering. *J. Am. Ceram. Soc.* **1992**, 75, 2520-2528; DOI:10.1111/j.1151-2916.1992.tb05606.x.

[42] Oren, E.E.; Taspinar, E.; Tas, A. C. Preparation of Lead Zirconate by Homogeneous Precipitation and Calcination. *J. Am. Ceramc. Soc.* **1997**, 80, 2714-2716; DOI:10.1111/j.1151-2916.1997.tb03181.x.

[43] Camargo, E.R.; Frantti, J.; Kakihana, M. Low-temperature chemical synthesis of lead zirconate titanate (PZT) powders free from halides and organics. *J. Mater. Chem.* **2001**, 11, 1875-1879; DOI:10.1039/B0090960.

[44] Blum, J.B.; Gurkovich, S.R. Sol-gel-derived PbTiO$_3$. *J. Mater. Sci.* **1985**, 20, 4479-4483; DOI:10.1007/BF00559337.

[45] Kim, S.; Jun, M.-c.; Hwang, S.-c. Preparation of Undoped Lead Titanate Ceramics via Sol-Gel Processing. *J. Am. Ceram. Soc.* **1999**, 82, 289-296; DOI:10.1111/j.1551-2916.1999.tb20060.x.

[46] Tartaj, J.; Moure, C.; Lascano, L.; Durán, P. Sintering of dense ceramics bodies of pure lead titanate obtained by seeding-assisted chemical sol-gel. *Mater. Res. Bull.* **2001**, 36, 2301-2310; DOI:10.1016/S0025-5408(01)00712-7.

[47] Sato, S.; Murakata, T.; Yanagi, H.; Miyasaka, F.; Iwaya, S. Hydrothermal synthesis of fine perovskite PbTiO$_3$ powders with a simple mode of size distribution. *J. Mater. Sci.* **1994**, 29, 5657-5663; DOI:10.1007/BF00349961.

[48] Moon, J.; Li, T.; Randall, C.A.; Adair, J.H. Low temperature synthesis of lead titanate by a hydrothermal method. *J. Mater. Res.* **1997**, 12, 189-197; DOI:10.1557/JMR.1997.0025.

[49] Peterson, C.R.; Slamovich, E.B. Effect of Processing Parameters on the Morphology of Hydrothermally Derived $PbTiO_3$ Powders. *J. Am. Ceram. Soc.* **1999**, 82, 1702-1710; DOI:10.1111/j.1151-2916.1999.tb01989.x.

[50] Chen, D.-R.; Jiao, X.-L.; Xu, R.-R. Hydrothermal synthesis of $PbZrxTi_{1-x}O_3$ (x=0.45-0.65) powders without using alkaline mineralizer. *J. Mater. Sci. Lett.* **1998**, 17, 53-56; DOI:10.1023/A:1006545708617.

[51] Narendar, Y.; Messing, G.L. Kinetic Analysis of Combustion Synthesis of Lead Magnesium Niobate from Metal Carboxylate Gels. *J. Am. Ceram. Soc.* **1997**, 80. 915-924; DOI:10.1111/j.1151-2916.1997.tb02922.x.

[52] Arendt, R.H.; Rosolowski, J.H.; Szymaszek, J.W. Lead zirconate titanate ceramics from molten salt solvent synthesized powders. *Mater. Res. Bull.* **1979**, 14, 703-709; DOI:10.1016/0025-5408(79)90055-2.

[53] Chiu, C.C.; Li, C.C.; Desu, S.B. Molten Salt Synthesis of a Complex Perovskite, $Pb(Fe_{0.5}Nb_{0.5})O_3$. *J. Am. Ceram. Soc.* **1991**, 74, 38-41; DOI:10.1111/j.1151-2916.1991.tb07293.x.

[54] Santos, I.C.M.S.; Loureiro, L.H.; Silva, M.F.P.; Cavaleiro, A.M.V. Studies on the hydrothermal synthesis of niobium oxides. *Polyhedron* **2002**, 21, 2009-2015; DOI:10.1016/S0277-5387(02)01136-1.

[55] Grossmann, M.A.; Bain, E.C. *PINCIPLES OF HEAT TREATMENT*, 5th. ed.; America Society of Metals, Metals Park, Ohio, 1964.

[56] Rajan, T.V.; Sharma, C.P.; Sharma, A. *Heat Treatment: Principles and Techniques,* 2nd. ed.; PHI Learning Private Limited: New Delhi, India, 2011, ISNB 978-81-203-4095-4.

[57] Czichos, H. A.3. Materials and Their Characteristics: Overview. In *Springer Handbook of Materials Measurement Methods*, 1st ed.; Czichos, H., Saito, T., Smith, L., Eds.: Springer-Verlag: Leipzing, Germany, 2006, pp. 95-102, ISBN-13 978-3-540-20785-6.

[58] Czichos, H.; Saito, T.; Smith, L. (Eds.). *Springer Handbook of Materials Measurement Methods,* 1st. ed.; Springer-Verlag: Leipzing, Germany, 2006, ISBN-13 978-3-540-20785-6.

[59] Cullity, B.D. *ELEMENTS OF X-RAY DIFFRACTION,* 1st. ed.; Addison-Wesley: Reading, Massachusetts, USA, 1956, Library of Congress Catalog No. 56-10137.

[60] Compton, A.H.; Allison, S.K. *X-Rays in Theory and Experiment*, 2nd. ed.; D. VAN NOSTRAND COMPANY: 1935.

[61] Tilley, R.J.D. *Crystals and Crystal Structures*, 1st. ed.; John Wiley & Sons: England, 2006, ISBN-13 978-0-470-01820-0.

[62] Klug, H.P; Alexander, L.E. *X-RAY DIFFRACTION PROCEDURES: For Polycrystalline and Amorphous Materials*, 2nd. ed.; John Wiley & Sons: USA, 1974, ISBN 0-471-49369-4.

[63] Dinnebier, R.E.; Billinge, S.J.L. Principles in Powder Diffraction. In *Powder Diffraction: Theory and Practice,* 1st ed.; Dinnebier, R.E., Billinge, S.J.L., Eds.: The Royal Society of Chemistry: Cambridge, United Kingdom, 2008, pp. 1-19, ISBN 978-0-85404-231-9.

[64] Pecharsky, V.K.; Zavalij, P.Y. *Fundamentals of Powder Diffraction and Structural Characterization of Materials,* 2nd. ed.; Springer: New York, USA, 2009, DOI:10.1007/978-0-387-09579-0.

[65] Will, G. *Powder Diffraction: The Rietveld Method and the Two-Stage Method to Determine and Refine Crystal Structures from Powder Diffraction Data,* 1st. ed.; Springer-Verlag: Berlin/Heidelberg, Germany, 2006, ISBN -13 978-3-540-27986-0.

[66] Wilson, A.J.C. *MATHEMATICAL THEORY OF X-RAY POWDER DIFFRACTOMETRY,* 1st. ed.; N.V. Phillips' Gloeilampenfabrieken: Eindhoven, Netherlands, 1963.

[67] Maeda, K.; Mizubayashi, H. B.5. Nanoscopic Architecture and Microstructure. In *Springer Handbook of Materials Measurement Methods*, 1st ed.; Czichos, H., Saito, T., Smith, L., Eds.: Springer-Verlag: Leipzing, Germany, 2006, pp. 153-227, ISBN-13 978-3-540-20785-6.

[68] v. Laue, M. Lorentz-Faktor und Intensitätsverteilung in Debye-Scherrer-Ringen. *Zeitschrift für Kristallographie-Crystalline Materials* **1926**, 64, 115-142; DOI:10.1524/zkri.1926.64.1.115.

[69] Bragg, L. *The Crystalline State Vol I: A General Survey;* G. Bell & Sons: London, 1966.

[70] Seljakow, N. Eine röntgenographische Methode zur Messung der absoluten Dimensionen einzelner Kristalle in Körpern von fein-kristallinischem Bau. *Zeitschrift für Physik* **1925**, 31, 439-444; DOI:10.1007/BF02980596.

[71] Rietveld, H.M. The Rietveld method. *Phys. Scr.* **2014**, 89, 098002; DOI:10.1088/0031-8949/89/9/098002.

[72] Rietveld, H.M. Line profiles of neutron powder-diffraction peaks for structure refinement. *Acta Cryst.* **1967**, 22, 151-152; DOI:10.1107/S0365110X67000234.

[73] Rietveld, H.M. A Profile Refinement Method for Nuclear and Magnetic Structures. *J. Appl. Cryst.* **1969**, 2, 65-71; DOI:10.1107/S0021889869006558.

[74] XRD Software-DIFRAC.SUITE, TOPAS Software. Available online: https://www.bruker.com/products/x-ray-diffraction-and-elemental-analysis/x-ray-diffraction/xrd-software/topas.html (accessed on 16 October 2019).

[75] BGMN Home Page, Site map. Available online: http://www.bgmn.de/ (accessed on 16 October 2019).

[76] Malvern Panalytical, HighScore Plus. Available online: https://www.malvernpanalytical.com/en/products/category/software/x-ray-diffraction-software/highscore-with-plus-option?creative=338893424388&keyword=x%20pert%20highscore%20plus&matchtype=e&network=g&device=c&gclid=EAIaIQobChMIwK708OSg5QIVDtvACh1vLAubEAAYASAAEgJf3PD_BwE (accessed on 16 October 2019).

[77] FullProf Suite. Available online: https://www.ill.eu/sites/fullprof/ (accessed on 16 October 2019).

[78] GSAS-II. Available online: https://subversion.xray.aps.anl.gov/trac/pyGSAS (accessed on 16 October 2019).

[79] Degen, T.; Sadki, M.; Bron, E.; König, U.; Nènert, W. The HighScore suite. *Powder Diffr.* **2014**, 29, S13-S18; DOI:10.1017/S0885715614000840.

[80] Young, R.A. *The Rietveld Method*, 1st ed.; Oxford University Press: New York, USA, 1993, ISBN 0-19-855912-7.

[81] Bish, D.L.; Howard, S.A. Quantitative Phase Analysis Using the Rietveld Method. *J. Appl. Cryst.* **1988**, 21, 86-91; DOI:10.1107/S0021889887009415.

[82] v. Dreele, R.B. Rietveld Refinement. In *Powder Diffraction: Theory and Practice,* 1st ed.; Dinnebier, R.E., Billinge, S.J.L., Eds.: The Royal Society of Chemistry: Cambridge, United Kingdom, 2008, pp. 266-281, ISBN 978-0-85404-231-9.

[83] Pezzotti, G. Raman spectroscopy of piezoelectrics. *J. Appl. Phys.* **2013**, 113, 211301; DOI:10.1063/1.4803740.

[84] Lewis, I.R.; Edwards, H.G.M. (Eds.) *Handbook of Raman Spectroscopy: From the Research Laboratory to the Process Line,* 1st. ed.; Marcel Dekker: New York, USA, 2001, ISBN 0-8247-0557-2.

[85] Long, D.A. *The Raman Effect: A Unified Treatment of the Theory of Raman Scattering by Molecules,* 1st ed.; John Wiley & Sons: England, 2002, ISBN 0-471-49028-8.

[86] Torrent, J. Barrón, V. Diffuse Reflectance Spectroscopy. In *Methods of Soil Analysis Part 5—Mineralogical Methods,* 1st. ed.; Ulery, A.L., Drees, R., Eds.; Soil Society of America: Wisconsin, USA, 2008, pp. 367-385; ISBN 978-0-89118-846-9.

[87] Kubelka, P. New Contributions to the Optics of Intensely Light-Scattering Materials. Part I. *J. Opt. Soc. Am.* **1948**, 38, 448-457; DOI:10.1364/JOSA.38.000448.

[88] Kubelka, P. New Contributions to the Optics of Intensely Light-Scattering Materials. Part II: Nonhomogeneous Layers. *J. Opt. Soc. Am.* **1954**, 44, 330-335; DOI:10.1364/JOSA.44.000330.

[89] Karathanasis, A.D. Thermal Analysis of Soil Minerals. In *Methods of Soil Analysis Part 5—Mineralogical Methods,* 1st. ed.; Ulery, A.L., Drees, R., Eds.; Soil Society of America: Wisconsin, USA, 2008, pp. 367-385; ISBN 978-0-89118-846-9.

[90] Speyer, R.F. *THERMAL ANALYSIS OF MATERIALS*, 1st. ed.; Marcel Dekker: New York, USA, 1994, ISBN 0-8247-8963-6.

[91] Flegler, S.L.; Heckman, J.W.Jr.; Klomparens, K.L. *SCANNING AND TRANSMISSION ELECTRON MICROSCOPY: AN INTRODUCTION*,1st. ed.; W. H. Freeman and Company: New York, USA, 1993.

[92] White, G.N. Scanning Electron Microscopy. In *Methods of Soil Analysis Part 5—Mineralogical Methods,* 1st. ed.; Ulery, A.L., Drees, R., Eds.; Soil Society of America: Wisconsin, USA, 2008, pp. 367-385; ISBN 978-0-89118-846-9.

Chapter 4

[93] Crystallographic Open Database, Information for card entry 2101175. Available online: http://www.crystallography.net/cod/2101175.html (accessed online on 16 October 2019).
[94] FIZ Karlsruhe ICSD, ICSD- Inorganic Crystal Structure Database. Available online: www2.fiz-karlsruhe.de/icsd_home.html (accessed on 16 October 2019).
[95] Chowdhury, A.U.; Zhang, S.; Simpson, J. Powders Analysis by Second Harmonic Generation Microscopy. *Anal. Chem.* **2016**, 88, 3853-3863; DOI:10.1021/acs.analchem.5b04942.

PART III

RESULTS

(PRESENTATION AND DISCUSSION)

CONCLUSIONS AND PERSPECTIVES

Chapter 5: Materials Science

Results on the Chemical Composition of Lithium Niobate powders

In here, the results on the principal axis of this investigation, regarding only the material aspects of Lithium Niobate (LiNbO$_3$; LN) powders, are given. These can also be consulted in the corresponding article recently published [1].

5.1 Powder X-ray Diffraction and Rietveld refinement

The obtained XRD pattern for sample LN-STm (see section 4.1 in PART II) is shown in the bottom line of Figure III-1. The corresponding pattern of single crystalline LN is in agreement with the one indexed in COD-2101175 [2]. For all samples, the difference between the obtained XRD patterns (I_{exp}) and their respective calculated patterns by means of Rietveld refinement (I_{ref}) is also shown in the upper half of this figure; for the secondary phases LiNb$_3$O$_8$ and Li$_3$NbO$_4$, ICSD-2921 and ICSD-75264 from The Inorganic Crystal Structure Database were used, respectively [3]. For all cases, this difference function tends to a common baseline, so that neither the formation of thermodynamically stable phases (other than LiNbO$_3$, Li$_3$NbO$_4$, and LiNb$_3$O$_8$) nor the presence of one of the precursors in an interstitial fashion can be deduced, that is, without having been participated in the formation of one of the involved phases.
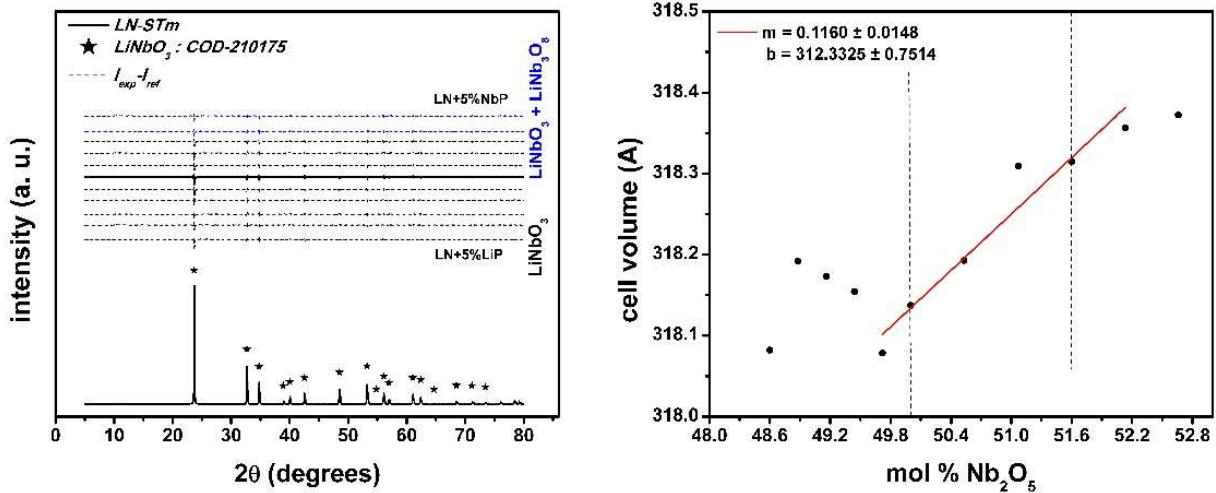
Figure III-1. XRD results. **Left:** experimental pattern of sample LN-STm and, for all samples, the differences between experimental and their respective calculated patterns by Rietveld refinement. The central sample, LN-STm, is distinguished from the rest by the solid line. **Right:** cell volume as a function of mol % Nb precursor. The edges of the ferroelectric pure LN phase are represented by the vertical dashed lines.

As seen in this figure, most of the synthesized powders resulted in a pure ferroelectric LN phase, except for samples LN+4%NbP and LN+5%NbP (blue lines). Figure III-2 and Table III-1 have been added for a better visualization of this argument. A loss of Li equivalent to the loss of 5 mol % Li_2CO_3 could be hastily addressed for the central sample LN-STm due to the calcination process. Nevertheless, this information can also be interpreted as having no loss of Li and thus the assumption of a non-ideal sensitivity for the XRD technique must be taken. In other words, a detection threshold of 5.0 mol % Li_2CO_3 = 1.4 mol % Nb_2O_5 exists for 'seeing' a secondary phase by the XRD analysis combined with the structure refinement done in this investigation. This assumption has been considered in this investigation, thus defining the boundaries that delimit the pure ferroelectric LN phase for samples LN-STm (Li excess) and LN+3%NbP (Nb excess). For the calculation of the mol % equivalence between the precursors, the values for the relative atomic masses of Li and Nb have been used as presented in the Periodic Table provided by the Royal Society of Chemistry [4].

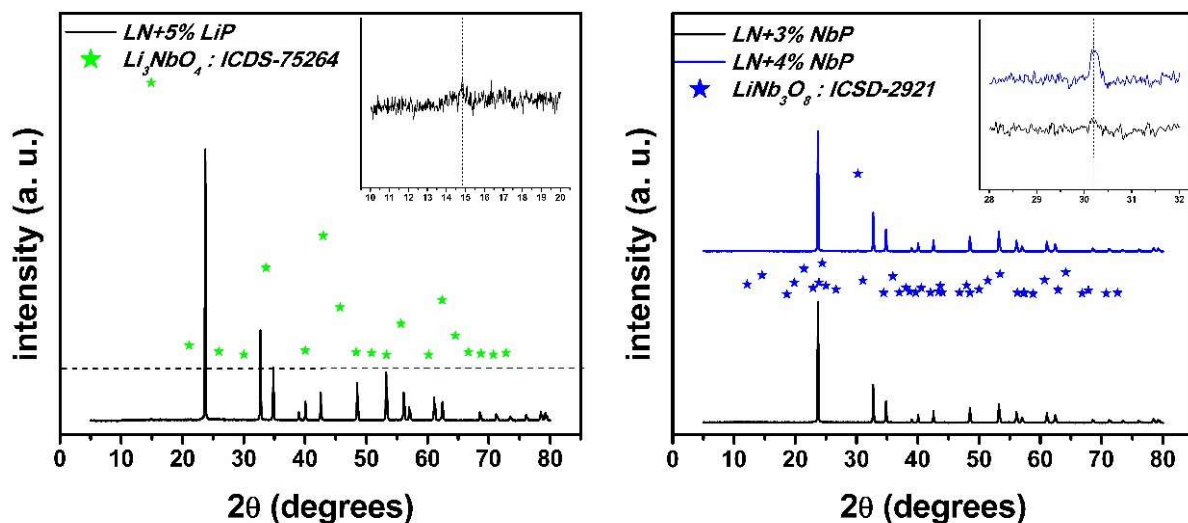**Figure III-2.** XRD patterns close to the boundaries of pure ferroelectric LN phase. **Left:** under the assumption of no Loss of Li, sample LN-STm is on the excess of the Li boundary. **Right:** sample LN+3%NbP is on the excess of Nb boundary.

Table III-1. Phase percentages present in the synthesized samples, along with the calculated cell volumes and relevant agreement indices of the refinement process.

Sample	% LiNbO$_3$	% Li$_3$NbO$_4$	% LiNb$_3$O$_8$	Cell Volume ($\dot{A}^3$)	Weighted R Profile	Goodness of Fit
LN+5%LiP	99.9	0.1	0	318.0820	5.82	2.03
LN+4%LiP	100	0	0	318.1917	5.24	1.48
LN+3%LiP	100	0	0	318.1732	5.58	1.50
LN+2%LiP	100	0	0	318.1546	5.60	1.49
LN+1%LiP	100	0	0	318.0787	5.70	1.52
LN-STm	100	0	0	318.1374	5.71	1.57
LN+1%NbP	100	0	0	318.1930	5.52	1.55
LN+2%NbP	100	0	0	318.3095	5.71	1.53
LN+3%NbP	100	0	0	318.3149	5.54	1.65
LN+4%NbP	98.2	0	1.8	318.3566	5.54	1.51
LN+5%NbP	97.8	0	2.2	318.2735	5.54	1.57

The calculated cell volumes are plotted in Figure III-1 (right side) as a function of the averaged Nb content in the crystallites $\langle c_{Nb} \rangle$, as calculated by the previous procedure (re-labeling of the samples in terms of their predicted chemical composition). A clear linear trend exists for a chemical composition (CC) range of 49.7–52.1 mol % Nb$_2$O$_5$. Hence, for future reference, it is first proposed the determination of $\langle c_{Nb} \rangle$ for LN powders (LNPws) in this CC range with the following equation:

$$\langle c_{Nb} \rangle = (8.6207 V_{cell} - 2692.5216) mol \% \pm 0.5 \ mol \%$$

Eq. III-1

where V_{cell} stands for the cell volume in (angstrom)^3 units, calculated by a standard structure refinement method. The 0.5 mol % uncertainty is determined by the sum of the uncertainty associated to the linear fitting (0.14 mol % Nb$_2$O$_5$) and half the longer step in the Nb precursor (0.53/2 = 0.27 mol % Nb$_2$O$_5$), both multiplied by the square root of the averaged goodness of fit factor for the six involved samples ($\sqrt{1.55}$). The uncertainty associated with the linear fitting has been determined following several calculations according to Baird [5]. See Appendix A for an example of the calculation of the overall uncertainty.

5.1.1 Justification of the assumption made in the X-ray Diffraction analysis

The reasoning behind the assumption made can be summarized in three main points. First, a good agreement can be seen with the phase diagram (Figure I-1), upon which by close inspection around T = 850 °C, a CC range of approximately 1.7 mol % Nb_2O_5 is deduced for the pure ferroelectric LN phase. In this investigation the observed range goes from the ST point = 50.0 mol % (sample LN-STm) to a near-CG point $\langle c_{Nb} \rangle = 53.0 - 1.4 = 51.6$ mol % (sample LN+3%NbP), that is $\Delta c_{pureLN} = 1.6$ mol % Nb_2O_5. A direct explanation would not be found for an estimated range of 4.4 mol % Nb_2O_5 if this assumption had not been taken. Secondly, under these circumstances it follows that out of 11 synthesized samples, only samples LN-STm, LN+1%NbP, LN+2%NbP, and LN+3%NbP resulted to have a pure ferroelectric LN phase. It will be soon shown that, for all the performed studies, unmistakable linear relationships happen to exist among these samples and their corresponding experimental parameters (related to the CC); a striking, very sensitive, deviation from these trends is observed for all samples out of this range, in some cases even under the consideration only of neighbor samples such as LN+1%LiP and LN+4%NbP. Lastly, besides the well-known difficulties to produce single-phase ST LN at temperatures used in solid-state reactions (T ≥ 1200 °C) [6, 7], much ambiguity can be found in the literature concerning deviation from stoichiometry in the formation of LNPws at calcination temperatures near T = 850 °C. Whereas only one work is found to report no loss of Li after two 16-hour reaction periods at 1120 °C [8], other authors have observed the loss of Li at 600–800 °C within at least three different investigations [7, 9, 10]. However, these methods of synthesis are very different from one from the other, except for those in the works published in 2006 (Liu et al.) [7] and 2008 (Liu et al.) [10], which are aqueous soft-chemistry methods. The deviation from stoichiometry tendency in the formation of LNPws through aqueous soft-chemistry methods, in comparison to non-aqueous (as in this investigation), has already been identified [11]. Besides, high-energy milling has previously been proposed as a method to prevent loss of Li, in contrast to Pechini's method, sol-gel, and coprecipitation [12].

It is also worth mentioning that De Figueiredo et al. [13] had a similar observation in their investigation: they had a small amount of non-reacted Li_2CO_3 not detected by XRD, but only identified after Differential Thermal Analysis (DTA) and Infrared Spectroscopy; the LNPws were synthesized via mechanical alloying. They explained this observation by

assuming that the number and size of the Li_2CO_3 nanocrystals were sufficiently low and small to not being detected by XRD. Hence, the assumption taken of no loss of Li and the existence of a detection threshold of 1.4 mol % Nb_2O_5 in XRD might have been justified with these lines. This detection threshold can be considered unique and expected to change according to different experimental variables and analysis tools, including spatial and temporal size of the step during the experiment, brand and model of equipment utilized, as well as the software used for Rietveld refinement, among others.

5.2 Raman Spectroscopy

Verification of the linear equation for the Raman active mode centered at 876 cm^{-1} [14-16] was done by using the assembled Raman system (Figure II-6, left side) on bought stoichiometric (ST) and congruent (CG) LN single-crystal wafers [17]. Even though the experimental conditions therein described were not exactly reproduced, this could be accomplished within the given absolute accuracy and, thus, calibration of this equipment could be done. At this instance, use of the equation for the Raman band located at 876 cm^{-1} has been done [15, 16]. A detailed description of the phonon branches of single crystal LN and their assignment can be found elsewhere [18, 19]. No specifications regarding the resolution of the Raman bands or fitting techniques are given by Schlarb et al. [15] or Malovichko et al. [16], although these procedures are critical for achieving great accuracy in the determination of the LN chemical composition (CC) [15, 18-20]. Moreover, it is not clearly stated whether the complete linewidth (Γ), or just the halfwidth, is to be entered in this equation.

The resolution of this Raman band was explored after normalization of the full spectra, by two distinct line shape fittings: Gaussian and Lorentzian (see Figure III-3). The Full Width at Half Maximum (FWHM; Γ) was extracted from the fitting (Origin Pro 8) and used in the calculations. Change of the intercept value from 53.29 to 54.8 had also been tried, as suggested whenever no polished single crystals are available [15]. From all the calculations performed, it was noticed that only for those (halfwidths) under a Lorentzian fit and using the intercept value of 54.8, the calculated Li contents follow this equation within the uncertainty of 0.2% mol, which "govern the absolute accuracy of the described method" [15]. As shown in Table III-2, the values obtained by this calculation were $\langle c_{Li} \rangle$ =50.3 mol

% for the ST wafer and 48.5 mol % for the CG one. Thus, this approach has been adopted for the investigation with the LNPws. Before presenting these results, one more point needs to be further discussed.
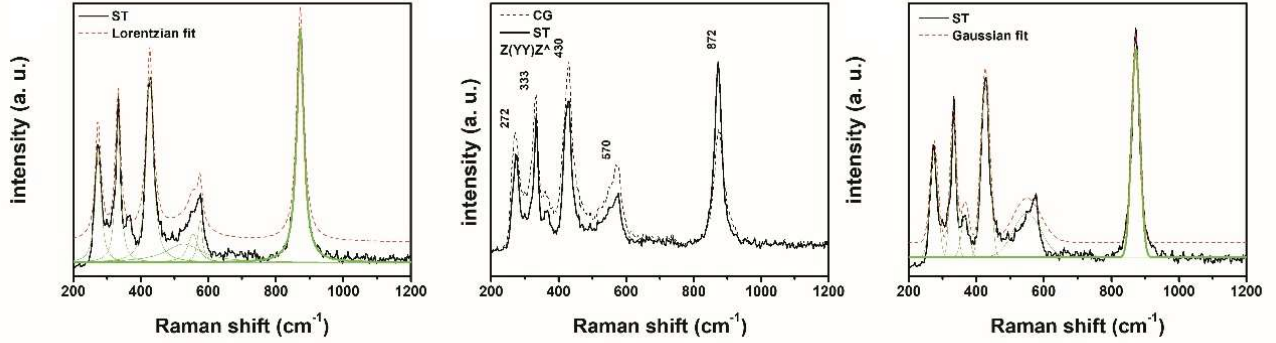

Figure III-3. Polarized Raman spectra of lithium niobate single crystals, measured with the custom-made Raman system (no detection of Raman intensity for shifts below 200 cm^{-1}). **Left:** resolution of the spectra by means of a multi-peak *Lorentzian* fitting, a good fitting of the band located at 872 cm^{-1} can be seen. **Center:** unresolved Raman bands of stoichiometric (ST) and congruent (CG) crystals. **Right:** resolution of the spectra by means of a multi-peak *Gaussian* fitting; in this case, a lesser agreement can be seen for the band at 872 cm^{-1}. For means of calculations, values from multi-peak fitting were not used, this type of fitting is here presented only for a better visualization.

Table III-2. Halfwidths determined by two different band resolution (876 cm^{-1}) procedures and Li contents calculated according to the equation given by Schlarb et al [15] and Malovichko et al [16]; * Γ=FWHM, these authors do not add the division by 2, it is not clearly stated whether Γ stands for the full width of the band or just the halfwidth. The measurements were done with the custom-made Raman system under polarization conditions in the experimental configuration $Z(YY)\bar{Z}$.

	Congruent crystal (48.6 mol%)	Stoichiometric crystal (50.0 mol%)
$\Gamma/2_{Lorentzian}$ **(cm^{-1})**	34.1122	24.5301
$\Gamma/2_{Gaussian}$ **(cm^{-1})**	20.2160	14.6859
$c_{Li}[mol\,\%] = 54.8 - 0.1837 * (\Gamma/2)$ **[cm^{-1}]**[15],* **(± 0.2 mol%)**		
$c_{Li,\,Lorentzian}$ **(mol%)**	48.5	50.3
$c_{Li,\,Gaussian}$ **(mol%)**	51.1	52.1
$c_{Li}[mol\,\%] = 53.29 - 0.1837 * (\Gamma/2)$ **[cm^{-1}]**[15, 16],* **(± 0.2 mol%)**		
$c_{Li,\,Lorentzian}$ **(mol%)**	47.0	48.8
$c_{Li,\,Gaussian}$ **(mol%)**	49.6	50.6

It can be argued that the value of 50.3 mol % for the ST wafer goes out of the uncertainty range, thus not justifying the implications made above. Nevertheless, it must be noticed that the experimental conditions used in this investigation are subtly different from those described by Schlarb et al. [15] and Malovichko et al. [16]. Succinctly, they used an

experimental *Z(YY)X* configuration (using Porto's convention [21]), whereas for our case, given certain technical limitations, a *Z(YY)Z̄* configuration was used in this investigation. Besides, no direct statement concerning the propagation of light along an axis of the studied crystals is done by these authors, but it can be inferred that they excited along the crystallographic Z-axis by recalling the condition of zero (or small) phonon directional dispersion to simplify their adjustments (band resolution) [15]. In the present case, wafers with Z-cuts were used, upon which light was made to impinge on normal to the surface. The incident radiation then propagates in a plane containing the extraordinary axis, inducing in this way short-range atomic forces (extraordinary refractive index) that compete to long-range atomic forces behind the splitting of longitudinal optic (LO) and transverse optic (TO) phonons [22]. Significant changes in the Raman spectra of LN single crystals, especially in the position of the bands located at 153 cm^{-1} and 578 cm^{-1} (red and blue shifts, respectively), have already been identified and addressed to the overlapping of the LO and TO lattice vibrations [22-24]. Such an overlapping is clearly a drawback for band resolution, and it might be the reason behind the discrepancy between predicted and measured values; interestingly, this is only relevant in single crystals of ST composition.

Application of the same procedure to the synthesized LN powders (LNPws) gives unsatisfactory results, according to the implications obtained from the XRD analysis (re-labeling of the samples in terms of their predicted CC, Figure III-1, right side). As expected, the same occurs if this is applied to the non-polarized Raman spectra, as shown in Table III-3. It worsens by considering the Raman band located at 153 cm^{-1}, where the corresponding linear equation is used and the Raman spectra are measured with the commercially available Raman system (Witec), which features the recording of intensity in the range 0–200 cm^{-1}. However, well defined linear trends can be seen for the calculated Raman halfwidths around the pure LN ferroelectric phase, but only for the case of the band at 876 cm^{-1} as measured under non-polarized experimental conditions. For both situations (Witec and self-assembled systems), the trend is of an increasing halfwidth with decreasing Li content; surprisingly, despite the great differences between both experimental configurations and conditions (Figure II-6), both trends are very similar. This feature can also be seen for the positions of the bands (x_c), and it remains for the resultant values of the halfwidths divided by the positions ($\Gamma/2x_c$). See Figure III-4.

Table III-3. Li contents calculated by Raman measurements for different experimental conditions. Equations given by Schlarb et al [15] and Malovichko et al [16] have been used; * Γ=FWHM, these authors do not add the division by 2, it is not clearly stated whether Γ stands for the full width of the band or just the halfwidth. The aim of this table is to show that these equations, which describe lithium niobate single crystals, are not suitable for the case of powders. The Li contents according to the phase percentage analysis done based on XRD data are given for each sample in between parentheses.

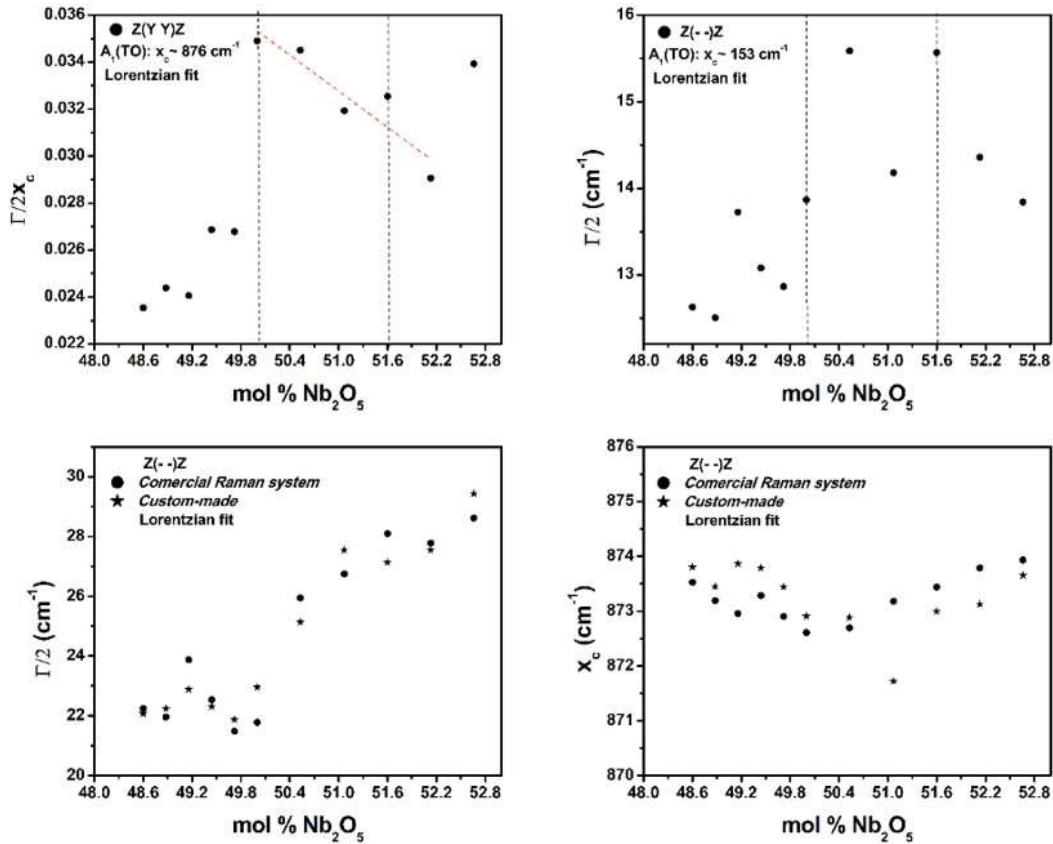| Sample	c_{Li} (mol%) $Z(YY)\bar{Z}$	c_{Li} (mol%) $Z(--)\bar{Z}$ (custom-made)	c_{Li} (mol%) $Z(--)\bar{Z}$ (Witec)	c_{Li} (mol%) $Z(--)\bar{Z}$ (Witec) *Equation for band at 153cm^{-1}*
	$c_{Li}[mol\%] = 54.8 - 0.1837 * (\Gamma/2)\ [cm^{-1}]^{[15],*}$			$c_{Li} = 53.03 - 0.4739 * (\Gamma/2)^{[15,16],*}$
NL+5%LiP (*51.4 mol%)*	51.0	50.7	50.7	47.0
NL+4%LiP (*51.1*)	50.9	50.7	50.8	47.1
NL+3%LiP (*50.8*)	50.9	50.6	50.4	46.5
NL+2%LiP (*50.6*)	50.5	50.7	50.7	46.8
NL+1%LiP (*50.3*)	50.5	50.8	50.9	46.9
LN-STm (*50.0*)	49.2	50.6	50.8	46.5
NL+1%NbP (*49.5*)	49.3	50.2	50.0	45.6
NL+2%NbP (*48.9*)	49.7	49.7	49.9	46.3
NL+3%NbP (*48.4*)	49.6	49.8	49.6	45.7
NL+4%NbP (*47.9*)	50.1	49.7	49.7	46.2
NL+5%NbP (*47.3*)	49.3	49.4	49.5	46.5

Figure III-4. Calculated parameters, halfwidth and center of Raman band, by Raman measurements obtained for different experimental conditions. **Upper left:** halfwidth as a function of the Nb content for p-polarized Raman band at 876 cm^{-1}; an apparent decreasing trend between these quantities is pointed out by the dashed red line. **Upper right:** same as the previous one, but for the non-polarized band at 153 cm^{-1}, measured with the commercially available (Witec) Raman system; not a trend can be seen in this case. **Bottom left:** same as 'Upper left', but for non-polarized measurements done with both available Raman systems; one curve closely resembles the other, despite of the great differences between both experimental configurations. **Bottom right**: as in the previous one, the similarity remains for the center positions of the Raman band at 876 cm^{-1}, for both experimental configurations.

Figure III-5 (right side) shows how this $\Gamma/2x_c$ parameter relates to the Nb content of the synthesized powders, as determined by XRD analysis. Given the similarity between the results obtained by both experimental configurations, this graph represents the average of such results. For sample LN-STm, the Raman spectra measured with the Witec system are shown in Figure III-5 (left side); these closely resemble those obtained in polycrystalline LN by Repelin et al [19].
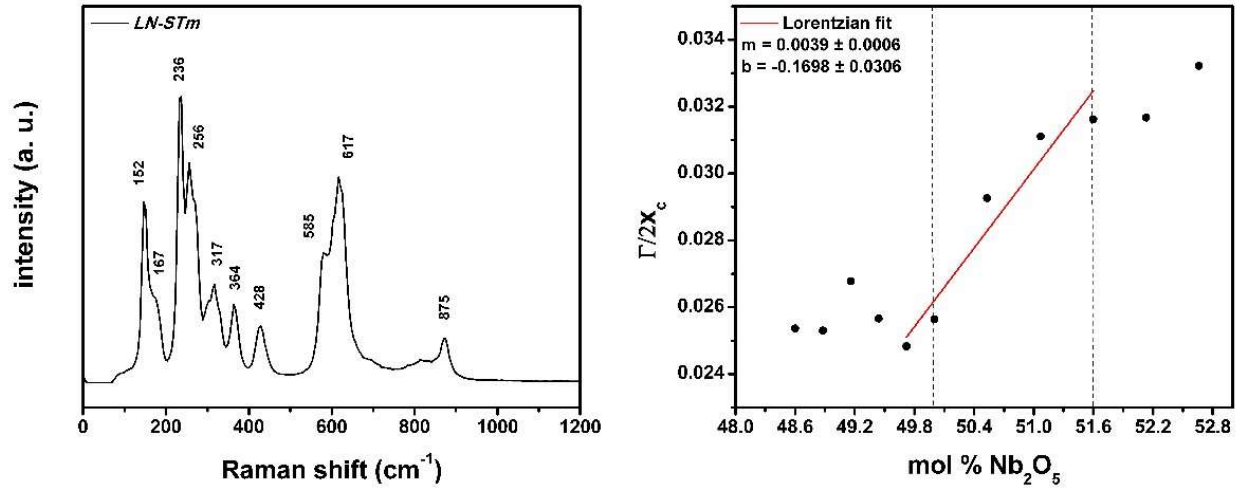
Figure III-5. Results obtained by Raman Spectroscopy. **Left:** non-polarized Raman spectra of the central sample LN-STm. Obtained with the commercially available Raman system. **Right:** linear trend upon which Eq. III-2 is based for the case of band resolution with a Lorentzian fit. The points represent the averaged calculated data from those obtained by the two distinct Raman systems.

As the resolution of this Raman band (876 cm^{-1}) by means of a Gaussian fitting does not entail significant changes either, the following equations are proposed for the determination of $\langle c_{Nb} \rangle$ in LNPws:

$$\langle c_{Nb} \rangle_L = \left(256.4103 * \left(\frac{\Gamma_L}{2x_c} \right) + 43.5385 \right) mol \% \pm 0.4 \, mol \%$$

$$\langle c_{Nb} \rangle_G = \left(588.2353 * \left(\frac{\Gamma_G}{2x_c} \right) + 42.7059 \right) mol \% \pm 0.5 \, mol \%$$

Eq. III-2

where Γ_i stands for the FWHM in cm^{-1} of the Raman band around 876 cm^{-1}, resolved by linear fitting either using a Lorentzian or a Gaussian line shape, x_c denotes the center of this Raman band. Normalization of the full Raman spectra precedes the linear fitting and, regardless of the line shape, enlargement around this band is suggested, extending as much as possible (precise determination of the baseline) and applying a single or double-peak fitting, rather than performing a multi-peak fitting of the full Raman spectra. Like in the XRD analysis, the uncertainty is determined by summation over half the longer step in the Nb precursor (0.53/2 = 0.27 mol % Nb$_2$O$_5$), the uncertainty associated to the linear fitting (0.12 mol % Nb$_2$O$_5$ (0.23 mol % Nb$_2$O$_5$) for the Lorentzian (Gaussian) case, and dividing by the square root of the averaged (five involved samples) reduced χ^2 fit factor obtained in the

resolution of the band $\sqrt{0.9823}$ ($\sqrt{0.9866}$). Once more, the uncertainty associated to the linear fitting is determined following several calculations according to Baird [5].

The fact that the trend remains linear is not surprising. Scott and Burns [8] have previously demonstrated this, based on experimentation; showing in this way that the Raman spectra from poly-crystalline LN inherits the essential features of those from single crystal LN [25]. Conceptually, this can be understood by recalling the intrinsic nature of LN to deviate from the stoichiometric point. Under regular circumstances, LN contains high amounts of intrinsic defects such as anti-site Nb ions (Nb_{Li}), which are compensated by their charge-compensating Li vacancies (V_{Li}) [26, 27]. Such a substitution mechanism imposes fundamental changes on the electronic structure, inducing in this way, variations in the macroscopic dielectric tensor of LN [15]. Yet, because in this substitution mechanism the gradual Nb increments are proportional to the decreasing of Li, the variations of the dielectric tensor are expected to be linear as far as the Nb-Li interchange is sufficiently small. Lastly, interestingly it can be noticed that the graph in Figure III-4 (bottom right) is akin to those reported by Doyle and Forbes after application of the method of continuous variations to determine the stoichiometry –that is, the coefficients within a chemical balanced equation— of solid products in inorganic solid-solid reactions by Diffuse Reflectance measurements [28]. Further investigation on this observation could bring new insights into the subject of the determination of the CC of powders, at least within the categories of oxides and/or materials adopting a perovskite-like structure.

123

5.3 UV-vis Diffuse Reflectance and Scanning Electron Microscopy

The sensitivity of the chemical composition (CC) of LN to the fundamental band gap or fundamental absorption edge has been previously reported for LN single crystals [29, 30]. Kovács et al have given a corresponding linear equation with different sets of fitting parameters, depending on the character of the refractive index (ordinary and extraordinary) and the definition of the absorption edge (either as corresponding to a value in the absorption coefficient of 20 cm^{-1} or 15 cm^{-1}) [30]. There is no point in using this equation to describe the CC of LN powders (LNPws) since these terms (refractive index and absorption coefficient) make no sense when related to powders.

In this investigation, the direct measurements of the Diffuse Reflectance (DR) spectra for the 11 samples are transformed to the Kubelka-Munk or *remission* function $F(R_\infty)$, straightforwardly with the acquisition software (*Spectra Suite*). Since this function is a proxy of the actual absorption spectrum [31], these data are used to find the fundamental absorption edge for all the samples. For practical purposes, a direct band gap is assumed for LN – noticing that it could also be assumed to be indirect [32]. Thus, under this assumption, the fundamental band gap is proportional to the square of the remission function, as is shown in Figure III-6 (left and central). The Nb content of the LNPws is linearly related to the fundamental band gap E_g (Figure III-6, right side). Eq. III-3 allows then to accurately determine the Nb content of a determined sample, in terms of E_g (in eV units).

$$\langle c_{Nb} \rangle = \left(3.9078 * E_g + 34.6229\right) mol\,\% \pm 0.4\,mol\,\%$$

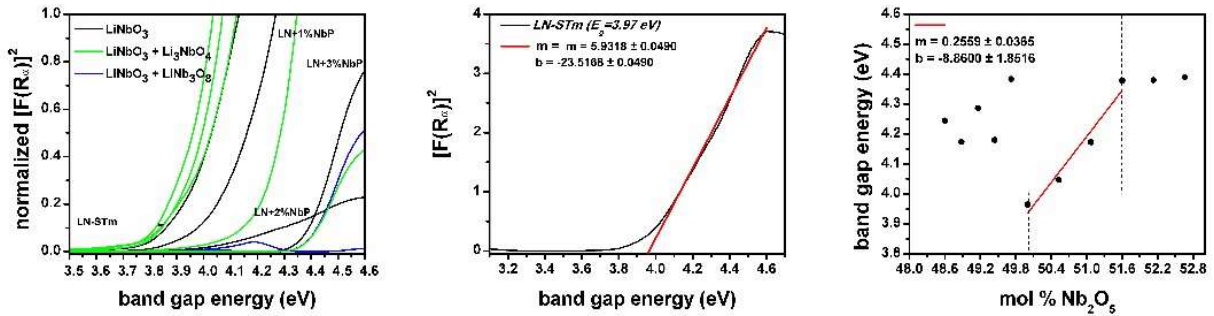<div align="right">Eq. III-3</div>

Figure III-6. Graphics derived from the analysis of the data obtained by UV-vis Diffuse Reflectance measurements. **Left:** normalized Kubelka-Munk or remission functions in terms of the energy of the light in eV units. **Central:** demonstration of the determination of the onset for sample LN-STm (assuming a direct interband transition) to determine the fundamental band gap energy. **Right:** fundamental band gap energy as a function of mol % Nb precursor.

On the other hand, the interaction of light with matter at a fundamental level must be considered in the DR and Raman Spectroscopy techniques. In other words, because of the ubiquitous randomness of the media, strong scattering effects are present in both Rayleigh (crystallite size) and Mie scattering (particle size) regimes. The study of the intensity and angular distribution of the scattered field by the powders has not been done on this investigation, however, certainty of the results obtained by these techniques is expected under certain limits if no large variations in the crystallite and particle average sizes are found.

Considering all the synthesized samples, the resultant average crystallites are distributed in a 100–300 nm range, with overall mean and standard deviation values of 157 and 58 nm, respectively. Also, for four randomly chosen samples, the distributions in particle size were determined by statistical analysis of micrographs obtained by Scanning Electron Microscopy (SEM). The obtained distributions were very similar and the centers (x_c) of these distributions fall within a band 1 µm thick, centered at 2.6 µm, as shown in Figure III-7.
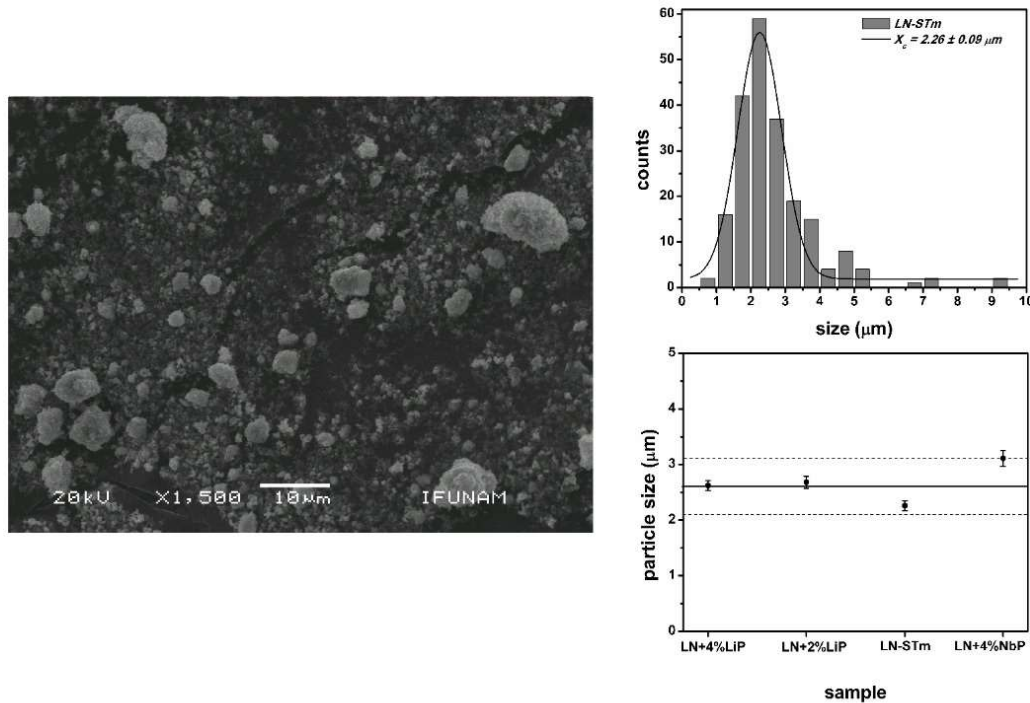
Figure III-7. Information derived from SEM. **Left:** micrograph of sample LN-STm. **Upper right:** particle size distribution for sample LN-STm. **Bottom right:** centers of the particle size distributions obtained for four randomly-chosen samples.

5.4 Differential Thermal Analysis

Regarding the ferroelectric-paraelectric phase transition, a change in the crystalline structure of LN occurs in which the symmetry of the system increases [26]. This second-order phase transition is described by the Landau order-disorder theory, where a finite discontinuity in the heat capacity of the system having this transition has been addressed as a direct thermodynamic consequence [33]. Figure III-8 (left side) shows the difference in temperature between the reference container for each of the studied samples; with this technique, only samples presenting a pure LN ferroelectric phase have been investigated. The Curie

temperatures are determined by the extrapolated departure from the baseline, these being plotted in Figure III-8 (right side) in terms of the Nb content. A nonlinear quadratic trend better describes this relation, with fitting coefficients A = 18623.560, B = -667.969, and C = 6.383; as expected, this is also the case for LN single crystals [34]. Nevertheless, use of the linear fitting coefficients is done in the analysis that follows, so that a simple calculation of an uncertainty value follows by use of Eq. III-4, where the Curie temperature T_C is in Celsius.

$$\langle c_{Nb} \rangle = (-0.0515 * T_C + 110.8505)mol\ \% \pm 0.4\ mol\ \%$$
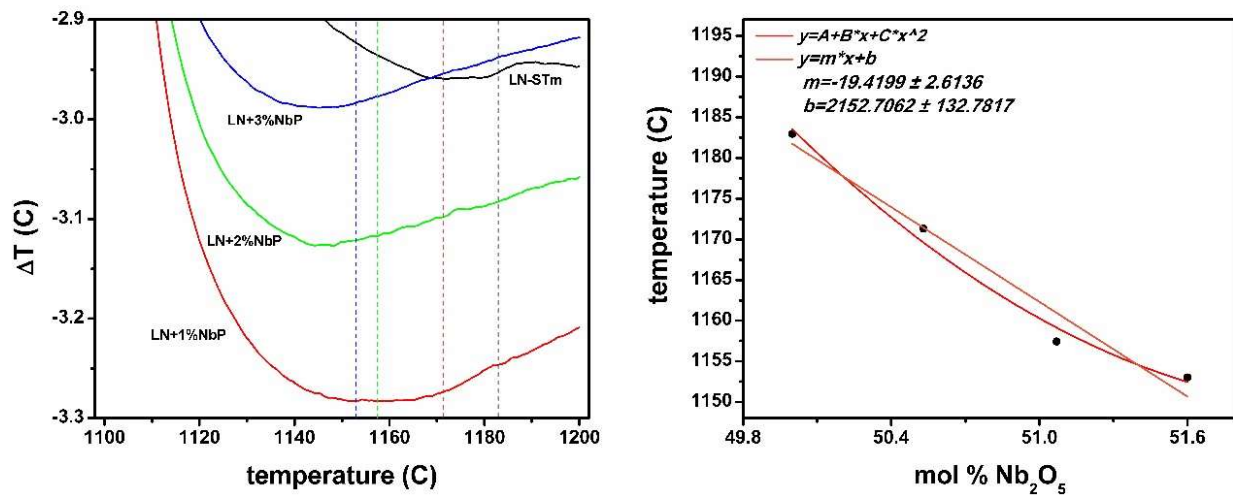
Eq. III-4

Figure III-8. Thermometric results. **Left:** Curie temperatures as a function of mol % Nb precursor. **Right:** obtained curves for samples within the pure LN phase. The Curie temperatures are determined by extrapolation of the departure from the baseline.

Use of this equation gives an estimate of T_C = 1181.56 °C (1153.41 °C) for a ST (CG) powder, whereas with the quadratic expression it is of 1182.61 °C and 1153.01 °C, respectively. These values vary in no more than 0.1%. Regarding single crystals, a variation of 0.7% can be found for the Curie temperatures calculated for these CCs, by use of equations reported in two independent investigations [34, 35]. Using the equation given by Bordui et al. [35], the calculated values are T_C = 1206.47 °C (1149.83 °C) for the ST (CG) crystal. Thus, contrary to what was believed, not a unique description of the LN CC regardless of its version (powder or single crystal) can be formulated by Differential Thermal Analysis (DTA) neither. This observation of the T_C being lower for ST LNPws with respect to ST LN crystals, has been previously noticed [36]. A straight explanation of this subtlety cannot be found

nowadays in the literature. A classic theoretical development shows that the energy of the vibrations within the structure is the dominant contribution to the heat capacity—if the elastic response of a crystal is a linear function of the applied forces [37]. Thus, it is inferred that this might be explained under consideration of anharmonic crystal interactions, that is, phonon-phonon coupling. Still, further investigations on these matters are needed.

5.5 Grinding of a single crystal

The bought single crystal with stoichiometric (ST) composition, described above, was turned into powder with ST composition. Low-energy grinding with an agate mortar was employed discontinuously in several steps until an averaged particle size of 1.6 μm (checked by SEM) was reached. In some instances, commercial acetone (purity $\geq$ 99.5%, Sigma-Aldrich) was used to ease the grinding, especially during its initial stages. Verification of Equations III-1 and III-2 was sought by repeating the experimental procedures performed on the synthesized powders; in the case of Raman Spectroscopy (RS), only the commercially available system (Witec alpha 300R) was used.

The results obtained are shown in Table III-4. While RS does imply a chemical composition according to what was expected, stoichiometrically (50 mol % Nb_2O_5), the structure refinement does not. This can be attributed to changes of the lattice parameter (lattice distortion) due to a variable local lattice strain frequently observed in nanocrystalline materials, induced by excess of volume at the grain boundaries [38]. Remarkably, the powdered single crystal differs from the synthesized powders in the averaged crystallite size: whereas on the latter, a myriad of nanosized crystals (100–300 nm) form large particles of the order of 2–3 μm (see Figure III-7, bottom right), on the former it can be argued that crystallite size equals the particle size; actually, the applied Rietveld refinement for the calculation of the averaged crystallite size of the grinded crystal did not converge. These implications must be confirmed and scrutinized by further investigation. Lastly, since Eq. III-2 is strongly dependent on the XRD analysis (re-labeling of the samples in terms of their predicted CC), the Raman results shown in Table III-4 demonstrate the reliability of the method.

Table III-4. Estimated chemical composition for the grinded single crystal.

Experimental technique	Measured parameter	Associated error parameter	Equation utilized	Nb content (mol % Nb_2O_5)
XRD + Rietveld refinement	Cell volume: 317.9234 A°	Goodness of Fit: 1.8756	(2)	48.2
Raman Spectroscopy	Γ/x_c: 45.3038cm^{-1}/873.9676 cm^{-1}	Reduced $\chi^{(2)}_c$: 4.70x10^{-6}	(3), Lorentz fit	50.2
	Γ/x_c: 21.8202cm^{-1}/874.1964 cm^{-1}	Reduced $\chi^{(2)}_c$: 8.38x10^{-6}	(3), Gaussian fit	50.1

5.6 Equations in terms of the averaged Li content in the powders

It is acknowledged that in contrast to pioneering works (on LN single crystals, references in [14-16]), the Equations III-:1–4 here give the averaged Nb content in the crystallites $\langle c_{Nb} \rangle$ instead of $\langle c_{Li} \rangle$. Although a simpler comparison with data in the literature could have been attained by putting these equations in terms of $\langle c_{Li} \rangle$, it was decided to do it in terms of $\langle c_{Nb} \rangle$ because of a simpler interpretation and association with a phase diagram describing LN, like that given in Figure I-1. It has been noticed that most of the phase diagrams existent in the literature to describe LN, not to say all, are presented in terms of Nb_2O_5 mol %. This is readily understood since even in the fabrication of large LN single crystals, melts of Nb_2O_5 and another compound containing Li are used [26, 38]. The equivalent equations in terms of $\langle c_{Li} \rangle$ are:

$$\langle c_{Li} \rangle = (-7.6453 V_{cell} + 2482.2171) mol \% \pm 0.5 \ mol \%$$

Eq. III-1*

$$\langle c_{Li} \rangle_L = \left(-259.0674 * \left(\frac{\Gamma_L}{2x_c}\right) + 56.8135\right) mol \% \pm 0.4 \ mol \%$$

$$\langle c_{Li} \rangle_G = \left(-588.2353 * \left(\frac{\Gamma_G}{2x_c}\right) + 58.0412\right) mol \% \pm 0.5 \ mol \%$$

Eq. III-2*

$$\langle c_{Li} \rangle = \left(-3.9602 * E_g + 65.5987\right) mol \% \pm 0.4 \ mol \%$$

Eq. III-3*

$$\langle c_{Li} \rangle = (0.0519 * T_C - 11.3805)mol\ \% \pm 0.4\ mol\ \%$$

<div align="right">Eq. III-4*</div>

Chapter 6: Nonlinear Optics

Results on the depth profile of the polarization-resolved Second Harmonic Generation in a pressed and compacted sample of LiNbO$_3$ micropowders

The Second Harmonic Generation (SHG) intensity profile obtained from Z-sectioning the powder-print is shown in Figure III-9 (left side). The step is of 2 µm, a power of 0.5 mW was measured before the objective, and the exposure time of the photomultiplier was of 1 s. The data is plotted as obtained. No z-correction is needed as in [39] for the case of single nanocrystals measurements. Because this plot is symmetric, itself represents the squared intensity profile of the fundamental beam (Gaussian) and thus a Lorentzian distribution fits satisfactorily with parameters y_0 = -0.0411, x_c = 0.0012, w = 0.02996, and A = 0.05018. To get information on the scattering properties, the same treatment is applied as in [39]: the plotted data is considered a convolution integral resulting from the convolution of an arbitrary Lorentzian function (impulse response function) and an exponential function (sample response function). Hence, by deconvolution a decaying exponential function is obtained (Figure III-9, right side), which describes the optical extinction of light at the harmonic frequency according to the Beer-Lambert law. Since no absorption is present, the scattering length or mean free path l_s= (14 ± 2) µm is extracted from the fitting. This means that light tends to scatter more forwardly, as observed typically on the Mie scattering regime (R≫λ) [40]. The collected SH light thus corresponds only to a small fraction of the scattered light, the backscattered one, differentiating in this way the SHG from the bulk at all instances. Hence, the surface properties of the powder-print can readily be probed at the air/powder interface and at layers beneath it, down to the powder/substrate interface.
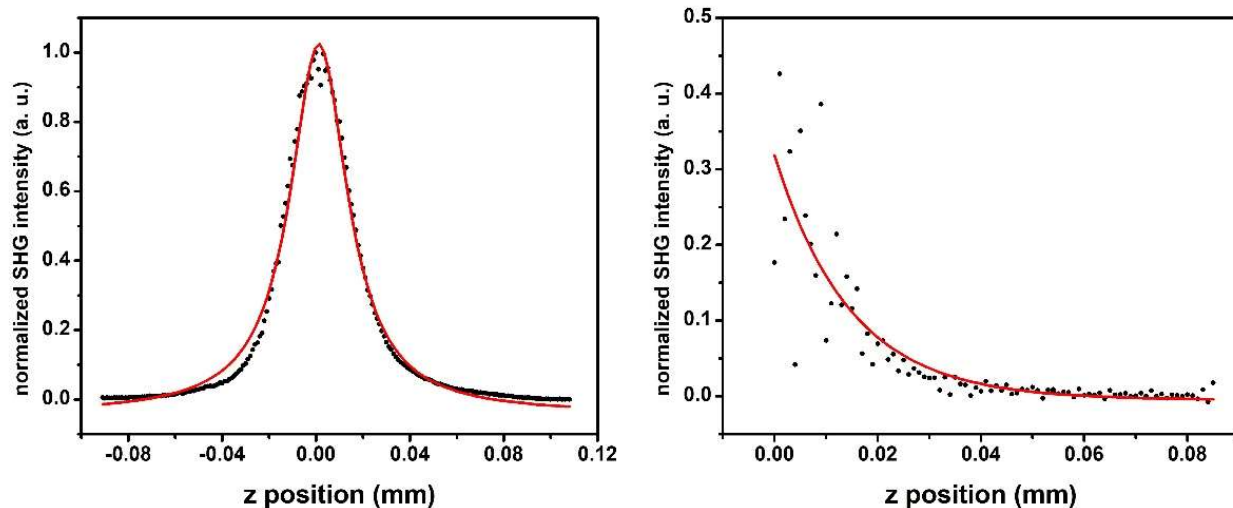
Figure III-9. Intensity profile of the powder-print sample preparation (powder with a ST composition). **Left:** Z-sectioning with a 2μ step. **Right:** after deconvolution, obeying a decaying exponential function according to the Beer-Lambert law.

Figure III-10 shows the polar plots extracted from the polarization-resolved (PR) experiments done at the air/powder interface (z=0) and at two consecutive positions to both, above and beneath this plane, as shown by the scheme on the inset. These have not been corrected for distortions caused by the dichroic mirror, as pointed out in [41]. Correction could have been done by means of recording the polar plots of a known reference sample with and without the dichroic mirror; this is in the process of being done by collaborators from France. We also recall that the used 10x objective has a sufficiently small numerical aperture (0.25) so that polarization distortion effects can be neglected [41], while this NA is large enough to neglect a significant contrast between the phase-matched SHG arising from properly oriented crystallites and the most probable non-phase-matched SHG that arises from a larger number of randomly oriented crystallites [39]. For lower numerical apertures $I_{PM}^{(2\omega)} \gg I_{NPM}^{(2\omega)}$, this dramatic difference becoming small for a NA=0.3 has been attributed to the effect of the material coherence length l_c becoming small relative to depth of field, set by the NA of the objective and the wavelength incident on it [39]. On this investigation, the depth of field has been calculated to be of approximately 15 μm for the fundamental wave (λ=800 nm), as being twice the Rayleigh range, which is determined by measuring a beam waist radius at the focal plane of $\omega_0 = 1.4$ μm. On the other hand, for bulk single LN crystals it has

been roughly estimated that $l_c \approx 5\lambda$ [42], resulting thus on a l_d/l_c ratio of nearly 4. Lastly, influence by the Gouy phase shift on the results is also discarded for this low NA [39].
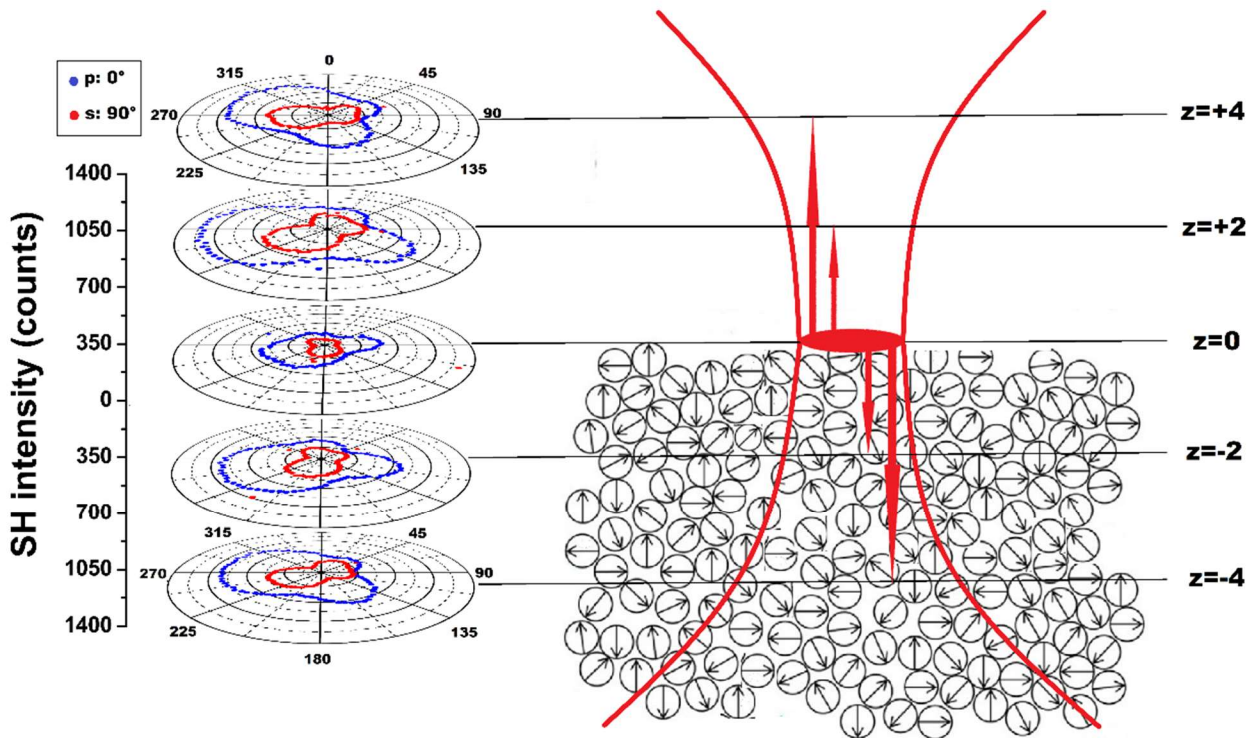

Figure III-10. Stack of the characteristic polar plots obtained after polarization-resolved experiments done at different Z positions of the beam focus, showing the sensitivity of SHG to surface properties of powdered samples. A corresponding scheme displaying the possible physical situations has been drawn in the inset.

Let us focus first on the results obtained for the analyzer set at 90 degrees with respect to the zero position of the incident-on-sample linear polarized light (red data points). A full 90° rotation in the counter-clockwise direction is observed as the focal point translates 4 μm from the z=+4 plane to the z=0 one, passing through intermediate positions. The sense of rotation is reversed as the focal point moves further into the sample, and the initial polar plot at z=+4 is almost recovered for a physical situation where the focal point is close to the bottom of the powder-print at z=-4. Hence, it seems that the coupling of both surfaces of the sample to their respective surroundings have been probed. At the edges of the sample this coupling varies according to the change in refractive index ratio $n_{surrounding}/n_{powder}$, however, it also appears to vanish for z=0 which has been previously defined as the air/powder interface. Thus, the layer at z=0 looks more like it to be the physical center of the sample (separated enough from both edges), a situation that would imply that the maximum SHG observed in Figure III-9 (left side) corresponds to the SH light collected from a layer 4 μm beneath the

air/interface. Such an implication might seem natural if it is considered the existence of Weak Localization of light or Coherent Backscattering (CBS) [43, 44]; for an effective constructive interference between the incident photons at the second harmonic frequency and the counter-propagating ones, it is admissible to think that incident photons must penetrate the random media first, and secondly, they also must have enough energy to participate in several scattering events. This argument will be further discussed below.

The five polar plots in Figure III-10 have not been normalized to the maximum SH intensity on purpose. According to Knabe et al, the differences in intensity can be addressed to the size and orientation distributions of *single* LN nanosized crystals. Only the former being closely related to the minimum, whereas both to the maximum [45]. This can be further extended to powders made of a myriad of crystallites, in this case however the characteristic dipole moment emission pattern is not addressed to the polarization of incident light lying on the a-axes of a single (*nano*) crystal, but to a net macroscopic polarization of an ensemble of crystallites resulting in an overall polar distortion along the direction of the characteristic double-lobe plot. As it can be seen in Figure III-10, a constant minimum SHG intensity of approximately 175 counts remains for all instances, except perhaps for the case $z=0$. This agrees with the small dispersion in the distribution of average crystallite sizes, determined to be of 100-300 nm by Rietveld refinement; as previously stated by Knabe et al, the minimum values in a polar plot obtained by polarization-resolved-SHG (PR-SHG) is a "hard benchmark" to test the SH response of single nanocrystals [45]. Likewise, a variation is indeed observed for the maximum value that goes from 300 to 700 counts approximately, accounting for a larger spread of possible orientations of the crystallites. Noteworthy, at $z=0$ the difference between maxima in minima is less evident, compared to the other planes, implying a smaller distribution of orientations.

Considering the re-definition made above, that is, the $z=0$ plane being the physical center of the powder-print, this implies that the crystallites closer to the edges are more easily randomly oriented than those that have been more compacted inside the powder. In other words, at the center of the sample it is more likely to exist a single-type of domain in which most of the crystallites are oriented along a common axis, this being induced doubly by the exerted pressure on both ends, although it was gentle. This interpretation of results agrees satisfactorily to previous results highlighted in [46]. In fact, by taking into account the 90° full rotation of SH response with the HWP at the detection stage, it can be seen that the obtained polar plots in this investigation (in red color) are identical in

orientation to those presented in figure 8 in [46]: the horizontally oriented (vertically in here) addressed to the probing of a single c-domain state emerging from a large strain in $PbZr_{0.2}Ti_{0.8}O_3$ ultrathin films (less than 60 nm thick), while the vertically oriented (different from vertically in here) to a mixture of a-/c- domain state, a coexistence which results from strain relaxation (film thickness above 60 nm) and the c-domains nucleating either from the top or the lower interface. In the present investigation, both the maximum and the minimum intensities at z=0 being less than the corresponding maxima and minima to the other planes can be attributed to a slight difference between the 90° axis of detection and the direction of net macroscopic induced polarization at this layer; the maxima and minima at the other planes are larger because in those cases the other orientations of crystallites, absent at z=0, contribute as well to the overall SHG.

The results obtained for the analyzer set at 0° with respect to the zero position of the incident-on-sample linear polarized light (blue data) are rather intriguing. Identical patterns to those in red color were expected but rotated 90°. Although the appropriate characteristics of the material and experimental conditions are unknown, it is possible that the prepared powder-print acts as an efficient HWP for light at λ=400 nm. For example, it has been reported that a 3 μm thick particle of calcite suffices to have an HWP for light at 1064 nm [47]. Thus, any linearly polarized light at the harmonic frequency that enters the HWP with a polarization angle of 45° respect to its fast axis would emerge as a circularly polarized light. This would explain both the form of the polar plots in blue color and the larger SHG intensities compared to the other polarization channel. It is interesting that, according to this conceptual frame, the polarized SH light emerging from the sample emerges at fixed angle of 45° with respect to the zero polarized state defined at the entrance of the setup, irrespective of the angle of linear polarization of the fundamental wave.

6.1 Determination of the powder-print thickness and the possibility of the observation of Coherent Backscattering at the harmonic wave

In the corresponding experimental section pertaining this second investigation (section 4.6), it was mentioned that the (8 ± 2) μm thickness of the powder-print has been determined by comparing several depth profiles performed by roster scanning a 10x10 μm square (2 μm step) with a XY piezo-translation stage. Again, this was done by use of half-wave-plate (HWP), which is a crystal quartz made of two different layers: the thickness of the powder-print could be estimated by depth profiling the SHG intensity of the HWP and subtracting the z_{max} position of this profile to that of a profile done

on the HWP placed on top of another coverslip, as exemplified in Figure II-8. Besides it was needed to do the estimation, also to test this method, the thickness of the coverslip (and a thicker microscope slide) was determined in this fashion and compared to values given by the corresponding providers, giving satisfactory results. The obtained profiles for the crystal-on-top and crystal-on-bottom configurations are shown in Figure III-11.
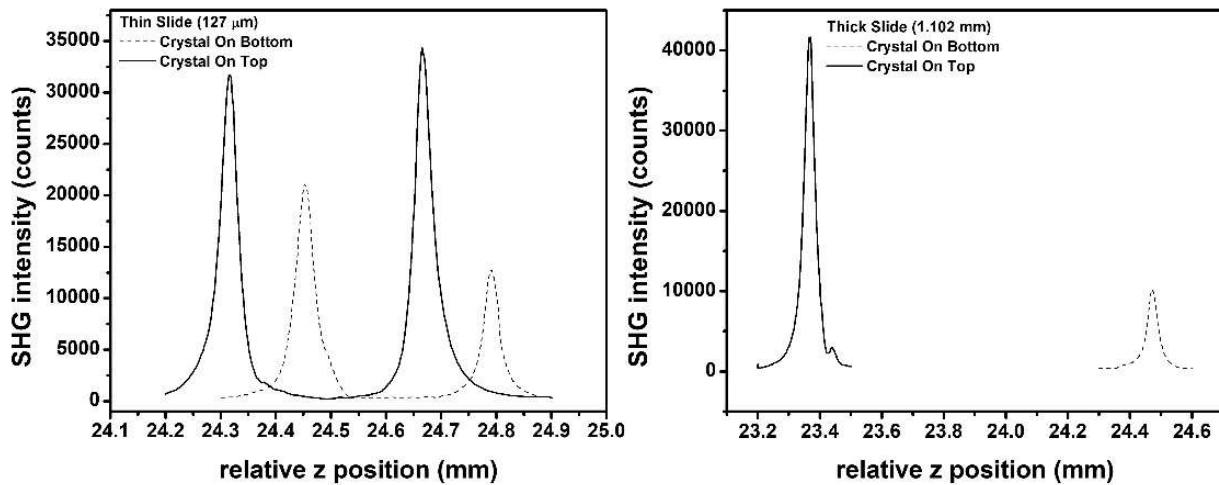
Figure III-11. Depth profiles obtained for both experimental configurations to determine the thickness of various elements including the powder-print. **Left:** thin coverslip. **Right:** thick microscope slide.

The sensitivity of SHG to measure a high contrast at the microscale can also be noticed by means of Figure III-12. On this instance, a thick powder sample was prepared and incised on purpose with an edge of a coverslip. The furrow could be tracked with the very same method used to determine the thickness of the powder-print, coverslip and microscope slide; in this case, however, only a lower limit on the thickness of the sample can be determined since no external aiding object is used.
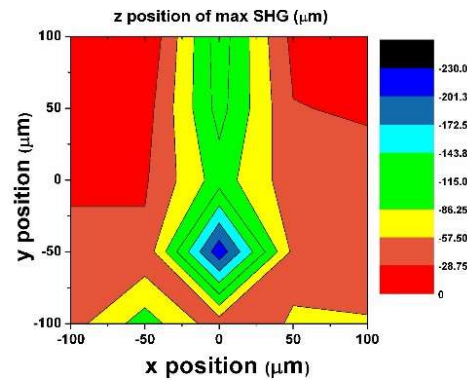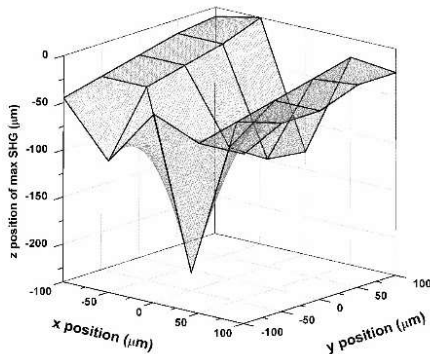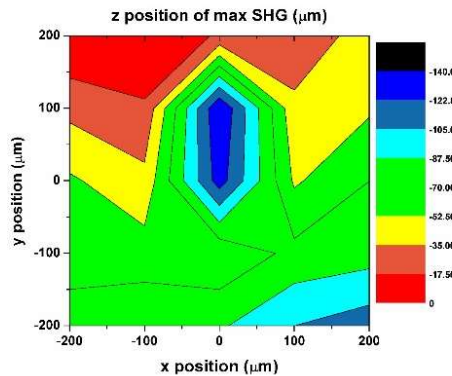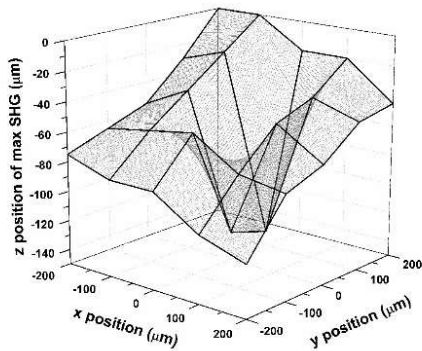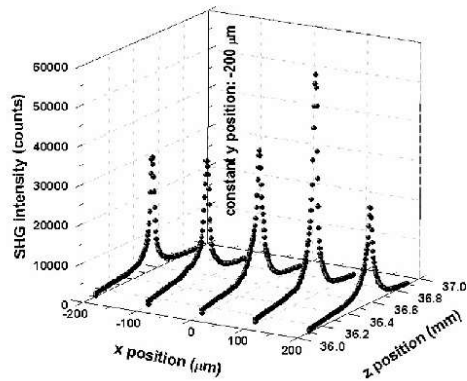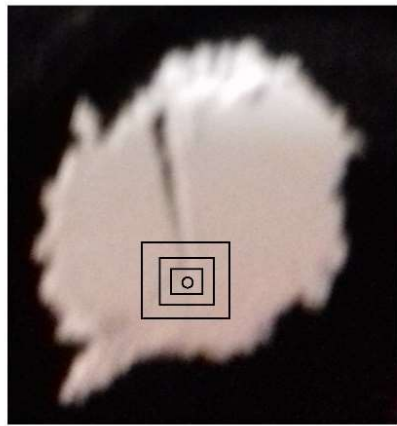
Figure III-12. Aiding figure to show the surface sensitivity of SHG Z-sectioning. **Left Top:** picture of the prepared powder sample, which was incised on purpose with an edge of a thin coverslip. **Right top:** typical stack of profiles extracted from the roster scan and for a fixed *y*-position. **Left central:** reconstruction of the surface within a 400x400 μm rectangle. **Right central:** mapping of the normalized SHG intensities within a 400x400 μm rectangle. **Left bottom:** reconstruction of the surface within a 200x200 μm rectangle. **Right bottom:** mapping of the normalized SHG intensities within a 200x200 μm rectangle.

Now regarding the possibility of the observation of the phenomenon of Coherent Backscattering (CBS) –implying Weak Localization of light conditions—, a striking result is herein described. For another powder-print sample preparation (not the same as in Figure III-9 and Figure III-10) and by

simple modification of the experimental apparatus (insertion of a closed iris laterally, before the lens at the detection stage, see Figure II-7), it has been able to observe what appears to be the CBS characteristic cone for the harmonic light (λ = 400 nm). Notwithstanding, this result is not considered as conclusive, given the known difficulties to experimentally achieve CBS for photons at the harmonic frequency created in a medium which is both nonlinear and disordered [48, 49].

The apparent CBS cone is shown in Figure III-13. It was observed for a z=0 position, located after performing a depth-profile. Several measurements had to be performed at this position, so that the resulted signal could be effectively averaged on sample rotation along the optical axis, avoiding this way noise of the results due to speckle. The polarization state of light is disregarded both at the entrance and detection stages. From the FWHM of the cone, the transport mean free path $l_s^* \approx 30$ μm is calculated from a simple linear equation given elsewhere [43, 50]. On the other hand, deconvolution of the depth-profile gives a scattering length of $l_s \approx 53$ μm, having thus an asymmetry parameter of $g = \langle \cos \theta \rangle = 1 - l_s/l_s^* \approx$-0.77 which describes anisotropic scattering of light which favors backscattering [40]. This might be the reason the CBS cone could be observed, and interestingly, an almost equal value of $l_s \approx 51$ μm was extracted from the deconvolution of the depth-profile of a thicker powdered sample of approximately 200 μm. Thicker samples of powder are known to ease the visualization of the CBS cone, but on this instance somehow the preparation a thinner powder-print (8 μm) allows for it. Thus, the powder-print might enhance coherent interference between propagating and counter-propagation photons at the harmonic frequency. We also recall that the powder-print sample preparation to which Figure III-9 and Figure III-10 correspond to, a l_s=14 μm was calculated, and if $l_s^* \approx 30$ μm holds for this sample preparation, then g ≈ 0.53. This describes a situation in which light is scattered more to the forward direction, as discussed above. Further investigation on these issues is needed.
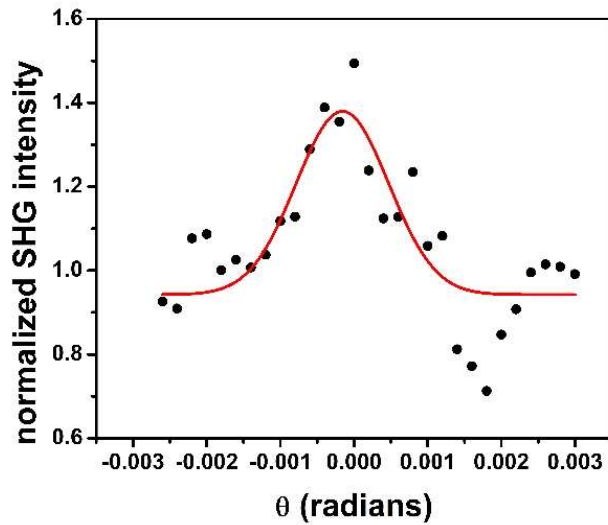
Figure III-13. Characteristic CBS cone obtained for a powder-print sample preparation, measured at the harmonic wave $\lambda = 400$nm.

Conclusions and perspectives

FIRST INVESTIGATION-LITHIUM NIOBATE:

Despite the increasing interest in lithium niobate powders (LNPws) due to their importance in possible applications in actual and future nanooptoelectronic devices, as well as the facility to produce them in large quantities, an accurate and trusting method to determine their chemical composition (CC) does not exist, to the best of my knowledge. Therefore, in this work a first step is given in this direction by developing a facile method based mainly on imposing X-Ray Diffraction (XRD) as a seed characterization technique. Raman Spectroscopy, UV-vis Diffuse Reflectance and Differential Thermal Analysis enrich this work, representing various alternatives for the independent and accurate determination of the CC of LNPws. An empirical equation that describes this fundamental property in terms of a corresponding experimental parameter is given for each of these four characterization techniques.

I wish to underline here the main aspects of the method. It is primarily based on the quantification of pure and secondary phase percentages by XRD, followed by Rietveld structure refinement. Secondly, relying on the LN phase diagram, the CCs of the studied samples are inferred, and thereafter labeled in terms of the Nb content in the crystallites. Lastly, having done this, any of the mentioned characterization techniques can be used to

relate such a labeling with their corresponding experimental parameter. In the case of a user who wants to determinate the CC of LNPws only, he/she would only need to perform the last step and make use of any of Equations III–:1–4 (or in terms of the Li content, Equations III-1*-4*), respectively. On the other hand, in the case of wanting to describe other powders apart from LNPws, the whole method (three main steps described above) might be further applied inasmuch as akin materials are to be investigated, lithium tantalate ($LiTaO_3$) powders for example.

The validity of this methodology is proven self-consistently with the determination of the CC of several samples, where the content of Li and Nb is varied in a controlled way. However, the main shortcoming of this investigation is the large uncertainty associated with Equations III–:1–4. Rigorously, they should not be used for a practical composition determination and, instead, it only could be stated with more confidence that, by using these equations, the composition of a LN powder would be closer to the stoichiometric or congruent compositions, or rather in an intermediate state.

Both the resolution and the associated uncertainties of this methodology can be significantly improved by analyzing larger quantities of powder. As mentioned in the details related to the uncertainty calculations, the major contribution to uncertainty emerges from the determination of the boundaries of the pure ferroelectric LN phase: determined by dividing the Δc_{pureLN} = 1.6 mol % Nb_2O_5 by three increasing steps of Nb content, and then dividing by 2 (0.53/2 = 0.27 mol % Nb_2O_5). The associated uncertainty to Equations III–:1–4 can be significantly reduced if a larger number of samples are synthesized in this range, which can be more easily achieved if larger quantities of powder are prepared. As an example, it is expected that by synthesizing approximately 10 g of powder, around 40 points would be available for analysis if the increasing step is fixed at 0.1% in the mass of the Nb precursor, resulting in a decrease in the overall uncertainties of about 50–80% (noticing that the uncertainty associated with the linear fitting would also be reduced significantly).

Conclusively, although it is acknowledged that the proposed equations are not universal in the sense that they may only describe the CC of LNPws with specific physical properties (crystallite and particle dimensions), this work paves the way to furnish a general description and claims the attention of the community advocated to this field to broaden the present results. For a more general description, besides the synthesis of larger number of samples,

138

the influence of other experimental factors and parameters such as the method of synthesis, the beam spot size, the intensity of light (Raman Spectroscopy), the averaged crystallite and particle size, and randomness (among others) should be considered in future investigations. At last, apart from providing four distinct alternatives to describe accurately the CC of LNPws (instead of single crystalline LN), what is innovative in the present work is the self-consistency character of the whole method: no other technique is needed to confirm the CC of the powders since the determination of the pure ferroelectric LN phase boundaries by XRD analysis suffices for this purpose. The four distinct methods are based on standard characterization techniques, accessible nowadays to large scientific communities in developing countries.

SECOND INVESTIGATION-SECOND HARMONIC GENERATION:

By combining the depth profiling with polarization-resolved experiments it was found that the overall polar distortion along a direction of a characteristic double-lobe plot, rotated in counter-clokwise sense for instances in which the focal point stood above the air/powder interface and rotated back (not fully) for layers beneath this interface. Analysis of the collected double-lobe plots happened to shed light on the size and orientation distributions of the crystallites constituting the powder. In accordance to previous reports, it was found that a small dispersion in the values for the Second Harmonic Generation (SHG) intensity minima stands for a fixed averaged crystallite size which is consistent layer by layer of the prepared sample, while variations in the maxima values stand for various distributions of possible orientations of the crystallites. It is believed that the crystallites closer to the edges are more easily randomly oriented than those that have been more compacted inside the powder; at the center of the sample it is more likely to exist a single-type of domain in which most of the crystallites are oriented along a common axis, this being induced doubly by the exerted pressure on both ends, although it was gentle.

This puts in evidence the SHG potential application for non-invasive and remote sensing, which in turn may open interesting areas for the nonlinear optics of granular media such as the study of earthquakelike dynamics by SHG, among others. Such a visionary statement has been constructed based on recent reports found in [51-55]; although no mention has been done on these references to SHG, it is believed that the experimental developments presented

in this work of thesis (or similar) might give a further insight into this subject. Yet it is still in a very early stage and, thus, most of the concepts involved need to be scrutinized. It is out of the scope of this work of thesis. Soon further experimental developments will be designed and performed so that further information in this direction can be achieved. A first theoretical approach will also be constructed (details are omitted). These two main working perspectives will take place in a close collaboration with the *Optique Non Linéaire et Interfaces* group, at the *Institut Lumiere Matiere, Université Claude Bernard Lyon 1*. Lastly, the possibility of have had been detected the characteristic CBS cone at the harmonic wave is promising since, according to the revised literature, this has not been beforehand achieved. This will also be soon further investigated.

References

Chapter 5

[1] Sánchez-Dena, O.; Villagómez, C.J.; Fierro-Ruíz, C.D.; Padilla-Robles, A.S.; Farías, R.; Vigueras-Santiago, E.; Hernández-López, S.; Reyes-Esqueda, J.A. Determination of the Chemical Composition of Lithium Niobate Powders. *Crystals* **2019**, 9, 340; DOI:10.3390/cryst9070340.

[2] Crystallographic Open Database, Information for card entry 2101175. Available online: http://www.crystallography.net/cod/2101175.html (accessed online on 16 October 2019).

[3] FIZ Karlsruhe ICSD, ICSD- Inorganic Crystal Structure Database. Available online: www2.fiz-karlsruhe.de/icsd_home.html (accessed on 16 October 2019).

[4] The Royal Society of Chemistry, Periodic Table. Available online: http://www.rsc.org/periodic-table (accessed on 17 October 2019).

[5] Baird, D.C. *Experimentation: An Introduction to Measurement Theory and Experiment Design,* 3rd ed.; Prentice-Hall:Englewood Cli_s, NJ, USA, 1995; pp. 129–133.

[6] Kalinnikov, V.T.; Gromov, O.G.; Kunshina, G.B.; Ku'zmin, A.P.; Lokshin, E.P.; Ivanenko, V.I. Preparation of LiTaO$_3$, LiNbO$_3$, and NaNbO$_3$ from Peroxide Solutions. *Inorg. Mater.* **2004**, 40, 411-414; DOI:10.1023/B:INMA.0000023967.76203.61.

[7] Liu, M.; Xue, D.; Luo, C. Wet chemical synthesis of pure LiNbO$_3$ powders from simple niobium oxide Nb$_2$O$_5$. *J. Alloys Compd.* **2006**, 426, 118-122; DOI:10.1016/j.jallcom.2006.02.019.

[8] Scott, B.A.; Burns, G. Determination of Stoichiometry Variations in LiNbO3 and LiTaO3 by Raman Powder Spectroscopy. *J. Am. Ceram. Soc.* **1972**, 55, 225-230; DOI:10.1111/j.1151-2916.1972.tb11266.x.

[9] Liu, M.; Xue, D. An efficient approach for the direct synthesis of lithium niobate powders. *Solid State Ionics* **2006**, 177, 275-280; DOI:10.1016/j.ssi.2005.11.007.

[10] Liu, M.; Xue, D.; Li, K. Soft-chemistry synthesis of LiNbO$_3$ crystallites. *J. Alloys Compd.* **2008**, 449, 28-31; DOI:10.1016/j.jallcom.2006.03.104.

[11] Nyman, M.; Anderson, T.M.; Provencio, P.P. Comparison of Aqueous and Non-aqueous Soft-Chemical Syntheses of Lithium Niobate and Lithium Tantalate Powders. *Cryst. Growth Des.* **2009**, 9, 1036-1040; DOI:10.1021/cg800849y.

[12] Kong, L. B.; Chang, T. S.; Ma, J.; Boey, F. Progress in synthesis of ferroelectric ceramic materials via high-energy mechanochemical technique. *Prog. Mater. Sci.* **2008**, 53, 207-322. DOI:10.1016/j.pmatsci.2007.05.001.

[13] De Figueiredo, R.S.; Messaia, A.; Hernandes, A.C.; Sombra, A.S.B. Piezoelectric lithium niobate obtained by mechanical alloying. *J. Mater. Sci. Lett.* **1998**, 17, 449-451; DOI:10.1023/A:1006563924005.

[14] Wöhlecke, M.; Corradi, G.; Betzler, K. Optical methods to characterise the composition and homogeneity of lithium niobate single crystals. *Appl. Phys. B* **1996**, 63, 323-330. DOI:10.1007/BF01828734.

[15] Schlarb, U.; Klauer, S.; Wesselmann, M.; Betzler, K.; Wöhlecke M. Determination of the Li/Nb ratio in Lithium Niobate by Means of Birefringence and Raman Measurements. *Appl. Phys. A* **1993**, 56, 311-315. DOI:10.1007/BF00324348.

[16] Malovichko, G. I.; Grachev, V. G.; Kokanyan, E. P.; Schirmer, O. F.; Betzler, K.; Gather, B.; Jermann, F.; Klauer, S.; Schlarb, U.; Wöhlecke, M. Characterization of stoichiometric LiNbO$_3$ grown from melts containing K$_2$O. *Appl. Phys. A: Mater. Sci. Process.* **1993**, 56, 103-108. DOI:10.1007/BF00517674.

[17] MTI Corporation, LiNbO3 & Doped. Available online: http://www.mtixtl.com/linbo3.aspx (accessed on 02 July 2019).

[18] Pezzotti, G. Raman spectroscopy of piezoelectrics. *J. Appl. Phys.* **2013**, 113, 211301; DOI:10.1063/1.4803740.

[19] Repelin, Y.; Husson, E.; Bennani, F.; Proust, C. Raman spectroscopy of lithium niobate and lithium tantalite. Force field calculations. *J. Phys. Chem. Solids* **1999**, 60, 819-825: DOI:10.1016/S0022-3697(98)00333-3.

[20] Thermo Fisher Scientific, Application Note: Curve Fitting in Raman and IR Spectroscopy. Available online:https://www.thermofisher.com/search/results?query=Curve%20Fitting%20in%20Raman&focusarea=Search%20All (accessed on 25 September 2019).

[21] Porto, S.P.S.; Krishnan, R.S. Raman Effect of Corundum. *J. Chem. Phys.* **1967**, 47, 1009-1011; DOI:10.1063/1.1711980.

[22] Tuschel, D. The Effect of Microscope Objectives on the Raman Spectra of Crystals. *Spectroscopy* **2017**, 32, 14-23.

[23] Maïmounatou, B.; Mohamadou, B.; Erasmus, R. Experimental and theoretical directional dependence of optical polar phonons in the LiNbO$_3$ single crystal: New and complete assignment of the normal mode frequencies. *Phys. Status Solidi B* **2016**, 253, 573-582; DOI:10.1002/pssb.201552428.

[24] Yang, X.; Lan, G.; Li, B.; Wang, H. Raman Spectra and Directional Dispersion in LiNbO$_3$ and LiTaO$_3$. *Phys. Status Solidi B* **1987**, 142, 287-300; DOI:10.1002/pssb.2221420130.

[25] Balanevskaya, A.É.; Pyatigorskaya, L.I.; Shapiro, Z.I.; Margolin, L.N.; Bovina, E.A. DETERMINATION OF THE COMPOSITION OF LiNbO$_3$ SPECIMENS BY RAMAN SPECTROSCOPY. *J. Appl. Spectrosc.* **1983**, 38, 491-493; DOI:10.1007/BF00662367.

[26] Volk, T.; Wöhlecke, M. Point defects in LiNbO3. In *Springer Series in Materials Science 115. Lithium Niobate. Defects, Photorefraction and Ferroelectric Switching*, 1st ed.; Hull, R., Osgood, R.M., Jr., Parisi, J.,Warlimont, H., Eds.; Springer: Berlin/Heidelberg, Germany, 2009; Volume 115, pp. 9–50, ISBN 978-3-540-70765-3.

[27] Kovács, L.; Kocksor, L.; Szaller, Z.; Hajdara, I.; Dravecz, G.; Lengyel, K.; Corradi, G. Lattice site of rare-earth ions in stoichiometric lithium niobate probed by OH⁻ vibrational spectroscopy. *Crystals* **2017**, 7, 230; DOI:10.3390/cryst7080230.

[28] Doyle, W.P.; Forbes, F. Determination by diffuse reflectance of the stoichiometry of solid products in solid-solid additive reactions. *J. Inorg. Nucl. Chem.* **1965**, 27, 1271-1280; DOI:10.1016/0022-1902(65)80090-2.

[29] Redfield, D.; Burke, W.J.; Optical absorption edge of LiNbO$_3$. *J. Appl. Phys.* **1974**, 45, 4566-4571; DOI:10.1063/1.1663089.

[30] Kovács, L. Ruschhaupt, G.; Polgár, K.; Corradi, G.; Wöhlecke, M. Composition dependence of the ultraviolet absorption edge in lithium niobate. *Appl. Phys. Lett.* **1997**, 70, 2801-2803; DOI:10.1063/1.119056.

[31] Torrent, J.; Barrón, V. Diffuse Reflectance Spectroscopy. In *Methods of Soil Analysis Part 5—Mineralogical Methods,* 1st. ed.; Ulery, A.L., Drees, R., Eds.; Soil Society of America: Wisconsin, USA, 2008, pp. 367-385; ISBN 978-0-89118-846-9.

[32] Thierfelder, C.; Sanna, S.; Schindlmayr, A.; Schmidt, W.G. Do we know the band gap of lithium niobate? *Phys. Status Solidi C* **2010**, 7, 362-365; DOI:10.1002/pssc.200982473.

[33] Devonshire, A.F. Theory of ferroelectrics. *Adv. Phys.* **1954**, 3, 85-130; DOI:10.1080/00018735400101173.

[34] O'Bryan, H.M.; Gallagher, P. K.; Brandle, C. D. Congruent Composition and Li-Rich Phase Boundary of LiNbO$_3$. *J. Am. Ceram. Soc.* **1985**, 68, 493-496. DOI:10.1111/j.1151-2916.1985.tb15816.x.

[35] Bordui, P.F.; Norwood, R.G.; Jundt, D.H.; Fejer, M.M. Preparation and characterization of off-congruent lithium niobate crystals. *J. Appl. Phys.* **1992**, 71, 875-879; DOI:10.1063/1.351308.

[36] Liu, M.; Xue, D.; Li, K. Soft-chemistry synthesis of LiNbO$_3$ crystallites. *J. Alloys Compd.* **2008**, 449, 28-31; DOI:10.1016/j.jallcom.2006.03.104.

[37] Kittel, C. *Introduction to Solid State Physics,* 7th ed.; John Wiley & Sons: New York, USA, 1996, pp. 99-130.

[38] Hatano, H.; Liu, Y.; Kitamura, K. Growth and Photorefractive Properties of Stoichiometric LiNbO$_3$ and LiTaO$_3$. In *Photorefractive Materials and Their Applications 2,* 1rst ed.; Günter, P., Huignard, J. P., Eds.; Springer Series in Optical Series: New York, USA, 2007, pp. 127-164.

Chapter 6

[39] Chowdhury, A.U.; Zhang, S.; Simpson, J. Powders Analysis by Second Harmonic Generation Microscopy. *Anal. Chem.* **2016**, 88, 3853-3863; DOI:10.1021/acs.analchem.5b04942.

[40] Bohren, C.F.; Huffman, D.R. *Absorption and Scattering of Light by Small Particles,* 1st ed.; John Wiley & Sons: New York, USA, 1983, ISBN 0-471-05772-X.

[41] Schön, P.; Munhoz, F.; Gasecka, A.; Brustlein, S.; Brasselet, S. Polarization distortion effects in polarimetric two-photon microscopy. *Opt. Express* **2008**, 16, 20891-20901; DOI:10.1364/OE.16.020891.

[42] Volk, T.; Wöhlecke, General Introduction to Photorefraction in LiNbO$_3$. In *Springer Series in Materials Science 115. Lithium Niobate. Defects, Photorefraction and Ferroelectric Switching*, 1st ed.; Hull, R., Osgood, R.M., Jr., Parisi, J.,Warlimont, H., Eds.; Springer: Berlin/Heidelberg, Germany, 2009; Volume 115, pp. 51–74, ISBN 978-3-540-70765-3.

[43] vand der Mark, M.B.; van Albada, M.P.; Lagendijk, A. Light scattering in strongly scattering media: Multiple scattering and weak localization. *Phys. Rev. B* **1988**, 3575-3592; DOI:10.1103/PhysRevB.37.3575.

[44] Aegerter, C.M.; Maret, G. Chapter 1. Coherent Backscattering and Anderson Localization. In *Progress in Optics,* 1st ed.; Wolf, E., Ed.; Elsevier B.V.: 2009, Volume 52, pp. 1-62, ISSN 0079-6638, DOI:10.1016/S0079-6638(08)00003-6.

[45] Knabe, B.; Buse, K.; Assenmacher, W.; Mader, W. Spontaneous polarization in ultrasmall lithium niobate nanocrystals revealed by second harmonic generation. *Phys. Rev. B* **2012**, 86, 195428; DOI:10.1103/PhysRevB.86.195428.

[46] Nordlander, J.; De Luca, G.; Strkalj, N.; Fiebig, M.; Trassin, M. Probing Ferroic States in Oxide Thin Films Using Optical Second Harmonic Generation. *Appl. Sci.* **2018**, 8, 570; DOI:10.3390/app8040570.

[47] Friese, M.E.J.; Nieminen, T.A.; Heckenberg, N.R.; Rubinsztein-Dunlop, H. Optical alignment and spinning of laser-trapped microscopic particles. *Nature* **1998**, 394, 348-350; DOI:10.1038/28566.

[48] Kratsov, V.E.; Agranovich, V.M.; Grigorishin, K.I. Theory of second-harmonic generation in strongly scattering media. *Phys. Rev. B* **1991**, 44, 4931-4942; DOI:10.1103/PhysRevB.44.4931.

[49] Yoo, K.M.; Lee, S.; Takiguchi, Y.; Alfano, R.R. Search for the effect of weak photon localization in second-harmonic waves generated in a disordered anisotropic nonlinear medium. *Opt. Lett.* **1989**, 14, 800-801; DOI:10.1364/OL.14.000800.

[50] Sapienza, R.; Mujumdar, S.; Cheung, C.; Yodh, A.G.; Wiersma, D. Anisotropic Weak Localization of Light. *Phys. Rev. Lett.* **2004**, 92, 033903; DOI:10.1103/PhysRevLett.92.033903.

Conclusions and perspectives

[51] Shmuel, M.; Rubinstein, G.C.; Fineberg, J. Detachment fronts and the onset of dynamic friction. *Nature* **2004**, 430, 1005-1009; DOI:

[52] Bérut, A.; Chauvet, H. ; Legué, V. ; Moulia, B. ; Pouliquen, O. ; Forterre, Y. Gravisensors in plant cells behave like an active granular liquid. *PNAS* **2018**, 115, 5123-5128; DOI:10.1073/pnas.1801895115.

[53] Lherminier, S.; Planet, R.; Levi dit Vehel, V.; Simon, G.; Vanel, L.; Måløy, K.J.; Ramos, O. Continuously Sheared Granular Matter Reproduces in Detail Seismicity Laws. *Phys. Rev. Lett* **2019**, 122, 218501; DOI:10.1103/PhysRevLett.122.218501.

[54] Zou, S.; Xu, Y.; Zatianina, R.; Li, C.; Liang, X.; Zhu, L.; Zhang, Y.; Liu, G.; Liu, Q.H.; Chen, H.; Wang, Z. Broadband Waveguide Cloak for Water Waves. *Phys. Rev. Lett.* **2019**, 123, 074501; DOI:10.1103/PhysRevLett.123.074501.

[55] Park, J.; Youn, J.R.; Song, Y.S. Hydrodynamic Metamaterial Cloak for Drag-Free Flow. *Phys. Rev. Lett.* **2019**, 123, 074502; DOI:10.1103/PhysRevLett.123.074502.

Appendix A: uncertainty associated to the linear fitting involving Eq. III-1

According to Baird (section 2-9, equation 2-2; reference in [5], Chapter 5), the general method for the calculation of the uncertainty of a function of two or more variables (derived value) $z=f(x, y)$ is:

$$\delta z = \frac{\partial f}{\partial x}\delta x + \frac{\partial f}{\partial y}\delta x, \tag{A}$$

where δx and δy are the uncertainties associated to quantities x and y, respectively. Moreover, by application of the statistical principle of least squares (section 6-7) to a set of points with a linear trend, the values of slope and intercept to best line are given by

$$m = \frac{N\sum(x_iy_i)-\sum x_i\sum y_i}{N\sum x_i^2-(\sum x_i)^2},$$

$$b = \frac{\sum x_i^2\sum y_i-\sum x_i\sum(x_iy_i)}{N\sum x_i^2-(\sum x_i)^2}, \tag{B}$$

where N is the number of observations or measurements. The uncertainties of these quantities are thus represented by their respective standard deviations, given by

$$S_m = S_y \times \sqrt{\frac{N}{N\sum x_i^2-(\sum x_i)^2}},$$

$$S_b = S_y \times \sqrt{\frac{\sum x_i^2}{N\sum x_i^2-(\sum x_i)^2}}, \tag{C}$$

where S_y is the standard deviation of the distribution of δy values about the best line, given by:

$$S_y = \sqrt{\frac{\sum(\delta y_i)^2}{N-2}}, \tag{D}$$

From Figure III-1 (right side), we have $m_1=0.1160$, $\delta m_1=0.0148$, $b_1=312.3325$ and $\delta b_1=0.7514$. But these values correspond for a least squares fitting to a relation of the cell volume in terms of the Nb content, and because for future reference it is preferable to give an equation that directly determines the latter in terms of the former, a second equation of the form $y=m_2+b_2$ is to be considered, where:

$$m_2 = \frac{1}{m_1}; \quad b_2 = -\frac{b_1}{m_1}$$

Thus, by use of equation (B), δm_2 and δb_2 are equal to:

$$\delta m_2 = \left| \frac{d\left(\frac{1}{m_1}\right)}{dm_1} \delta m_1 \right| = \frac{\delta m_1}{2m_1^2} = 0.5499$$

$$\delta b_2 = \left| \frac{d(\frac{b_1}{m_1})}{dm_1} + \frac{d(\frac{b_1}{m_1})}{db_1} \right| = \left| \left(-\frac{b_1}{2m_1^2}\right) \delta m_1 + \left(\frac{1}{m_1}\right) \delta b_1 \right| = 165.2741$$

Having then m_2=8.6207, δm_2=0.5499, b_2= -2692.5215 and δb_2=165.2741. Letting δm_2=S_m, δb_2=S_b, N=6, $\sum x_i^2 = \sum V_{cell,i}^2 = 607628.4880$ and $(\sum x_i)^2 = 3645770.5540$, we have by use of Equations (C):

$$\delta_y = S_y = \frac{S_m}{\sqrt{\dfrac{N}{N\sum x_i^2 - (\sum x_i)^2}}} = \frac{0.5499}{4.0053} = 0.1373$$

$$\delta_y = S_y = \frac{S_b}{\sqrt{\dfrac{\sum x_i^2}{N\sum x_i^2 - (\sum x_i)^2}}} = \frac{165.2741}{1274.6274} = 0.1297$$

where, $x_i := \{318.0787, 318.1374, 318.1930, 318.3095, 318.3149, 318.3566\}$.

Having thus an overall uncertainty associated to the linear fitting of 0.14 mol% Nb_2O_5. This procedure is repeated for the rest of the calculations regarding Equations III-:2-4.

PUBLISHED ARTICLE

(pages 145-163)

Determination of the Chemical Composition of Lithium Niobate Powders

Oswaldo Sánchez-Dena [1,*][iD]**, Carlos J. Villagómez** [1][iD]**, César D. Fierro-Ruíz** [2]**,**
Artemio S. Padilla-Robles [1]**, Rurik Farías** [3][iD]**, Enrique Vigueras-Santiago** [4]**,**
Susana Hernández-López [4] **and Jorge-Alejandro Reyes-Esqueda** [1,*]

[1] Instituto de Física, Universidad Nacional Autónoma de México, 04510 Mexico City, México
[2] Departamento de Mecátronica y Energías Renovables, Universidad Tecnológica de Ciudad Juárez, Avenida Universidad Tecnológica 3051, Colonia Lote Bravo II, 32695 Ciudad Juárez, Chihuahua, México
[3] Instituto de Ingeniería y Tecnología, Universidad Autónoma de Ciudad Juárez, Av. Del Charro 450 Norte, 32310 Ciudad Juárez, Chihuahua, México
[4] Laboratorio de Investigación y Desarrollo de Materiales Avanzados, Universidad Autónoma del Estado de México, Paseo Colón esquina Paseo Tollocan, 50120 Toluca, Estado de México, México
[*] Correspondence: ossdena@gmail.com (O.S.-D.); reyes@fisica.unam.mx (J.-A.R.-E.); Tel.: +52-55-5622-5184 (J.-A.R.-E.)

Abstract: Existent methods for determining the composition of lithium niobate single crystals are mainly based on their variations due to changes in their electronic structure, which accounts for the fact that most of these methods rely on experimental techniques using light as the probe. Nevertheless, these methods used for single crystals fail in accurately predicting the chemical composition of lithium niobate powders due to strong scattering effects and randomness. In this work, an innovative method for determining the chemical composition of lithium niobate powders, based mainly on the probing of secondary thermodynamic phases by X-ray diffraction analysis and structure refinement, is employed. Its validation is supported by the characterization of several samples synthesized by the standard and inexpensive method of mechanosynthesis. Furthermore, new linear equations are proposed to accurately describe and determine the chemical composition of this type of powdered material. The composition can now be determined by using any of four standard characterization techniques: X-Ray Diffraction (XRD), Raman Spectroscopy (RS), UV-vis Diffuse Reflectance (DR), and Differential Thermal Analysis (DTA). In the case of the existence of a previous equivalent description for single crystals, a brief analysis of the literature is made.

1. Introduction

Nowadays, more than 50 years after Ballman managed to grow large lithium niobate (LiNbO₃; LN) crystals with the Czochralski method [1], synthesizing stoichiometric LN single crystals is still a state-of-the-art matter: The reason behind this is the fact that a Z-cut of a stoichiometric grown crystal costs around 12 times more than one possessing a congruent chemical composition [2]. Compared to this version of the material, while comprehensively studied [3] and well exploited technologically [4–6], powders are tacitly considered easier and far less expensive to synthesize. LN powders (LNPws) have served in the past only as survey materials, for example, in the prediction of the nonlinear second order optical capabilities of unavailable single crystals by applying the Kurtz-Perry method in the powdered version [7,8]. Nevertheless, recent developments in LNPws are certainly attracting the attention of scientists and engineers who seek to exploit their potential use in a wide range of applications that span from the construction industry to nonlinear optics.

Cementation materials based on LN have been proposed as a way to improve the air quality of the environment by Artificial Photosynthesis; this is considered important for the reduction of global warming [9]. Regarding LNPws, we emphasize that not only would they be easier than single crystals to implement into cemented materials, but they would also probably enhance the intrinsic surface effects, which are the basis for an improvement of the lifetime of the carriers (photo-generated electrons and holes) involved in Artificial Photosynthesis [10]. Fe-doped LNPws also show, after a post-thermal treatment in a controlled reducing atmosphere, a rather strong ferromagnetic response at room temperature for a doping concentration of the order of 1% mol; this may be considered a first report of the manifestation of ferromagnetism in nanocrystalline LNPws within the regime of very low doping concentrations [11]. Yet in another application based on the powder-in-tube method, a novel fabrication process has been demonstrated for the realization of polarization-maintaining optical fibers [12]. Comprehension of the main mechanism behind this technology, and by looking at the LN mechanical properties [3], it can easily be seen that LNPws are, in principle, good candidates for the fabrication of this type of optical components. Also, possible tuning on the intensity of the Second Harmonic Generation (SHG) that arises from LN micro powders could be ascribed to a proper control of their chemical composition and grain size [13]. This could soon translate into major technical benefits given that neither a critical adjustment of the orientation or temperature in the material (phase matching condition) nor the accurate engineering of a microstructure (quasi-phase matching condition) are substantially needed when the SHG from disordered materials—such as LNPws—are exploited [14].

The performance of LNPws for most of their potentially attributable properties are expected to drastically depend upon their chemical composition (CC), like in the case of single-crystalline LN [3]. Indeed, it has been already demonstrated that size at the nanoscale does not affect the structural symmetry of single LN crystals and that nanosized LN single crystals (down to 5 nm) inherit the nonlinear optical properties from that of large or bulk single crystals [15]: Both the magnitude and the orientation nature of the nonlinear coefficient d_{mn} are preserved. Our work arises from noticing that at least one of the two linear equations that describe the CC of LN single crystals by polarized Raman Spectroscopy measurements [16,17] is not accurate for the case of powders. Hence, it is necessary to properly characterize LNPws, starting by unambiguously determining their CC. Most of the reports found in the literature are only devoted to LN single crystals, where optical and non-optical methods can be found [16–18]. Some of the non-optical methods might also be applied to powders; however, in some cases they would not be accessible to everyone, like neutron diffraction methods, and might also give rise to discrepancies like in cases determining the LN CC by measuring the Curie temperature T_C. Since temperature is a scalar quantity (light propagates and interacts with matter in vector-like form), it would be permissible to expect a single description of the LN CC in terms of T_C that serves for both large single crystals and powders. Interestingly, this is not the case: the systematic measurement of lower T_C values (about 10 °C) for LNPws compared to equivalent single crystals has already been addressed and the reason behind this remains unexplained [18].

In this investigation, a custom-made Raman system has been crafted to obtain control on the polarization state of the light at the excitation and detection stages. With this system, verification of the linear equation for the Raman active mode centered at 876 cm^{-1}, as given by Schlarb et al. [16] and Malovichko et al. [17], can be done on stoichiometric (ST) and congruent (CG) lithium niobate single-crystal wafers, according to the provider [2]. Likewise, this serves to calibrate this assembled system and to confidently state that the aforementioned linear equation does not describe LNPws. Then, with a commercially available system, we observed that the linear relationship remains between the CC of LNPws and the linewidth (Γ) of the same Raman mode (876 cm^{-1}), under which in simpler circumstances the polarization state of light at the excitation and detection stages would be disregarded. In accordance to References [16–19], the accurate determination of the CC of LNPws is proposed by means of a linear fit in terms of the calculated Γ from *non-polarized* Raman spectra. Yet, the main contribution of this work is based on an a priori probing of the formed phases from 11 different

synthesized samples by analysis of X-ray diffraction (XRD) experimental data, while relying on the existent information in the phase diagram that describes the pure LN phase along with its surrounding secondary phases (Figure 1). In this way the linear relationship obtained for the averaged Nb content in the crystallites $\langle c_{Nb} \rangle$, in terms of Γ, is affixed to two known or expected values of $\langle c_{Nb} \rangle$ for the two edges that delimit the pure ferroelectric phase: The boundary with phase $LiNb_3O_8$ on one side (Nb excess) and the boundary with phase Li_3NbO_4 on the other (Li excess).
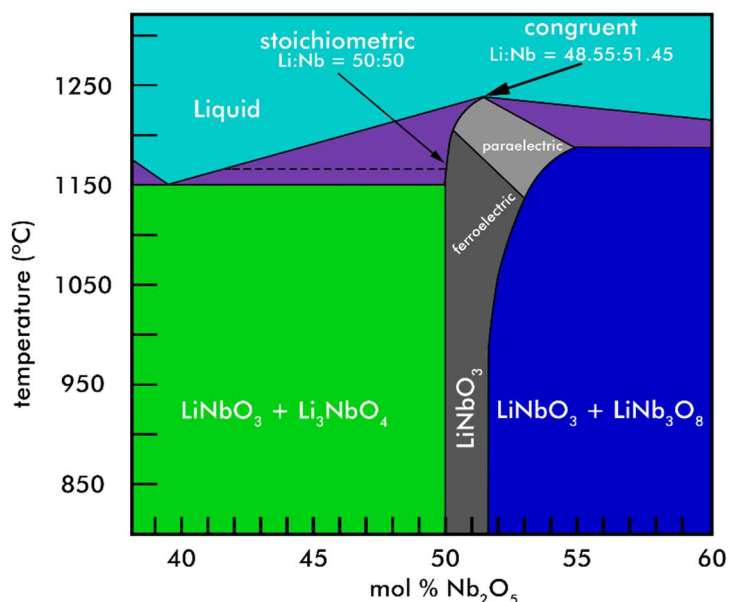

Figure 1. Schematic phase diagram of the Li_2O-Nb_2O_5 pseudo binary system in the vicinity of $LiNbO_3$—redrawn from the publications by Volk and Wöhlecke [3] and Hatano et al. [20].

The nanocrystalline LNPws are obtained by a mechanochemical-calcination route [21,22]. Gradual addition of Li or Nb has been systematically performed by increasing the mass percentage of a precursor containing the desired ion species. Quantification of secondary-phase percentages is carried out with structure refinement by a standard Rietveld method. An alternative linear equation to determine the CC is also given in terms of the calculated cell volumes by means of the same structure refinement. Additionally, linear fitting of the measured band gap energy (E_g), by means of UV-vis Diffuse Reflectance (DR), is also used for this purpose. Differential Thermal Analysis (DTA) is utilized as a verification technique for specific samples and a fourth empirical equation that describes the CC in terms of the Curie temperature is obtained this way. Scanning Electron Microscopy (SEM) is utilized to verify that the particle size distributions do not vary drastically from one sample to another.

2. Materials and Methods

2.1. Synthesis

High purity lithium carbonate (Li_2CO_3) and niobium pentoxide (Nb_2O_5), from Alpha Aesar, were used as starting reagents in a 1:1 molar ratio. The respective masses of the precursors were determined such that 1 g of lithium niobate ($LiNbO_3$; LN) was produced from the following balanced chemical equation:

$$Li_2CO_3 + Nb_2O_5 \rightarrow 2LiNbO_3 + CO_2 \tag{1}$$

The resultant product was labeled—and hereafter referred to—as LN-STm (ST: stoichiometric, m: mixture) because, in principle, a LN mixture was obtained after milling with a 1:1 molar ratio in terms of Li and Nb. Variations in the chemical composition (CC) of the final resultant powders were sought by adding, at the milling stage, 1–5% of the mass in one of the precursors (with steps of 1% with

resolution of 10^{-4} g) while keeping the mass of the other precursor constant, in both cases with respect to the masses measured for sample LN-STm (see Appendix A for table). In this way, 10 more samples were synthesized and labeled as LN + 1%LiP, LN + 1%NbP, LN + 2%LiP, and so on up to LN + 5%NbP (P stands for precursor). It must be clarified that the percentages that appear on these labels are not in terms of the ion species solely, but in terms of the whole mass of the precursors that contain them.

The high-energy milling was carried out in an MSK-SFM-3 mill (MTI Corporation) using nylon vials with YSZ balls; a powder:ball ratio of 0.1 was used for each sample preparation. The milling was performed in 30 min cycles, with 30 min pauses to avoid excessive heat inside the milling chamber, until 200 min of effective milling time was reached. Calcination of the resultant materials (amorphous) was done with a Thermo Scientific F21135 furnace in an air atmosphere. All samples were simultaneously calcined with the following programmed routine: 10 °C/min → 600 °C for 30 min → 2 °C/min → 850 °C for 120 min → cooling down slowly to room temperature.

2.2. X-Ray Diffraction

These patterns were measured in air at room temperature using a Bruker D-8 Advance diffractometer with the Bragg-Brentano θ-θ geometry, a source of CuKα radiation (λ = 1.5406 $\dot{A}$), a Ni 0.5% CuKβ filter in the secondary beam, and a 1-dimensional position sensitive silicon strip detector (Bruker, Linxeye, Karlsruhe, Germany). The diffraction intensity, as a function of the 2θ angle, was measured between 5.00° and 110.00°, with a step of 0.02° every 38.4 s. Sample LN-STm displays a pure ferroelectric lithium niobate (LN) phase, with Bragg peaks resembling those of the COD-2101175 card previously deposited with the Crystallographic Open Database; supplementary crystallographic data can be obtained free of charge from the Web page of the database [23].

Rietveld refinement was performed using computational package X'Pert HighScore Plus from PANalytical, version 2.2b (2.2.2), released in 2006 [24]. Instructions in the section named *Automatic Rietveld Refinement* from the HighScore Online Plus Help document were first followed and then adapted for phase quantification of the samples. In short, an archive with information about the atomic coordinates of LN ("2101175.cif") was downloaded from the Crystallopgraphic Open Database [23]. For the secondary phases $LiNb_3O_8$ and Li_3NbO_4, ICSD-2921 and ICSD-75264 from The Inorganic Crystal Structure Database were used, respectively [25]. The archives were then inserted, along with the experimental data, and Rietveld analysis in "Automatic Mode" was executed, followed by iterative executions in "Semi-automatic Mode," in which different "Profile Parameters" were allowed to vary until satisfactory indexes of agreement were obtained. The averaged crystallite size was also calculated by Rietveld refinement, following instructions from the *Size/Strain Analysis* section; a single lanthanum hexaboride (LaB_6) crystal was used in this case as the standard sample, analyzed with the ICSD-194636 card.

2.3. Raman Spectroscopy

Two Raman systems were employed in this investigation: One custom-made and one of standard use and commercially available. The former allowed for the set-up of different experimental conditions in terms of the polarization state of light at the incident-on-sample and detection stages, including non-polarized, parallel polarized (p), and cross polarized (s) situations. Adopting the so-called Porto's formalism, these experimental conditions were $Z(--)\overline{Z}$, $Z(YY)\overline{Z}$ and $Z(YX)\overline{Z}$, respectively; where, in general, *A(BC)D* stands for light propagating in the *A* direction with linear polarization *B*, before the sample, while selective detection is done on the *D* direction with polarization *C* [26].

The commercially available system only featured the non-polarized configuration. It was a Witec alpha300R Confocal-Raman microscope with a 532 nm source of excitation wavelength and 4–5 cm^{-1} of spectral resolution. With this equipment, the Raman spectra were collected in the range 100–1200 cm^{-1} at room temperature and light incident on the normal component of the sample with a power of 3.4 mW; a Nikon 10 objective was used to focus the incoming light on a 1:5 mm spot. An intensity of approximately 11Wcm^{-2} was delivered to the sample. The customized open-air Raman system

consisted of an excitation beam output of a continuous wave diode laser at 638 nm wavelength with a power of 37 mW (Innovative photonic solution). The beam was linearly polarized from variable angle mounting and transmitted through a beam splitter to focus the excitation beam into the sample by an aspherized achromatic lens (NA = 0.5, Edmund optics). The excitation spot diameter measured at the focus point had a ~10 μm radius. The collected Raman scattered light from the sample through the aspheric lens and the beam splitter was focused by two silver coated mirrors and one bi-convex lens into a fiber Raman Stokes probe (InPhotonics) that was connected to a QE65 Raman Pro spectrometer (Ocean optics) for a Raman shift range detection between 250–3000 cm^{-1}. In its use for the characterization of the powders, the light at λ = 638 nm was incident at razing angle with P = 10 mW. The Raman spectra were collected in the range 200–1200 cm^{-1} at room temperature with a spectral resolution of 8 cm^{-1}. In this case, a laser intensity of approximately 3 $kWcm^{-2}$ was delivered to the sample. Due to technical issues, most of the utilized experimental conditions were different from one Raman system to another—it is shown how this did not alter the obtained results, except for the detection mode which in both cases was fixed at the backscattering-detection mode (Figure 2).
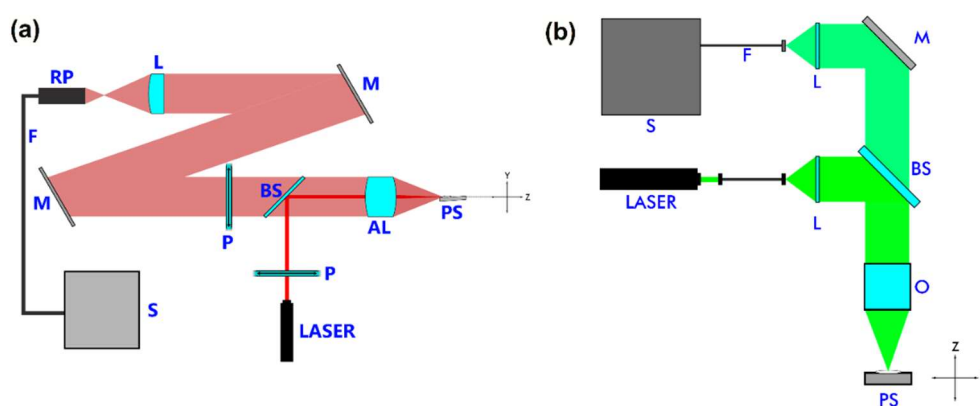

Figure 2. Scheme of the experimental configurations used for the acquisition of Raman spectra: (**a**) Custom-made featuring both configurations, polarized and non-polarized; (**b**) commercially available featuring only non-polarized measurements. From left to right: RP—Raman probe, F—filter, M—mirror, L—lens, P—polarizer, BS—beam splitter, AL—aspheric lens, PS—powdered sample, S—spectrometer, O—objective.

2.4. UV-Vis Diffuse Reflectances and Differential Thermal Analysis

An Ocean Optics USB2000+ UV-VIS Spectrometer and an R400-Angle-Vis Reflection probe were used to collect the diffuse reflectance (DR) spectra of the samples and an Ocean Optics DH-2000-BAL Deuterium-Halogen light source was utilized. Commercially available aluminum oxide (Al_2O_3) was chosen as the standard reference. Precautions were taken so that the approximations necessary to apply the Kubelka-Munk Theory were accomplished [27–29]. These approximations are, mainly speaking, a preparation of the sample being thick enough so that the measured reflectance does not change with further increasing of this parameter (avoidance of Fresnel reflection) and an averaged size of the particles being smaller than such thickness, but larger relative to the wavelength (scattering independent of the wavelength).

The first of these experimental conditions was fulfilled by using a self-supporting pressed powder rectangular mount ($3 \times 3 \times 3$ mm); in all the experiments, an amount of approximately 1 g of powder was deposited. The second requirement was fulfilled by determination of the average size particle in the powders, using a field emission Scanning Electron Microscopy (SEM), with a JEOL JSM 5600-LV microscope (V = 20 kV, at 1500×, Mitaka, Tokyo, Japan). The micrographs were analyzed with *ImageJ* software: The edge length histograms were obtained from statistical analysis of at least 200 particles. Lastly, we followed the recommendation of grinding the powders in an agate mortar for a few minutes

to avoid sample heterogeneity and regular reflection [29]: All samples were ground for 10 min before measurements.

On the other hand, the Curie temperatures for the samples LN-STm, LN + 1%NbP, LN + 2%NbP, and LN + 3%NbP were measured using differential scanning calorimetry (DSC) equipment coupled to thermogravimetry (TGA), SDT Q600 of TA instruments. The calorimeter was calibrated with respect to the copper melting point (1084 °C). The samples were analyzed in a wide temperature range between room temperature and 1200 °C, at a heating rate of 20 °C/min under a nitrogen atmosphere and using alumina containers. The ferroelectric-paraelectric state transition was observed around 1050–1080 °C. Subsequently, the samples were analyzed in four cooling cycles from 500 °C to 1200 °C at the same heating rate, 20 °C/min, and the process was seen to be reproducible, indicating that there was no permanent change in the volume of the pseudo-ilmenites.

3. Results and Discussion

3.1. X-Ray Diffraction

The obtained XRD pattern for sample LN-STm is shown in the bottom line of Figure 3a. The corresponding pattern of single crystalline LN is in agreement with the one indexed in COD-2101175 [23]. The difference, for all samples, between the obtained XRD patterns (I_{exp}) and their respective calculated patterns by means of Rietveld refinement (I_{ref}) is also shown in the upper half of this figure; for the secondary phases $LiNb_3O_8$ and Li_3NbO_4, ICSD-2921 and ICSD-75264 from The Inorganic Crystal Structure Database were used, respectively [25]. For all cases, this difference function tends to a common baseline, so that neither the formation of thermodynamically stable phases (other than $LiNbO_3$, Li_3NbO_4, and $LiNb_3O_8$) nor the presence of one of the precursors in an interstitial fashion can be deduced, that is, without participating in the formation of one of the involved phases. As seen in this figure, most of the synthesized powders resulted in a pure ferroelectric LN phase, except for samples LN + 4%NbP and LN + 5%NbP (blue lines). Figure 4 and Table 1 have been added for a better visualization of this argument. A loss of Li equivalent to the loss of 5 mol % Li_2CO_3 could be hastily addressed for the central sample LN-STm due to the calcination process. Nevertheless, this information can also be interpreted as having no loss of Li and thus the assumption of a non-ideal sensitivity for the XRD technique must be taken. In other words, a detection threshold of 5.0 mol % Li_2CO_3 = 1.4 mol % Nb_2O_5 exists for 'seeing' a secondary phase by the XRD analysis, combined with the structure refinement, done in this investigation. This assumption has been taken into account in this investigation, thus defining the boundaries that delimit the pure ferroelectric LN phase for samples LN-STm (Li excess) and LN+3%NbP (Nb excess). For the calculation of mol % equivalence between precursors, the values for the relative atomic masses of Li and Nb have been used as presented in the Periodic Table provided by the Royal Society of Chemistry [30].

The calculated cell volumes are plotted in Figure 3b, as a function of the averaged Nb content in the crystallites $\langle c_{Nb} \rangle$, as calculated by the previous procedure (re-labeling of the samples in terms of their predicted CC). A clear linear trend exists for a CC range of 49.7–52.1 mol % Nb_2O_5. Hence, for future reference, we first propose the determination of $\langle c_{Nb} \rangle$ for LNPws in this CC range with the following equation:

$$\langle c_{Nb} \rangle = (8.6207 V_{cell} - 2692.5216) mol \% \pm 0.5 \, mol \% \tag{2}$$

where V_{cell} stands for the cell volume in (angstrom)^3 units, calculated by a standard structure refinement method. The 0.5 mol % uncertainty is determined by the sum of the uncertainty associated to the linear fitting (0.14 mol % Nb_2O_5) and half the longer step in the Nb precursor (0.53/2 = 0.27 mol % Nb_2O_5), both multiplied by the square root of the averaged goodness of fit factor for the six involved samples ($\sqrt{1.55}$). The uncertainty associated with the linear fitting has been determined following several calculations according to Baird [31].
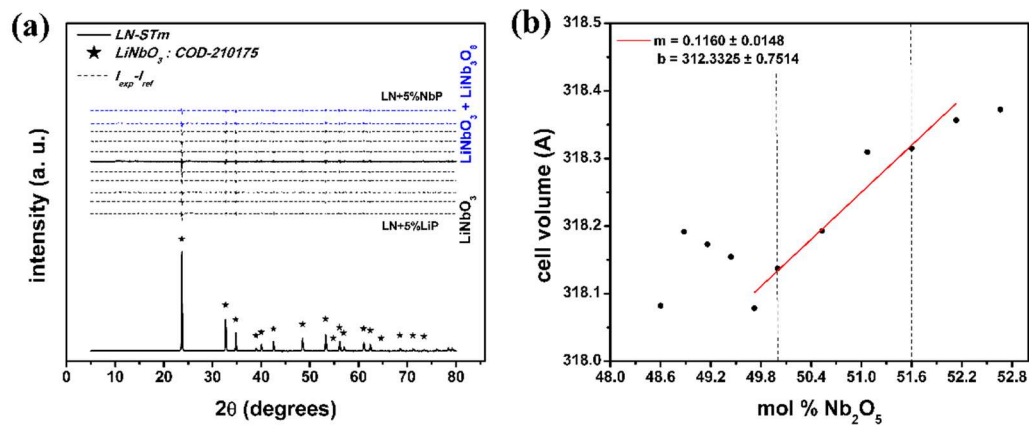
Figure 3. XRD results: (**a**) Experimental pattern of sample LN-STm and, for all samples, the differences between experimental and their respective calculated patterns with Rietveld refinement. The central sample, LN-STm, is distinguished from the rest by the solid line; (**b**) cell volume as a function of mol % Nb precursor. The edges of the ferroelectric pure LN phase are represented by the vertical dashed lines.
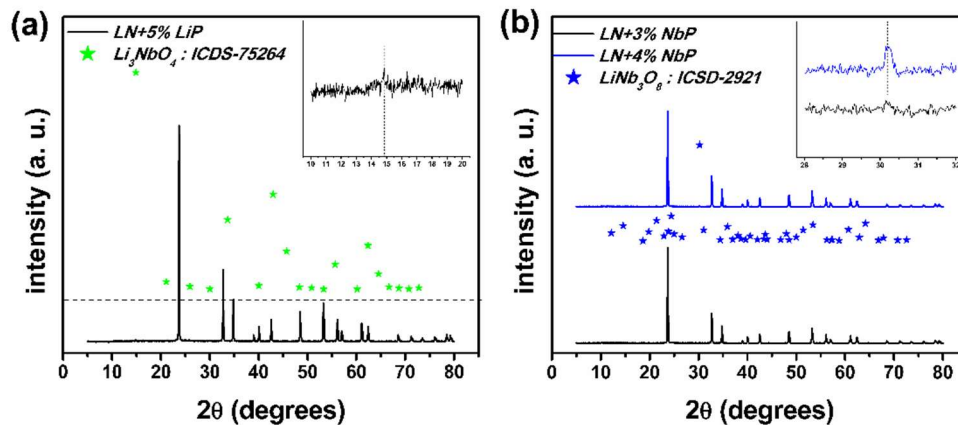

Figure 4. X-ray diffraction patterns close to the boundaries of the pure ferroelectric LN phase: (**a**) Under the assumption of no loss of Li, sample LN-STm is on the excess of the Li boundary; (**b**) sample LN + 3%NbP is on the excess of Nb boundary.

Table 1. Phase percentages present in the synthesized samples, along with the calculated cell volumes and relevant agreement indices of the refinement process.

Sample	% LiNbO3	% Li3NbO4	% LiNb3O8	Cell Volume ($\mathring{A}^3$)	Weighted R Profile	Goodness of Fit
LN+5%LiP	99.9	0.1	0	318.0820	5.82	2.03
LN+4%LiP	100	0	0	318.1917	5.24	1.48
LN+3%LiP	100	0	0	318.1732	5.58	1.50
LN+2%LiP	100	0	0	318.1546	5.60	1.49
LN+1%LiP	100	0	0	318.0787	5.70	1.52
LN-STm	100	0	0	318.1374	5.71	1.57
LN+1%NbP	100	0	0	318.1930	5.52	1.55
LN+2%NbP	100	0	0	318.3095	5.71	1.53
LN+3%NbP	100	0	0	318.3149	5.54	1.65
LN+4%NbP	98.2	0	1.8	318.3566	5.54	1.51
LN+5%NbP	97.8	0	2.2	318.2735	5.54	1.57

Justification of the Assumption made in the X-Ray Diffraction Analysis

The reasoning behind the assumption made can be summarized in three main points. First, a good agreement can be seen with the phase diagram (Figure 1), upon which by close inspection, around T = 850 °C, a CC range of approximately 1.7 mol % Nb_2O_5 is deduced for the pure ferroelectric LN phase. In this investigation, the observed range goes from the ST point $\langle c_{Nb} \rangle = 50.0$ mol % (sample LN-STm) to a near-CG point $\langle c_{Nb} \rangle = 53.0 - 1.4 = 51.6$ mol % (sample LN + 3%NbP), that is $\Delta c_{pureLN} = 1.6$ mol % Nb_2O_5. A direct explanation would not be found for an estimated range of 4.4 mol % Nb_2O_5 if this assumption had not been taken. Secondly, under these circumstances it follows that, out of 11 synthesized samples, only samples LN-STm, LN + 1%NbP, LN + 2%NbP, and LN+3%NbP resulted to have a pure ferroelectric LN phase. It will be soon shown that, for all the performed studies, unmistakable linear relationships happen to exist among these samples and their corresponding experimental parameters (related to the CC); a striking, very sensitive, deviation from these trends is observed for all samples out of this range, in some cases even under the consideration only of neighbor samples such as LN + 1%LiP and LN + 4%NbP. Lastly, besides the well-known difficulties to produce single-phase ST LN at temperatures used in solid-state reactions (T ≥ 1200 C) [32,33], much ambiguity can be found in the literature concerning deviation from stoichiometry in the formation of LNPws at calcination temperatures near T = 850 °C. While only one work is found to report no loss of Li after two 16-hour reaction periods at 1120 °C [34], other authors have observed the loss of Li at 600–800 °C within at least three different investigations [33,35,36]. However, these methods of synthesis are very different from each other, except for those in the works published in 2006 (Liu et al.) [33] and 2008 (Liu et al.) [36], which are aqueous soft-chemistry methods. The deviation from stoichiometry tendency in the formation of LNPws through aqueous soft-chemistry methods, in comparison to non-aqueous (as in this investigation), has already been identified [37]. Besides, high-energy milling has previously been proposed as a method to prevent loss of Li, in contrast to Pechini's method, sol-gel, and coprecipitation [21].

It is also worth mentioning that De Figueiredo et al. [38] had a similar observation in their investigation: They had a small amount of non-reacted Li_2CO_3 not detected by XRD, but only identified after DTA and Infrared Spectroscopy; the LNPws were synthesized via mechanical alloying. They explained this observation by assuming that the number and size of the Li_2CO_3 nanocrystals were sufficiently low and small to not being detected by XRD. Hence, the assumption taken of no loss of Li and the existence of a detection threshold of 1.4 mol % Nb_2O_5 in XRD might have been justified with these lines. This detection threshold can be considered unique and expected to change according to different experimental variables and analysis tools, including spatial and temporal size of the step during the experiment, brand, and model of equipment utilized, as well as the software used for Rietveld refinement, among others.

3.2. Raman Spectroscopy

Verification of the linear equation for the Raman active mode centered at 876 cm^{-1} [16,17] was done by using the assembled Raman system (Figure 2a) on the aforementioned stoichiometric (ST) and congruent (CG) lithium niobate (LN) wafers. Even though the experimental conditions therein described were not exactly reproduced, this could be accomplished within the given absolute accuracy and, thus, calibration of this equipment could be done. At this instance, use of the equation for the Raman band located at 876 cm^{-1} has been done [16,17]. A detailed description of the phonon branches of single crystal LN and their assignment can be found elsewhere [39,40]. No specifications regarding the resolution of the Raman bands or fitting techniques are given by Schlarb et al. [16] or Malovichko et al. [17], although these procedures are critical for achieving great accuracy in the determination of the LN CC [16,39–41]. Moreover, it is not clearly stated whether the complete linewidth (Γ), or just the halfwidth, is to be entered in this equation.

The resolution of this Raman band was explored, after normalization of the full spectra, by two distinct line shape fittings: Gaussian and Lorentzian. The Full Width at Half Maximum (FWHM; Γ)

was extracted from the fitting (*Origin Pro 8*) and used in the calculations. Change of the intercept value from 53.29 to 54.8 had also been tried, as suggested whenever no polished single crystals are available [16]. From all the calculations performed, we noticed that only for those (halfwidths) under a Lorentzian fit and using the intercept value of 54.8, the calculated Li contents follow this equation within the uncertainty of 0.2% mol, which "govern the absolute accuracy of the described method" [16]. The values obtained by this calculation were $\langle c_{Li} \rangle$ =50.3 mol % for the ST wafer and 48.5 mol % for the CG one. Thus, this approach has been adopted for the investigation with the LNPws. Before presenting these results, one more point needs to be further discussed.

It can be argued that the value of 50.3 mol % for the ST wafer goes out of the uncertainty range, thus not justifying the implications made above. Nevertheless, it must be noticed that the experimental conditions used in this investigation are subtly different from those described by Schlarb et al. [16] and Malovichko et al. [17]. Succinctly, they used an experimental *Z(YY)X* configuration (using Porto's convention [26]), whereas for our case, given certain technical limitations, a $Z(YY)\overline{Z}$ configuration was used in this investigation. Besides, no direct statement concerning the propagation of light along an axis of the crystals studied is done by these authors, but it can be inferred that they excited along the crystallographic Z-axis by recalling the condition of zero (or small) phonon directional dispersion to simplify their adjustments (band resolution) [16]. In our case, wafers with Z-cuts were used, upon which light was made to impinge on normal to the surface. The incident radiation then propagates in a plane containing the extraordinary axis, inducing in this way short-range atomic forces (extraordinary refractive index) that compete to long-range atomic forces behind the splitting of longitudinal optic (LO) and transverse optic (TO) phonons [42]. Significant changes in the Raman spectra of LN single crystals, especially in the position of the bands located at 153 cm^{-1} and 578 cm^{-1} (red and blue shifts), have already been identified and addressed to the overlapping of the LO and TO lattice vibrations [42–44]. Such an overlapping is clearly a drawback for band resolution and it might be the reason behind the discrepancy between predicted and measured values; interestingly, this is only relevant in single crystals of ST composition.

Application of the same procedure to the synthesized LNPws gives unsatisfactory results, according to the implications obtained from the XRD analysis (re-labeling of the samples in terms of their predicted CC, Figure 3b). As expected, the same occurs if this is applied to the non-polarized Raman spectra. It worsens considering the Raman band is located at 153 cm^{-1}, where the corresponding linear equation is used, and the Raman spectra are measured with the commercially available Raman system (Witec), which features recording of intensity in the range 0–200 cm^{-1}. However, well defined linear trends can be seen for the calculated Raman halfwidths around the pure LN ferroelectric phase, but only for the case of the band at 876 cm^{-1} as measured under non-polarized experimental conditions. For both situations (Witec and self-assembled systems), the trend is of an increasing halfwidth with decreasing Li content; surprisingly, despite the great differences between both experimental configurations and conditions (Figure 2), both trends are very similar. This feature can also be seen for the positions of the bands (x_c), and it remains for the resultant values of the halfwidths divided by the positions ($\Gamma/2x_c$). Figure 5b shows how this $\Gamma/2x_c$ parameter relates to the Nb content of the synthesized powders, as determined by XRD analysis. Given the similarity between the results obtained by both experimental configurations, this graph represents the average of such results. For sample LN-STm, the Raman spectra measured with the Witec system are shown in Figure 5a; these closely resemble those obtained in polycrystalline LN by Repelin et al. [40].
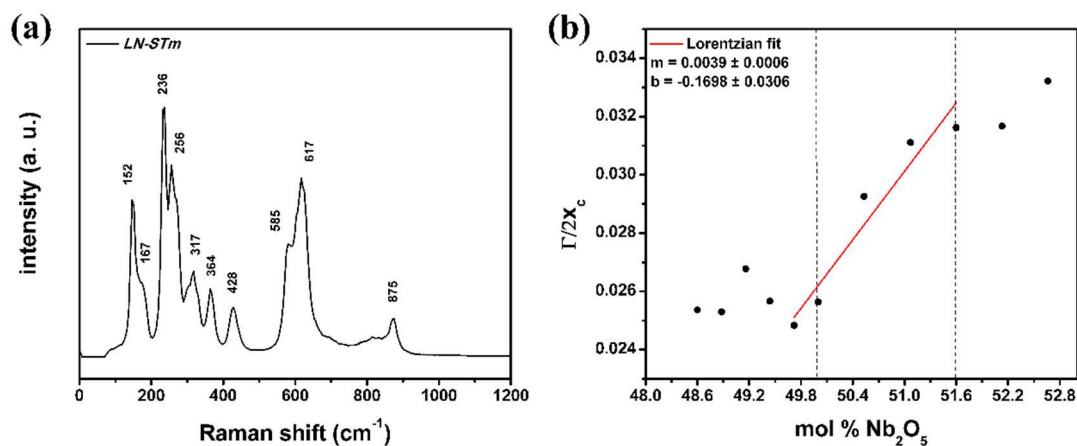
Figure 5. Results obtained by Raman Spectroscopy: (**a**) Non-polarized Raman spectra of the central sample LN-STm, obtained with the commercially available Raman system; (**b**) Linear trend upon which Equation (3) is based for the case of band resolution with a Lorentzian fit, averaged calculated data from those obtained by two distinct Raman systems.

As the resolution of this Raman band (876 cm^{-1}) by means of a Gaussian fitting does not entail significant changes either, the following equations are proposed for the determination of $\langle c_{Nb} \rangle$ in LNPws:

$$\langle c_{Nb} \rangle_L = \left(256.4103 * \left(\frac{\Gamma_L}{2x_c} \right) + 43.5385 \right) mol \,\% \ \pm 0.4 \ mol \,\%$$

$$\langle c_{Nb} \rangle_G = \left(588.2353 * \left(\frac{\Gamma_G}{2x_c} \right) + 42.7059 \right) mol \,\% \ \pm 0.5 \ mol \,\%$$

(3)

where Γ_i stands for the FWHM in cm^{-1} of the Raman band around 876 cm^{-1}, resolved by linear fitting either using a Lorentzian or a Gaussian line shape, x_c denotes the center of this Raman band. Normalization of the full Raman spectra precedes the linear fitting and, regardless of the line shape, enlargement around this band is suggested, extending it as much as possible (precise determination of the baseline) and applying a single or double-peak fitting, rather than performing a multi-peak fitting to the full Raman spectra. Like in the XRD analysis, the uncertainty is determined by summation over half the longer step in the Nb precursor (0.53/2 = 0.27 mol % Nb_2O_5), the uncertainty associated to the linear fitting (0.12 mol % Nb_2O_5 (0.23 mol % Nb_2O_5) for the Lorentzian (Gaussian) case), and dividing by the square root of the averaged (five involved samples) reduced χ^2 fit factor obtained in the resolution of the band $\sqrt{0.9823}$ ($\sqrt{0.9866}$). Once more, the uncertainty associated to the linear fitting is determined following several calculations according to Baird [31].

Lastly, the fact that the trend remains linear is not surprising. Scott and Burns [34] have previously demonstrated this, based on experimentation; showing in this way that the Raman spectra from poly-crystalline LN inherits the essential features of those from single crystal LN [45]. Conceptually, this can be understood by recalling the intrinsic nature of LN to deviate from the stoichiometric point. Under regular circumstances, LN contains high amounts of intrinsic defects such as anti-site Nb ions (Nb_{Li}), which are compensated by their charge-compensating Li vacancies (V_{Li}) [3,46]. Such a substitution mechanism imposes fundamental changes on the electronic structure, inducing in this way, variations in the macroscopic dielectric tensor of LN [16]. Yet, because in this substitution mechanism gradual Nb increments are proportional to the decreasing of Li, the variations of the dielectric tensor are expected to be linear, as far as the Nb-Li interchange is sufficiently small.

3.3. UV-Vis Diffuse Reflectances and Differential Thermal Analysis

The sensitivity of the chemical composition (CC) of lithium niobate (LN) to the fundamental band gap or fundamental absorption edge has been previously reported for LN single crystals [47,48]. Kovács et al. have given a corresponding linear equation with different sets of fitting parameters, depending on the character of the refractive index (ordinary and extraordinary), and the definition

of the absorption edge (either as corresponding to a value in the absorption coefficient of 20 cm^{-1} or 15 cm^{-1}) [48]. There is no point in using this equation to describe the CC of LNPws, since these terms (refractive index and absorption coefficient) make no sense when related to powders.

　　In this investigation, the direct measurements of the DR spectra for the 11 samples are transformed to the Kubelka-Munk (K-M) or *remission* function $F(R_\infty)$, straightforwardly with the acquisition software (*Spectra Suite*). Since this function is a proxy of the actual absorption spectrum [29], these data are used to find the fundamental absorption edge for all the samples. For practical purposes, a direct band gap is assumed for LN—notice that it could also be assumed to be indirect [49]. Thus, under this assumption, the fundamental band gap is proportional to the square of the remission function, as is shown in Figure 6a,b. The Nb content of LNPws is linearly related to the fundamental band gap E_g (Figure 6c). Equation (4) allows us to accurately determine the Nb content of a determined sample, in terms of E_g (in eV units).

$$\langle c_{Nb}\rangle = \left(3.9078 * E_g + 34.6229\right)mol\ \%\ \pm 0.4\ mol\ \%\tag{4}$$
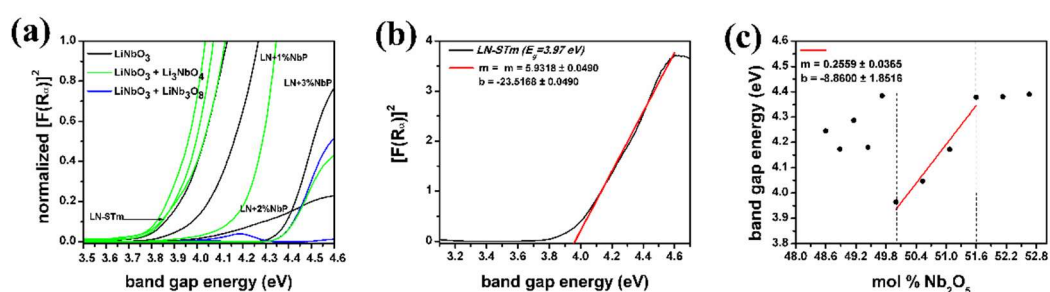

Figure 6. Graphics derived from analysis of the data obtained by UV-vis Diffuse Reflectance measurements: (**a**) Normalized Kubelka-Munk or remission functions in terms of the energy of the light in eV units; (**b**) Demonstration of the determination of the onset for sample LN-STm (assuming a direct interband transition) to determine the fundamental band gap energy; (**c**) Fundamental band gap energy as a function of mol % Nb precursor.

　　Interaction of light with matter at a fundamental level must be considered in the DR and Raman Spectroscopy techniques. In other words, because of the ubiquitous randomness of the media, strong scattering effects are present in both Rayleigh (crystallite size) and Mie scattering (particle size). The study of the intensity and angular distribution of the scattered field by the powders has not been done on this investigation; however, certainty of the results obtained by these techniques is expected under certain limits if no large variations in the crystallite and particle average sizes are found. Considering all the synthesized samples, the resultant average crystallites are distributed in a 100–300 nm range, with overall mean and standard deviation values of 157 and 58 nm, respectively. Also, for four randomly chosen samples, the distributions in particle size were determined by statistical analysis of micrographs obtained by Scanning Electron Microscopy (SEM). The obtained distributions were very similar and the centers (x_c) of these distributions fall within a band 1 μm thick, centered at 2.6 μm, as shown in Figure 7.
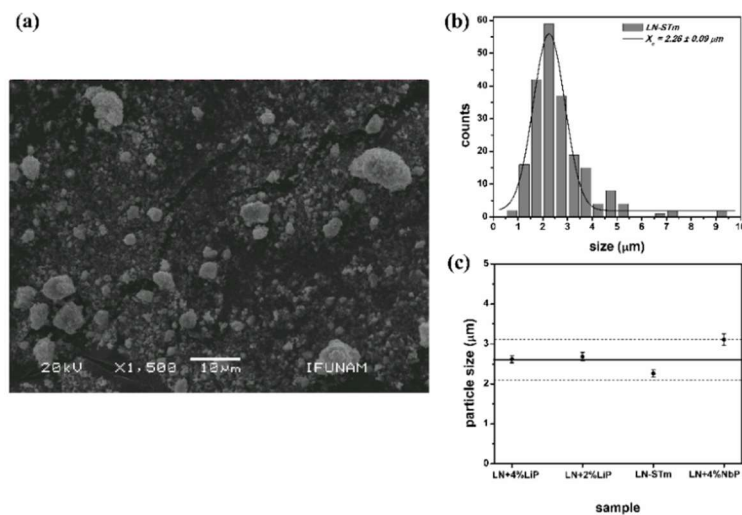
Figure 7. Information derived from SEM: (**a**) and (**b**) Micrograph and particle size distribution for sample LN-STm, respectively; (**c**) Centers of the particle size distributions obtained for four randomly-chosen samples.

Regarding the ferroelectric-paraelectric phase transition, a change in the crystalline structure of LN occurs in which the symmetry of the system increases [3]. This second-order phase transition is described by the Landau order-disorder theory, where a finite discontinuity in the heat capacity of the system having this transition has been addressed as a direct thermodynamic consequence [50]. Figure 8a shows the difference in temperature between the reference container for each of the studied samples; with this technique, only samples presenting a pure LN ferroelectric phase have been investigated. The Curie temperatures are determined by the extrapolated departure from the baseline, these being plotted in Figure 8b in terms of the Nb content. A nonlinear quadratic trend better describes this relation, with fitting coefficients A = 18623.560, B = -667.969, and C = 6.383; as expected, this is also the case for LN single crystals [51]. Nevertheless, use of the linear fitting coefficients is done in the analysis that follows, so that a simple calculation of an uncertainty value follows by use of Equation (5), where the Curie temperature T_C, is in Celsius.

$$\langle c_{Nb} \rangle = (-0.0515 * T_c + 110.8505) mol \% \ \pm 0.4 \ mol \% \tag{5}$$
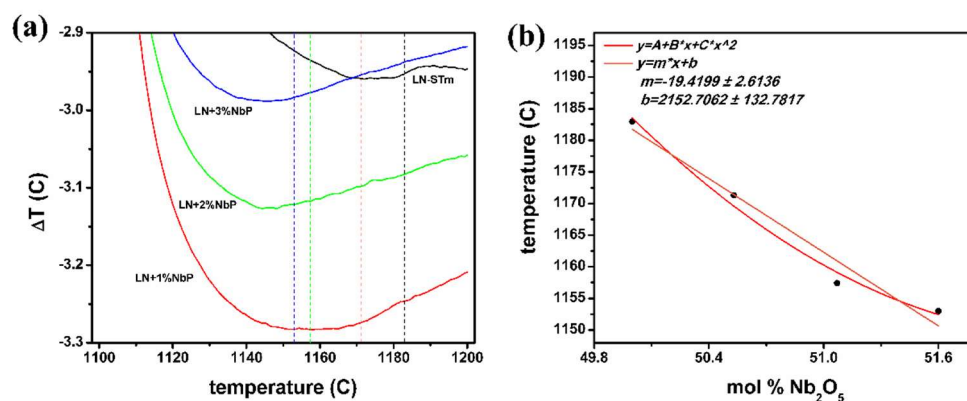

Figure 8. Thermometric results: (**a**) Curie temperatures as a function of mol % Nb precursor; (**b**) Obtained curves for samples within the pure LN phase. The Curie temperatures are determined by extrapolation of the departure from the baseline.

Use of this equation gives an estimate of T_C = 1181.56 °C (1153.41 °C for a ST (CG) powder); whereas, with the quadratic expression, it is of 1182.61 °C and 1153.01 °C, respectively. These values vary in no more than 0.1%. Regarding single crystals, a variation of 0.7% can be found for the Curie temperatures calculated for these CCs, by use of equations reported in two independent investigations [51,52]. Using the equation given by Bordui et al. [52], the calculated values are T_C = 1206.47 °C (1149.83 °C) for the ST (CG) crystal. Thus, contrary to what was believed, not a unique description of the LN CC regardless of its version (powder or single crystal) can be formulated by DTA either. This observation of the T_C being lower for ST LNPws, with respect to ST LN crystals, has been previously noticed [36], apart from the observations highlighted in the introduction. A straight explanation of this subtlety cannot be found nowadays in the literature. A classic theoretical development shows that the energy of the vibrations within the structure is the dominant contribution to the heat capacity—if the elastic response of a crystal is a linear function of the applied forces [53]. Thus, it is inferred that this might be explained under consideration of anharmonic crystal interactions, that is, phonon-phonon coupling. Still, further investigations on these matters are needed.

Lastly, it is acknowledged that in contrast to pioneering works (on LN single crystals, References [16] and [17]) the Equations (2)–(5) here give the averaged Nb content in the crystallites $\langle c_{Nb} \rangle$ instead of $\langle c_{Li} \rangle$. Although a simpler comparison with data in the literature could have been attained by putting these equations in terms of $\langle c_{Li} \rangle$, it was decided to do it in terms of $\langle c_{Nb} \rangle$ because of a simpler interpretation and association with a phase diagram describing LN, like that given in Figure 1. It has been noticed that most of the phase diagrams existent in the literature to describe LN, not to say all, are presented in terms of Nb_2O_5 mol %. This is readily understood since even in the fabrication of large LN single crystals, melts of Nb_2O_5 and another compound containing Li are used [3,20]. The equivalent equations in terms of $\langle c_{Li} \rangle$ are given in Appendix B.

3.4. Grinding of a Single Crystal

The bought single crystal with stoichiometric composition, described above, was turned into powder with ST composition. Low-energy grinding with an agate mortar was employed discontinuously in several steps until an averaged particle size of 1.6 μm (checked by SEM) was reached. In some instances, commercial acetone (purity ≥ 99.5%, Sigma-Aldrich) was used to ease the grinding, especially during its initial stages. Verification of Equations (2) and (3) was sought by repeating the experimental procedures performed on the synthesized powders; in the case of Raman Spectroscopy (RS), only the commercially available system (Witec alpha 300R) was used. The results obtained are shown in Table 2. While RS does imply a chemical composition according to what was expected, stoichiometrically (50 mol % Nb_2O_5), the structure refinement does not. This can be attributed to changes of the lattice parameter (lattice distortion) due to a variable local lattice strain frequently observed in nanocrystalline materials, induced by excess of volume at the grain boundaries [54]. Remarkably, our powdered single crystal differs from the synthesized powders in the averaged crystallite size: On the latter, a myriad of nanosized crystals (100–300 nm) form large particles of the order of 2–3 μm (see Figure 7c), while on the former it can be argued that crystallite size equals the particle size; actually, the applied Rietveld refinement for the calculation of the averaged crystallite size of the grinded crystal does not converge. These implications must be confirmed and scrutinized by further investigation. Lastly, since Equation (3) is strongly dependent on the XRD analysis (re-labeling of the samples in terms of their predicted CC), the Raman results shown in Table 2 demonstrate the reliability of our method.

Table 2. Estimated chemical composition for the grinded single crystal.

Experimental Technique	Measured Parameter	Associated Error Parameter	Equation Utilized	Nb Content (mol % Nb_2O_5)
XRD + Rietveld refinement	Cell volume: 317.9234 A°	Goodness of Fit: 1.8756	(2)	48.2
Raman Spectroscopy	Γ/x_c: 45.3038cm^{-1}/873.9676 cm^{-1}	Reduced $\chi^{(2)}$: 4.70 × 10^{-6}	(3), Lorentz fit	50.2
	Γ/x_c: 21.8202cm^{-1}/874.1964 cm^{-1}	Reduced $\chi^{(2)}$: 8.38 × 10^{-6}	(3), Gaussian fit	50.1

4. Conclusions

Despite the increasing interest in lithium niobate powders (LNPws) due to their importance in possible applications in actual and future nanooptoelectronic devices, as well as the facility to produce them in large quantities, an accurate and trusting method to determine their chemical composition (CC) does not exist, to the best of our knowledge. Therefore, in this work a first step is given in this direction by developing a facile method based mainly on imposing X-Ray Diffraction (XRD) as a seed characterization technique. Raman Spectroscopy, UV-vis Diffuse Reflectance and Differential Thermal Analysis enrich this work, representing various alternatives for the independent and accurate determination of the CC of LNPws. An empirical equation that describes this fundamental property in terms of a corresponding experimental parameter is given for each of these four characterization techniques.

We wish to underline here the main aspects of our method. It is primarily based on the quantification of pure and secondary phase percentages by XRD, followed by Rietveld structure refinement. Secondly, relying on the LN phase diagram, the CCs of the studied samples are inferred, and thereafter labeled in terms of the Nb content in the crystallites. Lastly, having done this, any of the mentioned characterization techniques can be used to relate such a labeling with their corresponding experimental parameter. In the case of a user who wants to determinate the CC of LNPws only, he/she would only need to perform the last step and make use of any of Equations (2)–(5), respectively. On the other hand, in the case of wanting to describe other powders apart from LNPws, the whole method (three main steps described above) might be further applied inasmuch as akin materials are to be investigated, lithium tantalate ($LiTaO_3$) powders for example.

The validity of this methodology is proven self-consistently with the determination of the CC of several samples, where the content of Li and Nb is varied in a controlled way. According to a paramount observation made in the peer reviewing process of this article, the main shortcoming of this investigation is the large uncertainty associated with Equations (2)–(5). Rigorously, they should not be used for a practical composition determination and, instead, it only could be stated with more confidence that, by using these equations, the composition of a LN powder would be closer to the stoichiometric or congruent compositions, or rather in an intermediate state. However, both, the resolution and the associated uncertainties of this methodology, can be significantly improved by analyzing larger quantities of powder. As mentioned in the details related to the uncertainty calculations and given after introducing Equations (2) and (3), the major contribution to uncertainty emerges from the determination of the boundaries of the pure ferroelectric LN phase: Determined by dividing the $\Delta c_{pureLN} = 1.6$ mol % Nb_2O_5 by three increasing steps of Nb content, and then dividing by 2 (0.53/2 = 0.27 mol % Nb_2O_5). The associated uncertainty to Equations (2)–(5) can be significantly reduced if a larger number of samples are synthesized in this range, which can be more easily achieved if larger quantities of powder are prepared. As an example, it is expected that by synthesizing approximately 10 g of powder, around 40 points would be available for analysis if the increasing step is fixed at 0.1% in the mass of the Nb precursor, resulting in a decrease in the overall uncertainties of about 50–80% (noticing that the uncertainty associated with the linear fitting would also be reduced significantly). Conclusively, although it is acknowledged that the proposed equations are not universal in the sense that they may only describe the CC of LNPws with specific physical properties (crystallite and particle dimensions), this work paves the way to furnish a general description and claims the attention of the community advocated to this field to broaden the present results. For a more general description, besides the synthesis of larger number of samples, the influence of other experimental factors and parameters such as the method of synthesis, the beam spot size, the intensity of light (Raman Spectroscopy), the averaged crystallite and particle size, and randomness, among others, should be considered in future investigations.

No full credit for all the ideas developed in this work is to be taken. The idea of determining the CC of LNPws by means of a linear fit to data obtained from Raman spectra was first conceived in the pioneering work of Scott and Burns in 1972 [34]. Indeed, no equation is given in this work, but it could be easily extracted from Figure 3 (in Reference [34]) to describe LNPws instead of LN single crystals;

again, it would not be easy to decide whether the complete linewidth (Γ), or just the halfwidth, is to be entered in such a hypothetical equation, and if a Lorentizian or Gaussian distribution is to be used. The work of Scott and Burns is also a pioneer to the ideas conceived by Schlarb et al. [16] and Malovichko et al. [17], whom later in 1993 exploited this fruitful result and demonstrated that other optical processes, besides Raman Spectroscopy, resulted into data that fit linearly with the LN CC. Also, regarding Equation (2), the previous observation of an increase of the lattice parameters or cell volume with increasing Nb content is also acknowledged [55]. An equation is formulated in Reference [18] from the data given in [55]. Interestingly, equation (4) in Reference [18] is almost the same as Equation (A1), given in Appendix B, if the slope and intercept values of the latter are divided by a constant value of 2.58; the very small discrepancy might be attributed to variation in the local lattice strain, as discussed above where the results of grinding a LN single crystal of stoichiometric composition are presented. At last, apart from providing four distinct alternatives to describe accurately the CC of LNPws (instead of single crystalline LN), what is innovative in the present work is the self-consistency character of the whole method: no other technique is needed to confirm the CC of the powders since the determination of the pure ferroelectric LN phase boundaries by XRD analysis suffices for this purpose. The four distinct methods are based on standard characterization techniques, accessible nowadays to large scientific communities in developing countries.

Author Contributions: Conceptualization, O.S.-D., C.D.F.-R. and R.F.; methodology, O.S.-D. and C.D.F.-R.; software, O.S.-D.; validation, A.S.P.-R. and S.H.-L.; formal analysis, O.S.-D.; investigation, O.S.-D., C.J.V., C.D.F.-R., E.V.-S. and S.H.-L.; resources, C.J.V., R.F., E.V.-S. and J.-A.R.-E.; writing—original draft preparation, O.S.-D.; writing—review and editing, J.-A.R.-E.; visualization, C.D.F.-R. and A.S.P.R.; supervision, R.F. and J.-A.R.-E.; project administration, J.-A.R.-E.; funding acquisition, J.-A.R.-E.

Conflicts of Interest: The authors declare no conflict of interest. The funders had no role in the design of the study; in the collection, analyses, or interpretation of data; in the writing of the manuscript, or in the decision to publish the results.

Appendix A

In the following table the measured values for the masses of the precursors used in each of the 11 synthesis procedures are given.

Sample	Nb$_2$O$_5$ Mass (g)	Li$_2$CO$_3$ Mass (g)	Sample	Nb$_2$O$_5$ Mass (g)	Li$_2$CO$_3$ Mass (g)
LN+5%LiP	0.8989	0.2622	LN+1%NbP	0.9079	0.2498
LN+4%LiP	0.8988	0.2598	LN+2%NbP	0.9167	0.2496
LN+3%LiP	0.8991	0.2574	LN+3%NbP	0.9259	0.2497
LN+2%LiP	0.8990	0.2547	LN+4%NbP	0.9348	0.2498
LN+1%LiP	0.8989	0.2523	LN+5%NbP	0.9438	0.2498
LN-STm	0.8990	0.2498			

Appendix B

Equations in terms of the averaged Li content in the crystallites $\langle c_{Li} \rangle$ would also be useful, especially when comparing to measurements on single crystals described elsewhere [16–18]. Equations (2)–(5) in terms of $\langle c_{Li} \rangle$ are:

$$\langle c_{Li} \rangle = (-7.6453 V_{cell} + 2482.2171) mol\,\% \ \pm 0.5\ mol\,\% \tag{A1}$$

$$\langle c_{Li} \rangle_L = \left(-259.0674 * \left(\frac{\Gamma_L}{2x_c}\right) + 56.8135\right) mol \% \ \pm 0.4 \ mol \%$$

$$\langle c_{Li} \rangle_G = \left(-588.2353 * \left(\frac{\Gamma_G}{2x_c}\right) + 58.0412\right) mol \% \ \pm 0.5 \ mol \% \tag{A2}$$

$$\langle c_{Li} \rangle = \left(-3.9602 * E_g + 65.5987\right) mol \% \ \pm 0.4 \ mol \% \tag{A3}$$

$$\langle c_{Li} \rangle = \left(0.0519 * T_c - 11.3805\right) mol \% \ \pm 0.4 \ mol \% \tag{A4}$$

References

1. Ballman, A.A. Growth of Piezoelectric and Ferroelectric Materials by the Czochralski Technique. *J. Am. Ceram. Soc.* **1965**, *48*, 112–113. [CrossRef]

2. MTI Corporation, LiNbO3 & Doped. Available online: http://www.mtixtl.com/linbo3.aspx (accessed on 29 January 2019).

3. Volk, T.; Wöhlecke, M. Point Defects in LiNbO$_3$. In *Springer Series in Materials Science. Lithium Niobate. Defects, Photorefraction and Ferroelectric Switching*, 1rst ed.; Hull, R., Osgood, R.M., Jr., Parisi, J., Warlimont, H., Eds.; Springer: Berlin/Heidelberg, Germany, 2009; Volume 115, pp. 9–50. ISBN 978-3-540-70765-3.

4. Weis, R.S.; Gayklord, T.K. Lithium Niobate. Summary of Physical Properties and Crystal Structure. *Appl. Phys. A* **1985**, *37*, 191–203. [CrossRef]

5. Luo, R.; Jiang, H.; Rogers, S.; Liang, H.; He, Y.; Lin, Q. On-chip second-harmonic generation and broadband parametric down-conversion in a lithium niobate microresonator. *Opt. Exp.* **2017**, *25*, 24531–24539. [CrossRef] [PubMed]

6. Pang, C.; Li, R.; Li, Z.; Dong, N.; Cheng, C.; Nie, W.; Bötger, R.; Zhou, S.; Wang, J.; Chen, F. Lithium Niobate Crystal with Embedded Au Nanoparticles: A New Saturable Absorber for Efficient Mode-Locking of Ultrafast Laser Pulses at 1μm. *Adv. Opt. Mater.* **2018**, *6*, 1800357. [CrossRef]

7. Kurtz, S.K.; Perry, T.T. A Powder Technique for the Evaluation of Nonlinear Optical Materials. *J. Appl. Phys.* **1968**, *39*, 3798–3812. [CrossRef]

8. Aramburu, I.; Ortega, J.; Folcia, C.L.; Etxebarria, J. Second harmonic generation by micropowders: A revision of the Kurtz-Perry method and its practical application. *Appl. Phys. B: Lasers Opt.* **2014**, *116*, 211–233. [CrossRef]

9. Nath, R.K.; Zain, M.F.M.; Kadhum, A.A.H. Artificial Photosynthesis using LiNbO$_3$ as Photocatalyst for Sustainable and Environmental Friendly Construction and Reduction of Global Warming: A Review. *Catal. Rev. Sci. Eng.* **2013**, *56*, 175–186. [CrossRef]

10. Yang, W.C.; Rodriguez, B.J.; Gruverman, A.; Nemanich, R.J. Polarization-dependent electron affinity of LiNbO$_3$ surfaces. *Appl. Phys. Lett.* **2004**, *85*, 2316–2318. [CrossRef]

11. Fierro-Ruíz, C.D.; Sánchez-Dena, O.; Cabral-Larquier, E.M.; Elizalde-Galindo, J.T.; Farías, R. Structural and Magnetic Behavior of Oxidized and Reduced Fe Doped LiNbO$_3$ Powders. *Crystals* **2018**, *8*, 108. [CrossRef]

12. Kudinova, M.; Humbert, G.; Auguste, J.L.; Delaizir, G. Multimaterial polarization maintaining optical fibers fabricated with powder-in-tube technology. *Opt. Mater. Express* **2017**, *10*, 3780–3790. [CrossRef]

13. Sánchez-Dena, O.; García-Ramírez, E.V.; Fierro-Ruíz, C.D.; Vigueras-Santiago, E.; Farías, R.; Reyes-Esqueda, J.A. Effect of size and composition on the second harmonic generation from lithium niobate powders at different excitation wavelengths. *Mater. Res. Express* **2017**, *4*, 035022. [CrossRef]

14. Skipetrov, S.E. Disorder is the new order. *Nature* **2004**, *432*, 285–286. [CrossRef]

15. Knabe, B.; Buse, K.; Assenmacher, W.; Mader, W. Spontaneous polarization in ultrasmall lithium niobate nanocrystals revealed by second harmonic generation. *Phys. Rev. B* **2012**, *86*, 195428. [CrossRef]

16. Schlarb, U.; Klauer, S.; Wesselmann, M.; Betzler, K.; Wöhlecke, M. Determination of the Li/Nb ratio in Lithium Niobate by Means of Birefringence and Raman Measurements. *Appl. Phys. A* **1993**, *56*, 311–315. [CrossRef]

17. Malovichko, G.I.; Grachev, V.G.; Kokanyan, E.P.; Schirmer, O.F.; Betzler, K.; Gather, B.; Jermann, F.; Klauer, S.; Schlarb, U.; Wöhlecke, M. Characterization of stoichiometric LiNbO$_3$ grown from melts containing K$_2$O. *Appl. Phys. A: Mater. Sci. Process.* **1993**, *56*, 103–108. [CrossRef]

18. Wöhlecke, M.; Corradi, G.; Betzler, K. Optical methods to characterise the composition and homogeneity of lithium niobate single crystals. *Appl. Phys. B* **1996**, *63*, 323–330. [CrossRef]

19. Zhang, Y.; Guilbert, L.; Bourson, P.; Polgár, K.; Fontana, M.D. Characterization of short-range heterogeneities in sub-congruent lithium niobate by micro-Raman spectroscopy. *J. Phys. Condens. Matter* **2006**, *18*, 957–963. [CrossRef]

20. Hatano, H.; Liu, Y.; Kitamura, K. Growth and Photorefractive Properties of Stoichiometric LiNbO$_3$ and LiTaO$_3$. In *Photorefractive Materials and Their Applications 2*, 1st ed.; Günter, P., Huignard, J.P., Eds.; Springer Series in Optical Sciences: New York, NY, USA, 2007; pp. 127–164.

21. Kong, L.B.; Chang, T.S.; Ma, J.; Boey, F. Progress in synthesis of ferroelectric ceramic materials via high-energy mechanochemical technique. *Prog. Mater. Sci.* **2008**, *53*, 207–322. [CrossRef]

22. Suryanarayana, C. Mechanical alloying and milling. *Prog. Mater. Sci.* **2001**, *46*, 1–184. [CrossRef]

23. Crystallographic Open Database, Information for card entry 2101175. Available online: http://www.crystallography.net/cod/2101175.html (accessed on 29 January 2019).

24. Degen, T.; Sadki, M.; Bron, E.; König, U.; Nènert, W. The HighScore suite. *Powder Diffr.* **2014**, *29*, S13–S18. [CrossRef]

25. FIZ Karlsruhe ICSD, ICDS- Inorganic Crystal Structure Database. Available online: www2.fiz-karlsruhe.de/icsd_home.html (accessed on 29 January 2019).

26. Porto, S.P.S.; Krishnan, R.S. Raman Effect of Corundum. *J. Chem. Phys.* **1967**, *47*, 1009–1011. [CrossRef]

27. Kubelka, P. New Contributions to the Optics of Intensely Light-Scattering Materials. Part I. *J. Opt. Soc. Am.* **1948**, *38*, 448–457. [CrossRef]

28. Kubelka, P. New Contributions to the Optics of Intensely Light-Scattering Materials. Part II: Nonhomogeneous Layers. *J. Opt. Soc. Am.* **1954**, *44*, 330–335. [CrossRef]

29. Torrent, J.; Barrón, V. Diffuse Reflectance Spectroscopy. In *Methods of Soil Analysis Part5—Mineralogical Methods*, 1st ed.; Ulery, A.L., Drees, R., Eds.; Soil Science Society of America: Wisconsin, WI, USA, 2008; pp. 367–385.

30. The Royal Society of Chemistry, Periodic Table. Available online: http://www.rsc.org/periodic-table (accessed on 29 January 2019).

31. Baird, D.C. *Experimentation: An Introduction to Measurement Theory and Experiemtn Design*, 3rd ed.; Prentice-Hall: Englewood Cliffs, NJ, USA, 1995; pp. 129–133.

32. Kalinnikov, V.T.; Gromov, O.G.; Kunshina, G.B.; Kuz'min, A.P.; Lokshin, E.P.; Ivanenko, V.I. Preparation of LiTaO$_3$, LiNbO$_3$, and NaNbO$_3$ from Peroxide Solutions. *Inorg. Mater.* **2004**, *40*, 411–414. [CrossRef]

33. Liu, M.; Xue, D.; Luo, C. Wet chemical synthesis of pure LiNbO$_3$ powders from simple niobium oxide Nb$_2$O$_5$. *J. Alloys Compd.* **2006**, *426*, 118–122. [CrossRef]

34. Scott, B.A.; Burns, G. Determination of Stoichiometry Variations in LiNbO$_3$ and LiTaO$_3$ by Raman Powder Spectroscopy. *J. Am. Ceram. Soc.* **1972**, *55*, 225–230. [CrossRef]

35. Liu, M.; Xue, D. An efficient approach for the direct synthesis of lithium niobate powders. *Solid State Ionics* **2006**, *177*, 275–280. [CrossRef]

36. Liu, M.; Xue, D.; Li, K. Soft-chemistry synthesis of LiNbO$_3$ crystallites. *J. Alloys Compd.* **2008**, *449*, 28–31. [CrossRef]

37. Nyman, M.; Anderson, T.M.; Provencio, P.P. Comparison of Aqueous and Non-aqueous Soft-Chemical Syntheses of Lithium Niobate and Lithium Tantalate Powders. *Cryst. Growth Des.* **2009**, *9*, 1036–1040. [CrossRef]

38. De Figueiredo, R.S.; Messaia, A.; Hernandes, A.C.; Sombra, A.S.B. Piezoelectric lithium niobate obtained by mechanical alloying. *J. Mater. Sci. Lett.* **1998**, *17*, 449–451. [CrossRef]

39. Pezzotti, G. Raman spectroscopy of piezoelectrics. *J. Appl. Phys.* **2013**, *113*, 211301. [CrossRef]

40. Repelin, Y.; Husson, E.; Bennani, F.; Proust, C. Raman spectroscopy of lithium niobate and lithium tantalite. Force field calculations. *J. Phys. Chem. Solids* **1999**, *60*, 819–825. [CrossRef]

41. Thermo Fisher Scientific, Application Note: Curve Fitting in Raman and IR Spectroscopy. Available online: https://www.thermofisher.com/search/results?query=Curve%20Fitting%20in%20Raman&focusarea=Search%20All (accessed on 29 January 2019).

42. Tuschel, D. The Effect of Microscope Objectives on the Raman Spectra of Crystals. *Spectroscopy* **2017**, *32*, 14–23.

43. Maïmounatou, B.; Mohamadou, B.; Erasmus, R. Experimental and theoretical directional dependence of optical polar phonons in the LiNbO$_3$ single crystal: New and complete assignment of the normal mode frequencies. *Phys. Status Solidi B* **2016**, *253*, 573–582. [CrossRef]

44. Yang, X.; Lang, G.; Li, B.; Wang, H. Raman Spectra and Directional Dispersion in LiNbO$_3$ and LiTaO$_3$. *Phys. Status Solidi B* **1987**, *142*, 287–300. [CrossRef]

45. Balanevskaya, A.É.; Pyatigorskaya, L.I.; Shapiro, Z.I.; Margolin, L.N.; Bovina, E.A. Determination of the composition of LiNbO$_3$ specimens by Raman spectroscopy. *J. Appl. Spectrosc.* **1983**, *38*, 491–493. [CrossRef]

46. Kovács, L.; Kocsor, L.; Szaller, Z.; Hajdara, I.; Dravecz, G.; Lengyel, K.; Corradi, G. Lattice Site of Rare-Earth Ions in Stoichiometric Lithium Niobate Probed by OH$^-$ Vibrational Spectroscopy. *Crystals* **2017**, *7*, 230. [CrossRef]

47. Redfield, D.; Burke, W.J. Optical absorption edge of LiNbO$_3$. *J. Appl. Phys.* **1974**, *45*, 4566–4571. [CrossRef]

48. Kovács, L.; Ruschhaupt, G.; Polgár, K.; Corradi, G.; Wöhlecke, M. Composition dependence of the ultraviolet absorption edge in lithium niobate. *Appl. Phys. Lett.* **1997**, *70*, 2801–2803. [CrossRef]

49. Thierfelder, C.; Sanna, S.; Schindlmayr, A.; Schmidt, W.G. Do we know the band gap of lithium niobate? *Phys. Satus Solidi C* **2010**, *7*, 362–365. [CrossRef]

50. Devonshire, A.F. Theory of ferroelectrics. *Adv. Phys.* **1954**, *3*, 85–130. [CrossRef]

51. O'Bryan, H.M.; Gallagher, P.K.; Brandle, C.D. Congruent Composition and Li-Rich Phase Boundary of LiNbO$_3$. *J. Am. Ceram. Soc.* **1985**, *68*, 493–496. [CrossRef]

52. Bordui, P.F.; Norwood, R.G.; Jundt, D.H.; Fejer, M.M. Preparation and characterization of off-congruent lithium niobate crystals. *J. Appl. Phys.* **1992**, *71*, 875–879. [CrossRef]

53. Kittel, C. *Introduction to Solid State Physics*, 7th ed.; John Wiley & Sons: New York, NY, USA, 1996; pp. 99–130.

54. Quin, W.; Nagase, T.; Umakoshi, Y.; Szpunar, J.A. Relationship between microstrain and lattice parameter change in nanocrystalline materials. *Philos. Mag. Lett.* **2008**, *88*, 169–179. [CrossRef]

55. Iyi, N.; Kitamura, K.; Izumi, F.; Yamamoto, J.K.; Hayashi, T.; Asano, H.; Kimura, S. Comparative study of defect structures in lithium niobate with different compositions. *J. Sol. State Chem.* **1992**, *101*, 340–352. [CrossRef]